Modelling Jupiter in the Juno-era: Non-uniform Internal Heat Flux and the Water-ammonia Cycle



DPhil Thesis

submitted in partial fulfillment of the
requirements for the degree of

Doctor of Philosophy

in

Atmospheric, Oceanic & Planetary Physics

Author: Xinmiao Hu
Supervisors: Prof. P. L. Read & Prof. V. Parmentier

Oxford, United Kingdom, July 3, 2026

Xinmiao Hu

July 3, 2026

Abstract

The Juno mission has transformed our understanding of Jupiter's atmosphere by revealing its dynamics and composition in greater depth than previously possible. To understand these findings, general circulation models (GCMs) require further development to capture the relevant physical processes. This thesis explores two aspects of this effort using the Jason GCM.

We investigated the effect of lower boundary thermal conditions on Jovian atmospheric dynamics, using a series of simulations with different latitudinal flux gradients and the same global mean internal heat flux. The internal heat flux profile is based on that inferred from Voyager observations. We demonstrate that the internal heat flux distribution plays an important role in the thermodynamic structure, dynamics and energetics of the atmosphere. Increasing the equator-to-pole heat flux gradient reduces the meridional temperature contrast, weakens baroclinic instability, leading to the progressive decline of mid-latitude jets, while the equatorial jet persists in all cases. A complementary 'deep adiabat' simulation with a uniform temperature imposed at the lower boundary results in the disappearance of the mid-latitude jets. In this case, the diagnosed heat flux required to maintain the imposed temperature exhibits a similar latitudinal distribution to that in the prescribed-flux case, with a gradient just below the maximum value. These findings emphasise the significance of the thermal boundary condition in the large-scale dynamics and tracer distribution of Jupiter-like atmospheres. It also serves as a first step toward developing more realistic thermal bottom boundary conditions and exploring the interaction between deep convection and the overlying weather layer, which becomes increasingly relevant as Juno probes progressively deeper into Jupiter's atmosphere.

A simple parameterisation scheme for the water-ammonia hailstones, or 'mushballs', has been developed for the Jason GCM. This scheme was first tested in a two-dimensional setup, which showed that the mushball transport could produce an ammonia depletion in the mid-latitudes similar to that observed by the Juno Microwave Radiometer, supporting mushballs as a potential mechanism to explain Juno's ammonia observations. The effect of the mushball precipitation on water and ammonia distribution depends on poorly constrained parameters, including formation efficiency, ammonia fraction in mushballs, and water abundance. Extending the simulations to three dimensions revealed that including the mushball parameterisation does

not significantly alter the large-scale circulation, but strongly modifies the distribution of water and ammonia, producing fragmented cloud decks and mid-latitude ammonia depletion. We also produce, for the first time in a GCM, a reversal of the ammonia belt–zone contrast with depth. However, the equatorial depletion of ammonia, contrary to observations, highlights the need for improvements to mitigate the strong meridional circulation at the equator. These results also motivate further development of simplified analytic and idealised models to elucidate the fundamental processes governing the atmospheric response to interior heating and mushball dynamics, complementing the GCM approach.

Contents

Acknowledgements **3**

1 Introduction **5**

1.1 Observations of Jupiter . . . 5

1.2 Wind and Temperature . . . 6

1.2.1 Zonal Jets and Banded Structure . . . 6

1.2.2 Vortices . . . 9

1.2.3 Temperature . . . 9

1.2.4 Internal Heat Flux . . . 10

1.3 Cloud-forming Species . . . 11

1.3.1 Clouds . . . 11

1.3.2 Water and Moist Convection . . . 14

1.3.3 Gaseous Ammonia . . . 15

1.4 Cloud-forming Condensibles in Numerical Models . . . 16

1.4.1 1D Cloud Models . . . 16

1.4.2 Moist Convection Resolving Models . . . 17

1.4.3 General Circulation Models . . . 18

1.5 Project Outline . . . 20

2 GCM **21**

2.1 Dynamical Core . . . 21

2.1.1 Primitive Equations . . . 22

2.1.2 Configuring the Dynamical Core . . . 23

2.2 Domain . . . 24

2.2.1 Horizontal Resolutions and Justification . . . 24

2.2.2 Vertical Resolutions . . . 25

2.3 Dry Jupiter Parameterisations . . . 26
2.3.1 Two Stream Radiation . . . 27
2.3.2 Convective Adjustment . . . 31
2.3.3 Deep Adiabat Setup . . . 32
2.3.4 Vertical Mixing . . . 33
2.3.5 Bottom Drag . . . 34
2.3.6 Sponge Layer . . . 35
2.4 Jupiter Cloud Scheme . . . 35
2.4.1 Phase Change . . . 36
2.4.2 Sedimentation . . . 37
2.4.3 Additional Adjustments . . . 38
2.5 The Active Water Cycle . . . 38
2.5.1 Latent Heating . . . 38
2.5.2 Moist Convection . . . 39
2.5.3 Effect of Moist Convection on Ammonia . . . 44

3 Effect of Non-uniform Bottom Heat Flux 45
3.1 Introduction . . . 45
3.2 Method . . . 47
3.2.1 Internal Heat Flux Profile . . . 47
3.2.2 Model Setup . . . 50
3.3 Results . . . 51
3.3.1 Properties of the Zonal Jet . . . 51
3.3.2 Temperature Structure . . . 58
3.3.3 Meridional Transport . . . 66
3.3.4 Water Distribution and Moist Convection . . . 69
3.4 Lorenz Energy Cycle Analysis . . . 73
3.4.1 Formulation of the Lorenz Energy Cycle . . . 73
3.4.2 Lorenz Energy Cycle on JasonGCM Output . . . 77
3.5 Comparison with a Deep Adiabat Run . . . 83
3.5.1 Run Setup . . . 84
3.5.2 Zonal and Meridional Flow . . . 85

3.5.3 Temperature and Stability Structure . . . 86
3.5.4 Water Distribution and Moist Convection . . . 89
3.5.5 Lorenz Energy Cycle Analysis . . . 90
3.5.6 Equivalent Heat Flux . . . 91
3.6 Discussion and Conclusion . . . 97

4 Mushball Parameterisation and Its Effect on Two-dimensional Simulations 101
4.1 Introduction . . . 101
4.2 Mushball parameterisation scheme . . . 103
4.2.1 The Source Term . . . 103
4.2.2 Mushball Related Mass Flux . . . 106
4.2.3 Tendencies . . . 107
4.2.4 Choice of Default Parameters . . . 107
4.3 Model Setup . . . 109
4.3.1 (Quasi) Two-Dimensional Model Configuration . . . 109
4.3.2 Simulation Runs and Naming Convention . . . 110
4.4 Results for the Nominal Case . . . 111
4.4.1 General Features of Water and Ammonia Distribution . . . 111
4.4.2 Mushball Diagnostics . . . 113
4.5 Effect of Varying Mushball Parameters . . . 115
4.5.1 Varying Water Abundance . . . 115
4.5.2 Varying Mushball Efficiency . . . 119
4.5.3 Varying Ammonia Fraction . . . 123
4.6 Effect of Changing Temperature Profile . . . 124
4.7 Conclusion . . . 126

5 Three-dimensional Simulations with Mushball Parameterisation 129
5.1 Simulation Runs . . . 129
5.2 N0 and N1: Nominal-depth Simulations . . . 131
5.2.1 Zonal Mean Flow . . . 131
5.2.2 Water and Ammonia Distribution . . . 133
5.2.3 Mushball Properties . . . 136

5.3 Zonal Mean Tracer Balance . . . 137
5.4 W1: Simulation with Greater Domain Depth and Different Temperature Profile 140
5.4.1 Zonal Wind . . . 140
5.4.2 Tracer Distribution . . . 142
5.5 Summary and Discussion . . . 143

6 Summary and Outlook 145
6.1 Thesis Summary . . . 145
6.1.1 Latitudinally-varying Internal Heat Flux . . . 145
6.1.2 Mushball . . . 146
6.2 Limitations and Future Work . . . 147
6.2.1 Internal Heat Flux . . . 147
6.2.2 Mushball Parameterisation . . . 148
6.2.3 JasonGCM Formulation . . . 148
6.2.4 Extension to Other Planets . . . 149

A The Eulerian Mean Tracer Equation 151

Bibliography 157

List of Figures

1.1 Timeline of space exploration to Jupiter. Image credit: ESA. 6
1.2 Jupiter's zonal wind and belt-zone structure 8
1.3 Jupiter's energy balance as obtained by *Pirraglia* (1984). Reproduced with permission from Elsevier. 10
1.4 Schematic of cloud structure inferred from observation and ECCM 12
1.5 Molar mixing ratio of ammonia retrieved from Juno/MWR 16
1.6 Different cloud scheme used in numerical simulations of Jupiter 19

2.1 Schematics of the Arakawa-C grid 24
2.2 Temperature profiles from Jupiter observations and JasonGCM with different reference optical depth. 30

3.1 Interior heat flux profile used in different simulations 48
3.2 Time-latitude diagrams of zonal mean velocity 52
3.3 Zonal velocity profile for varying heat flux runs 54
3.4 Mean migration speed as a function of a_f at resolution L and M. 55
3.5 Evolution of super-rotation index and its off-equator component 56
3.6 Zonal mean zonal velocity at 1 bar for all varying heat flux simulations 58
3.7 Zonal-time mean temperature profile 58
3.8 Temperature of the RCM compared with the GCM at selected pressures. 59
3.9 Global mean RCM and GCM temperature profiles. 61
3.10 Equator-to-pole temperature difference profile 63
3.11 Global mean N^2 profiles 64
3.12 Zonal-time N^2 profiles 65
3.13 Eulerian mean meridional streamfunction 67
3.14 Total, Zonal mean and eddy heat flux in different layers 68

3.15 Global mean water ice and vapour profile 69
3.16 Water cloud column density at the end of each run. 70
3.17 Zonal-time mean water ice mass mixing ratio 71
3.18 Zonal-time mean water vapour mass mixing ratio. 71
3.19 Total convective available energy (TCAPE) as a function of latitude. 73
3.20 Schematic of the Lorenz energy cycle 74
3.21 Interpretation of the Lorenz energy cycle, adapted from *James* (1994). 77
3.22 Zonal mean kinetic energy and eddy kinetic energy for different a_f 78
3.23 Conversion and dissipation terms of the Lorenz energy cycle for different a_f . . . 78
3.24 Latitude-Pressure profile of the C_Z term of the Lorenz energy cycle (Eq. (3.21)). 80
3.25 Latitude-Pressure profile of the C_E term of the Lorenz energy cycle (Eq. (3.22)). 80
3.26 Latitude-Pressure profile of the full C_K term (Eq. (3.23)). 82
3.27 Latitude-Pressure profile of the first part of the C_K term 82
3.28 Lorenz energy cycle box diagram for the F-series runs. 83
3.29 TOA fluxes and kinetic energy densities over time for the deep adiabat run. . . . 85
3.30 Zonal-time mean of the zonal velocity of the deep adiabat run. 85
3.31 Time-latitude diagram of zonal mean zonal velocity of the deep adiabat run. . . 86
3.32 Eulerian meridional streamfunction at the end of the deep adiabat run. 87
3.33 Zonal-time mean temperature at the end of the deep adiabat run. 87
3.34 Potential temperature at different pressure levels for the deep adiabat run. . . . 88
3.35 Static stability for the deep adiabat run. 88
3.36 Time-zonal mean water vapour and ice mass mixing ratio at the end of the deep adiabat run. 89
3.37 Time-zonal mean TCAPE as a function of latitude at the end of the deep adiabat run. 91
3.38 Latitude-Pressure profile of the conversion terms of the Lorenz energy cycle for the deep adiabat run. 92
3.39 Lorenz energy cycle box diagram for the deep adiabat run. 93
3.40 Zonal mean radiative and convective component of the equivalent heat flux. . . . 94
3.41 Mollweide projections of the equivalent convective heat flux at different time . . 95
3.42 Time-zonal mean of the equivalent interior heat flux and its fitting result. 96

4.1 Schematic diagram of processes involved in mushball parametrisation. 104
4.2 Zonal-mean jet profile at the end of the 2D simulation. 110
4.3 Water and ammonia volume mixing ratio for the simulation with and without mushball. 112
4.4 Meridional mass stream function and zonal jet profile. 113
4.5 Mushball associated flux and TCAPE 114
4.6 Ammonia source term and ammonia available for mushball formation. 114
4.7 Ammonia-limited fraction and saturation ratio for mushball formation. 115
4.8 Ammonia volume mixing ratio for all 2D simulations. 116
4.9 Water volume mixing ratio for all 2D simulations. 117
4.10 Mushball diagnostics for the simulations with different water abundance. 118
4.11 Mushball diagnostics for the simulations with different mushball formation efficiencies. 121
4.12 Mushball diagnostics for the simulations with different ammonia fraction. 122
4.13 Water and ammonia volume mixing ratio for the simulation with a warmer temperature profile. 124
4.14 Mushball diagnostics for the case with a warmer temperature profile. 125

5.1 Zonal jet profile for the 3D mushball simulation 131
5.2 Zonal jet profile at 1 bar for the 3D mushball simulation 132
5.3 Meridional mass streamfunction for the 3D case with and without mushball . . . 133
5.4 Zonal mean volume mixing ratio of water and ammonia for the nominal 3D simulation. 134
5.5 Zonal mean velocity gradient and ammonia volume mixing ratio at selected pressure levels for the nominal three dimensional simulations. 135
5.6 Mushball diagnostics for the nominal 3D simulation. 137
5.7 Terms in the zonal mean tracer transport equation for water vapour 138
5.8 Terms in the zonal mean tracer transport equation for water ice. 139
5.9 Zonal mean velocity and streamfunction for the 56 bar simulation. 141
5.10 Zonal jet profile for the 3D simulation that extends to 56 bars vs the 18 bar one. 141
5.11 Pressure-latitude profile of water and ammonia volume mixing ratio for the deep run 142

5.12 Zonal mean velocity gradient and ammonia volume mixing ratio at selected pressure levels for the 56 bar simulation. 143

A.1 Components of the advection terms for ammonia vapour. 153
A.2 Terms in the zonal mean tracer transport equation for ammonia vapour. 154
A.3 Terms in the zonal mean tracer transport equation for ammonia ice. 155
A.4 Terms in the zonal mean tracer transport equation for water liquid cloud. 156

List of Tables

2.1 Summary of symbols and their meanings for the equations in the dynamics core 23
2.2 Model parameters used in this study. 26
2.3 Saturation vapour pressure curve parameters for the phase changes included in the JasonGCM. 36
2.4 Rates of change per unit area of water mass and heat in updrafts and downdrafts at different levels. 43
2.5 Ammonia mass change rate at different levels in a moist convective plume 44

3.1 Simulation time for runs with varying heat flux and the deep adiabat setup . . . 50
3.2 a_f and b_f parameters of the deep adiabat run with different fit range. 96

4.1 List of symbols used in the mushball scheme. 105
4.2 Mapping of run name digits to physical parameter values. 110

5.1 Summary of the 3D mushball simulations. 130

All models are wrong,
but some are useful.

(SUPPOSELY) GEORGE E. P. BOX

The vastness of heavens stretches my imagination...
Why do the poets of the present not speak of it?
What men are poets who can speak of Jupiter if he
were like a man, but if he is an immense spinning
sphere of methane and ammonia must be silent?

RICHARD P. FEYNMAN

Acknowledgements

O mihi praeteritos referat si Iuppiter annos.

VERGIL

There is an old proverb that 'It takes a village to raise a child', and it certainly takes more than a town to complete a thesis. Hence, this thesis will not be complete without an acknowledgement of the various supports I received. First and foremost, I would like to thank my DPhil supervisor, Peter Read and Vivien Parmentier, for their enormous support and their patience with me while they have many other bright protégés. Thanks to my 'technical' advisor, Greg Colyer, who provided enormous help in various science and technical issues. Roland Young, who has built the foundation of the model used in this project and many analysis scripts, without him, this project would not be possible.

I have also received support from the wider planetary science community. Noticeably, Arymeric Spiga for always being overly impressed with my work, Tristan Guillot for some useful advice during my visit to Nice, Glen Orton, for mentoring me during my first conference. I'm also grateful to many peers I've met through the conference, while we may not have contributed to each other's science progress, your kindness, such as sharing a table just upon seeing my conference name badge, touches me deeply.

Thanks for the Clarendon Scholarship for recognising my research potential, which I constantly doubt I have. Without their funding, I would not be able to start the degree, Brasenose College for providing various supports during my DPhil, and my college advisor, Jayne Birkby, for clearing up some of my general confusion about DPhil.

I also owed a great deal to many people in the AOPP sub-department: Mainly Yixin for many helpful discussions, Cherry, Zhixiao and Shanshan for bearing my rant on science and life, Joost for being a role model (though I didn't follow well) and the best office mate, my other office mates in 114, who had endured my prolonged occupation, David Marshall, for his constructive feedback and for giving me reassurance when paperwork went missing. Thanks to many others with whom I had many good chats (academic or not), but never learned their name.

Many friends I met through college have also contributed indirectly. Dana has gone through peer supporter training with me and provided me the peer support when I need it. Kexin pulled

me to spin classes to let some steam out (both literally and figuratively) while writing the thesis. Lin always reminds me there is a greater world outside Oxford. Piotrek and Robert, thanks for the various health and LLM advice.

I also received enormous support from my friends outside Oxford: notably Alice for reminding me of my thesis every time I visit her in London, Catherine for reminding her friends not to remind me of my thesis (and so much more from both of you). A great thank to many members of the online study group 'goodgoodstudy' who has been with me in this journey at various point (especially during Covid). Thanks, twisteddoodles and phdcomics, for providing entertainment about science and DPhil/PhD life: many issues seem bearable with a sense of humour.

Finally, I'd like to thank my parents, mainly as an obligatory formality, but also for sheltering me every time I go back to China, especially in the middle of the pandemic. A similar acknowledgement extends to other relatives, with a special shout-out to my cousin Ziyu, who is not only an understanding friend but also an inspiration for me to be a better person.

Chapter 1

Introduction

1.1 Observations of Jupiter

Jupiter is a gas giant planet composed mainly of hydrogen and helium. Visually, it is marked by alternating light and dark bands of clouds. Tracking of cloud features revealed seven or eight stable alternating bands of the east-west jet. Embedded in these jets is a plethora of meteorological structures, such as wave-like features, convective storms and coherent vortices.

Telescopic observations of Jupiter date back to 1610, when Galileo Galilei discovered its four largest moons. Since then, ground-based telescopes have provided centuries of monitoring (e.g. *Sánchez-Lavega et al.* 2024). Modern ground-based and space telescopes have expanded this capability. For example, the Very Large Array (VLA) probes the deep atmosphere at radio wavelengths (*de Pater et al.* 2016), while the Hubble Space Telescope (HST) has delivered continuous high-resolution imaging in the visible and ultraviolet (*Simon et al.* 2015). More recently, the James Webb Space Telescope (JWST) has provided high-quality infrared observations that are inaccessible from the ground (*Norwood et al.* 2016).

Our knowledge of Jupiter was further transformed by spacecraft flybys, beginning with the *Pioneer 10* encounter in December 1973, providing the first close-up look of Jupiter (*Hall* 1975). This was followed by *Pioneer 11* in December 1974. The *Voyager 1* and *2* flybys in 1979 provided higher resolution images of Jupiter's atmosphere and observed lightning on the night side (*Kohlhase and Penzo* 1977; *Smith et al.* 1979). *Ulysses* in 1992 and 2004 focused on the solar wind interaction with Jupiter's magnetosphere (*Smith et al.* 1992). *Cassini* in 2000 provides higher-resolution images (*Hansen et al.* 2004; *Porco et al.* 2003) *New Horizons* in 2007 provided a close-up look at the Little Red Spot formed by the merge of three smaller anticyclones (*Cheng et al.* 2008).

More detailed observations have been obtained from the two orbiters of Jupiter. The *Galileo* spacecraft operated between 1995 and 2003, providing the first long-term orbital survey of the Jovian system. It also deployed the only atmospheric entry probe to date, providing crucial in situ measurements of elemental abundances, vertical wind shear and cloud structure

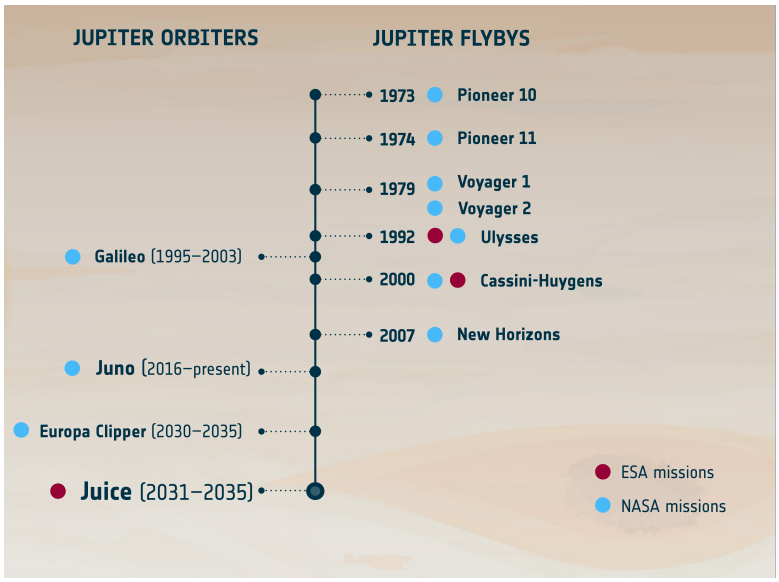


Figure 1.1: Timeline of space exploration to Jupiter. Image credit: ESA.

(*Young* 2003). More recently, the Juno mission, which has been in orbit since 2016 and is expected to continue until at least September 2025, has offered a new perspective by following a highly elliptical polar trajectory. Its instruments probe Jupiter's deep atmospheric dynamics using near-infrared imaging, microwave sounding and magnetic and gravity field measurements (*Bolton et al.* 2017). The Jupiter system will be explored further by two flagship missions: the *Europa Clipper* and the *Jupiter Icy Moons Explorer* (JUICE), which are expected to reach Jupiter in 2030 and 2031, respectively (*Grasset et al.* 2013; *Pappalardo et al.* 2024). Although both missions primarily focus on the moons, they will also deliver valuable contextual data on Jupiter itself. Fig. 1.1 summarises the timeline of Jupiter's exploration.

1.2 Wind and Temperature

1.2.1 Zonal Jets and Banded Structure

Historically, the light and dark bands on Jupiter have been referred to as 'belts' and 'zones', respectively. A more common approach is to define zones and belts by their vorticities, which correlate weakly with the colour of the region. In this framework, belts correspond to cyclonic regions ($d\bar{u}/dy < 0$ in the northern hemisphere and $d\bar{u}/dy > 0$ in the southern hemisphere), while zones correspond to anticyclonic regions (e.g. *Read et al.* 2006; *Vasavada and Showman* 2005). The jet structure therefore aligns with this pattern: eastward (prograde) jets are situated

on the equatorward flanks of belts, whereas westward (retrograde) jets are found on their poleward flanks. Fig. 1.2 illustrates the belt-zone structure and the zonal wind profile of Jupiter. The zonal wind is not symmetrical around the equator. In particular, the strongest prograde (eastward) jet at 24° has no southern counterpart. However, the southern hemisphere exhibits a strong retrograde (westward) jet at -20° and the GRS at -23° (*Tollefson et al.* 2017). The double-peak structure of the equatorial jet also appears asymmetrical. At the cloud level, detailed tracking revealed that the jets have been stable since the beginning of the Voyager era, except at certain latitudes. The intensity of the 24° jet shows the greatest fluctuations, ranging from 135 ms^{-1} and 160 ms^{-1} in 2001-2016 (*Tollefson et al.* 2017), after slowing down by 50 ms^{-1} between 1979 and 1995-1998 (*García-Melendo et al.* 2000). These fluctuations are associated with morphological changes and plume outbreaks. Variations in velocity at other locations are related to the seasonal cycle and wave activity.

More recently, Doppler velocimetry has been employed to measure cloud-top winds, yielding zonal velocities that are largely consistent with those derived from cloud tracking (*Gonçalves et al.* 2019; *Machado et al.* 2023; *Shaw et al.* 2022). This technique infers wind speeds from Doppler shifts of solar absorption lines in sunlight reflected by Jupiter's clouds, providing line-of-sight velocities that can be projected onto the planetocentric frame. Beyond confirming zonal flows, this technique also offers the capability to retrieve meridional and even vertical wind components, as demonstrated by *Schmider et al.* (2024).

Above the cloud tops, the structure of the wind can be inferred from three-dimensional temperature fields. The maximum in the temperature gradient occurs at the boundary between the warm belts and the cold zones (e.g. *Simon-Miller et al.* 2006). The thermal wind relation implies that zonal jets decay with altitude in the upper troposphere.More recently, observations from the James Webb Space Telescope (JWST) have enabled direct tracking of stratospheric haze features, revealing an intense equatorial jet within the latitude range of ±3° (*Hueso et al.* 2023).

Below the clouds, the most direct in situ profile comes from the Galileo Probe Doppler Wind Experiment (DWE) (*Atkinson et al.* 1998). Winds increased rapidly with depth, reaching approximately 175 m s^{-1} at 4–5 bar, after which they remained nearly constant (or showed weak decrease) to approximately 170 m s^{-1} at 21 bar. However, the uncertainties of the observation permit wind shear of either sign. Furthermore, the probe entry site (PES) was the southern

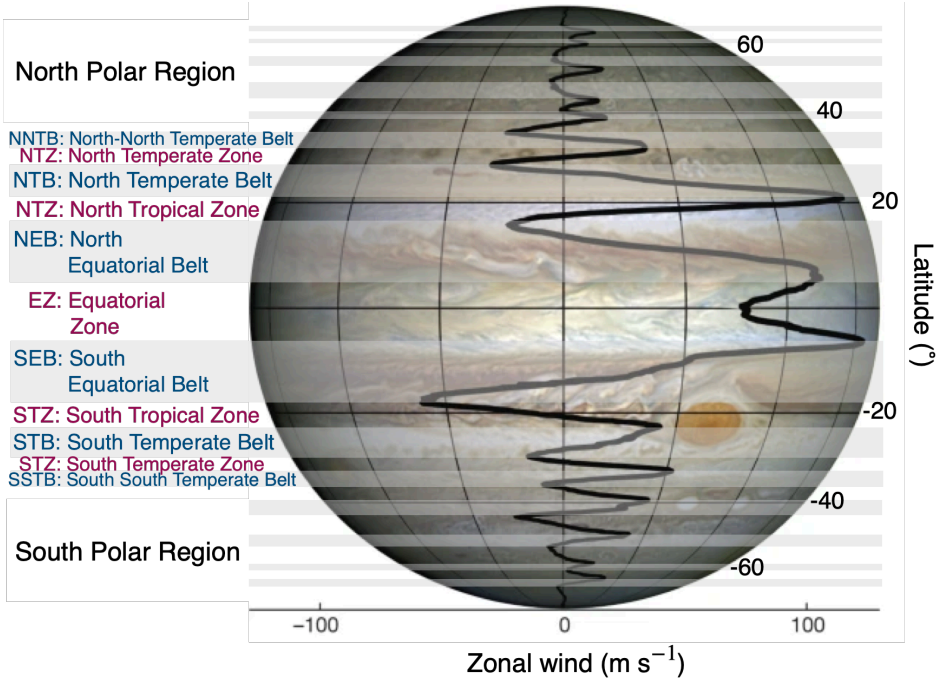


Figure 1.2: Jupiter's full disk view (image), cloud-level zonal flows (thick black line) and belt zone structure (legends). The image was taken by the Hubble Wide Field Camera in 2014. The zonal flows were measured during Juno's Perijove 3 in 2016 (*Tollefson et al.* 2017). Grey bands are belts, and white bands are zones. Grid latitude is shown on the right. Image adapted from *Kaspi et al.* (2018) (their Fig. 1a).

region of a 5μm hot spot (*Young* 2003), a region that is dominated by Rossby wave dynamics in numerical models (*Showman and Dowling* 2000). Hence, the measured wind profile may not represent the global condition. Indirect evidence comes from several sources. Firstly, planetary-scale convective storms in the NTB imply that winds increase slightly down to the water-cloud level (*Sánchez-Lavega et al.* 2008). Secondly, microwave brightness temperatures from Juno have been used to infer wind shear (*Fletcher et al.* 2021), which flips in sign at different pressure levels depending on whether the brightness temperature contrast is interpreted as temperature variation (resulting in a 'pseudo shear') or ammonia variation (resulting in a 'moist windshear'). Retrieval of ammonia concentration from Juno/MWR measurements is discussed further in Section 1.3.3.

Wind structure in greater depth is revealed by magnetic and gravity measurements. *Kaspi et al.* (2023) shows the gravitational harmonics signals are more consistent with a cylindrically oriented zonal flow profile that extends inwards to depths of 10^5 bar, or 3,000 km, but the

wind magnitude decays radially. At greater depths, constraints come from Juno's gravity and magnetic field measurements (*Kaspi et al.* 2023). Although most of the gravity signal originates from low-latitude jets within ±25° (*Galanti et al.* 2021).

Two main classes of jet generation mechanisms have been proposed for Jupiter. In the deep convection model, the zonal jets observed in the weather layer are the surface manifestation of deep circulations driven by convection in the planet's interior. Such models extend through a significant fraction of the planetary radius (e.g. *Duer et al.* 2023; *Heimpel et al.* 2016; *Wulff et al.* 2022; *Yadav et al.* 2022). In contrast, the weather-layer model confines the dynamics to a relatively shallow region near the cloud tops, typically a few hundred kilometres in depth. In this framework, the jets are powered by weather-layer processes such as baroclinic instabilities (e.g. *Schneider and Liu* 2009; *Yamazaki et al.* 2005) or moist convection (e.g. *Showman* 2007; *Thomson and McIntyre* 2016), and the models can explicitly represent the effects of latent heating and cloud formation (e.g. *Boissinot et al.* 2024; *Lian and Showman* 2010; *Liu and Schneider* 2015; *Young et al.* 2019a). Despite operating in different dynamical regimes, both model classes are capable of reproducing Jupiter-like, eddy-driven jets at cloud level. Comprehensive reviews of their respective strengths and limitations can be found in *Read et al.* (2020b) and *Sánchez-Lavega et al.* (2019).

1.2.2 Vortices

In addition to jets and banded structures, Jupiter's atmosphere hosts a variety of vortices. The most prominent of these is the Great Red Spot: a long-lived anticyclonic storm system located near 23°S that has persisted for centuries (e.g. *Sánchez-Lavega et al.* 2024). At high latitudes, Juno revealed remarkable clusters of cyclones, with a stable pattern of five in the south and eight in the north encircling each pole (*Adriani et al.* 2018; *Mura et al.* 2022; *Tabataba-Vakili et al.* 2020). More detailed discussions of Jovian vortices can be found in *Read* (2024) and *Vasavada and Showman* (2005).

1.2.3 Temperature

The earliest constraints of Jupiter's temperature came from radio occultations by Pioneer 10 and 11, which sounded the atmosphere down to ∼0.25 bar (*Kliore et al.* 1975). Later Voyager provided temperature profiles at multiple latitudes down to 1 bar and has recently been

reanalysed (*Gupta et al.* 2022). In situ measurements were obtained by the Galileo Probe Atmospheric Structure Instrument, which returned a vertical profile to 22 bar (*Seiff et al.* 1998). Thermal infrared observations from Voyager/IRIS and Cassini/CIRS maps down to 1 bar (*Simon-Miller et al.* 2006). Thermal infrared spectroscopy, including Ground-based observations and Voyager/IRIS, provides latitudinal profiles of temperature (e.g. *Simon-Miller et al.* 2006). Subsequent Cassini/CIRS mapped temperatures down to ∼1 bar with high spatial resolution (*Fletcher et al.* 2009). More recently, Juno MWR and ground-based telescopes have offered indirect constraints on the deep thermal structure below the clouds (*Fletcher et al.* 2021). Interpretation is complicated by degeneracies with ammonia, to which the measurements are generally more sensitive than to temperature (*de Pater et al.* 2016). JWST now provides a new generation of infrared spectra with higher sensitivity, providing a regional temperature map down to 0.8 bar (*Harkett et al.* 2024).

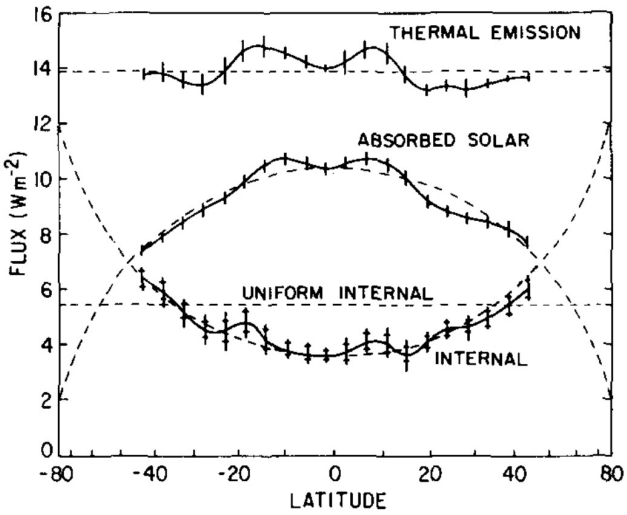


Figure 1.3: Jupiter's energy balance as obtained by *Pirraglia* (1984). Reproduced with permission from Elsevier.

1.2.4 Internal Heat Flux

Since the Voyager era, it has been known that Jupiter emits more energy than it absorbs from the Sun (*Hanel et al.* 1981). This excess is supplied by the planet's internal heat flux, which originates from residual heat left over from its formation (*Hubbard* 1968). Estimates of the global mean internal heat flux have evolved from ∼5.7 $\mathrm{W\,m^{-2}}$ in the Galileo era (*Gierasch et al.* 2000) to more recent values of ∼7.5 $\mathrm{W\,m^{-2}}$ (*Li et al.* 2018b). This internal heat flux

implies a convective interior and a temperature profile close to an adiabat below ∼0.5 bar. This is supported by the aforementioned temperature measurements. While the internal heat flux is often quoted as a global average, *Pirraglia* (1984) suggested a spatial variation in the internal heat flux profile. As shown in Fig. 1.3, the outgoing thermal emission is approximately latitudinally uniform. Given the strong variation in solar radiation, they inferred that the internal heat flux must increase with latitude. *Aurnou et al.* (2008) used a deep convection model to study the effect of atmospheric circulation on the thermal heat flux, and found that the large-scale atmospheric heat transport can partially explain the observed thermal emission. This will be discussed in detail in Chapter 3.

1.3 Cloud-forming Species

1.3.1 Clouds

Remote sensing uses reflected sunlight and the 5 μm spectrum, as well as correlations of the 5 μm spectrum with visible images, to constrain the Jovian cloud structure and composition. Fig. 1.4shows the overall picture that emerged from these observations, as proposed by *West et al.* (1986, 2004). This picture includes a ubiquitous, small-particle haze layer in the upper troposphere and multiple cloud layers. The upper haze, consisting of sub-micron particles, extends up to approximately 200 mbar above the cloud tops, with enhancements over the Great Red Spot and near the equator. Beneath this haze, Galileo/SSI observations identified a highly variable cloud deck at $p = 750 \pm 200$ mbar (*Banfield et al.* 1998; *Simon-Miller et al.* 2001). This altitude is consistent with the position of ammonia cloud predicted by equilibrium models.

Many observations support the existence of a deeper, more optically thick cloud between 1 and 2 bar, including Galileo/NIMS (*Irwin et al.* 1998, 2001), Cassini/CIRS (*Matcheva et al.* 2005), and Cassini/VIMS (*Giles et al.* 2015). This deeper cloud is often considered to be NH_4SH, although some authors, such as *Atreya et al.* (1999) and *Wong et al.* (2015), have briefly mentioned the possibility of $(NH_4)_2S$ as a cloud constituent. *Irwin et al.* (2025) found that the main level of reflection in Jupiter's atmosphere is at an even deeper level of 2–3 bar.

The *West et al.* (2004) scheme also includes a deep water cloud. Observation of this cloud is difficult due to its obstruction by the clouds above and its position below the maximum

sounding depth for many instruments. Convective storms (*Gierasch et al.* 2000) and lightning (*Little et al.* 1999), discussed in Section 1.3.2, provide indirect evidence for the water cloud. *Banfield et al.* (1998) identified a deep cloud extending below 4 bar in the northwest of the GRS. Such depth implies that it can only be a water cloud. The occurrence of deep clouds is also supported by *Bjoraker et al.* (2015), who analysed spectrally resolved CH_3D line shapes and confirmed the presence of an opaque cloud with a cloud top at $4-5$ bars in the STZ. The existence of water clouds is also inferred in some other latitudes. *Dahl et al.* (2021) also found a deep cloud base in an SEB outbreak region, extending down to 4-5 bars.

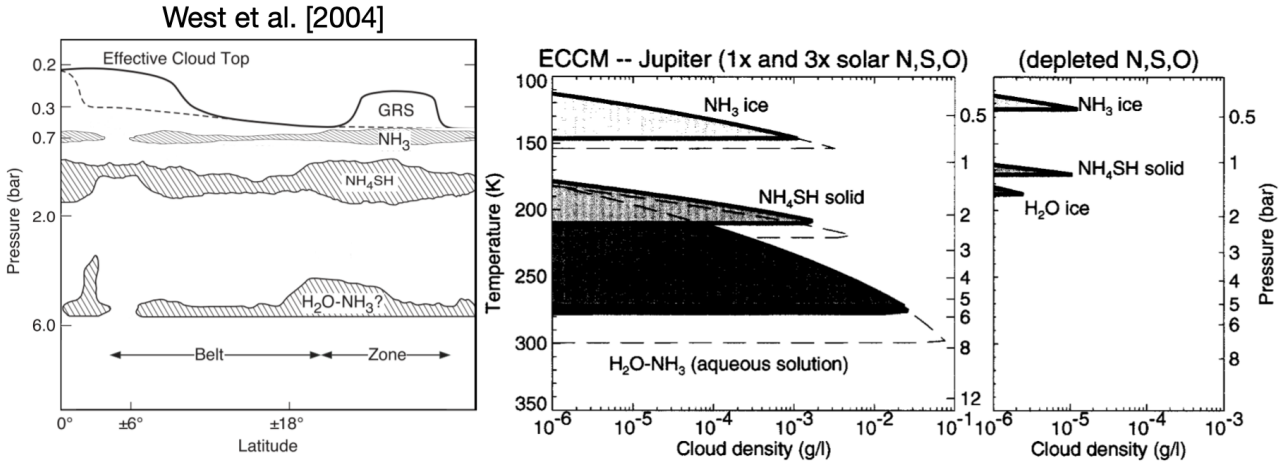


Figure 1.4: Schematic of structure inferred from observation (left), and that predicted by ECCMs (middle and right). The ECCM result for depleted volatile used the profile measured by the Galieo probe (*Niemann et al.* 1998) (right). The schematic was adapted from *West et al.* (2004) with the vertical axis adjusted to match that of the ECCM profile, which is taken from *Atreya et al.* (1999).

The most direct measurements of clouds come from the Nephelometer (NEP) and Net Flux Radiometer (NFR) on board the Galileo entry probe. The NEP (*Ragent et al.* 1998) revealed a three- or four-layer cloud structure: a cloud layer at $0.46-0.55$ bars, possibly consisting of ammonia; a denser cloud at $0.76-1.34$ bar, possibly of NH_4SH; a thin cloud layer at around 1.65 bars; and a weak structure at $1.9-4.5$ bars. The nature of the last two layers is inconclusive. The former could either be a detached structure from the cloud above, or a tenuous water cloud compatible with the low water abundance in the PES. The latter is suspected to be a thin water cloud due to lateral transport from wetter regions. The NFR also suggests an NH_3 cloud at pressure above 0.45-0.50 bars and a cloud based at around 1.35 bars. However, no signal of a water cloud was detected (*Sromovsky et al.* 1998).

In the aforementioned studies, the nature of the cloud constituents was inferred from equi-

librium cloud condensate models (ECCMs). Spectral identification of the cloud particles is sparse. Some studies even provide negative evidence for these cloud constituents. For example, *Giles et al.* (2015) noted that pure NH_3-ice and pure NH_4SH are incompatible with the Cassini/VIMS spectra. Similarly, *Grassi et al.* (2021) found that the data from Juno/JIRAM is inconsistent with the spectral features of an NH_4SH cloud or a cloud of a water-ammonia ice mixture.

However, a few studies did provide some evidence for spectrally identifiable clouds (SICs), albeit often in restricted areas. The first spectral evidence for ammonia ice comes from the 3 μm spectrum of Jupiter obtained by the Infrared Space Observatory (ISO) (*Brooke et al.* 1998). *Baines et al.* (2002) spectrally identified NH_3 ice from Galileo/NIMS images, and found that it covered 1% of the globe. These localised SICs are associated with hot spots in the equatorial region and near the GRS, suggesting that they are associated with regions of vigorous upwelling. This result is further supported by the analysis of Cassini/CIRS spectra (*Wong et al.* 2004). More recently, *Biagiotti et al.* (2025) analysed infrared spectral data from Juno/JIRAM and identified ammonia SICs within a white vortex structure in the NTB. Regarding water clouds, *Simon-Miller et al.* (2000) reported possible signatures of water ice in approximately 1% of Voyager IRIS spectra. Like the ammonia ice, these detections were clustered in regions with strong convective activity.

The scarcity of spectrally identifiable clouds (SICs), despite ECCM predictions, can be reconciled if cloud particles are coated in photochemical hazes. This inhibits the spectral signatures of ammonia ice except in freshly formed clouds (*Atreya et al.* 2005). Such coatings, together with the poorly constrained nature of Jupiter's chromophores, make it difficult to infer cloud the inference of cloud properties, since the optical properties of the condensates are strongly affected by the absorbing material.

A recent development in this area is the so-called Crème Brûlée model, in which a thin chromophore layer sits on top of a deeper condensate cloud. This configuration has been shown to reproduce Cassini/VIMS spectra (*Sromovsky et al.* 2017) and ground-based visible observations (*Dahl et al.* 2021), assuming the chromophore proposed by *Carlson et al.* (2016). Variants of this scheme have been tested: *Braude et al.* (2020) suggested steeper blue absorption of the chromophore, while *Pérez-Hoyos et al.* (2020) found that an extended chromophore layer provided a better fit to HST observations. *Anguiano-Arteaga et al.* (2023) found an intermediate

scenario. These results illustrate that the retrieved properties of the cloud, such as particle size, composition and opacity, are subject to significant uncertainty as they depend on the assumed chromophore distribution and optical properties.

The overall latitudinal structure for clouds from these studies is such that zones and GRS have thicker and higher clouds than the belts. For example, *Grassi et al.* (2021) found that the maximum cloud altitude, occurs over the GRS (20 km) and zones (15 km), and decreases over the belts and towards higher latitudes. They also found that the clouds in the zones are more compact, as the aerosol opacity scale height is higher there. An exception to this pattern is the study by *Braude et al.* (2020), which found little spatial variation in their thick clouds at around 1.4 bars in their model. The standard interpretation of these results is that the zones are regions of upwelling and the belts are regions of downwelling.

1.3.2 Water and Moist Convection

Water is arguably the most important condensible for Jupiter's meteorology, as indicated by the observations of lightning and convective plumes (see the review by *Palotai et al.* 2023). Detection of water vapour is, however, extremely challenging due to the degeneracy with cloud structure in retrievals (e.g. *Roos-Serote et al.* 2004). The Galileo entry probe measured an increasing water vapour mixing ratio between 12 and 19 bar (*Niemann et al.* 1998), which is likely to be the effect of Rossby wave dynamics (*Showman and Dowling* 2000). Even the abundance of water is not well constrained. The water abundance from the Galileo probe is subsolar, though this is often attributed to the entry site being a dry area. The first Juno/MWR estimate suggested a water abundance of $2.7^{+2.4}_{-1.7}\times$ solar in the equatorial region (*Li et al.* 2020a). In contrast, the ammonia abundance is better constrained at $2.76^{+0.17}_{-0.16}\times$ solar. More recent analyses have found evidence for a superadiabatic temperature gradient and inferred a higher water abundance of $4.9 \pm 3.4\times$ solar (*Li et al.* 2024).

Lightning, detected as optical flashes (*Gierasch et al.* 2000; *Little et al.* 1999) and microwave sferics (*Brown et al.* 2018), occurs primarily in belts (*Little et al.* 1999) with increasing radio signal intensity at mid-to-high latitudes (*Brown et al.* 2018). This spatial preference is suggested to be the consequence of the cyclonicity of belts, where lower pressure elevates the boundary between the dry and moist convecting regions (*Dowling and Gierasch* 1989). The correlation between cyclonic features and powerful plumes further supports this idea, as demonstrated

in multi-instrument case studies by *Fletcher et al.* (2017) using ground telescopes, and by *Brueshaber et al.* (2025) using Juno data.

The conventional theory of lightning requires strong updrafts and charge separation involving both liquid and solid phases (e.g. *Aglyamov et al.* 2021). While the liquid is often assumed to be water, water–ammonia liquids may explain the shallow lightning observed above the 2-bar level (*Becker et al.* 2020).

1.3.3 Gaseous Ammonia

Pre-Juno, Earth-based observations showed that ammonia is generally depleted down to at least the 6-bar level, relative to an abundance approximately three times that of the Sun (*De Pater et al.* 2001). Such depletion is greater in belts than in zones, which is also confirmed by telescopic observations (*Hill et al.* 2024). *Showman and de Pater* (2005) argue that this distribution can be explained by the interaction between moist convection and Jupiter's cloud-layer circulation. In their model, upwelling occurs over zones and downwelling over belts at 0.5 bar; at around 6 bar, thunderstorm dominance in the belts leads to upwelling in the belts and downwelling in the zones. Horizontal divergence, therefore, leads to a transfer of ammonia from belts to zones.

However, the scenario in *Showman and de Pater* (2005) is unlikely to account for the belt-to-zone contrast below the water cloud base and the level at which the raindrops evaporate (10-12 bars). Juno/MWR reveals that the ammonia depletion extends down to at least 40–60 bars, especially in the NEB, except at 0-5° (*Li et al.* 2017).This result is also confirmed by VLA observation (*de Pater et al.* 2019), which used longitude-averaged data taken two years before *Li et al.* (2017), as well as a combined Juno/MWR and VLA retrieval (*Moeckel et al.* 2023). At these depths, the mixing ratios of the belts appear to be slightly higher than those of the zones. Peaks and troughs in the ammonia profile suggest weak upwelling within the belts themselves (*Ingersoll et al.* 2017). A simple interpretation of the contrast between the EZ and the NEB is that ammonia-rich air rises in the EZ and ammonia-poor air sinks in the NEB. However, *Ingersoll et al.* (2017) pointed out that this Hadley-like circulation would not be in a steady state, as it implies net upward transport of ammonia. The ammonia budget must therefore be balanced by additional downward transport, either in regions poleward of ±40° (which they considered unlikely), or on a smaller scale than the detection threshold of Juno/MWR. Dry

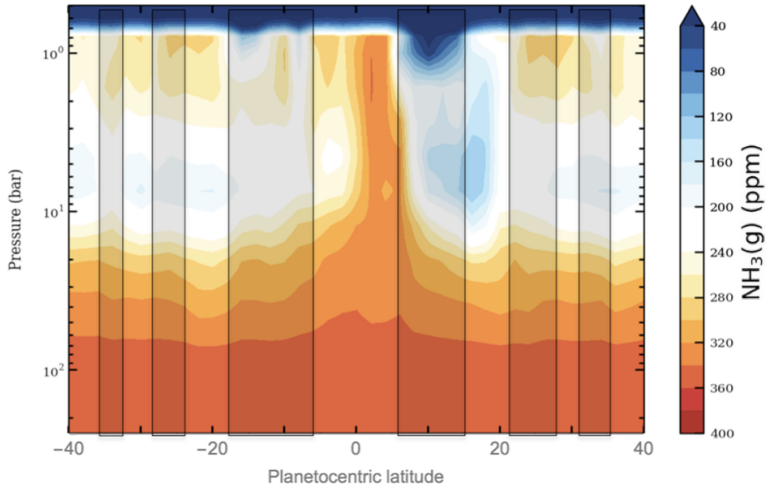


Figure 1.5: Molar mixing ratio of ammonia retrieved from Juno/MWR measurement. Grey bands are belts, and white bands are zones. Image adapted from *Ingersoll et al.* (2017).

downdrafts induced by moist convection plumes seem unlikely to be the cause, as *Li and Chen* (2019) showed that they only deplete ammonia gas down to about 10 bars.

Guillot et al. (2020a) propose a novel mechanism that transports ammonia to deep levels by hailstones of a water-ammonia mixture, or 'mushball'. Subsequent study by *Guillot et al.* (2020b) developed a simplified model based on this mechanism, and showed that variability in ammonia abundance can be linked to lightning-generating storms. (A more detailed discussion of the mushball mechanism can be found in Chapter 4.) How this mechanism interacts with atmospheric dynamics is unknown and would require testing in general circulation models.

1.4 Cloud-forming Condensibles in Numerical Models

1.4.1 1D Cloud Models

The first investigations of the Jovian cloud considered its structure in thermodynamic and hydrostatic equilibrium (*Lewis* 1969; *Weidenschilling and Lewis* 1973). These equilibrium cloud condensation models (ECCMs), generally predicted the three-layer structure of NH_3 ice, NH_4SH and H_2O ice/NH_3-H_2O, as shown in Fig. 1.4. The effect of transport and microphysics, which is missing from these models, was evaluated by *Carlson et al.* (1988), who followed the approach of *Rossow* (1978) to compute characteristic time constants of processes such as droplet condensation, coalescence and sedimentation. The computed time constant would depend on uncertain factors, such as updraft speeds and the properties of condensation nuclei. This study

also did not predict vertical profiles of the condensates.

To incorporate the effect of vertical transport, *Ackerman and Marley* (2001) took a different approach by computing the cloud density profile based on the balance between eddy diffusion and sedimentation. By including the adjustable parameter f_{rain}, defined as the ratio of the mass-weighted droplet sedimentation velocity to the convective velocity, their model addresses the dynamical processes that are missing from previous ECCMs for a steady state cloud. To address transient or regional cloud formation, *Wong et al.* (2015) developed a complementary model that incorporates the effects of local updrafts during condensation. Their ECCM computes a 'cloud density rate' as a measure of condensate production, making it better suited to newly formed and evolving clouds.

1.4.2 Moist Convection Resolving Models

Several regional-scale model has been developed to resolves moist convection in the Jovian atomsphere. Parameterisations used in general circulation models (GCMs) will be discussed in Section 1.4.3. By definition, moist convection involves the condensation of volatiles and therefore requires the treatment of cloud processes.

Some studies that include detailed parameterisation of microphysics involve interaction between vapour, ice and liquid. Early examples of such studies include the 2D, axisymmetric cloud model in *Yair et al.* (1995), which was used to study the evolution of Jovian water cumulus clouds. Their detailed microphysics parameterisation includes nucleation, diffusional growth, evaporation of drops and ice crystals, coagulation, freezing, melting, and sedimentation of precipitation particles. They revealed that diffusional growth and coagulation processes were faster and more efficient on Jupiter compared to Earth, with large particles of a diameter of more than 100 μm forming rapidly and remaining suspended by strong updrafts. The model predicted clouds reaching depths of approximately 25 km with water condensate content of $2.5 - 5$ g/m^3.

Other studies of moist convection on Jupiter employ a simplified scheme similar to that developed by *Kessler* (1969) for terrestrial conditions. As illustrated in the middle panel of Fig. 1.6, this scheme represents the conversions between the three phases of a condensible gas: vapour, cloud, and precipitation. Both cloud and precipitation are condensates, but differ in that cloud does not sediment whilst precipitation does. For instance, *Hueso and*

Sánchez-Lavega (2001) used a three-dimensional model to study the formation and evolution of Jupiter's water-ammonia storms. They assumed that phase change was instantaneous and represented precipitation as the removal of a constant fraction of liquid water from the model domain. Their simulations demonstrated that highly energetic water-based storms can reach the 150 mbar level with vertical velocities around 150 m/s, though they were more difficult to initiate than their terrestrial counterparts. By contrast, ammonia storms developed more easily but exhibited much lower intensity, unless very large ammonia abundances (10 × solar) were present. The study also highlighted the important role of Coriolis forces in determining storm morphology and properties. *Sugiyama et al.* (2014) implemented the Kessler type of scheme for H_2O, NH_3, and NH_4SH in a two-dimensional model to study the effect of the autoconversion timescale from vapour to cloud, and of the deep abundances of condensibles, on the properties of the moist convection layer. They found that stable layers associated with condensation and chemical reactions acted as effective dynamical and compositional boundaries, leading to the development of intense cumulonimbus clouds with temporal intermittency. The intermittency period of cloud activity was roughly proportional to the deep abundance of H_2O, while varying autoconversion timescale has only minor effects.

More recently, *Li and Chen* (2019) developed a non-hydrostatic cloud-resolving model for studying moist convection in planetary atmosphere, using a Kessler-type scheme involving both water and ammonia. Their simulation of an idealized Jovian atmosphere in radiative-convective equilibrium produced a super-adiabatic temperature gradient near the water condensation level, due to changes in mean molecular weight. Their model also showed depletion of ammonia far below the ammonia cloud level, though they noted that this behaviour is not yet understood in their model.

1.4.3 General Circulation Models

Moist convection is often considered as a potential source of eddies that generate zonal jets in jet-formation studies. Early studies on jet formation represented moist convection as the injection of vorticity (e.g. *Showman* 2007; *Thomson and McIntyre* 2016).

Several approaches to represent more realistic cloud cycles and moist convection have been developed for Jovian GCMs. *Palotai and Dowling* (2008) developed a microphysics model for water and ammonia clouds in the EPIC GCM (*Dowling et al.* 2006) that includes five phases

for each species: gas, cloud ice, cloud water, snow and rain. This model has been used to study regional phenomena, such as the ammonia cloud in the GRS (*Palotai et al.* 2014), and the atmospheric response to convective outburst (*Sankar et al.* 2021). Later *Sankar and Palotai* (2022) introduced a relaxed Arakawa–Schubert scheme to this model, which represents moist convection as an ensemble of convective plumes. In parallel with these efforts, *Boissinot et al.* (2024) implemented a Kessler-type cloud scheme in their Jupiter-DYNAMICO model. They also include a plume model involving entrainment and detrainment at each level for dry and water moist convection.

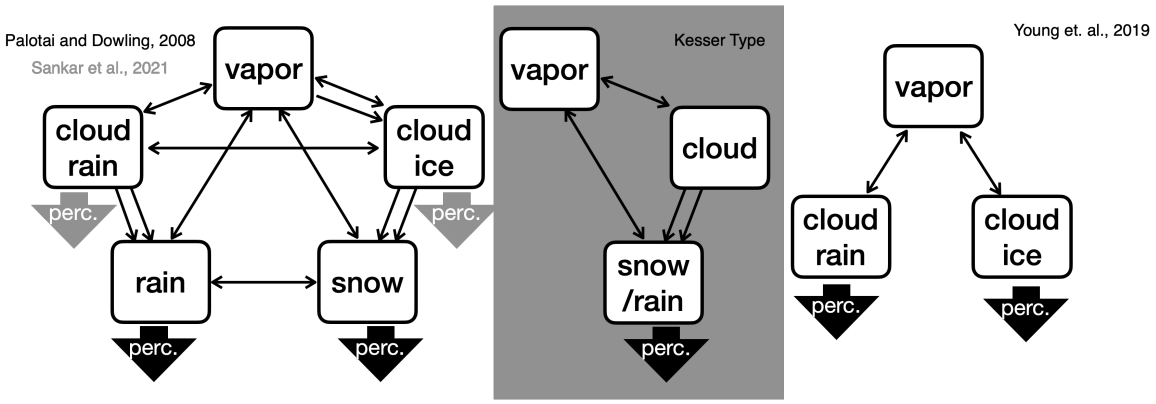


Figure 1.6: Different cloud scheme used in numerical simulations of Jupiter. Line arrows represent processes that convert between different phases. Solid arrows represent precipitation, either parameterised or resolved. Grey arrows are updates by *Sankar et al.* (2021) to the scheme implemented by *Palotai and Dowling* (2008).

The microphysical parameters required for *Palotai and Dowling* (2008), and by many moist convection schemes, often lack observational constraints. Therefore, *Zuchowski et al.* (2009b) developed a bulk cloud scheme for NH_3, NH_4SH and H_2O, and a simple flux-based moist convection scheme (*Zuchowski et al.* 2009a). This cloud scheme is similar to the parameterisation developed for Mars (*Böttger* 2003) and Venus (*Lee et al.* 2010). The cloud deck position shows reasonable agreement with ECCMs and exhibits a belt-zone contrast consistent with that deduced from observations. Manual cloud tracking on cloud column density produced by this model indicated that clouds are good tracers of atmospheric motion. This cloud scheme was updated by *Young et al.* (2019b) to study the global tracer distribution, which will be described in Chapter 2. Fig. 1.6 summarized the aforementioned cloud schemes.

1.5 Project Outline

As discussed in previous sections, recent observations and modelling efforts have transformed our understanding of Jupiter's atmosphere, particularly through the Juno mission. Nevertheless, many fundamental questions remain unanswered. This thesis uses a series of numerical experiments with the Jason General Circulation Model (GCM) to study the interplay between large-scale energetics and the microphysical processes that govern the water–ammonia cycle. Specifically, the work aims to explore the following questions:

- How does latitudinal variation in internal heat flux affect atmospheric dynamics and the distribution of condensible species?
- How do the proposed water–ammonia hailstones ('mushball') interact with the large-scale dynamics?
- What is the relative role of the large-scale overturning circulations and small-scale transport, such as convective storms and 'mushball', in shaping the water and ammonia distribution?

This thesis is divided into two main parts, both of which use the Jason GCM, as detailed in Chapter 2. The first part, documented in Chapter 3, investigates the effect of latitudinally varying internal heat flux on Jupiter's zonal jet, meridional circulation and the water distribution. The second part involves developing a mushball parameterisation scheme for the Jason GCM. We first test the scheme and explore the effect of changing the parameters in a two-dimensional configuration in Chapter 4. Then in Chapter 5, we present the results of the three-dimensional simulations. We conclude the thesis in Chapter 6, where we summarise the results and discuss their implications in the broader context of planetary science.

Chapter 2

The JasonGCM

This chapter summarises the technical details of the Jason[1] GCM (General Circulation Model), which was used for this project. While much of this model has been detailed previously in *Young et al.* (2019a), *Young et al.* (2019b) and *Young and Read* (2019), a few adjustments have been made to improve the physical parameterisation and to extend its modelling capacity. We recapitulate their parameterisations to give a comprehensive view of the model, and highlight the adjustments made throughout the way.

The remainder of this chapter is organised as follows: Section 2.1 describes the dynamical core used in this model and its specific setups. In Section 2.2, we explore the model's domain and resolutions, justifying the choices made. The subsequent sections delineate the parameterisation specific to Jupiter, partitioned according to different atmospheric processes. Section 2.3 presents the parameterisation of non-cloud atmospheric processes. Section 2.4 discusses the passive cloud cycles, during which tracers undergo phase changes, sedimentation (in condensed phases), and advection by atmospheric flows, but do not influence the atmospheric dynamics. Finally, Section 2.5 addresses the active water cycle, which includes latent heating and moist convection parameterisation.

2.1 Dynamical Core

The JasonGCM is based on the MITgcm, a finite volume GCM that solves the primitive equations for an incompressible fluid on a rotating sphere. Although it is frequently used as an oceanographic model, the use of a generalised vertical coordinate, r, makes it suitable for both the ocean (where r is interpreted as height, z) and the atmosphere (where r is interpreted as pressure, p).

[1]The name "Jason" is derived from the first letters of the four giant planets in the Solar System: Jupiter, Saturn, Uranus and Neptune (JSUN), as this model intends to simulate the weather layers of these giant planets. It has also been suggested that this acronym also pays homage to the Greek mythological explorer Jason.

2.1.1 Primitive Equations

We use the hydrostatic version of the atmospheric mode with thin shell approximation. Under this setup, the dynamical core essentially solves the following equations:

The horizontal component of the simplified Navier-Stokes equation,

$$\frac{D\mathbf{v}_h}{Dt} + \hat{\mathbf{k}} \times \mathbf{v}_h + \nabla_p \mathbf{\Phi}' = \mathbf{F}_h, \tag{2.1}$$

The vertical (hydrostatic) component,

$$\frac{\partial \Phi'}{\partial p} + \alpha' = 0. \tag{2.2}$$

The continuity equation,

$$\nabla_p \cdot \mathbf{v}_h + \frac{\partial \omega}{\partial p} = 0. \tag{2.3}$$

The evolution of the pressure at the bottom of the domain,

$$\frac{\partial p_s}{\partial t} + \nabla \cdot \int_0^{p_s} \mathbf{v}_h dp = 0. \tag{2.4}$$

The ideal gas law,

$$c_p \frac{D\Pi}{Dt} \theta' = \alpha'. \tag{2.5}$$

The thermodynamic energy equation,

$$c_p \frac{D\theta}{Dt} = \frac{\mathcal{Q}}{\Pi}. \tag{2.6}$$

The physical meanings of the symbols are listed in Table 2.1. The dynamical core is chosen to be consistent with the focus of our study on large-scale circulation under long-timescale equilibration in Jupiter's weather layer. Non-hydrostatic effects associated with convective plumes are not explicitly resolved at the current model resolution and are instead parameterised. Previous non-hydrostatic sensitivity tests conducted within our research group using the MITgcm indicate that non-hydrostatic effects make a negligible contribution to the large-scale circulation at the resolutions considered here. Fully non-hydrostatic models that explicitly resolve storm-scale moist convection, such as those described in Section 1.4.2 are typically limited to

much smaller spatial domains and address a complementary regime to our work.

$D/Dt = \partial/\partial t + \mathbf{v}_h \cdot \nabla_p + \omega\partial/\partial p$	Total derivative
$\mathbf{v}_h = (u, v, 0)$	Horizontal velocity on pressure surfaces
∇_p	Gradient operator in pressure coordinates
$\omega = Dp/Dt$	Vertical velocity in pressure coordinates
$f = 2\Omega \sin\phi$	Coriolis parameter
$\Phi = gz$	Geopotential
$\mathbf{F}_h$	Additional mechanical forcing
$\alpha = 1/\rho$	Specific volume
p_s	Pressure at the bottom of the domain
c_p	Specific heat capacity of dry air at constant pressure
$\Pi = (p/p_0)^\kappa$	Exner function
κ	$= R_d/c_p$ where R_d is the specific gas constant of dry air
Q	Heating rate per unit mass due to external forcing
$\theta = T/\Pi$	Potential temperature
$'$	Deviation from the one-dimensional reference profile

Table 2.1: Summary of symbols and their meanings for the equations in the dynamics core

The dynamical core solves the primitive equations globally with respect to longitude (λ) and latitude (ϕ). u, v and θ are the prognostic variables, while others are derived as diagnostic variables. The Jupiter-specific parametrisations described in Section 2.3 and Section 2.5) are included in the forcing terms F and Q on the right-hand side of the prognostic equations. The equations are discretised on an Arakawa-C grid as illustrated in Fig. 2.1 (*Adcroft et al.*).

2.1.2 Configuring the Dynamical Core

Several configurations have been implemented to optimise the functionality of the dynamical core. The vector invariant form of the momentum equation is used for its efficiency in spherical coordinates. The time-stepping method is the Adams-Bashforth III method with a fixed time step of δt that satisfies stability criteria and ensures computational efficiency. For the potential temperature, the central second-order advection-diffusion scheme with viscosity is employed. A linear free surface is used as the boundary condition. To ensure numerical stability, two filters are implemented: a 4th-order (∇^8) Shapiro filter on a timescale of δt, which attenuates grid-scale noise in the velocity and temperature fields; and a zonal filter applied poleward of 45° to mitigate small-scale longitudinal.

Additionally, the MITgcm supports the advection of multiple tracers in terms of their mass mixing ratios. Details of the setup for these tracers can be found at the beginning of Section 2.4.

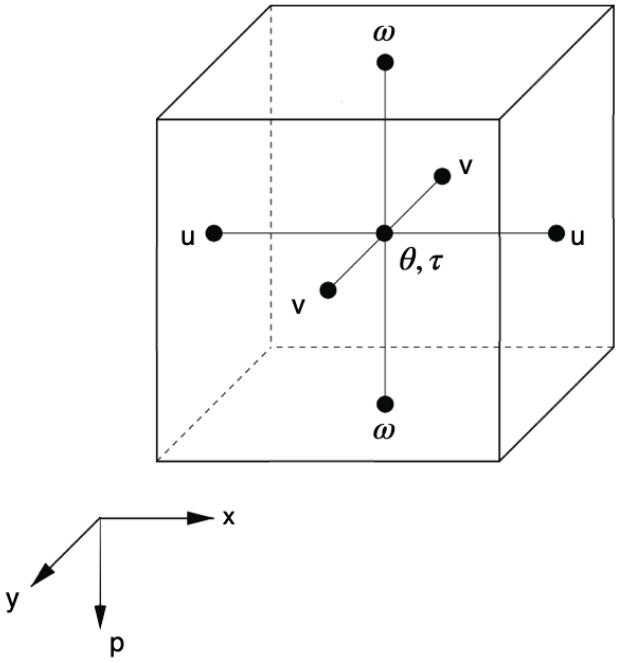


Figure 2.1: Schematics of the Arakawa-C grid in the pressure coordinate, where temperature and tracer grid points are located in the centre of each grid box and velocity points are at the boundary.

2.2 Domain

2.2.1 Horizontal Resolutions and Justification

Our simulations utilise two horizontal resolutions. The low resolution (L) consists of 256×128 grid points at approximately 1.4° per cell, with a time step of 600 seconds. This resolution is used at the beginning of the simulation, starting with the temperature profile at radiative-convective equilibrium and the atmosphere at rest. Following an initial period of equilibration, the medium (M) resolution of 512×256 grid points ($\sim 0.7^\circ$) and $\delta t = 300$s is employed. [2] This increase in resolution is crucial in order to resolve the deformation radius $L_d = NH/f$, where N is the buoyancy frequency and H is the pressure scale height. With an approximate value of 2000 km for the deformation radius, L_d, at mid-latitudes on Jupiter (*Showman et al.* 2010), resolution M marginally resolves this scale with 2–3 grid points per L_d, capturing the transition where turbulent dynamics begin to dominate over larger-scale, rotationally influenced flows.

[2] Although we do not use a higher resolution in this work, we use the same notation as in *Young et al.* (2019a), where 'high' resolution denote the 1024×512 simulations.

2.2.2 Vertical Resolutions

We have used two model depths in our simulations. The upper boundary of the model is always set to vacuum. The default depth is 18 bar, which is sufficient to position several model levels below the water cloud base. For simulations involving mushballs, a greater depth of 56 bar was required to account for their deeper penetration. In addition, with the more realistic temperature profile (discussed in Section 2.3.1), the cloud base is deeper, requiring a deeper model base to maintain adequate resolution below the water clouds.

The cell centre of the uppermost cell in the model is set to 0.01 bar. The cells below are spaced approximately equally in the logarithm of the pressure ($\log p$), meaning that the difference in $\log p$ between two adjacent cell centres is about 0.1 (and the difference between the cell surface and the centre of the same cell is 0.05). This arrangement provides approximately five levels per pressure scale height. For pressures below 10 bar, there are exactly ten cells per $\log p$. For pressures above 10 bar, the model base is first chosen as the nearest integer to $10^{n/10+0.05}$, where n is the number of model levels below 10 bar. Then the cells between 10 bars and the model bottom are equally divided in $\log p$ space. This method is used because it is consistent with *Young et al.* (2019a). Imposing an exact spacing of 0.1 $\log p$ and allowing the bottom pressure of the model to be non-integer would make vertical pressure settings easier and ensure greater consistency between different simulations. However, as the difference in vertical resolution is small, we don't expect such a setup to cause any significant difference in model behaviour between simulations at different depths.

The top boundary mimics a solid surface with $\omega = 0$ at $p = 0$, and the lower boundary is modelled as an impermeable free surface where $p = p_s = p_{base} + \eta$ and $\omega = \frac{Dp_s}{Dt}$. A free-slip boundary condition is also applied at the bottom boundary (i.e. no normal flow and zero tangential stress), which is most appropriate given the uncertainties in observations of the deep atmosphere. In addition, a parameterised bottom drag is included in the lowest layers to represent the effects of MHD drag and to close the momentum budget. As this drag is implemented as a physical parameterisation rather than a dynamical core setup, it is described separately in Section 2.3.5.

2.3 Dry Jupiter Parameterisations

Table 2.2 lists the parameters used in our Jupiter model, including both planetary parameters and those used for the parameterisation schemes. For parameters with different values, the values and the corresponding code are also listed.

Symbol	Meaning		Values
Planetary parameters			
R_m	Mean radius at 1 bar		69911 km
a	Radius at model base		69803 km
R_d	Specific gas constant for dry air		3750 J kg^{-1} K^{-1}
c_p	Specific heat of dry air at constant pressure		12360 J kg^{-1} K^{-1}
Ω	Rotation rate		1.75865×10^{-4} rad s^{-1}
M_J	Planet mass		1.8988×10^{27} kg
g	Acceleration due to gravity		25.923 m s^{-2}
Radiative scheme			
S_0	Solar constant		50.66 W m^{-2}
A_{bond}	Bond albedo		0.343
$\tau_{0,SW}$	Reference shortwave optical depth	OA	3.0
		OB	2.45
$\tau_{0,LW}$	Reference longwave optical depth	OA	80
		OB	53.3
p_{ref}	Pressure of reference optical depth		3 bar
n_{year}	Number of days in the tropical year		10478.3 d
	Length of a Jupiter day		9.92425 hr
ϵ	Orbit obliquity		3.13°
F_{int}	Internal heat flux		5.7 W m^{-2}
Bottom drag			
τ_{drag}	Drag timescale at reference pressure		20 d
Cloud scheme			
d_p	Cloud particle diameter		1 μm
τ_{pchg}	Phase change timescale		10,000 d
Moist convection			
$\sigma(p_{\text{ref,mc}})/\sqrt{\mu}$	Convective index ratio		1
n_{mix}	Maximum mixing layer height		4 grid cells

Table 2.2: Model parameters used in this study.

2.3.1 Two Stream Radiation

A two-stream, double-grey radiation scheme is employed to represent the effects of solar heating, interior heating and radiative emission. Assuming that the shortwave (SW) and longwave (LW) blackbody curves for the Sun and Jupiter are sufficiently distant from each other, these two bands are treated separately. The two-stream radiation scheme in our model simulates the following processes within the atmosphere: SW absorption, LW absorption and LW radiation. Furthermore, an optional interior LW heat source is included.

To determine the heating due to radiative transfer, first we calculate the annual mean insolation at latitude ϕ:

$$\overline{F(\phi)} = \frac{1}{N_{\text{year}}} \sum_{j=1}^{N_{\text{year}}} F(\phi, j) = \frac{1}{N_{\text{year}}} \sum_{j=1}^{N_{\text{year}}} \frac{S_0(1 - A_{bond})}{\pi} \mu(\phi, j) H(\phi, j) \tag{2.7}$$

where N_{year} is the number of local days per year, S_0 is the solar constant at Jupiter, A_{bond} is the bond albedo, $\mu(\phi, j)$ is the daily average of cosine of solar zenith angle, and $H(\phi, j)$ is the half day length in radian. $\mu(\phi, j)$ and $H(\phi, j)$ are given by (*Vardavas and Taylor* 2007):

$$\mu(\phi, j) = \sin\phi \sin\delta_j + \cos\phi \cos\delta_j \frac{\sin H(\phi, j)}{H(\phi, j)} \tag{2.8}$$

$$H(\phi, j) = \arccos\left(-\tan\phi \tan\delta_j\right) \tag{2.9}$$

where $\delta_j = -\epsilon \cos\left(2\pi j / N_{\text{year}}\right)$ is the solar declination angle, ϵ is the obliquity of Jupiter.

With SW radiation at the top of the atmosphere set by Eq. (2.7) and LW radiation set to zero, the downward SW and LW fluxes at the cell surface $\tilde{k}$ flux are then integrated downward:

$$F^{\downarrow}_{\text{S},\tilde{k}} = F^{\downarrow}_{\text{S},\tilde{k}+1} \mathcal{T}_{\text{S},\tilde{k},\tilde{k}+1} \tag{2.10}$$

$$F^{\downarrow}_{\text{L},\tilde{k}} = F^{\downarrow}_{\text{L},\tilde{k}+1} \mathcal{T}_{\text{L},\tilde{k},\tilde{k}+1} + E^{\downarrow}_{k} \tag{2.11}$$

where

$$E^{\downarrow}_{k} = \frac{\left(B\left(T_{\tilde{k}}\right) - B\left(T_{\tilde{k}+1}\right) \mathcal{T}_{\text{L},\tilde{k},\tilde{k}+1}\right) \Delta\tau_{\text{L},\tilde{k},\tilde{k}+1}}{\Delta\tau_{\text{L},\tilde{k},\tilde{k}+1} - D_{\tilde{k},\tilde{k}+1} \log\left[B\left(T_{\tilde{k}+1}\right) / B\left(T_{\tilde{k}}\right)\right]} \tag{2.12}$$

is the downward thermal emission from cell k. $B(T) = \sigma T^4$ represents the blackbody radiation

flux. $\mathcal{T}_{\tilde{k},\tilde{k}+1}$, is the transmission for each band of cell k, given by

$$\mathcal{T}_{\mathrm{S},\tilde{k},\tilde{k}+1} = \exp\left[-\left(\tau_{\mathrm{S}}\left(p_{\tilde{k}}\right) - \tau_{\mathrm{S}}(p_{\tilde{k}+1})\right)\right] \tag{2.13}$$

$$\mathcal{T}_{\mathrm{L},\tilde{k},\tilde{k}+1} = \exp\left[-\left(\tau_{\mathrm{L}}\left(p_{\tilde{k}}\right) - \tau_{\mathrm{L}}(p_{\tilde{k}+1})\right)/D_{\tilde{k},\tilde{k}+1}\right], \tag{2.14}$$

for longwave and shortwave, respectively. Here

$$D_{\tilde{k},\tilde{k}+1} = \left(1.5 + \frac{0.5}{1 + 4\Delta\tau_{\mathrm{L},\tilde{k},\tilde{k}+1} + 10\left(\Delta\tau_{\mathrm{L},\tilde{k},\tilde{k}+1}\right)^2}\right)^{-1} \tag{2.15}$$

is the LW diffusivity factor, which represents the scaling of optical depth due to integration over different directions within a hemisphere under the plane-parallel approximation. Following *Schneider and Liu* (2009), the optical depth profiles are given by

$$\tau_{\mathrm{S}}(p) = \tau_{0,\mathrm{S}}\left(\frac{p}{p_{\mathrm{ref}}}\right), \quad \tau_{\mathrm{L}}(p) = \tau_{0,\mathrm{L}}\left(\frac{p}{p_{\mathrm{ref}}}\right)^2 \tag{2.16}$$

where the reference values p_{ref}, $\tau_{0,\mathrm{S}}$ and $\tau_{0,\mathrm{L}}$ are listed in Table 2.2. The reference optical depths are treated as tunable parameters, chosen to produce a realistic Jovian thermal structure rather than being derived from wavelength-resolved opacities. Two sets of reference optical depths are considered in this work: set OA follows the value used in *Young et al.* (2019a), and set OB reflects an update discussed later in this section.

At the bottom of the domain, we impose a flux balance:

$$F^{\uparrow}_{\mathrm{L},\tilde{1}} = F^{\downarrow}_{\mathrm{S},\tilde{1}} + F^{\downarrow}_{\mathrm{L},\tilde{1}} + F_{\mathrm{int}}, \tag{2.17}$$

Where F_{int} is the internal heat flux. The LW flux is then integrated back upwards

$$F^{\uparrow}_{\mathrm{L},\tilde{k}+1} = F^{\uparrow}_{\mathrm{L},\tilde{k}}\mathcal{T}_{\mathrm{L},\tilde{k},\tilde{k}+1} + E^{\uparrow}_{k} \tag{2.18}$$

where

$$E^{\uparrow}_{k} = \frac{\left(B\left(T_{\tilde{k}+1}\right) - B\left(T_{\tilde{k}}\right)\mathcal{T}_{\mathrm{L},\tilde{k},\tilde{k}+1}\right)\Delta\tau_{\mathrm{L},\tilde{k},\tilde{k}+1}}{\Delta\tau_{\mathrm{L},\tilde{k},\tilde{k}+1} - D_{\tilde{k},\tilde{k}+1}\log\left[B\left(T_{\tilde{k}}\right)/B\left(T_{\tilde{k}+1}\right)\right]} \tag{2.19}$$

is the upward thermal emission. Given the logarithmic spacing of the pressure domain, the variation in optical depth within a cell is considerable. To achieve more accurate upward or downward thermal emission, this is evaluated in two parts, split at the cell centre at pressure p_k. The total emission, for example, for downward emission at cell face $\tilde{k}$, is given by:

$$E^{\downarrow}_{k} = E^{\downarrow}_{k,\text{ lower}} + E^{\downarrow}_{k,\text{ upper}}\,\mathcal{T}_{\mathrm{L},\tilde{k},k} \tag{2.20}$$

where $E^{\downarrow}_{k,\text{ lower}}$ and $E^{\downarrow}_{k,\text{ upper}}$ are determined by Eq. (2.12), but with the emission at level k used in lieu of either $\tilde{k}$ or $\tilde{k}+1$, respectively.

The potential temperature tendency is then

$$\left.\frac{\partial\theta_k}{\partial t}\right|_{\text{rad}} = \frac{\Gamma_d}{\Pi_k}\frac{\Delta F_{\mathrm{S},k} + \Delta F_{\mathrm{L},k}}{p_{\tilde{k}} - p_{\tilde{k}+1}} \tag{2.21}$$

where

$$\Delta F_{\mathrm{S},k} = F^{\downarrow}_{\mathrm{S},\tilde{k}+1} - F^{\downarrow}_{\mathrm{S},\tilde{k}} \tag{2.22}$$

$$\Delta F_{\mathrm{L},k} = F^{\downarrow}_{\mathrm{L},\tilde{k}+1} - F^{\downarrow}_{\mathrm{L},\tilde{k}} + F^{\uparrow}_{\mathrm{L},\tilde{k}} - F^{\uparrow}_{\mathrm{L},\tilde{k}+1} \tag{2.23}$$

are the net fluxes into cell k for LW and SW respectively, and $\Gamma_d = g/c_p$ is the dry adiabatic lapse rate.

Change in Reference Optical Depth

To enable comparison with previous studies using the JasonGCM model, we adopt the same reference optical depth in *Young et al.* (2019a) as OA in Table 2.2. This set produced a temperature profile that is hotter than observed, resulting in different cloud condensation levels than predicted by the ECCMs (*Young et al.* 2019b). This discrepancy arise because the optical depths set OA are not calibrated to observations: While the original values from *Schneider and Liu* (2009) are loosely based on the Galileo probe measurements, our radiative scheme is different from theirs, as we have included a longwave diffusivity factor D (our Eq. (2.14)) and omitted the shortwave semi-finite scattering (Γ in their Eq. B3). Therefore, the effective optical depths of these two models are different.

We therefore introduce a new set of reference optical depths so that the effective reference optical depths of the two models are approximately equal, listed in Table 2.2 as OB. Since D is

not a constant, the LW optical depth profile will not be identical to *Schneider and Liu* (2009), and we use a value of D that is representative of the atmosphere in calculating the new $\tau_{0,\mathrm{L}}$.

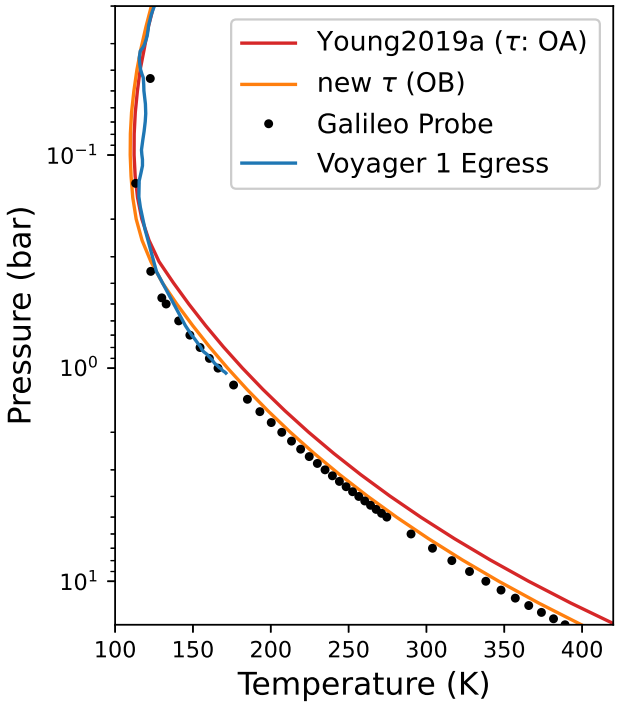


Figure 2.2: Temperature profiles of Jupiter obtained from observations (Voyager 1 egress at 0° (*Gupta et al.* 2022) and Galileo probe at 6.5°N (*Seiff et al.* 1998)) and from JasonGCM simulation using the old reference optical depth (*Young et al.* 2019a) and the updated values. The JasonGCM results are the zonally averaged value at the end of the three-dimensional simulation at the latitude as the Galileo probe profile.

To test whether the new optical depths produce a temperature profile that is consistent with the observations, we ran the model at the low resolution for 100,000 days to reach statistical equilibrium. As illustrated in Fig. 2.2, the temperature profile is in better agreement with the measurement from the Galileo probe. At 1 bar, the model temperature differs from the Galileo probe measurement by 6.2 K, and the difference increases to 10.5 K at the model bottom. Such a difference is equivalent to shifting the model temperature profile upwards by half of a vertical level. However, this temperature profile may not be representative of conditions on Jupiter, as the entry point of the Galileo probe is at the edge of a 5μm hotspot, a region of extremely active dynamics (*Showman and Dowling* 2000). We therefore also compared our model results with more recent results of the reanalysed Voyager 1 egress profile (*Gupta et al.* 2022). The retrieved temperature at 1 bar is 167.3 ± 3.8 K, which differs from our model output by 5.0 K. Our updated reference optical depth therefore yields a temperature profile that is only slightly warmer than the observed values.

It is important to acknowledge the limitations of further refining the model at the end of this section. While additional simulations could potentially achieve better agreement with observations, the accuracy gained from such improvements may not justify the resources expended, especially given the small difference between the updated set of reference optical depths and observations, and the long equilibration time required for simulations. This is particularly relevant given that the accuracy achievable through further parameter tuning is inherently limited by the simplifications of the two-stream and double-grey approximation in our radiative transfer scheme, and the exclusion of cloud radiative effects. While these simplifications reduce the computational resources required by our radiative transfer scheme, they also limit its ability to accurately capture the details of realistic radiative transfer.

In addition, the value of the internal heat flux (in Eq. (2.17)) should be updated to reflect more recent observations (*Li et al.* 2018b). However, incorporating such a change would require experimenting with different LW and SW reference optical depths. Analytic radiative–convective models (e.g. *Robinson and Catling* 2012) could, in principle, provide guidance for such parameter tuning, but the difference between global mean temperature in radiative–convective equilibrium and the dynamically equilibrated GCM state (see Section 3.3.2) makes this a non-trivial extension. We currently use a set of values to produce a temperature profile that is sufficiently similar to the observations. However, we acknowledge that updating these values in the future would be valuable to ensure that our model reflects the current understanding of Jupiter's atmospheric processes.

Internal Heat Flux

The bottom heat flux F_{int} has two modes. The first is to set it to a constant value across the globe. The default value is 5.7 W m^{-2}, with the rationale discussed previously. The second and recently added option is to prescribe a spatially varying internal heat flux through an external file. This setup maximises the flexibility of our model for studying the effects of inhomogeneous heat fluxes, from latitudinal variations to localised hotspots, as discussed in Chapter 3.

2.3.2 Convective Adjustment

A simple adjustment scheme derived from *Manabe et al.* (1965) is used to represent the effect of dry convection on temperature. If a pair of adjacent vertical levels is found to be convectively

unstable ($\partial\theta/\partial p > 0$) within a column, then the vertical extent $[k_{bot}, k_{top}]$ of this unstable column is determined. The scheme then calculates the neutrally stable potential temperature profile that conserves the total potential energy within the column (*Andrews* 2010, Eq. 2.34),

$$\theta_{\text{k, stable}} = \left(\sum_{k=k_{\text{bot}}}^{k_{\text{top}}} \theta_k \Pi_k \Delta p_k \right) / \left(\sum_{k=k_{\text{bot}}}^{k_{\text{top}}} \Pi_k \Delta p_k \right). \tag{2.24}$$

Since this adjustment might introduce new instabilities at the edge of the stable profile, this process is repeated until the whole column is stable. The potential temperature profile of the column is then forced towards the stable profile:

$$\left.\frac{\partial \theta_k}{\partial t}\right|_{\text{dryconv}} = -\frac{\theta_k - \theta_{k,\text{ stable}}}{\tau_{\text{dryconv}}} \tag{2.25}$$

where we use the inertial timescale $f^{-1} = (2\Omega \sin\phi)^{-1}$ as the dry convection timescale τ_{dryconv} . If the centre of a grid cell lies exactly on the equator, the value of f at the adjacent cell face is used to avoid singular behaviour. In our resolutions this does not affect the convective adjustment, as the centre of the grid cell is always off the equator. The maximum value of this timescale occurs at the grid point closest to the equator, where it reaches approximately 2.6 days. This is much shorter than the typical radiative timescale ($\sim$ 6000 days; see Section 2.5.2). *Young et al.* (2019a) also noted that although this equatorial value is slightly longer than the dynamical timescale $\tau_d = L/U$, it is shorter than τ_d at all other latitudes.

2.3.3 Deep Adiabat Setup

An alternative approach to providing an intrinsic heat flux is to prescribe the potential temperature at a level below the vertical domain of the model, denoted by θ_{deep}. This modification affects both the radiative transfer and convective adjustment schemes.

For the radiative transfer scheme, instead of applying the standard radiative boundary condition given in Eq. (2.17), the upward longwave flux at the bottom boundary is specified as

$$F^{\uparrow}_{\text{L},\tilde{1}} = \sigma T^4_{\text{deep}}, \tag{2.26}$$

where $T_{\text{deep}} = \theta_{\text{deep}} \Pi_{\tilde{1}}$ is the temperature corresponding to the deep adiabat evaluated at the bottom model layer.

For the convective adjustment scheme, if convective instability extends to the bottom of the model domain, the right-hand side of Eq. (2.24) is replaced with θ_{deep}. This effectively forces the convective column to start from the bottom of the model domain and follow the deep adiabat. While this procedure does not conserve enthalpy within the model domain, it is physically justified as this reflects the coupling to the more massive interior, which supplies the energy to maintain the specified deep potential temperature.

2.3.4 Vertical Mixing

Our model incorporated a Richardson number based vertical mixing scheme to simulate sub-grid scale vertical mixing of horizontal velocities. By incorporating mixing with a strength dependend on the Richardson number, this scheme avoids the unrealistically abrupt mixing that can arise when adjustment is only triggered by static instability. It accounts for hydrodynamical instabilities associated with vertical shear, including Kelvin–Helmholtz and symmetric instabilities, which can occur even when the flow is statically stable (*Yamazaki et al.* 2004). Similar Richardson number based scheme are commonly used in meso-scale models (e.g. *Clark* 1977).

The local Richardson number at level k is computed using

$$\text{Ri}_k = -\frac{R_d \Pi_k \Delta p_k \Delta \theta_k}{p_k \left[(\Delta u_k)^2 + (\Delta v_k)^2 \right]}, \tag{2.27}$$

where Δ denotes the difference between the top and bottom of a grid cell. The mixing coefficient, $\tilde{K}$, is then determined:

$$\tilde{K} = \begin{cases} 0 & \text{Ri} \geq 3 & \text{No mixing} \\ (1 - \text{Ri}/3)^3 & 0 < \text{Ri} < 3 & \text{Partial mixing} \\ 1 & \text{Ri} \leq 0 & \text{Full mixing} \end{cases} \tag{2.28}$$

For the fluid mixed between adjacent levels over time τ_{mixing}, $(\tilde{K}/3)$ will go to the level above or below, $(1 - 2\tilde{K}/3)$ will stay at the same level. Thus, after a time step δt, the zonal velocity at level k is:

$$u_{k,\text{ new}} = u_k + \frac{\delta t}{3\tau_{\text{mixing}}} \left(\tilde{K}_{k-1} u_{k-1} - 2\tilde{K}_k u_k + \tilde{K}_{k+1} u_{k+1} \right), \tag{2.29}$$

and similarly for the meridional velocity. Note that this is equivalent to a vertical diffusion term

$$\left.\frac{\partial u}{\partial t}\right|_{\text{vdiff}} = \frac{\partial}{\partial p}\left(K\frac{\partial u}{\partial p}\right), \tag{2.30}$$

where the diffusion coefficient can be roughly related to the mixing coefficient by

$$K_k = \frac{\Delta p_k^2}{3\tau_{\text{mixing}}}\tilde{K}_k. \tag{2.31}$$

As with the dry convective adjustment, the inertia timescale is used as the mixing timescale.

2.3.5 Bottom Drag

At the bottom of the domain, a linear drag is applied to the horizontal velocity components u and v. While this drag was motivated by the potential effects of magnetohydrodynamic (MHD) drag from planetary interiors, as discussed by *Schneider and Liu* (2009), in our model, it is employed mainly for numerical stability. Including this drag is crucial to prevent growth of equatorial zonal velocities to unrealistically large values.

Our parameterisation scheme is similar to that in *Schneider and Liu* (2009): At the bottom of the domain, the drag timescale is set to τ_{drag}. This is then converted to a drag coefficient $k_{drag} = 1/\tau_{\text{drag}}$, which decreases linearly to zero at $\sigma = p/p_{base} = 0.8$ and above. Due to the log spacing of the pressure levels, effectively only the lowest level is damped. The forcing on the zonal velocity due to this drag is given by

$$\left.\frac{\partial u}{\partial t}\right|_{\text{drag}} = -k_{\text{drag}}u \quad \sigma > 0.8, \tag{2.32}$$

and similarly for the meridional velocity. The heating due to kinetic energy lost is then calculated and divided between adjacent grid cells according to their relative mass, given by

$$\left.\frac{\partial \theta}{\partial t}\right|_{\text{drag}} = \frac{\Delta E_K}{c_p m \Pi \delta t}, \tag{2.33}$$

where m is the mass of the grid cell and ΔE_K is the KE lost from adjacent velocity cells. Following *Schneider and Liu* (2009), we used $\tau_{\text{drag}} = 20$ d in all simulations. This value is empirically chosen to produce realistic jet structures, rather than being constrained by obser-

vations. Subsequent sensitivity studies by *Liu and Schneider* (2015) confirm that this value lies within the regime that produces Jupiter-like off-equatorial jets. Drag timescales that are significantly shorter or longer lead to jets that are too weak or excessively broad, respectively.

2.3.6 Sponge Layer

A sponge layer is applied to the uppermost levels to prevent reflection of the gravity wave from the top of the domain. The eddy components of the temperature and the horizontal velocities at the top three levels are damped. For example, at latitude ϕ_j and pressure level p_k, the zonal velocity damping is

$$\left.\frac{\partial u}{\partial t}\right|_{\text{sponge}} = -\frac{u_{ijk} - \langle u \rangle_{jk}}{\tau_{\text{damp},\, k}} \tag{2.34}$$

where $\langle u \rangle_{jk}$ is the zonal mean zonal velocity, $\tau_{damp,k}$ is the damping timescale, which takes the values 0.1, 1.0, and 10.0 Earth days, respectively, counting down from the top.

2.4 Jupiter Cloud Scheme

The cloud scheme employs the tracer package of MITgcm to solve the 4D tracer advection equation with the second-order flux limiter scheme. This can be expressed as follows:

$$\frac{Dq}{Dt} = G_{\text{q}} \tag{2.35}$$

for water (H_2O, in gas, liquid and solid phase) and ammonia (NH_3, gas and solid). Here q is the mass mixing ratio of the tracer, and G_{q} is the forcing of tracer due to cloud processes and moist convection. The following sections describe the different components of G_{tracer}, including phase change (Section 2.4.1), and sedimentation of the condensates (Section 2.4.2). The additional adjustment steps required are described in Section 2.4.3. While the Jason GCM includes a parameterization of the chemical reaction between ammonia and hydrogen sulphide to form ammonium hydrosulphide, this is not described here as it is not used in this thesis. The reader is referred to *Young et al.* (2019b) for details of the NH_3−SH_2 cycle.

2.4.1 Phase Change

Overall, the phase change tendency can be expressed as

$$G_{\mathrm{q,phase}} = -\frac{q - q_{\mathrm{eqm}}}{\tau_{\mathrm{pchg}}} \tag{2.36}$$

where τ_{pchg} is the phase change timescale, set to 10000 s according to *Lian and Showman* (2010), where it was taken to be comparable to typical convection time. q_{eqm} is the equilibrium tracer mass mixing ratios determined by the relationship between saturation mass mixing ratio (SMMR) and the total tracer mixing ratio, q^{tot}, within a cell. q^{tot} is calculated by summing the mixing ratios of all phases. The SMMR of the species is given by

$$q^*(T, p) = \epsilon \frac{p^*}{p} \tag{2.37}$$

where p^* is the saturation vapour pressure (SVP) of each gas, and $\epsilon = R_v / R_d$ is the ratio between gas constants for water or ammonia vapour and dry air. For latent heat that is a constant or a linear function of temperature, integrating the Clausius–Clapeyron relation gives the general form of SVP as

$$p^* = D \times E^{A + \frac{B}{T} + C \log_E T}. \tag{2.38}$$

The parameters A to E for each phase change are listed in Table 2.3.

Species	Transition	A	B (K)	C	D	E	Source
NH_3	g $\leftrightarrow$ s	41.67871	-4122.0	-1.8163	0.1	e	BS89, Table IV
H_2O	g $\leftrightarrow$ s	10.5553	-2667.0	0.0	100	10	IG93, Eq. (54)
H_2O	g $\leftrightarrow$ l, $-50°C \leq T \leq 50°C$	23.5518	-2937.4	-4.9283	100	10	IG93, Eq. (53)
H_2O	g $\leftrightarrow$ l, $T \leq -50°C$	9.8368	-2459.8	0	100	10	IG93, Eq. (53)
H_2O	g $\leftrightarrow$ l, $T \geq 50°C$	9.0443	-2245.8	0	100	10	IG93, Eq. (53)

Table 2.3: Saturation vapour pressure curve parameters for the phase changes included in the JasonGCM. For the H_2O gas-liquid transition, the latent heat fit is only applicable within the temperature range of $\pm 50°C$. For temperatures outside this range, the latent heat is set to values at the respective temperature limits, and the coefficients are adjusted accordingly and listed separately. BS89 refers to *Briggs and Sackett* (1989), and IG93 refers to *Iribarne and Godson* (1973).

If the SMMR is higher than the corresponding total mass mixing ratio of all phases, q_{eqm} is set to q^{tot} for the vapour MMR and zero for the condensate. Otherwise q_{eqm} is set to the SMMR for the vapour and (q^{tot} – SMMR) for the condensate (i.e. the excess).

For ammonia, only sublimation is considered. However, water can undergo either sublimation or evaporation. The corresponding phase change, and therefore the SMMR curve, depends on the temperature of the cell. Below the triple point of water at 611.73 Pa, only condensation occurs. Above the triple point, the melting point of water is used to determine the relevant phase change. The melting point is considered to be a linear function of $\log p$ between $-9°C$ at 1000 bar and 0°C at 1bar (*Lide* 1995, p. 6-53). If the temperature of the cell is below the melting point, q_{eqm} for water liquid is set to zero, and similarly for ice in cells above the melting point.

2.4.2 Sedimentation

Sedimentation tendencies for each condensate are calculated using Stokes' law and the Van Leer I (*Hourdin and Armengaud* 1999) method. Stokes' law (*Lee et al.* 2010) gives the sedimentation velocity of a particle on a cell face as

$$V_{\text{stokes}} = \frac{d_p^2 \rho_p}{18} g \frac{C_n}{\mu_{\text{bulk}}} \tag{2.39}$$

where d_p is the particle's diameter, ρ_p is its density, and C_n is the Cunningham slip factor, as calculated using Eqs. 13 and 14 in *Young et al.* (2019b). μ_{bulk} is the bulk atmosphere's dynamic viscosity, determined by a third-order polynomial fit to its values calculated at different temperatures ranging from 100 K to 600 K in 100 K increments. These calculations use Eq. 10 from *Brokaw* (1968), with Jupiter's bulk atmospheric composition of 86.2% H_2, 13.5% He, and 0.2% CH_4. The equivalent mass of the bulk atmosphere transferred downwards by sedimentation during a time step is then

$$w_{\text{sed}} = V_{\text{stokes}} \, \rho \delta t. \tag{2.40}$$

Next, the mass-conserving Van Leer I scheme with a maximum slope of 2 is used to calculate the redistribution of tracers by sedimentation between model levels. Finally, this adjustment is converted to the mass mixing ratio tendency for the condensate,

$$G_{\text{q,sed}} = \frac{q_{\text{after}} - q_{\text{before}}}{\delta t}. \tag{2.41}$$

2.4.3 Additional Adjustments

Three additional adjustments are made at the end of the time stepping. First, the MITgcm's zonal filter mentioned in Section 2.1 is applied to each of the tracer fields.

Second, in order to correct for the negative tracer mass introduced by the zonal filter, the negative values of each field are filled, and cells with positive tracer mass are scaled to conserve the total tracer mass:

$$q \to q\left(1 + \frac{M_-}{M_+}\right) \tag{2.42}$$

where M^- and M^+ are the total negative and positive tracer masses, respectively.

Finally, the total mass of each tracer is rescaled to its initial total mass every 24 h. This is necessary in order to conserve their mass over the long simulation time required for the JasonGCM.

2.5 The Active Water Cycle

2.5.1 Latent Heating

The latent heating due to water's phase change is included as a forcing term in the heat equation. The latent heat of sublimation is a constant, $L_{g\leftrightarrow s} = 2834.3$ J g^{-1}, and the latent heat of evaporation/condensation is a linear function of temperature, given by *Iribarne and Godson* (1973) p.215:

$$L_{g\leftrightarrow l} = \begin{cases} 2615.05 & \text{if } T \leq -50°\text{C}, \\ 3121.6 - 2.27T & \text{if } -50°\text{C} < T < 50°\text{C}, \\ 2388.05 & \text{if } T \geq 50°\text{C}. \end{cases} \tag{2.43}$$

where constant values are used outside the $\pm 50°$C range because the fitting function is only valid within that range.

The latent heat of fusion is not included explicitly, as in our model $l \to$ s is processed as

$\mathrm{l} \rightarrow \mathrm{g} \rightarrow \mathrm{s}$. The potential temperature forcing term due to latent heating is then

$$\left.\frac{\partial \theta}{\partial t}\right|_{\text{latht}} = \frac{L_{\mathrm{g}\leftrightarrow\mathrm{l}} G^{\mathrm{g}\rightarrow\mathrm{l}}_{\text{phase}} + L_{\mathrm{g}\leftrightarrow\mathrm{s}} G^{\mathrm{g}\rightarrow\mathrm{s}}_{\text{phase}}}{c_p \Pi} \tag{2.44}$$

2.5.2 Moist Convection

The moist convection scheme is adapted from the heat engine parameterisations developed by *Zuchowski et al.* (2009a), who combined the methods from *Del Genio and McGrattan* (1990) and *Rennó and Ingersoll* (1996). The basic idea is that moist convection acts as a heat engine, transporting heat upwards and converting potential energy into mechanical work. This work maintains convective motion against friction and is eventually dissipated as heat. By utilising the properties of the heat engine, the properties of the plume can be determined. Its effect on the environment, namely the transport of static energy and vapour, can then be calculated.

Our current scheme makes two key assumptions: First, the convective mass flux is constant with height. *Del Genio and McGrattan* (1990) justifies this assumption for the conditions on Jupiter, and the scheme is much simpler mathematically under such an assumption. Second, we assume that any moisture condensed during the ascent or descent of the parcel immediately falls to the bottom of the plume and re-evaporates. In the following sections, we highlight the essential steps in our moist convection parameterisation for the calculation of temperature and tracer tendencies. The reader is referred to *Young and Read* (2019) for a more detailed derivation.

The notation employed in this part aligns with that introduced in earlier sections and is augmented by a few additions to facilitate discussions associated with convective plumes: the superscripts ^{u} and ^{d} denote updraft and downdraft components, respectively. Additionally, the overline symbol $\bar{\cdot}$ denotes quantities for the environment.

Properties of the Convective Plume

By considering a hypothetical parcel rising adiabatically, the extent of the plume can be determined. For such a parcel, its temperature T_c follows

$$\frac{dT_c}{dp} = \frac{\Gamma}{g\rho}. \tag{2.45}$$

The adiabatic lapse rate used depends on the vapour pressure of the parcel: the dry adiabatic lapse rate Γ_d is used for an unsaturated parcel; otherwise the the saturated adiabatic lapse rate Γ_s (SALR) (*Andrews* 2010) is used, given by

$$\Gamma_s = \Gamma_d \left(1 + \frac{Lq^*}{R_d T}\right) \left(1 + \frac{L^2 q^*}{c_p R_v T^2}\right)^{-1}. \tag{2.46}$$

Moist convection occurs when both

1. the lifted parcel is (or becomes) saturated, and
2. the virtual temperature $T^v = T\frac{1+q/\epsilon}{1+q}(1-q_c)$ of the lifted parcel is higher than the ambient temperature.

If the parcel was initially saturated, the pressure at the updraft bottom p_b and the initial updraft temperature will be the ambient values at the initial level; otherwise, the values at the raised level will be used. As the parcel ascends, its temperature T^u follows the saturated adiabat calculated from the environmental temperature and density, and its vapour MMR, q^u, follows the SMMR at T^u.

The convective updraft stops (at pressure p_t) if either:

1. the updraft is unsaturated (unlikely in the troposphere); or
2. the virtual temperature of the updraft is lower than that of the environment.

After the updraft terminates, the uplifted air is mixed with the surrounding environment across several vertical levels. The number of levels in this mixing layer, n_{mix}, is a free parameter and is typically set to 4, or the vertical extent of the moist convective column, whichever is smaller.

Downdrafts are treated similarly to updrafts, with a few modifications. The downdraft starts at pressure p_d, located at the centre of the mixed layer (i.e. $n_{mix}/2$ levels below the updraft top) and extends to the updraft bottom at pressure p_b. The initial vapour MMR is the value at pressure p_d, or the SMMR at p_d if the air is supersaturated. For the latter case, any excess vapour remains at pressure p_d. The parcel then descends along a pseudo-adiabatic path with temperature of T^d. Although the parcel is unlikely to remain saturated due to the increasing SMMR as it moves downward, we use SALR in Eq. (2.46) for the downward integration. If the vapour MMR in the downdraft, q^d, is below the SMMR, it is held constant. Otherwise (although unlikely), the SMMR is used, and any excess immediately falls to the bottom of the downdraft as condensation.

The updraft/downdraft mass flux M_c is then calculated using the ideal heat engine assump-

tion. The efficiency of the heat engine is

$$\eta = 1 - \frac{T_d^d}{T_b^u}, \tag{2.47}$$

where we consider the updraft bottom as the hot source and the downdraft top as the cold source.

The TCAPE (Total Convective Available Potential Energy) of the plume is given by:

$$\text{TCAPE} = \eta \left[c_p (T_b^{\text{u}} - T_b^{\text{d}}) + (L_b^{\text{u}} q_b^{\text{u}} - L_b^{\text{d}} q_b^{\text{d}}) \right]. \tag{2.48}$$

Plumes with either $\eta \leq 0$ (which sometimes happens if there is a temperature inversion) or TCAPE ≤ 0 are not considered. Assuming that the TCAPE is fully converted into plume kinetic energy and mechanically dissipated, we obtain the convective velocity

$$w_{\text{conv}} = \sqrt{\text{TCAPE}/\mu}, \tag{2.49}$$

where μ is the dimensionless dissipation coefficient, which is a free parameter of our scheme with the default value 16 obtained from the first-principles estimate by *Rennó and Ingersoll* (1996).

The constant mass flux can be expressed as

$$M_c = \rho_b^{\text{u}} w_{\text{conv}} \sigma_{\tilde{b}} = \frac{p_b}{R_d T_b^{\text{u}}} \sqrt{\text{TCAPE}} \frac{\tau_r \left(p_{\text{ref}}\right)}{\tau_r} \frac{\sigma \left(p_{\text{ref}}\right)}{\sqrt{\mu}}, \tag{2.50}$$

where ρ_b^{u} denotes the parcel density at the updraft base, $p_{\tilde{b}}$ is the pressure at the cell interface of the updraft base, and $\sigma_{p_{\tilde{b}}}$ represents the fractional coverage of convective regions at this pressure level. The second step uses the ideal gas law and assumes that the convective coverage is inversely proportional to the radiative time constant, τ_r, which is estimated by

$$\tau_r = \frac{\int_0^p \frac{c_p T}{g} dp'}{S_0(1-A)/4 + F_{\text{int}}}. \tag{2.51}$$

The numerator in this expression represents the atmospheric thermal energy per area above the pressure level p, and the denominator estimates the outgoing heat flux at thermal equilibrium. For the default internal heat flux of 5.7 W m^{-2}, this yields a reference timescale of

approximately 5500–6000 d at 1 bar, consistent with estimates based on changes in the radiative cooling rate following a small perturbation from equilibrium. This value is also within an order of magnitude of earlier estimates by *Gierasch and Goody* (1969), *Conrath et al.* (1990), and *Kuroda et al.* (2014), but is substantially longer than the more recent estimate of *Li et al.* (2018a). Given that those studies employ more sophisticated radiative transfer schemes, this discrepancy likely reflects limitations of the simplified radiative transfer used here rather than shortcomings of the estimation method itself.

In practice, our scheme contains two free parameters: n_{mix} and $\sigma\left(p_{\mathrm{ref}}\right)/\sqrt{\mu}$. The latter controls the strength of the mass flux and is therefore named the convective index.

Heat and Moisture Transport within the Plume

Using the calculated plume properties and mass flux, the heat and water vapour transport through the plume can be derived. The general form of the tendency due to convective transport for a tracer χ is

$$\left(\frac{\partial\chi}{\partial t}\right)^{u}_{\mathrm{conv}} = \frac{g}{\Delta p}[-M^{u}_{\tilde{k}+1}\chi^{u}_{\tilde{k}+1} + M^{u}_{\tilde{k}}\chi^{u}_{\tilde{k}} + M^{u}_{\tilde{k}+1}\bar{\chi}_{k} - M^{u}_{\tilde{k}}\bar{\chi}_{k-1}] \tag{2.52}$$

for the updraft, and

$$\left(\frac{\partial\chi}{\partial t}\right)^{d}_{\mathrm{conv}} = \frac{g}{\Delta p}[+M^{d}_{\tilde{k}+1}\chi^{d}_{\tilde{k}+1} - M^{d}_{\tilde{k}}\chi^{d}_{\tilde{k}} - M^{d}_{\tilde{k}+1}\bar{\chi}_{k} + M^{d}_{\tilde{k}}\bar{\chi}_{k-1}] \tag{2.53}$$

for the downdraft. Here, M^{u} and M^{d} are the updraft and downdraft mass fluxes, respectively. The first two terms in these equations represent the effect of the updraft/downdraft, respectively, while the last two represent the effect of the environmental subsidence/uplift required to conserve the total air mass of the cell. As our convection scheme assumes a constant moist convective flux M_c, these equations can be simplified. The tendency term will have the same form throughout the plume, except at the top and bottom of each plume where entrainment or detrainment occurs. Table 2.4 summarises the rate of change per unit area of water, dry static energy and latent heat due to updraft and downdraft at different levels. Note that, for water, additional terms are added at the bottom of both updrafts and downdrafts to take evaporated rain into account. While the table shows the total plume transport, the code splits the terms into detrainment from the convective plume and compensating flow (subsidence for updrafts

and uplift for downdrafts) for diagnostic purposes.

	water transport (ΔW)		dry static energy (ΔS)		latent heating ($\Delta \mathcal{L}$)	
	updraft (^{u})	downdraft (^{d})	updraft	downdraft	updraft	downdraft
top ($_t$ or $_d$)	$M_c(q_t^{\mathrm{u}} - \bar{q}_t)$	$M_c(\bar{q}_{d-1} - q_d^{\mathrm{d}})$	$M_c\left(s_{t-1}^{\mathrm{u}} - \bar{s}_t\right)$	$M_c\left(\bar{s}_{d-1} - s_d^{\mathrm{d}}\right)$	$L_k^{\mathrm{u}} M_c\left(q_{k-1}^{\mathrm{u}} - q_k^{\mathrm{u}}\right)$	0
middle ($_k$)	$M_c(\bar{q}_{k+1} - \bar{q}_k)$	$M_c(\bar{q}_{k-1} - \bar{q}_k)$	$M_c\left(s_{k-1}^{\mathrm{u}} - s_k^{\mathrm{u}} + \bar{s}_{k+1} - \bar{s}_k\right)$	$M_c\left(s_{k+1}^{\mathrm{d}} - s_k^{\mathrm{d}} + \bar{s}_{k-1} - \bar{s}_k\right)$	$L_k^{\mathrm{u}} M_c\left(q_{k-1}^{\mathrm{u}} - q_k^{\mathrm{u}}\right)$	$L_k^{\mathrm{d}} M_c\left(q_{k+1}^{\mathrm{d}} - q_k^{\mathrm{d}}\right)$
bottom ($_b$)	$M_c(\bar{q}_{b+1} - q_t^{\mathrm{u}})$	$M_c(q_d^{\mathrm{d}} - \bar{q}_b)$	$M_c(\bar{s}_{b+1} - s_b^{\mathrm{u}})$	$M_c\left(s_{b+1}^{\mathrm{d}} - \bar{s}_b\right)$	$-\sum_{k=b+1}^{t} L_k^{\mathrm{u}} M_c\left(q_{k-1}^{\mathrm{u}} - q_k^{\mathrm{u}}\right)$	$-\sum_{k=b+1}^{d-1} L_k^{\mathrm{d}} M_c\left(q_{k+1}^{\mathrm{d}} - q_k^{\mathrm{d}}\right)$

Table 2.4: Summary of the rates of change per unit area for water mass, dry static energy, and latent heat due to updraft and downdraft at different plume levels. Symbols within parentheses indicate the specific variable (e.g., ΔW is the rate of change per unit area for water mass). Subscripts denote the plume levels (t for top, k for intermediate, b for bottom), and superscripts denote the type of plume (u for updraft, d for downdraft).

The specific dry static energy, $s = c_p T + gz$, combines the internal heat ($c_p T$) and gravitational potential energy (gz). The temperature T used for the internal heat corresponds to the notation used in the static energy expression: updraft (T^u), downdraft (T^d), or the environment ($\overline{T}$). The gravitational potential energy is calculated as the difference between levels using the hydrostatic equation, for example, between levels $k-1$ and k,

$$g\left(z_k - z_{k-1}\right) = \frac{p_{k-1} - p_k}{\rho_{\tilde{k}}}, \tag{2.54}$$

where $\rho_{\tilde{k}}$ denotes the density at the boundary between these two levels. Finally, the water concentration and potential temperature tendency due to moist convection can be computed with the rate of change per unit area given in Table 2.4 The water vapour tendency is

$$G_{\mathrm{w,mc}} = \left.\frac{\partial q_k}{\partial t}\right|_{\mathrm{mc}} = g\frac{\Delta W_k}{\Delta p_k}, \tag{2.55}$$

where ΔW is summed for updraft and downdraft.

The potential temperature tendency is

$$\left.\frac{\partial \theta_k}{\partial t}\right|_{\mathrm{mc}} = \frac{g}{c_p}\frac{\Delta S_k + \Delta L_k}{\Pi_k \Delta p_k}. \tag{2.56}$$

Again, the sum of the updraft and downdraft terms is used for ΔS and ΔL.

Mixing Region Treatment

Within the mixing region between $k = t - n_{mix}$ and $k = t$, the net dry static energy, latent heat, and water mass tendencies calculated above are distributed among the levels in proportion to each level's mass. This means that the mixing region is fully mixed.

2.5.3 Effect of Moist Convection on Ammonia

Additionally, we have developed a simple parameterisation for the advective impact of ammonia due to moist convection, an advancement from *Young and Read* (2019). Since the convective plume extends to the level at which ammonia condenses, we consider the transport of both ammonia vapour and ice. Our scheme treats both phases separately as passive tracers, meaning that the scheme does not treat condensation or evaporation of ammonia during moist convection. Instead, the phase change tendency is calculated by the module described in Section 2.4.1. This allows the transport of both phases to use the same set of equations.

Plume Level	**Updraft** (ΔX^u)	**Downdraft** (ΔX^d)
Top ($_t$ or $_d$)	$M_c(\bar{\chi}_b - \bar{\chi}_t)$	$M_c(\bar{\chi}_{d-1} - \bar{\chi}_d)$
Middle ($_k$)	$M_c(\bar{\chi}_{k+1} - \bar{\chi}_k)$	$M_c(\bar{\chi}_{k-1} - \bar{\chi}_k)$
Bottom ($_b$)	$M_c(\bar{\chi}_{b+1} - \bar{\chi}_b)$	$M_c(\bar{\chi}_d - \bar{\chi}_b)$

Table 2.5: Summary of the unit area mass change rate for ammonia, ΔX, due to updraft and downdraft at different plume levels. Note that this applies to both ammonia gas and ice, as the phase change is handled separately.

Table 2.5 summarises the rate of change of ammonia ice or solid mass in the cell per unit area, ΔX (in kg m^{-2} s^{-1}). This is slightly different to that for water vapour as our scheme does not take into account rainfall or the evaporation of ammonia through the plume. ΔX (in kg m^{-2} s^{-1}) is subsequently converted to the mass mixing ratio tendency by

$$\frac{\partial \chi_k}{\partial t}_{mc} = g\frac{\Delta X_k}{\Delta p_k}. \tag{2.57}$$

As with water, the ammonia mass tendencies in the mixing region are then equally redistributed among the levels in a mass-weighted manner.

Chapter 3

Effect of Non-uniform Bottom Heat Flux

3.1 Introduction

The formation and maintenance of zonal jets in giant planet atmospheres remains a central question in planetary atmospheric dynamics. On Jupiter, alternating prograde and retrograde jets extend from the equator to the poles and have persisted for decades, suggesting the presence of a robust driving mechanism. Measurements of the gravitational and magnetic fields indicate that these jets extend to great depths with little vertical decay, implying a predominantly barotropic structure (*Galanti and Kaspi* 2021; *Kaspi et al.* 2018). This constrains the vertical structure of the jets rather than their origin. In particular, it does not preclude the possibility that the jets generated and sustained by relatively shallow processes, such as baroclinic instability or moist convection near the cloud level (*Lian and Showman* 2008; *Liu and Schneider* 2010; *Showman et al.* 2006), produce deep-reaching flows. In this framework is consistent with the 'downward control' principle (*Haynes et al.* 1991): eddy momentum flux convergence in the weather layer drives a meridional circulation that redistributes angular momentum throughout the column, allowing jets to extend downward until they encounter magnetohydrodynamic drag at depth, where the flow is dissipated. This interpretation is supported by analyses of Cassini cloud-tracked winds, which indicate that baroclinic instability is likely the primary energy source maintaining Jupiter's equatorial and mid-latitude jets (*Young and Read* 2017).

Previous modelling work using the JasonGCM has demonstrated that jet formation mechanisms vary with latitude. Near the equator, jets are sustained by angular momentum convergence associated with the transport of Rossby waves, which is generated by barotropic instability. In contrast, mid-latitude jets are primarily driven by baroclinic instability (*Young et al.* 2019a).

Because baroclinic instability is highly sensitive to the thermal structure of the atmosphere, any factor that affects vertical and meridional temperature gradients can significantly influence jet dynamics. One such factor is the spatial distribution of the internal heat flux. Most weather layer GCMs for Jupiter assume a constant internal heat flux over latitude (e.g. *Boissinot et al.*

2024; *Schneider and Liu* 2009; *Young et al.* 2019a). *Liu and Schneider* (2011) explored how the jet responds to variations in top and bottom thermal forcing, but in all cases, the bottom heat flux was uniform.

Despite this common assumption, there are observational and theoretical reasons to consider a spatially varying internal flux. While global mean heat flux is measurable (*Gierasch et al.* 2000; *Li et al.* 2018b), there are no direct measurements on the latitudinal variation of this flux. This makes the lower boundary thermal condition a major modelling uncertainty in GCMs. Early infrared analyses by *Pirraglia* (1984, hereafter P84) found an approximately latitudinally uniform outgoing thermal emission, despite strong variations in absorbed solar radiation. Therefore, they inferred a meridional variation in the interior heat flux. *Aurnou et al.* (2008) argued that large-scale atmospheric heat transport can at least partially explain the observed uniform large-scale thermal emission, based on results from a deep convection model extending well below the weather layer. In addition, *Showman and Kaspi* (2013) showed that convective heat transport is intrinsically more efficient at high latitudes due to reduced rotational constraints, leading to enhanced polar heat fluxes even under spatially uniform forcing. Nevertheless, the possibility of a meridionally varying effective internal heat flux at the base of a weather-layer GCM, arising either from spatially varying interior heat generation or from deep convection that is not explicitly represented, remains plausible and worthy of investigation.

Ideally, a planetary GCM would resolve both the deep interior dynamics and the weather layer meteorology, capturing the full vertical structure of heat and momentum transport. However, the vast dynamical range and long equilibration times required for such simulations make them computationally prohibitive. Specifying lower boundary conditions in weather layer models is therefore particularly important: a physically motivated condition can represent the effect of deep processes on the weather layer, providing a bridge between deep convection models and weather layer GCMs.

In this chapter, we examine the impact of a non-uniform interior heat flux profile on the thermal structure, cloud formation, and jet dynamics in the weather layer of a Jupiter-like atmosphere. In particular, we ran a series of simulations with latitudinally varying interior heat flux based on the functional form derived by P84, and a progressively stronger meridional gradient through the parameter a_f. To complement these runs, we also present a simulation with a horizontally uniform deep adiabat configuration, representing a case in which the internal

heat flux distribution results in a constant potential temperature at the bottom of the domain.

The chapter is structured as follows. In Section 3.2, we describe the model setup and the spatially varying interior heat flux profile used. The results of the flux variation experiments are presented in Section 3.3, including analysis of the temperature structure, zonal winds, and the water cycle. In Section 3.4, we apply the Lorenz energy cycle framework to quantify the energy conversion pathways in the simulations and therefore identify the jet maintenance mechanism. The deep adiabat configuration and its results are discussed in Section 3.5. Finally, Section 3.6 summarises the main results and discusses their implications.

3.2 Method

3.2.1 Internal Heat Flux Profile

The internal heat flux imposed at the lower boundary of the model domain (see Eq. (2.17)) is specified as a function of latitude in the form of

$$F_{\mathbf{int}} = -a_f \cos(\theta) + b_f, \tag{3.1}$$

where the negative sign ensures that larger values of a_f correspond to enhanced interior heat flux at the poles.

This functional form was adopted because it most closely matches the latitudinal trend reported in P84, when small-scale, jet-related variations are excluded, i.e. it corresponds to the dashed line in their Fig. 5. Since the functional form and parameters of the interior heat flux profile were not explicitly stated in P84, we inferred them by fitting the published curve to several candidate functions. The internal heat flux as a function of $\sin\theta$ was first extracted using an online plot digitiser[1]. Although the x-axis in the original figure is labelled in degrees of latitude, the spacing is uniform in $\sin\theta$.[2] Consequently, interpreting the x-coordinates in terms of $\sin\theta$ is more appropriate and better aligned with the digitisation tool's capability. Assuming hemispheric symmetry about the equator, the best fit was given by a linear fit of

[1] `automeris.io`, version 4

[2] While P84 did not specify this feature, it can be confirmed by comparing the axes in Fig. 5 of P84 with those in Fig. 1 of *Kaspi et al.* (2018), the latter overlays zonal mean wind profiles onto a projected image of Jupiter.

interior heat flux against $\cos\theta$, which has an RMS error of 0.06. Part of the fitting error can be attributed to the slight north–south asymmetry present in the original profile. Specifically, the difference in flux between 80°N and 80°S is 0.08 W m^{-2}. This asymmetry is unlikely to be a digitisation error alone, as it is clearly visible in the original plot by P84. Given the time of publication, it is plausible that this discrepancy arose from the manual plotting of the figure. In the present study, we omitted any hemispheric asymmetry in the prescribed heat flux profile, as incorporating such asymmetry would introduce additional parameters for which there is limited observational constraint, making them difficult to justify.

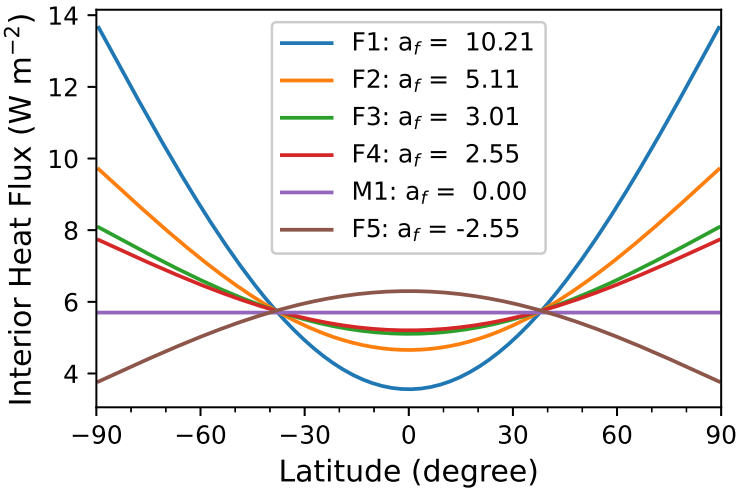


Figure 3.1: Interior heat flux profile used in different simulations and the corresponding value of a_f.

We note that more recent analyses have revised Jupiter's Bond albedo and, therefore, global-mean internal heat flux (*Li et al.* 2018b). However, we adopt the P84-based profile to remain consistent with the global-mean internal heat flux used in our radiative scheme, described in Section 2.3.1. Moreover, while *Li et al.* (2018b) provide an updated estimate of the global-mean internal heat flux, no corresponding constraint on its latitudinal distribution is currently available. Assessing how revised albedo estimates might affect latitudinal variation in thermal emission is beyond the scope of this work.

Instead, we systematically explore the dynamical response to different imposed latitudinal variations in the internal heat flux by exploring a range of latitudinal interior heat flux profiles by varying the parameter a_f: Run F1 adopts the value of a_f obtained from fitting the observational profile, which we interpret as the upper bound on plausible latitudinal variation in internal heat flux. This interpretation is based on our previous modelling efforts, which

indicate that atmospheric dynamics tend to transport heat from the equator toward the poles. Consequently, the imposed a_f in F1 represents the maximum possible contribution of the deep interior to the observed thermal emission, consistent with the net latitudinal flux distribution inferred from observations. We then consider cases with progressively smaller a_f values: half (F2), one-quarter (F4), and minus one-quarter (F5) of the value in F1. The negative value of a_f in F5 corresponds to a scenario in which the equator receives more internal heat flux than the poles, which is opposite to the trend derived in P84. Although this configuration is not observationally supported, it is included to examine the dynamical consequences of an inverted heat flux pattern. This allows for a broader exploration of the parameter space and determination of the effect of the latitudinal temperature gradient on atmospheric dynamics.

We also include an additional simulation (F3) with an a_f value slightly higher than that in F2. This profile was produced using a slightly different interior heat flux normalisation scheme, where a_f is halved, b_f remains fixed, and the entire profile is then rescaled to maintain the same global mean heat flux. As a result of the rescaling, the final a_f value is somewhat lower than half of the original value. We include this case to assess the robustness and sensitivity of the trends observed in the sequence of simulations from F1 to F5.

For simulations except F3, the value of b_f is chosen so that all simulations have the same globally averaged interior heat flux. By computing the area weighted interior heat flux analytically, it can be shown that b_f is given by

$$b_f = b_{f,0} - \frac{\pi}{4} a_f, \tag{3.2}$$

where $b_{f,0}$ is the area-weighted globally average interior heat flux. We adopt $b_{f,0} = 5.7$ W m^{-2} to match the value of *Young and Read* (2019), which corresponds to the default case with no latitudinal variation in interior heat flux. This value was also recovered from the curve fitting described above when using the best-fit parameters a_f and b_f from the aforementioned curve fitting. This is not surprising, given that the estimate in *Young and Read* (2019) was itself based on available observational constraints at the time. Fig. 3.1 summarises the interior heat flux profiles used and their corresponding values of a_f used in this study. These simulations will be referred to as 'the F series', especially when compared with the deep adiabat run.

3.2.2 Model Setup

The model used for this study and the parameter scheme involved have been extensively discussed in Chapter 2. The 'old' set of reference optical depth (OA) in Table 2.2 is used. The underlying rationale for this approach is rooted in the ability to make a comparison with an already documented case in *Young and Read* (2019). The model setup is largely consistent with the nominal moist convection case described in *Young and Read* (2019) (their M1), including a 1× solar water abundance, the default cloud scheme and the moist convection parameters listed in Table 2.2. This M1 case corresponds to simulations without latitudinal variation in interior heat flux and is used as a reference for comparison. The sole distinction between these simulations and those in *Young and Read* (2019) is the use of prescribed interior heat flux profiles at the bottom of the domain, as specified in Section 3.2. The ammonia cycle and the mushball parametrisation, as outlined in Chapter 4, were not incorporated to reduce the computation time.

Run	a_f (W m^{-2})	Starting State	End Time of Res L (days)	End Time of Res M (days)
F1	10.21	RCM	70000	94500
F2	5.11	RCM	50000	76000
F3	3.01	RCM	70000	96000
F4	2.55	RCM	70000	93700
M1	0.00	RCM	108300	140940
F5	-2.55	RCM	70000	95000
D	N/A	end of M1	0	25000

Table 3.1: Simulation time for each run in the F-series and deep adiabat configuration (as described in Section 3.5). Values indicate the end times for the low-resolution (Res L) and the final time for the medium-resolution (Res M) segments. For completeness, the deep adiabat run in Section 3.5 is also included in the table as run D.

Table 3.1 summarises the simulation time of the F-series simulations. A radiative–convective model (RCM), comprising only the radiative transfer (Section 2.3.1) and dry convection (Section 2.3.2) components of the GCM, is used to generate the initial potential temperature profile for each simulation. The RCM is initialized with an isothermal atmospheric column at each latitude, with the corresponding internal heat flux imposed, and is integrated until the net outgoing radiative flux and the internal heat flux differs by less than 0.01 W m^{-2}. To break horizontal symmetry, a uniformly distributed random perturbation with an amplitude of 0.01 K is added to the potential temperature field.

The simulation time of the runs with varying heat flux is significantly shorter than M1, as we only ran the simulation for the kinetic energy to equilibrate and a bit after to obtain time-averaged statistics. These were only integrated until the kinetic energy equilibrated, with additional time allowed for time-averaged diagnostics. Although the net top of atmosphere (TOA) flux in these runs continues to evolve slowly at the end, the decision not to extend the integration further is supported by the behaviour of the M1 run, in which the net flux exhibited a similarly slow decay even at the end of the run. Yet, the large-scale dynamical structures such as the zonal jets, overturning circulation, and cloud distributions remained largely unchanged throughout. This suggests that while the atmosphere continues to undergo gradual radiative adjustment, the dynamical state has reached a quasi-equilibrium. Consequently, extending the simulations is unlikely to yield qualitatively different results, and the state as presented here may be considered sufficiently equilibrated for the purposes of our analysis. Residual radiative adjustment at the end of the integrations is confined between 0.2-0.8 bars. while deeper layers exhibit negligible long-term temperature tendencies. The state variables and tracer concentration were stored every 100 Earth days during the runs in the F-series. At the end of each simulation, the simulation continued for an additional 100-day diagnostic period with state and tracer fields stored every 10 days. Unless otherwise stated, the results presented will be the mean of this diagnostic period. The choice of this diagnostic averaging period is motivated by tests performed on the reference case, which show that most diagnostics do not exhibit qualitative sensitivity to the length of averaging windows. As the model does not include an intrinsic seasonal cycle, a relatively short diagnostic period is sufficient to capture the statistically steady behaviour while reducing the computational and storage requirements to produce the diagnostics.

3.3 Results

3.3.1 Properties of the Zonal Jet

Fig. 3.2 and Fig. 3.3 show the zonal mean of the zonal wind and its evolution over time in our simulations. The equatorial jet is very similar across all runs. While a retrograde stratospheric jet appears at slightly different altitudes and strengths for different runs, the strong prograde equatorial jet consistently peaks near 0.2 bar. Notably, the width of the equatorial jets remains

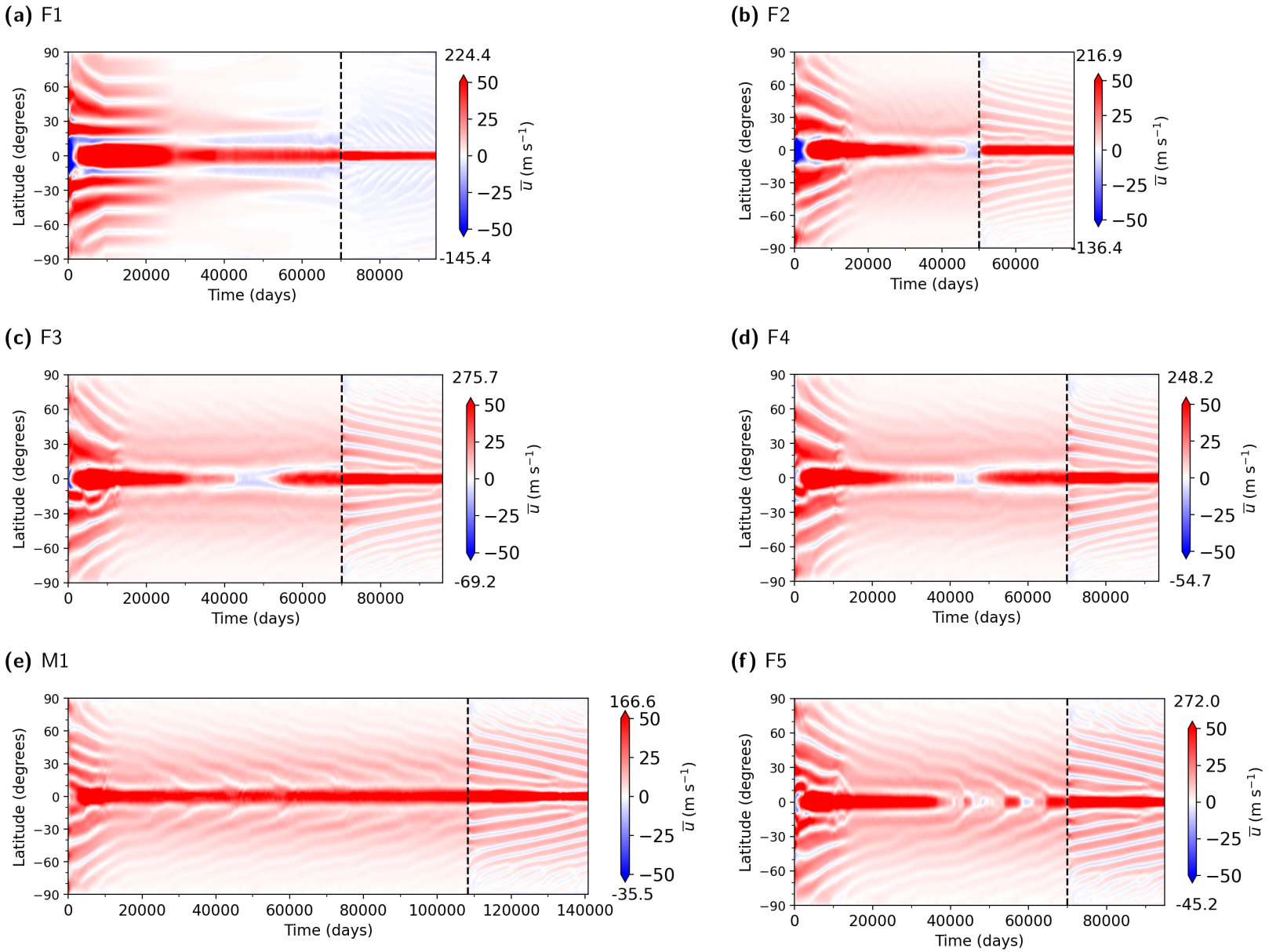


Figure 3.2: Time–latitude diagrams of zonal mean zonal velocity at 1 bar for simulations F1 to F5, ordered by decreasing a_f. Each panel uses the same aspect ratio for the time and latitude axis, and equal simulation time displays approximately the same length across panels. The vertical dashed line indicates the transition from resolution L to resolution M. Values at the top and the bottom of each colour bar denote the minimum and maximum wind speeds in m s^{-1}, respectively.

52

consistent across simulations and over time, indicating its robustness to variations in interior heat flux. In simulations F1 to F4, the equatorial jet weakens significantly below approximately 2 bars and splits into two distinct off-equatorial branches around 4 bars, just below the water cloud deck. In runs F1 and F5, a 'cusp'-like structure emerges near 0.4 bars, resembling the observed cloud-top zonal wind profile (e.g. *Tollefson et al.* 2017).

The off-equatorial jets across run F2 through F5 are characterised by a series of alternating eastward and westward jets. The eastward jets are generally stronger than their westward counterparts. The westward jets tend to broaden and intensify with increasing pressure, while the eastward jets become narrower and decrease in strength at depth. These jets also tend to weaken with increasing latitude. The jet pattern is approximately symmetric about the equator in all simulations. A weak increase in the number of zonal jets is observed with increasing a_f. This trend can be interpreted in the context of the Rhines scale, which provides an estimate for the characteristic latitudinal spacing of jets. The Rhines scale is given by

$$L_{\mathrm{Rh}} = \pi \left(\frac{2U}{\beta} \right)^{1/2} \tag{3.3}$$

where U is the typical velocity. As shown in Fig. 3.6, U decreases with increasing a_f, which leads to a reduction in the Rhines scale, allowing for the formation of more closely spaced jets.

In contrast to F2 to F5, run F1 exhibits a markedly different off-equatorial jet structure. Except in the uppermost layers, the atmosphere is predominantly characterised by weak, retrograde jets. These jets are also more irregular in width and shape compared to those in the other simulations.

Nonetheless, strong prograde jets in the polar stratosphere, consistent with thermal wind balance, are present in all runs. Their strength remains largely unaffected by a_f, except for M1 and F5, where the polar jets are slightly weaker. This is expected, as the temperature structure at these pressures is primarily governed by absorbed solar radiation and is relatively insensitive to variations in internal heat flux. This is further illustrated in Fig. 3.8, which shows similar polar temperatures across all simulations at 0.02 bar. The difference in behaviour in M1 and F5 is consistent with Fig. 3.10, where equator to pole temperature difference increases less rapidly for these two runs.

The zonal jets also exhibit notable time variability, most prominently through their migration toward the equator. At resolution M, this equatorward migration occurs at an approxi-

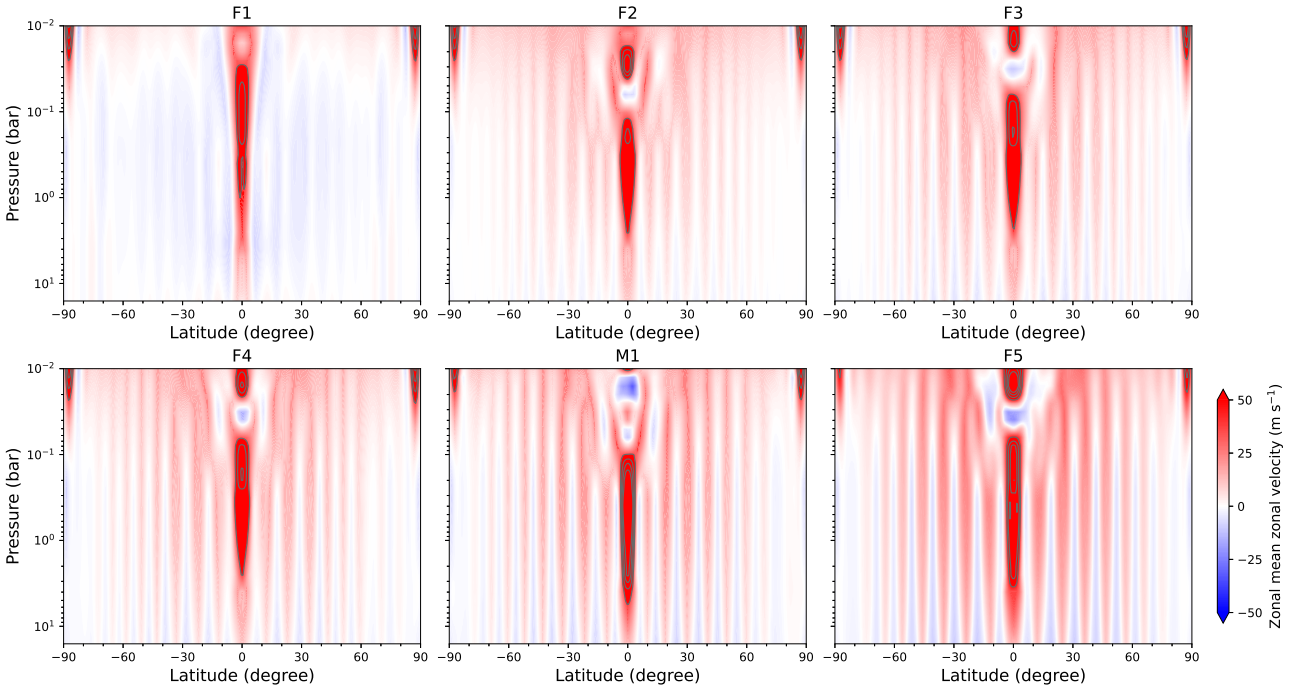


Figure 3.3: Zonal-time mean zonal velocity profiles of each run at the end of the stimulation. The grey contours are at 10 m s^{-1} increment at regions where zonal mean zonal velocity extends beyond the colour bar.

mately uniform rate in both time and latitude within each simulation. In contrast, the jets in the resolution L display more variability. For run F2-F4, the jet near 20° is relatively stationary after the initial spin-up period, altitude remains relatively stationary following the initial spin-up period, while jets at higher latitudes exhibit equatorward migration. For M1 and F5, the jets alternate between periods of relative stability and episodes of more rapid migration. Run F1 shows a markedly different evolution. Although the initial spin-up phase appears very similar to other simulations, the off-equatorial retrograde jets gradually intensify over time and remain largely stationary, in contrast to the migrating jets seen in other cases.

To better compare the migration speed across different simulations, we plot the mean migration speed of the prograde off-equator jet for each run at resolution L and M, respectively, in Fig. 3.4. The jet migration speed is measured by tracking the jet peaks (local maxima in $\overline{u}$) across time and dividing the latitude travelled by the time taken. The equator jets and any jets outside ±60° are excluded, as the latter appear more intermittent and are influenced by the polar filter. We do not have a measurement for F1 in resolution M as the off-equator jets are retrograde and much weaker. Overall migration speed decreases as a_f increases, and Resolution L shows generally higher migration speeds than Resolution M, and migration speed

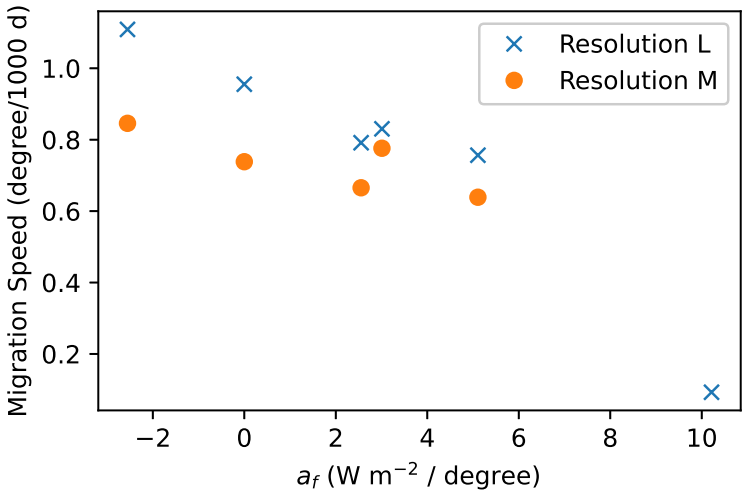


Figure 3.4: Mean migration speed as a function of a_f at resolution L and M.

decreases faster with increasing a_f in Resolution L. For resolution M, migration speed values range between 0.6 and 0.9 degrees per 1000 days equivalent to 2-3 degrees per decade.

It is not uncommon for zonal jets to migrate in GCMs. For example, *Chan et al.* (2007) observed an equatorward migration of zonal jets in their model for Earth's ocean, while jets migrate poleward in the idealised GCM of *Chemke and Kaspi* (2015). For Jupiter models, *Williams* (2003) reported equator-ward migration. In contrast, *Boissinot et al.* (2024) observed a poleward migration of the zonal jet in their GCM, though the migration rate was significantly reduced when moist convection was included. Jet migration also occurs in deep convection models of *Wulff et al.* (2022), although in a more stochastic nature. The observations, however, indicate that the location of the zonal jet on Jupiter is stable over decadal timescales (see Section 1.2 for a more detailed discussion), with no clear evidence of systematic latitudinal drift. Based on the simulation presented here, it is unlikely to have a value of a_f that gives migration speed consistent with the observation while maintaining Jupiter-like zonal jets. This suggests that other mechanisms are required to stabilise jet locations.

On top of this equator-ward migration, the runs with non-uniform interior heat flux also experience transient interruptions in the equatorial superrotation at resolution L. The onset and duration of these westward anomalies are influenced by a_f. Such a disturbance has also occurred in the Jason model previously, for the run with latent heating related to water phase change, but no moist convection parameterisation. Several dynamical mechanisms, including ave breaking or bursts of deep convection, might cause these disturbances. Here, we did not

explore these possibilities, as resolution L has about 1 grid point per deformation radius at mid-latitude, and therefore is not sufficient to represent Jupiter-like turbulent dynamics.

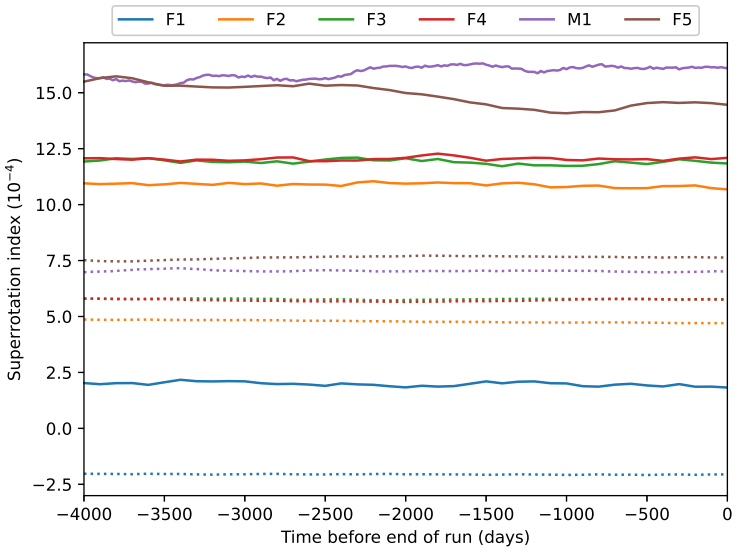


Figure 3.5: Evolution of super-rotation index (solid, defined in Eq. (3.6)) and its off-equatorial component (dotted, defined in Eq. (3.9)) across the last 4000 d of the runs.

To better compare the strength of zonal jets in different runs, Fig. 3.5 shows the evolution of the super-rotation index and its off-equator component at 1 bar for different simulations at the end of 4000 days. The global super-rotation index, S, is defined as

$$S = \frac{M_t}{M_0} - 1, \tag{3.4}$$

where M_t is the total angular momentum of the atmosphere, and M_0 is its value for an atmosphere in solid body rotation (e.g. *Read* 1986). The total angular momentum of the atmosphere can be expressed as

$$M_t = \int (m_0 + m_u)\, dM = M_0 + M_u \tag{3.5}$$

where dM denotes integration over mass, $m_0 = \Omega a^2 \cos^2\theta$ is the static component of specific angular momentum due to planetary rotation, and $m_u = ua\cos\theta$ is the dynamic component due to the winds. Substituting into the definition, the global super-rotation index becomes

$$S = \left(\int m_u dM\right) / \left(\int m_0 dM\right). \tag{3.6}$$

By considering integration over a single pressure level with approximately constant density, we

obtain the super-rotation index for a single pressure level,

$$S = \frac{3}{8\pi a^3 \Omega} \int u \cos\theta dA, \tag{3.7}$$

where dA denotes integration over area.

Since the equatorial jet is stronger than any off-equator jets in our simulations, it is convenient to define the equator and off-equator components of the super rotation index. The equator component is obtained by only evaluating the integral over the latitude range of the equatorial jet, i.e.,

$$S_{\text{equator}} = \frac{3}{8\pi a^3 \Omega} \int_{\text{equatorial jet}} u \cos\theta dA. \tag{3.8}$$

The integration limits are defined as the latitudes on either side of the equator at which the zonal-mean zonal velocity first crosses zero. These latitudes are determined by linear interpolation between adjacent grid points. The positions of these zero crossings are stable over time, with only minor temporal variability. The off-equator component of the super-rotation index is then:

$$S_{\text{off-equator}} = S - S_{\text{equator}} \tag{3.9}$$

Overall, both the total super-rotation index and its off-equatorial component remain relatively constant over time in most simulations, with the exception of run F5, where the total super-rotation index declines gradually. The temporal stability of the off-equatorial component for F5 suggests that the fluctuations in total super-rotation of this run are primarily driven by changes in the equatorial region. The total super-rotation index generally decreases with increasing latitudinal heat flux gradient. However, F5 is an exception to this trend, and the index remains relatively similar among cases with intermediate flux gradients (F2 to F4). For comparison, the observed super-rotation index near Jupiter's equator is estimated to lie between 0.005 and 0.011 (*Read and Lebonnois* 2018), which is much larger than the value here.

The off-equator component of the super rotation index also decreases with increasing a_f, reflecting the weakening of the off-equatorial eastward jets. In run F1, the off-equatorial index eventually becomes negative, indicating the development of net retrograde angular momentum outside the equator. This is consistent with the zonal mean zonal wind profiles shown in Fig. 3.6, where off-equatorial jets become progressively weaker and retrograde as the heat flux gradient increases.

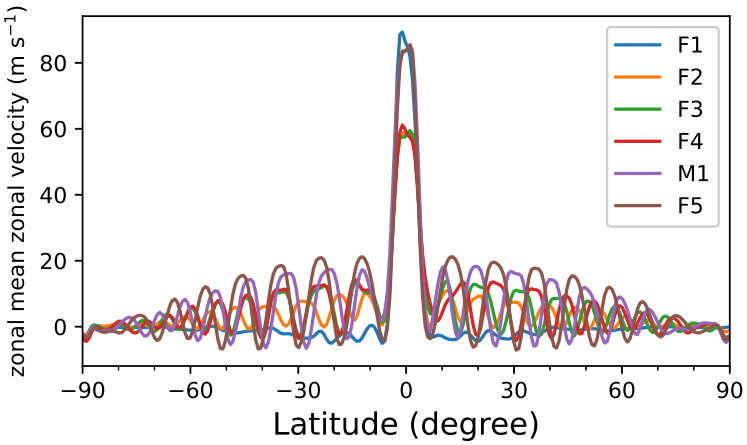


Figure 3.6: Zonal mean zonal velocity at 1 bar for all varying heat flux simulations

3.3.2 Temperature Structure

Fig. 3.9 presents the colour maps of the global mean potential temperature for the two simulations with the highest (F1) and lowest (F5) values of a_f. While a clear difference in latitudinal temperature gradient is evident between the two cases, their overall thermal structures remain broadly similar. Therefore, the zonal mean temperature for the RCM and the GCM for each run at four different pressure levels is plotted in Fig. 3.8 to better compare the temperature structure of the different simulations. The four pressure levels chosen are 0.02 bar (stratosphere), 0.6 bar, 3 bar (cloud base) and 16 bar (the bottom layer).

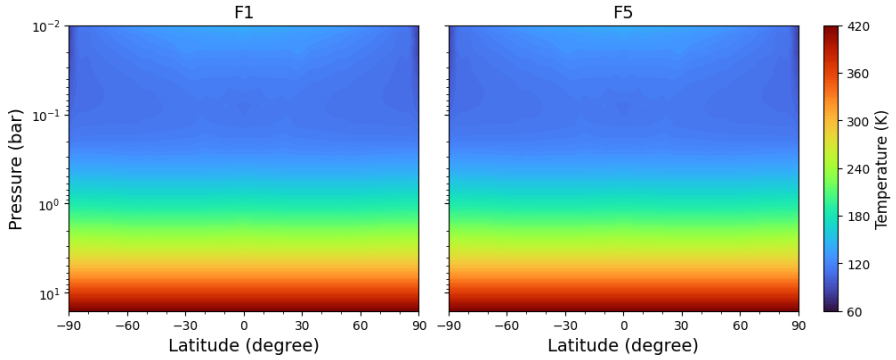


Figure 3.7: Zonal-time mean temperature of run F1 (highest a_f) and F5 (lowest a_f), averaged over 100 d at the end of each simulation.

For the RCM, temperature decreases from the equator to the poles at any latitude for F2 - F5, and the equator-to-pole temperature difference decreases with increasing a_{flux}. In contrast, the latitudinal gradient of the interior heat flux in F1 is so strong that the meridional temperature gradient reverses at depth. The exact transition point from a positive to a negative

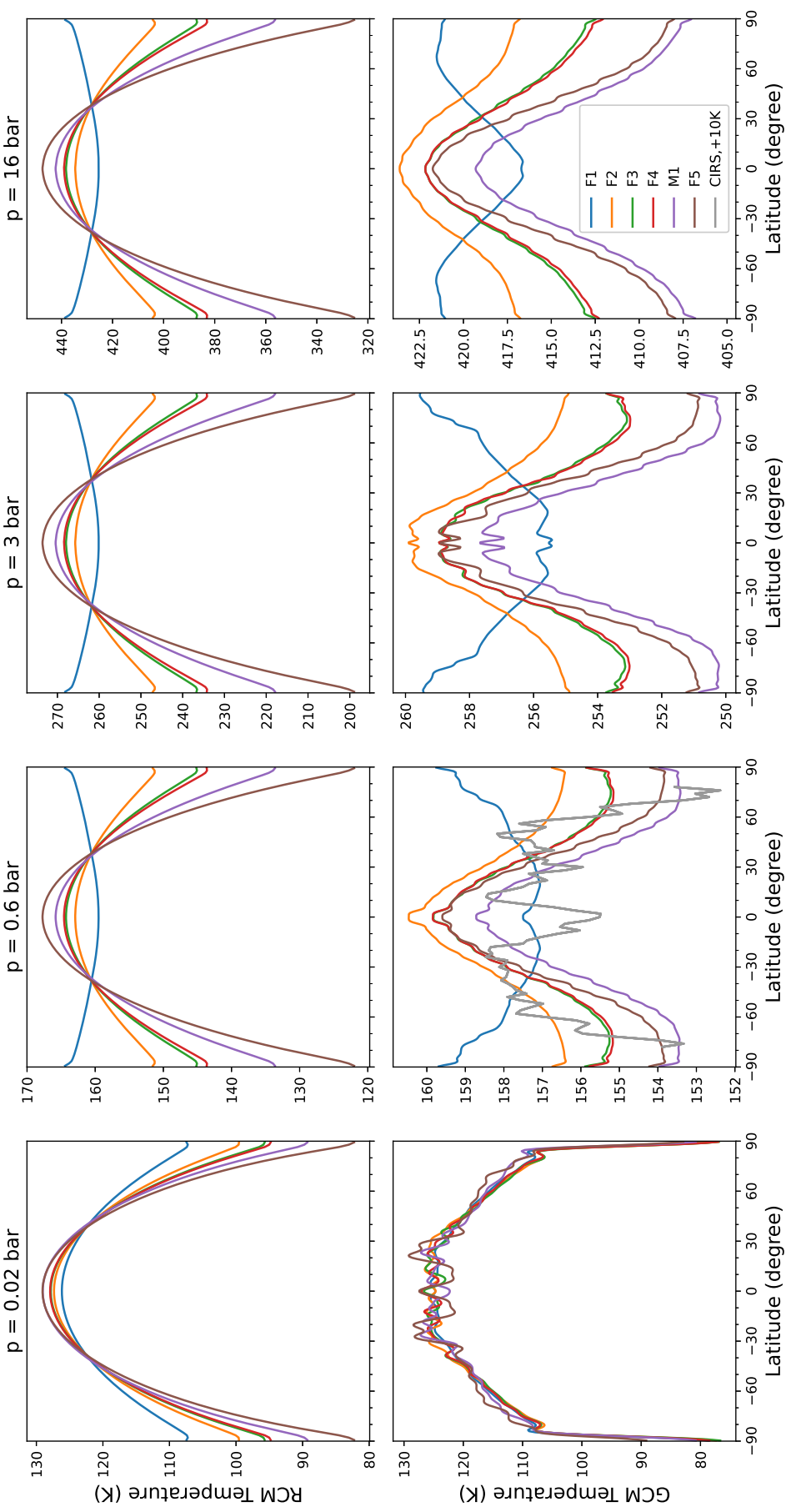


Figure 3.8: Temperature of the radiative-convective model (RCM) at radiative-convective equilibrium (top) and that of the general circulation model (GCM) averaged over the final 100 d of the simulation at 0.02 bar (stratosphere), 0.6 bar, 3 bar (cloud base) and 16 bar (middle of the bottom layer). Gray line in the 0.6 bar plot indicates the observed temperature profile from Cassini/CIRS (*Fletcher et al.* 2016), shifted by 10K to make it comparable to our results. Note that the temperature range and scales differ between panels to better highlight the relevant structures in each case.

latitudinal temperature gradient is at 0.22 bar for the RCM and 0.28 bar for the GCM, as shown by Fig. 3.10. At higher altitude, the effect of the differential heating due to the incoming solar radiation outweighs that due to internal heat flux, and a positive equator-to-pole temperature gradient is maintained.

The GCM temperature profiles exhibit more complex structures, with multiple peaks and troughs in the temperature profile due to the influence of jets and associated atmospheric dynamics. Large-scale atmospheric dynamics also results in a reduction in the equator-to-pole temperature contrast in the GCM compared to the RCM. In run F1, the temperature decreases overall with decreasing latitude, as in the RCM. However, there are notable local temperature minima near the equator, particularly at 0.6 bar and 3 bar. These features may reflect the influence of equatorial upwelling, which elevates temperatures locally against the background meridional gradient.

For comparison, the observed temperature profile from Cassini/CIRS (*Fletcher et al.* 2016) is shown for 0.6 bar. This profile has been shifted upward by 10 K to match the temperature range of the model results. This offset reflects the use of reference optical depths that are not fully calibrated to observations, as discussed in Section 2.3.1. Despite this adjustment, the latitudinal temperature structure differs significantly between the observations and the simulations. The observed profile exhibits a local temperature minimum within about 20° of the equator, whereas the model simulations generally show an equatorial maximum (or local maximum, in the F1 case). At mid-latitudes, the observed profile has a weaker large-scale temperature gradient than any of the model simulations, with substantial small-scale latitudinal variability. In contrast, the observed profile displays a steeper temperature gradient toward the poles. The differences likely reflect a combination of model limitations associated with the simplified radiative scheme and the limited temporal sampling of the observations, given that the temperature structure can vary significantly over time (e.g. *Simon-Miller et al.* 2006). This comparison should therefore be regarded as qualitative rather than diagnostic.

The global mean temperature is also different for different simulations, as indicated by the displacement between their curves. This is best illustrated in Fig. 3.9, where potential temperature is used to highlight the difference in global mean profiles. For the RCM, simulations with larger a_f show a higher global mean potential temperature (except for F5). The global mean potential temperature of the GCM is even lower than that in the RCM, reflecting the impor-

tance of global circulation in shaping the temperature structure. The potential temperature also shows a sudden increase at around 3 bars, reflecting the effect of water latent heating. The differences in global mean potential temperature also become larger in the GCM (about 3 K across all runs) than in the RCM (about 1 K). While the other simulations have been run for different lengths of time, this is unlikely to be the main contributor to the difference in the F runs, as the simulations had sufficient time to reach equilibrium, and the net cooling rate in the pressure range shown in Fig. 3.9 is small. M1, however, has a much longer simulation time of approximately twice as long as the other runs, potentially allowing small differences to amplify over time. Indeed, the global mean potential temperature is the lowest in run M1 compared to other simulations. While the difference in global mean temperature is undesirable, given its small magnitude, it is unlikely to cause a significant difference in the dynamics.

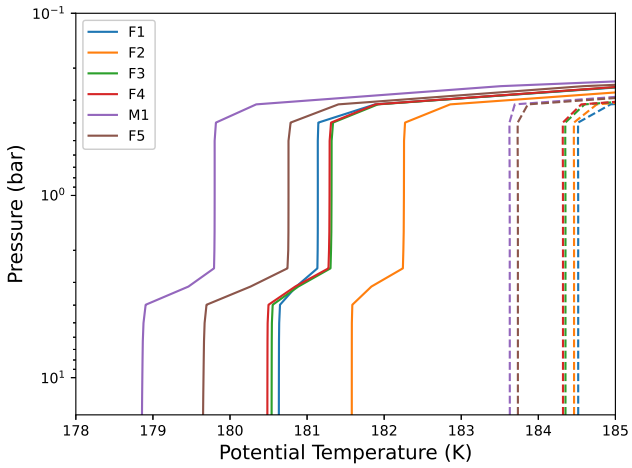


Figure 3.9: Vertical profiles of global mean potential temperature as a function of pressure for different simulation cases. Solid lines represent the 100-day average at the end of each GCM simulation, while dashed lines represent the result at the end of the RCM simulations.

To disentangle the difference in the meridional temperature gradient from the difference in overall temperature across different runs, we plot the vertical profile of equator-to-pole temperature difference in Fig. 3.10. As illustrated by the 0.6-bar temperature profile in Fig. 3.8, the observed temperature field of Jupiter exhibits a latitudinal structure that differs substantially from that produced by the GCM, making an equator–to–pole temperature difference poorly defined in the observations and a direct quantitative comparison less meaningful. We therefore restrict this metric to comparisons among different simulations, where the temperature changes approximately monotonically with latitude.

Across simulations F2 to F5, the equator-to-pole temperature difference generally decreases

with pressure down to approximately 0.3 bar, below which it begins to increase sharply with altitude. In F1, a transition also occurs near 0.3 bar, but instead of increasing with pressure, the increase in temperature contrast below this level becomes more gradual. A notable deviation from this trend appears around 3 bars, where a dip in the temperature difference is observed in F3 to F5, and a local 'kink' appears in F1 and F2. This behaviour likely reflects the influence of moist convection, as 3 bar corresponds to the base of the water cloud layer where latent heating processes become active. In F5, a secondary dip occurs near 0.01 bar. However, this region lies within the model's upper sponge layer, and the feature may not be physically meaningful. It could also be partially attributed to residual dynamical variability not fully averaged out over the selected time window, as suggested by the individual latitude–temperature profiles. Additionally, it is worth noting that in the uppermost layers, the equator-to-pole temperature contrast in simulation M1 exceeds the plotted range. This is a direct consequence of the different top boundary condition applied in M1, as discussed in Section 2.3.1.

In terms of inter-run differences, the equator-to-pole temperature contrast systematically decreases with increasing a_f. Moreover, the differences between simulations diminish with increasing pressure. Specifically, for the intermediate cases F2 to F4, the equator-to-pole temperature differences become negligible by approximately 3 bar. The differences in the equator-to-pole temperature difference between these runs and F1 converge at about 0.6 bar, while M1 and F5 behave differently above this level.

Buoyancy Frequency

To investigate the effect of interior heat flux on static stability, we evaluate the buoyancy frequency in three different forms, following the formulation of *Durran and Klemp* (1982). Firstly, for a dry atmosphere, the square of buoyancy frequency N^2 is given by

$$N^2 = \frac{g^2}{R_d T}\left(-\frac{d\ln T}{d\ln p} + \kappa\right), \tag{3.10}$$

where all symbols take their conventional meaning (see Table 2.2). The use of logarithmic derivatives in temperature and pressure ensures numerical accuracy, especially when the model grid is evenly spaced in $\log p$.

Secondly, when accounting for latent heating associated with the water phase change of

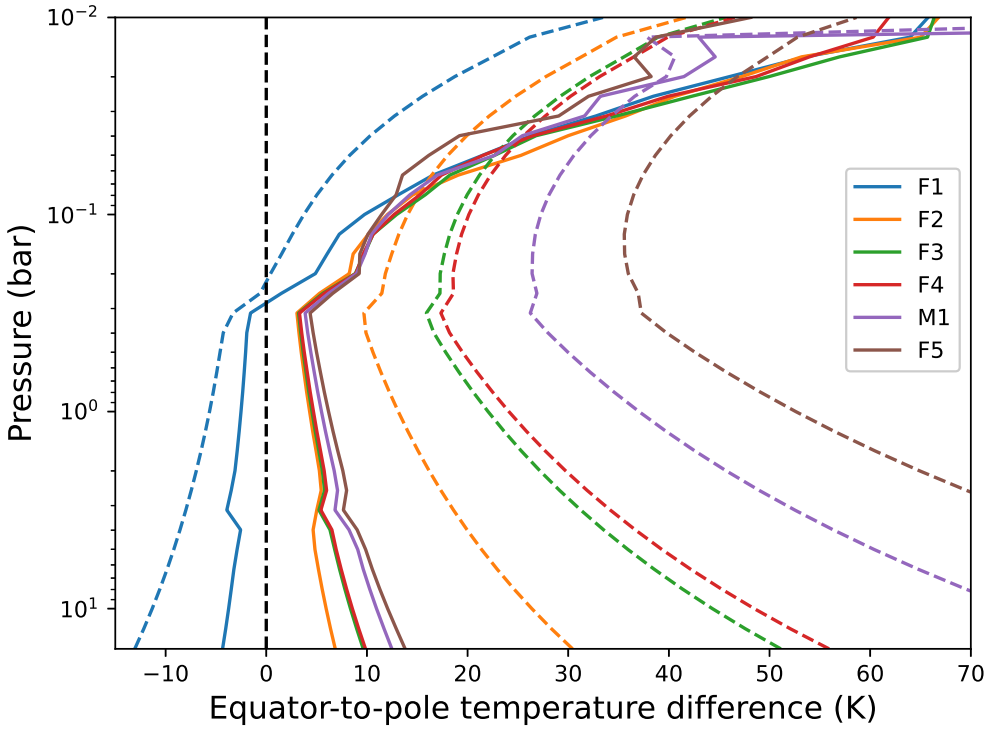


Figure 3.10: Vertical profile of equator-to-pole temperature difference for GCM (solid) and RCM (dashed), the profile used is the same as in Fig. 3.8

water, the saturated buoyancy frequency N_L^2 is given by

$$N_L^2 = \frac{g^2}{R_d T}\left(-\frac{d\ln T}{d\ln p} + \kappa A_{\text{bulk}}\right)(1+\Lambda), \tag{3.11}$$

where $A_{\text{bulk}} = \frac{1+\Lambda}{1+D}$ is a modification factor to the lapse rate to account for the effect of latent heat. Here, $\Lambda = H(q^t - q^*)\frac{Lq^*}{R_d T}$ is the non-dimensional latent heating term, with $H(q^t - q^*)$ being the Heaviside step function that activates moist processes only when the total water mixing ratio q^t exceeds the saturation value q^*, and L is the latent heat of water. The term in the denominator $D = H(q^t - q^*)\frac{\epsilon L^2 q^*}{c_p R_d T^2}$ accounts for the influence of latent heating on heat capacity.

Finally, by incorporating both latent heating and the effect of water's molecular weight, the full moist buoyancy frequency $N_{L,M}^2$ is given by

$$N_{L,M}^2 = \frac{g^2}{\gamma R_d T}\left[\left(-\frac{d\ln T}{d\ln p} + \kappa\gamma A\right)(1+\Lambda) + \frac{d\ln(1+q_t)}{d\ln p}\right], \tag{3.12}$$

where $\gamma = (1+q^g/\epsilon)/(1+q^t)$ accounts for the variation in mean molecular weight due to the

presence of water vapour. The lapse rate modifier $A = (1 + \Lambda)/(B + \gamma D)$ accounts for both latent heat and molecular weight effects, with $B = (1 + \sum c_p^i q^i / c_p^{\text{bulk}})/(1 + q^t)$ is the correction factor for specific heat capacity, c_p^i and q^i are the specific heat capacity and mass mixing ratio of water in different phase i, with $i = \text{g}, \text{l}$ or s denoting gas, liquid and solid phase. c_p^{bulk} is the bulk specific heat capacity of the moist air mixture.

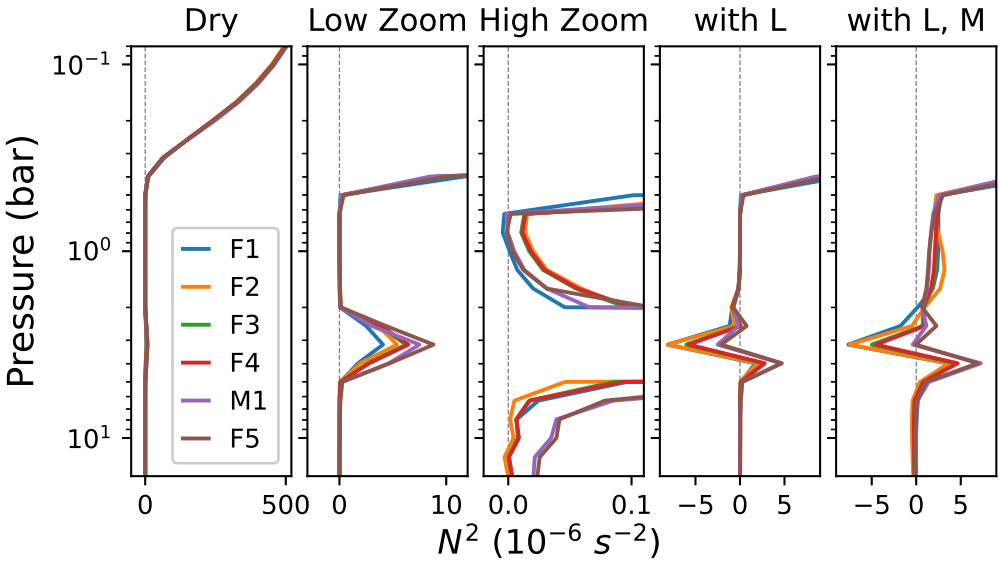
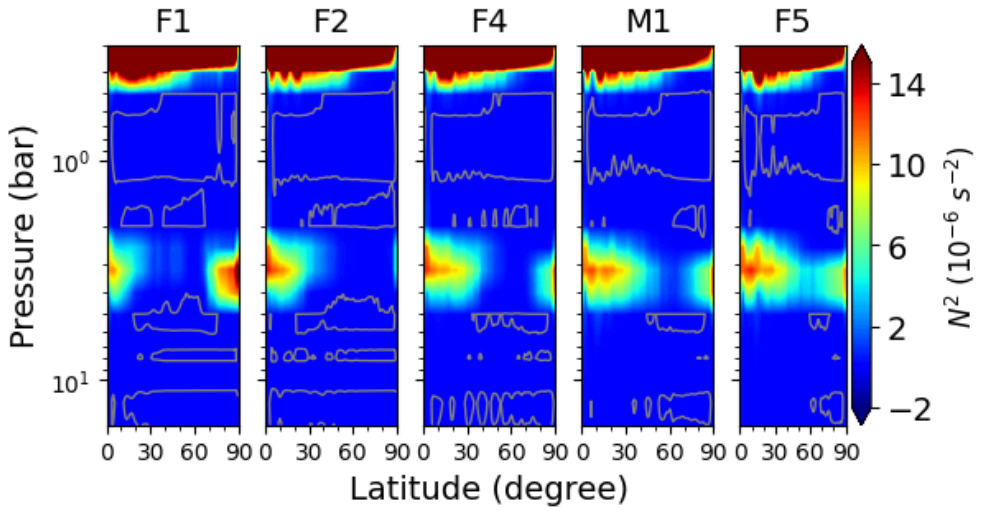
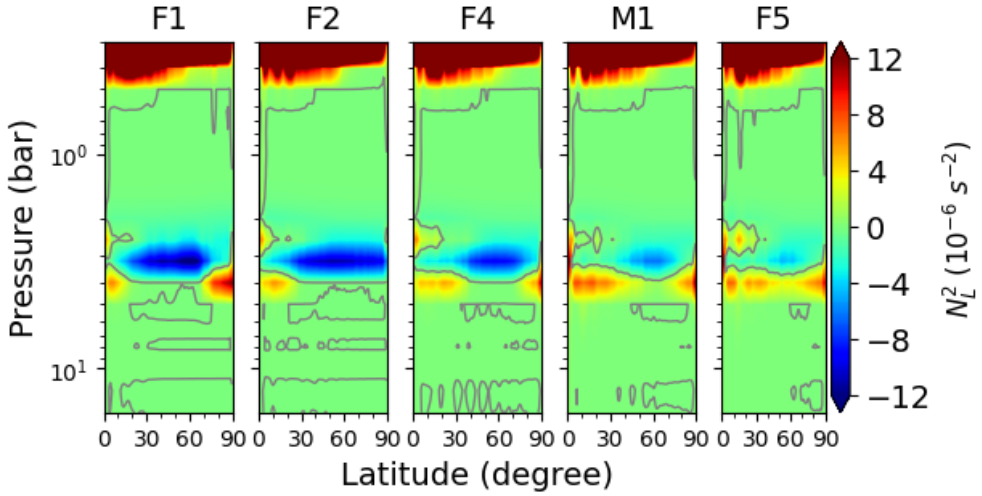


Figure 3.11: Vertical profiles of the squared Brunt–Väisälä frequency, N^2, as a function of pressure for different run. The first three panels show the dry static version with different zoom levels. The fourth panel shows the version with latent heating of water phase change included. The final panel shows the version with both latent heating and molecular weight of water included.

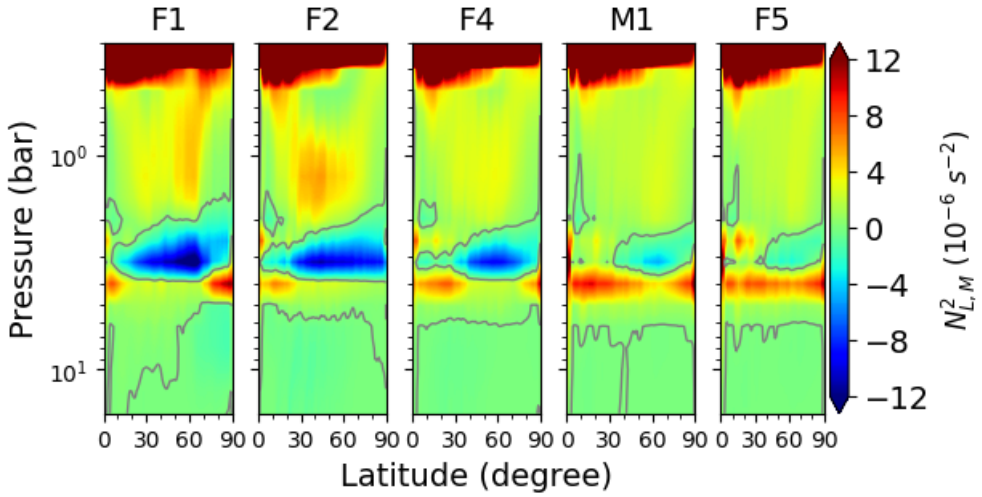
Fig. 3.11 shows the global mean of these three buoyancy frequency for F1 - F5, and Fig. 3.12 presents their zonal mean profile. An increase in dry static stability at 3 bar is observed for all simulations, with notable enhancement near the equator and poles. This pattern closely correlates with the distribution of water clouds, suggesting that the presence of moist convection plays a role in atmospheric stabilisation. However, this interpretation does not fully account for the fact that latent heat release due to water condensation inherently reduces static stability, thereby initiating moist convection. Indeed, both N_L^2 and $N_{L,M}^2$ exhibit a significant decrease, reaching negative values. While including latent heating reduces the buoyancy frequency in the water cloud layers, incorporating the molecular weight gradient has a more complex effect. The buoyancy frequency increases above 2 bars, but decreases in the lower atmosphere. This variation is primarily driven by the vertical distribution of water vapour, as later illustrated in Fig. 3.15 and Fig. 3.18, where the water vapour mixing ratio peaks just below the cloud



(a) Dry static stability



(b) Static stability with water latent heating



(c) Static stability with water latent heating and molecular mass.

Figure 3.12: Zonal mean static stability profile for different runs. Only the northern hemisphere is shown, as the profiles are nearly symmetric across the two hemispheres, with minor localised differences that do not affect the interpretation. The grey contour indicates where static stability crosses zero.

base. Overall, both global mean dry and moist static stability decrease with increasing a_f. This reduction in stability occurs across all latitudes. However, above 2 bars, moist stability increases with decreasing a_f, except in the case of F1. This is likely due to the difference in water vapour mass mixing ratio for these simulations, as shown in Fig. 3.15.

It is important to acknowledge certain limitations in incorporating molecular weight gradients into the calculation of static stability. Notably, the effect of water's molecular weight manifests primarily through its effect on moist convection, rather than being explicitly included in the equation of state used by the dynamical core. For dilute water vapour, this omission is expected to have a small effect on static stability in the bulk atmosphere. However, in regions where the atmosphere is close to neutral stability, the compositional contribution can be sufficient to alter the sign of the diagnosed stability, as demonstrated by our analysis. Consequently, the 'effective' static stability perceived by the dynamical core should correspond to the dry static stability in regions where moist convection is absent, while the full expression should apply in regions where moist convection is active.

3.3.3 Meridional Transport

To understand how energy, momentum and water are redistributed across latitudes, Fig. 3.13 shows the Eulerian mean meridional streamfunction for all runs. For all simulations, the streamfunction is strong and has a complex structure within a few degrees of the equator, indicating strong convection. Additionally, a disturbance in the streamfunction appears around the water cloud level, indicating the effect of moist convection on meridional transport. F1 is, again, distinct from F2 to F5.

For F2 to F5, meridional overturning cells are clockwise circulation in the Northern Hemisphere and anti-clockwise circulation in the Southern Hemisphere. The belt-zone structure is evident off the equator, with rising motion in belts and sinking motion in zones off the equator. Additional structures emerge at peaks of the jet, indicating complex secondary circulations. The streamfunction is disturbed at the water cloud, forming a similar structure above and below the water cloud. Hence, the effect of the disturbance is a stacked cell structure. We caution here that this structure is, however, different to the structure proposed by *Fletcher et al.* (2020) (see a detailed discussion in Chapter 1), as the two cells here circulate in the same direction rather than opposing each other.

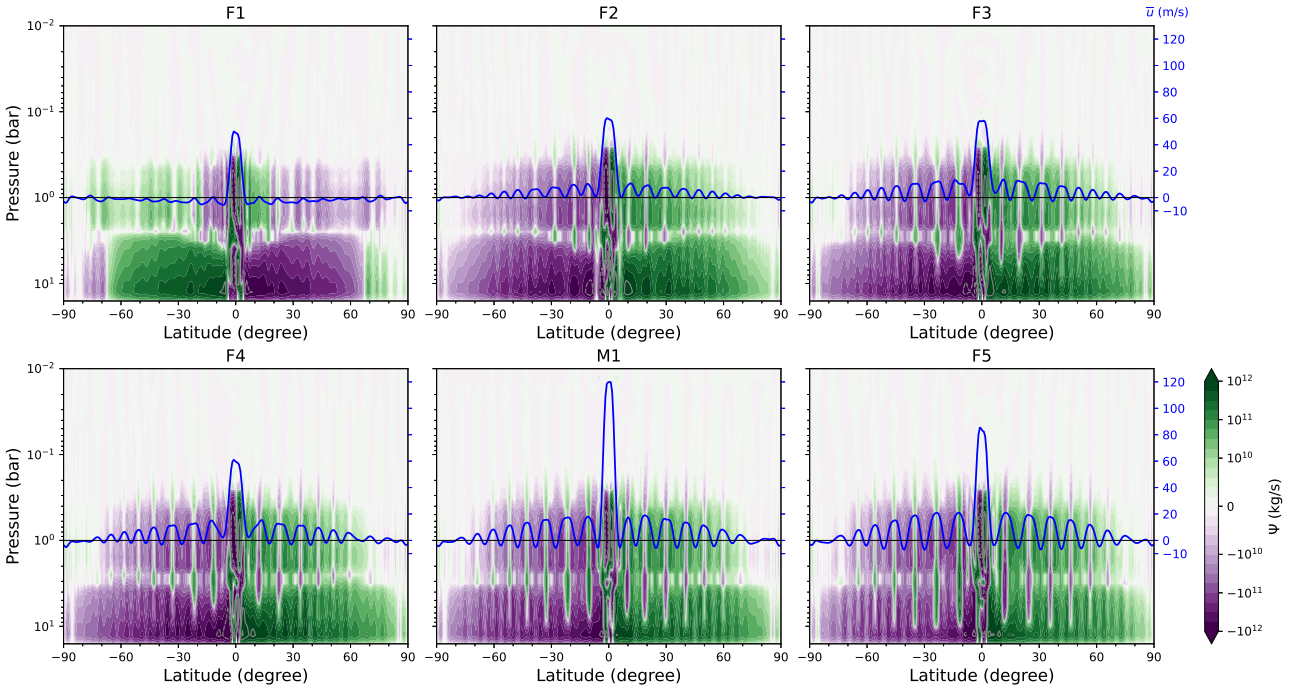


Figure 3.13: Eulerian mean meridional streamfunction computed using velocities averaged over the last 100 days of each run. The streamfunction is plotted on a symmetrical log scale, with 4 colour contours per decade. Blue lines and scale on the right of the figure show the zonal mean zonal velocity profile at 1 bar, with $\overline{u} = 0$ aligned with p = 1 bar.

For F1, the direction of meridional transport is largely opposite to that seen in F2 to F5 (i.e. anti-clockwise in the Northern Hemisphere and clockwise in the Southern Hemisphere), This is expected, as the latitudinal gradient in heat flux is sufficiently large to reverse the latitudinal temperature gradient; the pressure gradient force therefore drives the meridional circulation in a different direction to that in F2 to F5. The small patches in the tropics above the water cloud and near the pole below the water cloud are exceptions to this general trend. These cells are consistent with the local maxima (at 16 bar) and minima (at 1 bar and 3 bar) in zonal mean temperature. The correlation of the meridional streamfunction with jets is weaker, reflecting the overall weaker jet strength in F1. In general, with increasing a_f, meridional transport below the water cloud transitions from distinct belt-zone-associated overturning cells into a large hemispheric cell.

We note here that the Eulerian mean may not be a good representation of the overall material transport. As it could not capture the zonally asymmetric circulation of the baroclinic eddies, which is significant in mid-latitude. On Earth, taking the Eulerian mean gives a thermally indirect mid-latitude Ferrel cell. Such a circulation pattern is problematic as it cannot explain the heat transfer from low to high latitude. While alternative frameworks, such as

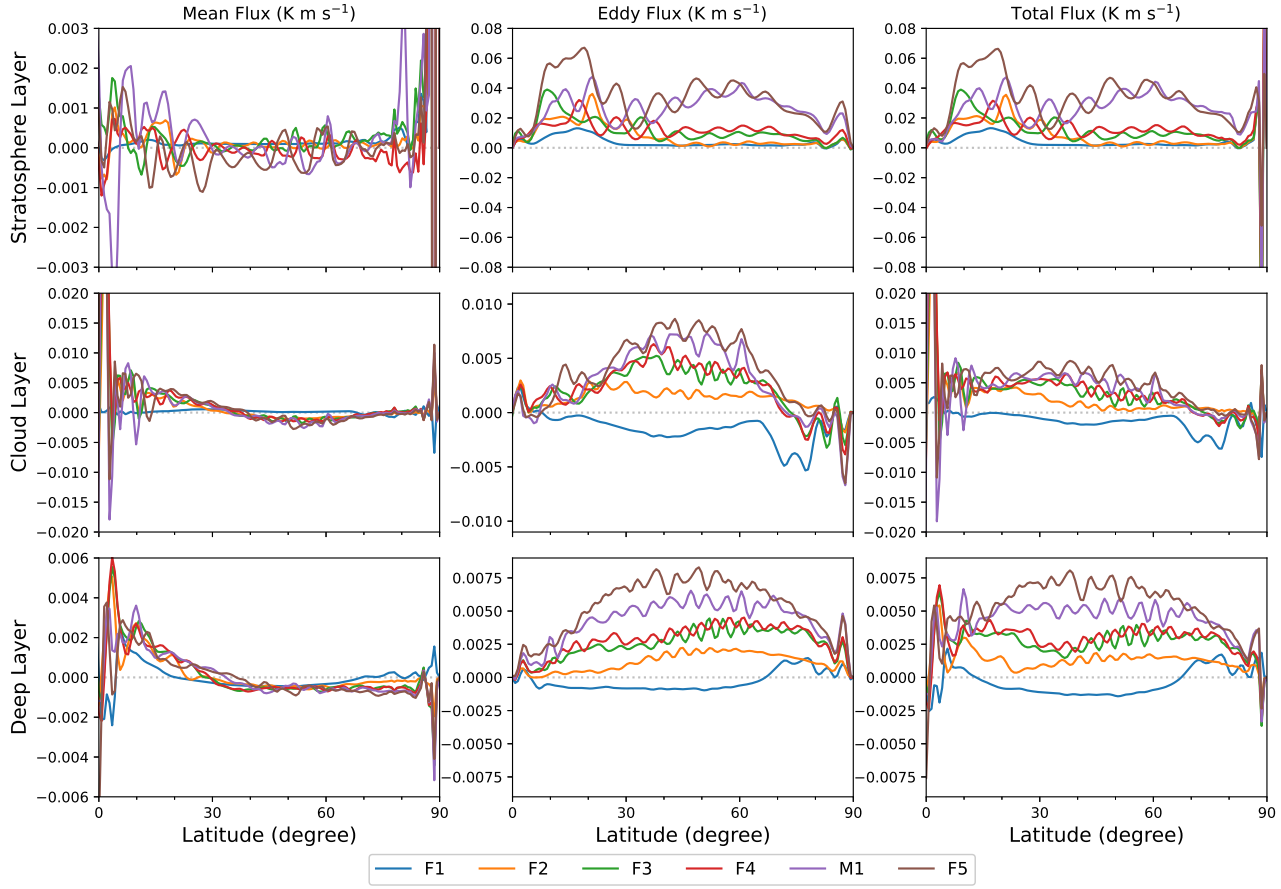


Figure 3.14: Vertically mass weighted average of the zonal mean (left), eddy (middle), and total (right) heat flux in the stratosphere (top), cloud layer (middle), and deep layer (bottom).

the transformed Eulerian mean, have been used in the Earth's atmosphere and ocean (*Vallis* 2017) and are successful in studying tracer transport (*Abalos et al.* 2017), We did not use this diagnostic as it is mainly driven by the static stability, which is very weak and changes signs.

To assess the dynamical contribution to the atmospheric temperature structure, we examine the meridional mean and eddy heat fluxes, as shown in Fig. 3.14. The eddy heat flux is consistently directed poleward in runs F2 through F5 and decreases in magnitude with increasing a_f. In contrast, run F1 exhibits distinct behaviour: the eddy heat flux becomes equatorward in the weather layer and also exhibits equatorward transport between approximately 5° and 70° latitude in both hemispheres in the deeper atmospheric layers.

The mean meridional heat flux is generally weaker than the eddy component across most regions. In the stratosphere, it is negligible in comparison. In the weather and deep layers, the mean flux is weaker than the eddy flux at latitudes poleward of approximately 40°. Between 20° and 40°, it tends to be directed equatorward rather than poleward, except in F1. Instead,

the mean heat flux in the weather layer of F1, although weaker than the eddy component, remains poleward up to 80° latitude. For simulations F2 to F5, there is no strong trend in the mean flux with increasing a_f.

3.3.4 Water Distribution and Moist Convection

Fig. 3.15 shows the global-mean mass mixing ratio of water vapour and ice as a function of pressure. The distribution of liquid water cloud is not shown, as it is negligible in all simulations considered here. Overall, the vertical profiles are highly similar across all runs. The water cloud base is consistently located between 2 and 3 bars, and the mass mixing ratio of water vapour remains uniform and nearly identical below approximately 4 bars. Significant differences in water vapour and ice mixing ratios only emerge above 0.2 bars, while a small divergence in vapour content also occurs near 0.4 bars. However, these differences are likely of limited physical significance, as the water mixing ratio at these altitudes is more than five orders of magnitude lower than the peak values at depth. Given the variations in temperature structure and meridional circulation between runs, the similarity in the vertical water profiles may seem surprising. Nonetheless, it is not entirely unexpected, as all simulations share the same water abundance and cloud microphysics parametrisation, and the global-mean temperature profiles are relatively consistent across cases.

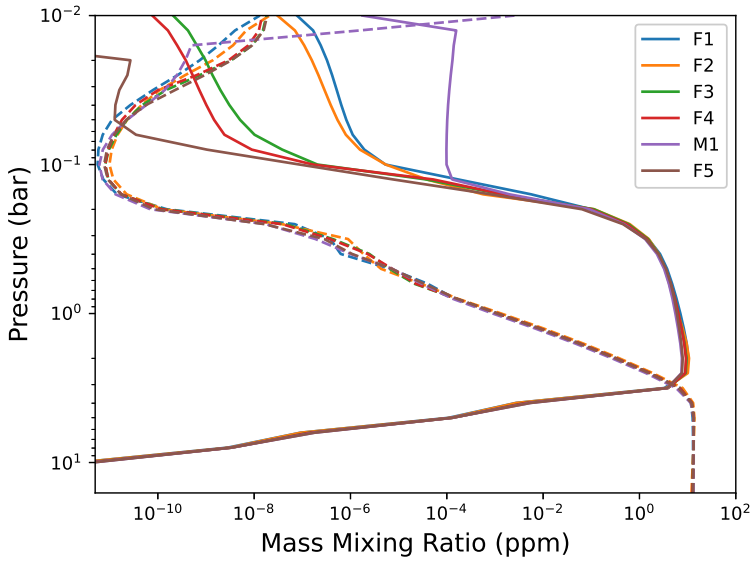


Figure 3.15: Global mean vertical profiles for water ice (solid) and vapour (dashed) mass mixing ratio at the end of each run.

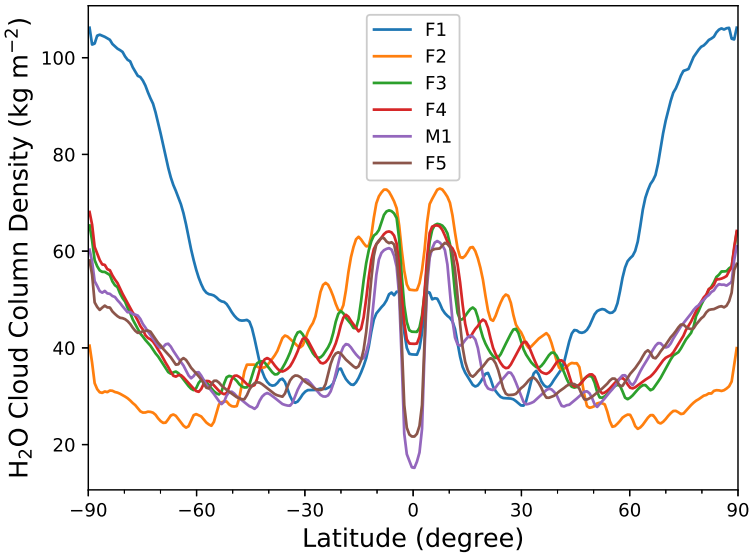


Figure 3.16: Water cloud column density at the end of each run.

To further compare the water cloud distribution across different simulations, we plot the column density of water ice cloud in Fig. 3.16, and its zonal mean mass mixing ratio profiles in Fig. 3.17. In general, the water cloud is symmetric across the equator. The cloud layer is more elevated both near the poles and around the equator. The concentration at the equator, however, is much lower. This reduction in concentration is reflected in column density as a dip at the equator. Additionally, the water cloud concentration correlates with the zonal jets, where local maxima of cloud concentration typically occur in zones and local minima typically occurs in belts. The water cloud distribution also shows significant variation among different runs. F1 exhibits a significantly higher concentration of water cloud at high latitudes compared to other cases, while showing much lower values at the equatorial peak. In contrast, F2 features the most pronounced peaks of cloud concentration near the equator, but a lower cloud density above approximately 50°. The other runs (F3, F4, F5, and M1) exhibit a broadly similar pattern, with less pronounced equatorial peaks and relatively consistent values across latitudes. This behaviour suggests a nonlinear response of the cloud distribution to a_f, likely influenced by changes in the meridional overturning circulation across the F-series. The cloud cycle involving phase change and sedimentation may further complicate this response, and a more detailed diagnosis of the coupled transport and microphysical processes would be valuable for fully understanding these variations.

We also note that in all simulations, the water cloud is unrealistically thick, extending

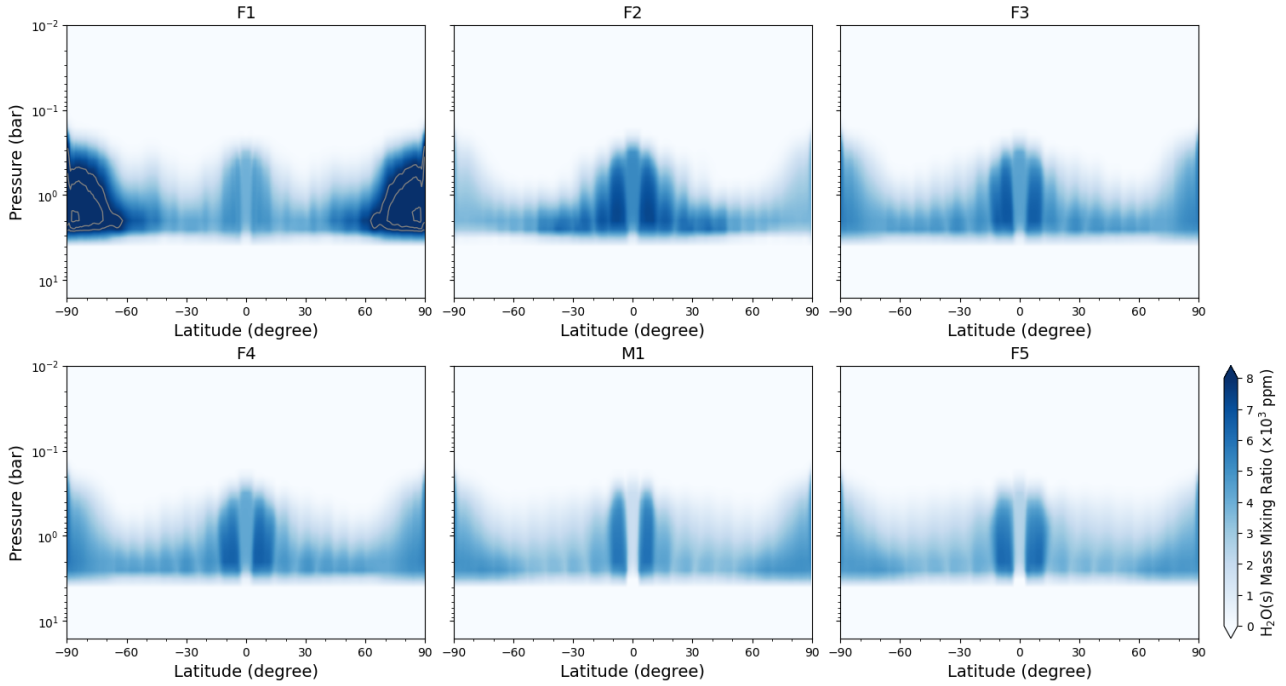


Figure 3.17: Zonal-time mean water ice mass mixing ratio. The grey contours are at 10^3 ppm increment for mass mixing ratio at and above the upper limit of the colour scale.

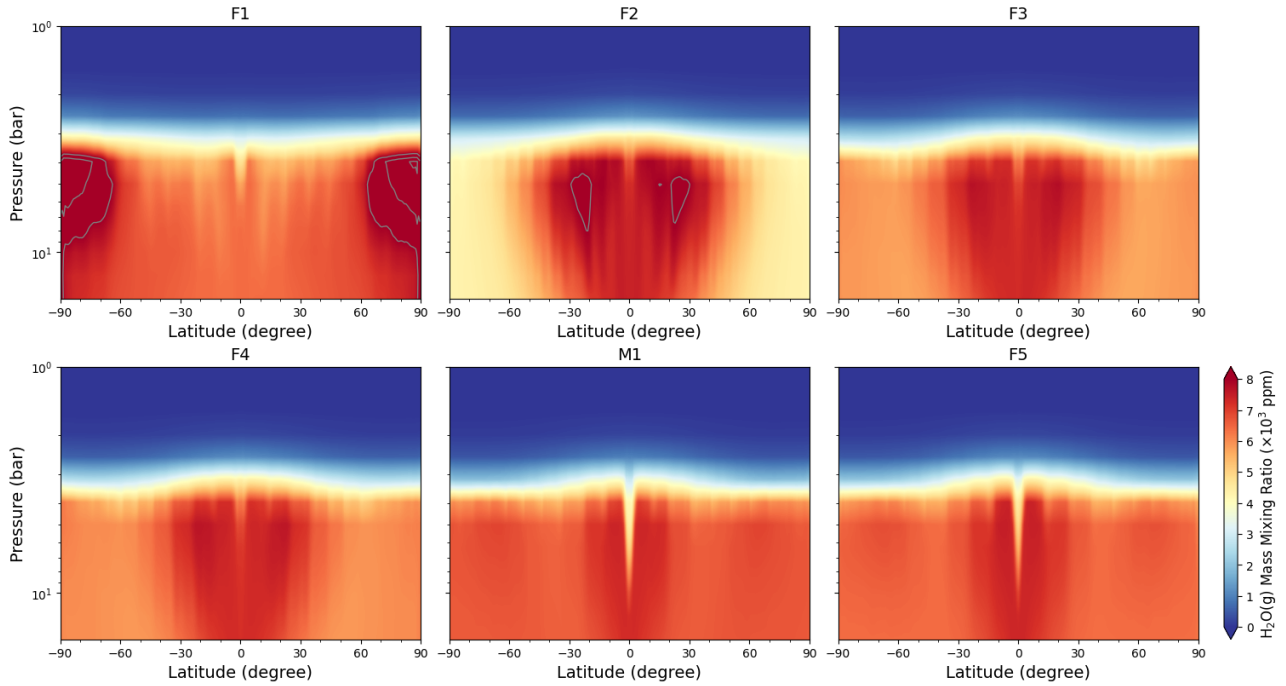


Figure 3.18: Zonal-time mean water vapour mass mixing ratio. Note the vertical domain is constrained to below 1 bar, as above this level, water vapour is mostly condensed into cloud.

to pressures of 0.2–0.3 bar, whereas the observed ammonia cloud level on Jupiter is near 0.7 bar. This behaviour is likely a consequence of the simplified cloud treatment adopted here, in particular the lack of precipitation and the assumption of a uniform particle size, which inhibits the rapid sedimentation of larger condensates. While we do not expect the cloud thickness to have a large impact on the large-scale dynamics, it may still influence the dynamics indirectly through latent heating and moist convection. A systematic study of the impact of different cloud schemes is beyond the scope of this study and is deferred to future work.

Fig. 3.18 shows the zonal mean water vapour distribution. The water vapour is not uniform below the water cloud. Instead, water vapour is enriched at latitudes with higher water cloud column density. Furthermore, water vapour is more concentrated below the water cloud than at greater depths, due to precipitation and re-evaporation of the cloud particles. Similar to the water cloud, water vapour concentration also correlates with the zonal jets, but to a lesser extent. A depletion of water vapour just below the water cloud at the equator appears in all runs, though to varying extents. The region of depletion narrows with increasing depth, forming the triangle feature on the figure. These characteristics cannot be directly compared with observations, as there is no pressure-latitude map of water vapour available for Jupiter.

Fig. 3.19 presents the zonal mean total convective available potential energy (TCAPE) for each simulation. Previous analysis using the JasonGCM (*Young and Read* 2019) has shown that TCAPE exhibits similar spatial and temporal variability to other commonly used diagnostics of moist convection, including convective mass flux and convective velocities. We therefore use TCAPE here as an indicator of moist convection stength. The TCAPE distribution exhibits a consistent general structure across all runs, although the precise latitudes of specific features varies between cases. In general, TCAPE increases with latitude and follows a three-part pattern: it first exhibits a local maximum, followed by a sharp increase, and then continues to increase more gradually toward the poles. The magnitude of TCAPE is broadly similar across all simulations, particularly in the high-latitude regions. An exception to this trend is observed in simulation F1, where TCAPE increases steadily toward the pole following the sharp jump near 60° latitude. Unlike the results reported by *Young and Read* (2019), these simulations do not show a clear belt-to-zone contrast in TCAPE. This discrepancy may be attributable to the shorter averaging period used in our analysis, since we use a 100-day mean from the end of the simulation, whereas *Young and Read* (2019) applied a 1000-day average. As a result, transient

features may not be sufficiently smoothed in our diagnostics.

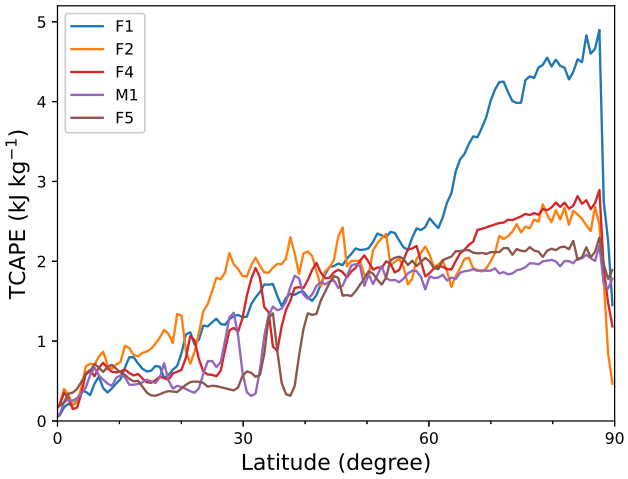


Figure 3.19: Total convective available energy (TCAPE) as a function of latitude.

3.4 Lorenz Energy Cycle Analysis

To understand how changes in the bottom thermal boundary condition modify the large-scale jet structure, we use the Lorenz energy cycle as a diagnostic framework.

3.4.1 Formulation of the Lorenz Energy Cycle

The Lorenz energy cycle (*Lorenz* 1955; *Schubert and Mitchell* 2013) provides a useful framework to interpret the energy conversions within the atmosphere in a heat-engine context. In this framework, atmospheric energy is partitioned into available potential energy and kinetic energy, each comprising zonal mean and eddy components. These energy reservoirs can be generated, converted between one another, or dissipated through various dynamical processes. Fig. 3.20 summarises the structure of the Lorenz energy cycle and how the different terms are interconnected.[3]

This framework is employed in various setups on Earth, including localised systems such as cyclones (*Dias Pinto and da Rocha* 2011) and the northern hemisphere winter jet (*Jiang et al.* 2013), as well as on a global scale to validate model simulations (*Boer and Lambert* 2008; *Marques et al.* 2011) or to study energy transformation, understand the influence of climate change

[3]The box diagram of the Lorenz energy cycle typically elevates the subscripts (e.g. A_E would be written as AE), especially in older texts. Here, we use subscripts for better consistency and readability.

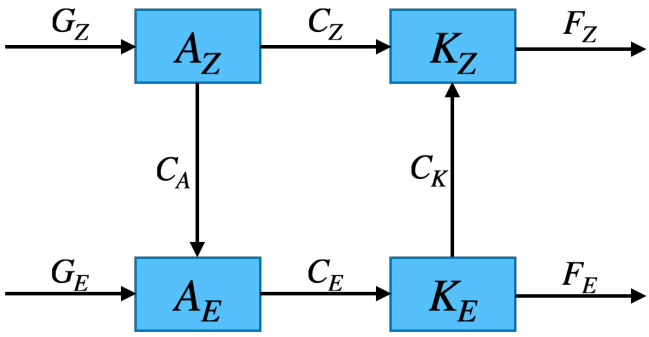


Figure 3.20: Schematic of the Lorenz energy cycle, A is *A*vailable potential energy, K is *K*inetic energy. Subscript Z indicates the *Z*onal mean components and subscript E indicates the *E*ddy component.

(*Michaelides* 2021; *Pan et al.* 2017). For planetary studies, *Del Genio et al.* (1993) applied a simplified version of the Lorenz energy cycle for GCM simulations of slowly rotating planets akin to Titan and Venus. *Lee and Richardson* (2010) used the Lorenz energy cycle to calculate the conversions between different kinds of energies in GCM simulations with different dynamical cores and sponge layer formulations. For Mars, *Tabataba-Vakili et al.* (2015) computed the Lorenz energy cycle using reanalysis data, and later compared it with that for simulation output with various diurnal and seasonal forcing (*Tabataba-Vakili* 2017). *Read et al.* (2018) applied the Lorenz energy cycle to study the dependency of global energetics on planetary parameters for terrestrial planets. Recently, this framework has also been applied to understand the atmospheric circulation of tidally locked exoplanets (*Wang and Yang* 2023), and qualitatively, to exoplanets in general (*Zhang* 2020). To the author's knowledge, no published study has yet applied a comprehensive Lorenz energy cycle analysis to gas giant atmospheres. This may be partially due to the limited observational coverage and the complexity of interpreting outputs from general circulation models (see discussion below). Work using the Jason model was reported in an internal document by *Kennedy et al.* (2016), and the preliminary results from the higher-resolution simulations were presented in Fig. 12 of *Read et al.* (2020a).

Different formulations of the Lorenz energy cycle have been developed, each based on specific assumptions and simplifications suited to different dynamical regimes. *James* (1994), for example, presented a version tailored to mid-latitudes under the quasi-geostrophic approximation. A more general formulation was proposed by *Boer* (1989), who incorporated additional terms to account for topographic effects, more flexible averaging procedures and other corrections to the Lorenz approximations. While the formulation by *Boer* (1989) is well suited to terrestrial climate systems with surface topography and land-sea contrasts, such complexities

are not relevant for gas giant atmospheres that lack solid surfaces. Moreover, the added mathematical and computational complexity may not yield significant improvements in insight for our current application. For this reason, we adopt the formulation in *Peixoto and Oort* (1992), which balances generality and computational tractability. Moreover, this framework is commonly used in planetary atmospheric studies, allowing for direct comparison with past work on both terrestrial and gas giant atmospheres (e.g., *Lee and Richardson* 2010; *Wang and Yang* 2023).

Following *Peixoto and Oort* (1992), the atmospheric energies are

$$K_Z = \left\langle \frac{1}{2}\overline{u^2 + v^2} \right\rangle, \tag{3.13}$$

$$K_E = \left\langle \frac{\overline{u'^2 + v'^2}}{2} \right\rangle, \tag{3.14}$$

$$A_Z = \left\langle \frac{h^2}{2s^2}\overline{\theta_A^2} \right\rangle, \tag{3.15}$$

and

$$A_E = \left\langle \frac{h^2}{2s^2}\overline{\theta'^2} \right\rangle, \tag{3.16}$$

where K_Z is the zonal mean kinetic energy, K_E is the eddy kinetic energy, A_Z is the zonal mean available potential energy and A_E is the eddy available potential energy. h is a conversion factor defined as

$$h(p) = \frac{R}{p}\left(\frac{p}{p_R}\right)^{\kappa}, \tag{3.17}$$

where p_R is a constant reference pressure, and s is the stratification parameter given by

$$s^2 = -h(p)\frac{\partial \theta_R}{\partial p}, \tag{3.18}$$

here θ_R is the state of minimal potential energy resulted from an adiabatic redistribution of mass, obtained by taking the global mean, and $\theta_A = \theta - \theta_R$. $\bar{f} = \frac{1}{2\pi}\int_0^{2\pi} f \mathrm{d}\lambda$ is the zonal mean of a quantity f, and $f' = f - \bar{f}$ refers to the deviation from the zonal mean. $\langle\cdot\rangle$ represents the global areal average of the vertical mass integral such that

$$\langle Q \rangle = \frac{1}{4\pi a^2}\iiint Q \ \mathrm{d}m. \tag{3.19}$$

The conversion rates are given by:

$$C_A = C\left(A_Z, A_E\right) = -\left\langle \frac{h^2}{s^2}\frac{\partial\bar{\theta}}{a\partial\phi}\overline{v'\theta'} + \frac{\partial}{\partial p}\left(\overline{\frac{h^2}{s^2}\theta}\right)\overline{w'\theta'}\right\rangle, \tag{3.20}$$

$$C_Z = C\left(A_Z, K_Z\right) = -\left\langle \bar{\omega}\bar{\alpha}\right\rangle, \tag{3.21}$$

$$C_E = C\left(A_E, K_E\right) = -\left\langle \overline{\omega'\alpha'}\right\rangle, \tag{3.22}$$

$$C_k = C\left(K_E, K_Z\right) = \left\langle \overline{v'u'}\cos\phi\frac{\partial(\bar{u}/\cos\phi)}{R\partial\phi} + \overline{\omega'u'}\frac{\partial\bar{u}}{\partial p} + \overline{v'^2}\frac{\partial\bar{v}}{R\partial\phi} - \bar{v}\frac{\tan\phi}{R}\overline{u'^2} + \overline{\omega'v'}\frac{\partial\bar{v}}{\partial p}\right\rangle. \tag{3.23}$$

The generation and dissipation terms can then be expressed as a residual that only depends on other quantities within the Lorenz energy cycle:

$$G_Z = C_Z + C_A + \frac{\mathrm{d}A_Z}{\mathrm{d}t}, \tag{3.24}$$

$$F_Z = C_Z + C_K - \frac{\mathrm{d}K_Z}{\mathrm{d}t}, \tag{3.25}$$

$$G_E = C_E - C_A + \frac{\mathrm{d}A_E}{\mathrm{d}t}, \tag{3.26}$$

$$F_E = C_E - C_K - \frac{\mathrm{d}K_E}{\mathrm{d}t}. \tag{3.27}$$

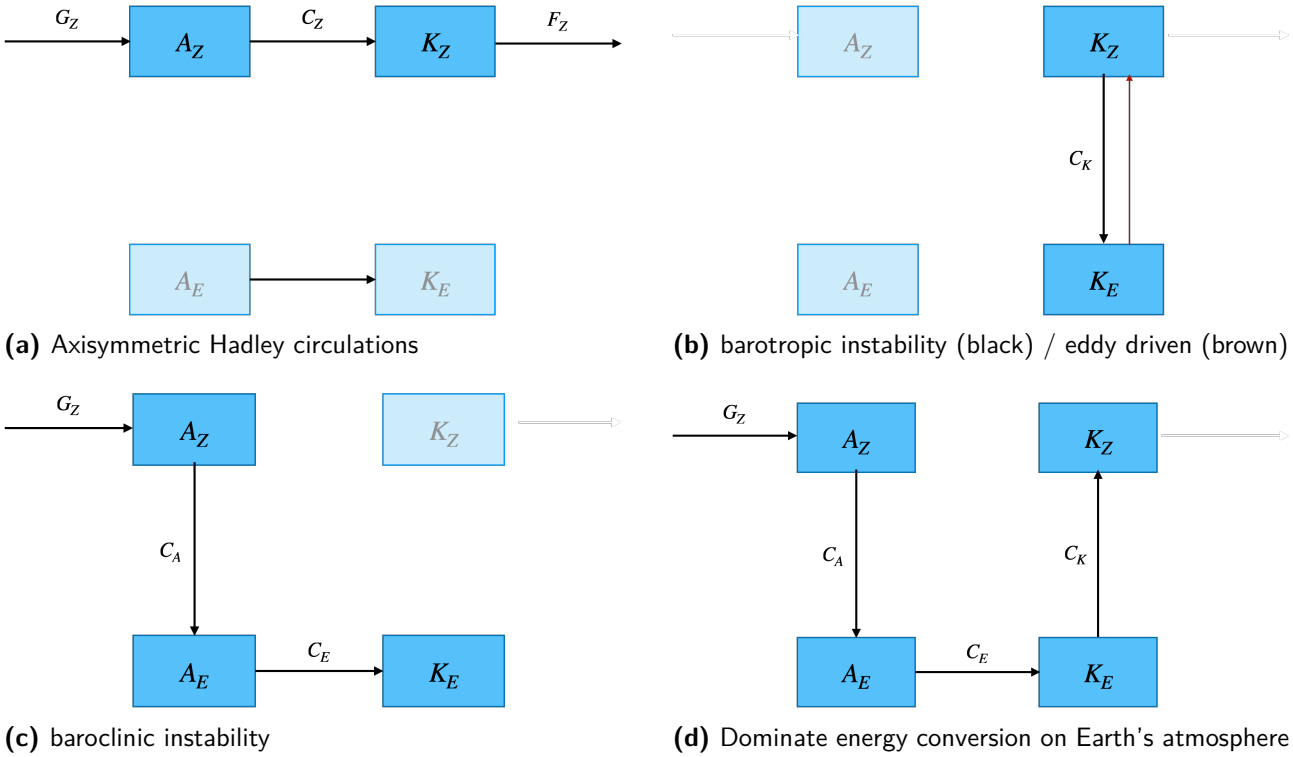
Three common paradigms can be applied to interpret the Lorenz energy cycle, as depicted in Fig. 3.21:

1. A positive C_Z indicates an axisymmetric circulation is driven by the latitudinal temperature gradient ($A_Z \rightarrow K_Z$). The Hadley circulation is a typical example of this process (Fig. 3.21a).

2. A positive C_K indicates energy transfer from eddies to zonal jets ($K_E \rightarrow K_Z$), meaning the jets are driven by eddy forcing. Conversely, a negative C_K signifies energy transfer from zonal jets to eddies ($K_Z \rightarrow K_E$), which is associated with barotropic instability (Fig. 3.21b).

3. When both C_A and C_E are positive, the energy pathway $A_Z \rightarrow A_E \rightarrow K_E$ represents temperature fluxes that convert zonal available potential energy into eddy available potential energy, and subsequently upward heat fluxes convert it to eddy kinetic energy. This process

indicates the presence of baroclinic instability (Fig. 3.21c).



(a) Axisymmetric Hadley circulations

(b) barotropic instability (black) / eddy driven (brown)

(c) baroclinic instability

(d) Dominate energy conversion on Earth's atmosphere

Figure 3.21: Interpretation of the Lorenz energy cycle, adapted from *James* (1994).

On Earth, the dominant energy conversions in the global Lorenz energy cycle are associated with baroclinic conversion and eddy forcing of the zonal flow Fig. 3.21d. Although the Hadley cell contributes positively to C_z, this signal is partially offset by the thermally indirect Ferrel cell, which contributes negatively to C_z. Early observational estimates suggested a weakly negative C_z (*Peixoto and Oort* 1992), while more recent reanalysis (*Li et al.* 2007) indicates a weakly positive contribution. In both cases, the magnitude of C_z remains small relative to other conversion terms.

3.4.2 Lorenz Energy Cycle on JasonGCM Output

The Lorenz energy cycle diagnostics are computed for each snapshot of the final 4000 days of all simulations. Available potential energies, C_A, along with the generation terms G_Z and G_E, are not presented here, as s^2 becomes vanishingly small and, in some regions, changes sign. Hence, these terms become dominated by variations in static stability. Consequently, the global mean values are not physically meaningful, and the local distributions are difficult to interpret.

Fig. 3.22 shows the kinetic energies as a function a_f. Both K_Z and K_E remain stable over

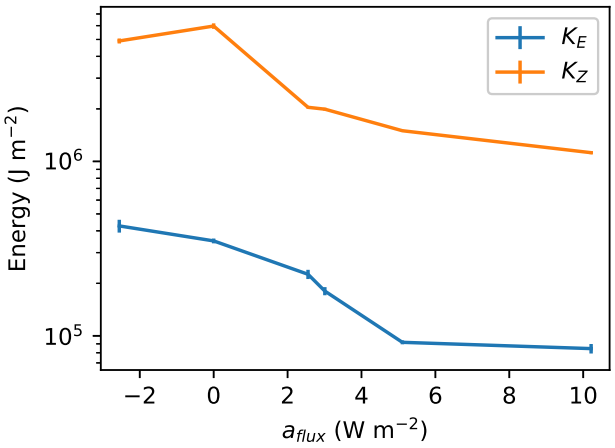
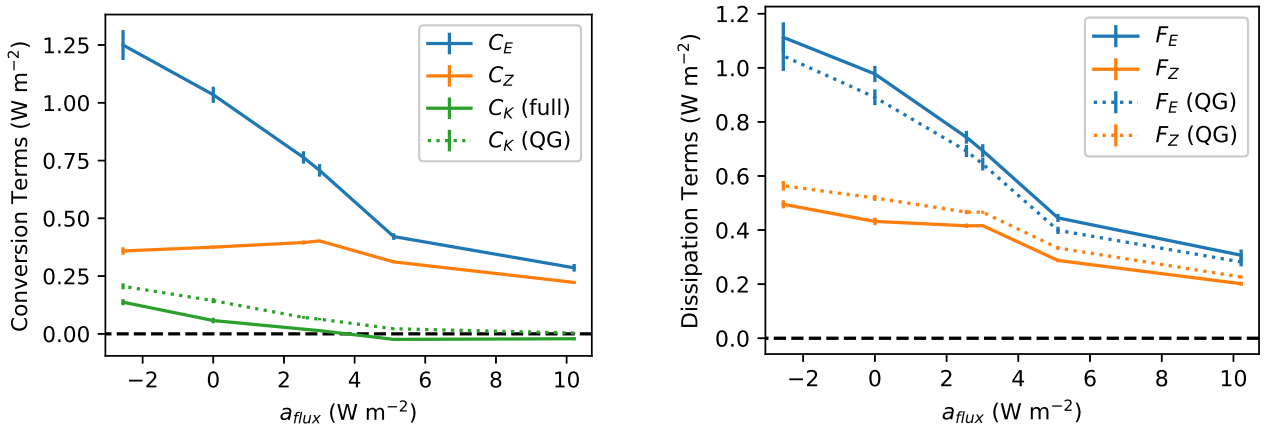


Figure 3.22: Zonal mean kinetic energy and eddy kinetic energy for different a_f. The values are averaged over the last 4000 d of the simulation, and the error bar shows the standard deviation of the values at each timestamp. The unit area value is used to be consistent with the conversion terms.

time, as indicated by the small error bars representing the standard deviation. This temporal stability is expected, given that the simulations have reached equilibrium. The kinetic energy is primarily contained in the zonal flow. The ratio K_Z/K_E ranges from approximately 9 to 16, with variation observed between different runs. In all cases except for run F1, the zonal kinetic energy decreases with increasing a_f. A similar trend is observed for the eddy kinetic energy , though the decline becomes more pronounced for $a_f > 5$, corresponding to runs F2 and F1. However, due to the absence of simulations with intermediate values of a_f between run F2 and F1, a definitive conclusion cannot be drawn regarding this trend, especially given that the latitudinal temperature gradient changes sign between these two runs.



(a) Conversion terms.

(b) Dissipation terms.

Figure 3.23: The conversion and dissipation terms of the Lorenz energy cycle are shown for different a_f. The error bars have the same meaning as in Fig. 3.22.

Fig. 3.23a shows the conversion terms as a function of a_f, while Figs. 3.24 to 3.26 shows the zonally integrated mass-weighted sum of C_E, C_K and C_Z respectively. For a conversion term $X = \langle x \rangle$, this is defined as

$$\hat{X}(\phi, p) = \sum_{\lambda} X(\lambda, \phi, p) \Delta m(\lambda, \phi, p), \tag{3.28}$$

where Δm is the mass of the cell. When plotted in the figures with a log-pressure scale, $\hat{X}$ indicates the contribution to X at each latitude-pressure location.

The conversion from zonal available potential energy to kinetic energy, $\hat{C}_Z$ exhibit an alternating pattern between positive and negative values at the sub-jet scale, with the strongest signature at the equator. This leads to a large degree of cancellation. Nevertheless, the global mean value, C_Z, remains positive, peaking at $a_f = 3$ W m^{-2} with a value in the range of 0.22 to 0.40 W m^{-2}. F1 also sees a significantly weaker signature compared to other runs. The reduction in C_Z with increasing a_f reflects the overall weakening of zonal-mean kinetic energy generation. This is consistent with the weakening of mid-latitude jets as the system becomes more barotropic.

The conversion from eddy available potential energy to kinetic energy, C_E, is predominantly positive in the troposphere, but becomes notably weakened around 3 bars. This reduction can be attributed to the effects of moist convection. Within approximately $\pm 20°$ of the equator, $\hat{C}_E$ even becomes negative. For runs F2 to F5, the distribution of $\hat{C}_E$ is closely related to the jets structure, and the magnitude of $\hat{C}_E$ decreases with increasing a_f. Run F1 exhibits the weakest $\hat{C}_E$ values overall, with the vertical structure appearing more diffuse at depth. Compared to C_Z, C_E is more sensitive to changes in a_f. Its global value decreases from 1.25 to 0.29 W m^{-2} as a_f increases, consistent with the weakening of baroclinic instability due to the reduction in meridional temperature gradient. The decline in C_E is more rapid for $a_f < 5$. As the latitudinal temperature gradient reverses sign beyond $a_f = 5$, C_E likely reaches a minimum between runs F1 and F2. This is plausible because F1 retains a stronger meridional temperature contrast than would be present in a case with a uniform bottom boundary temperature.

The kinetic energy conversion term, C_K, displays strong negative values near the equator. These are primarily associated with the second through fifth terms in Eq. (3.23). This is not surprising, given that strong upwelling is observed at the equator. Away from the equator, $\hat{C}_K$ is mostly positive, with the dominant contributions coming from the first term in Eq. (3.23).

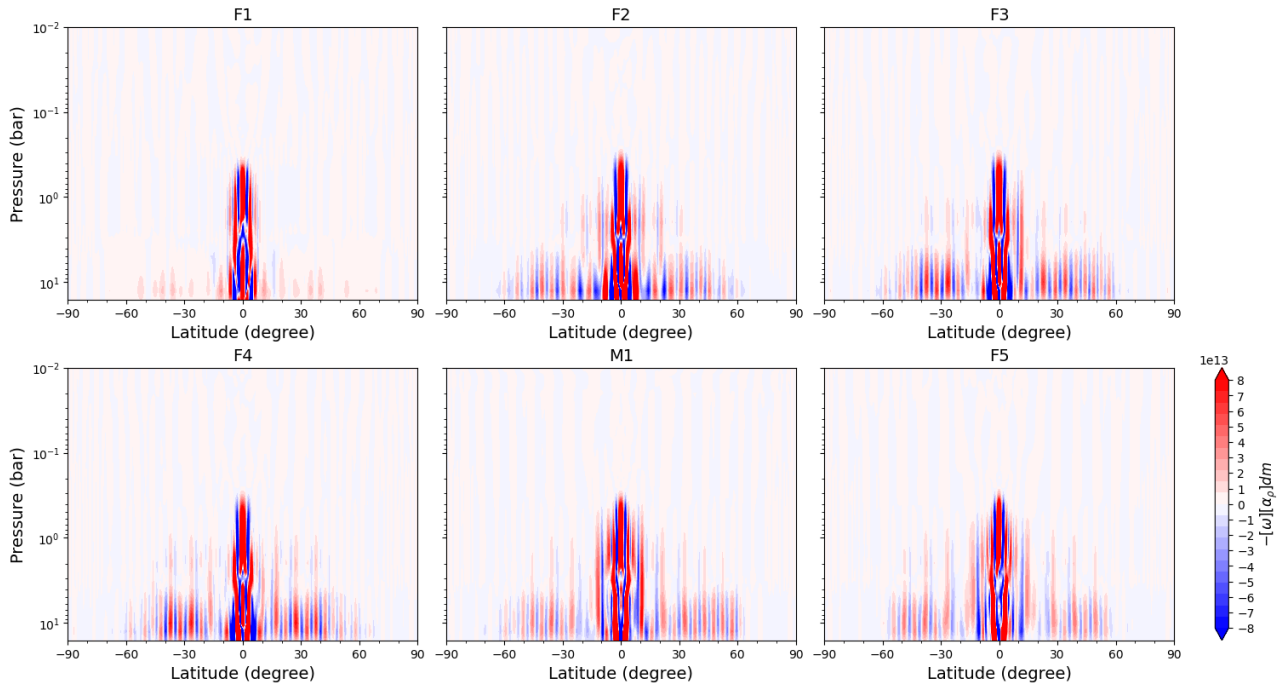


Figure 3.24: Latitude-Pressure profile of the C_Z term of the Lorenz energy cycle (Eq. (3.21)).

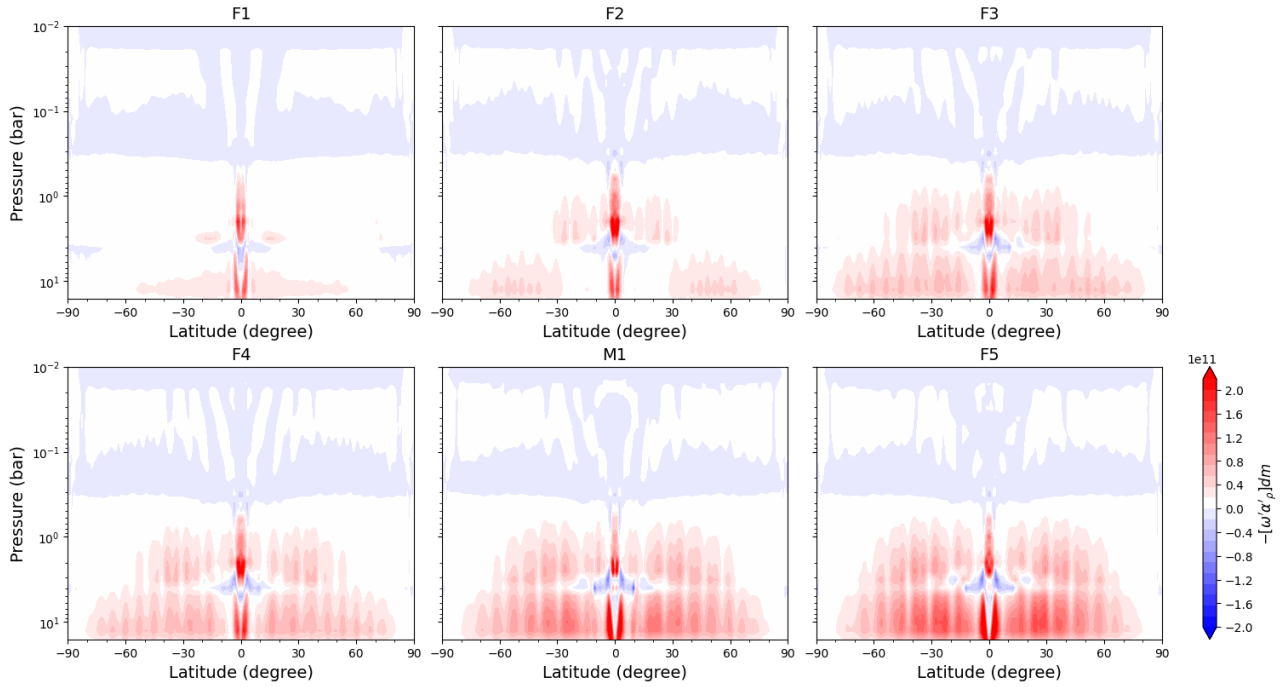


Figure 3.25: Latitude-Pressure profile of the C_E term of the Lorenz energy cycle (Eq. (3.22)).

This first term can also be derived from observational data, though a more locally meaningful expression is often used:

$$C_{K,1} = \left\langle -\bar{u}\frac{\partial(\overline{v'u'}\cos\phi)}{R\cos\phi\partial\phi} \right\rangle \tag{3.29}$$

Through integration by parts, it can be shown that when $\overline{u} = 0$ at the boundaries of the integration domain (e.g. over an individual jet), this form is equivalent to the first term in Eq. (3.23). Fig. 3.27 presents the zonally integrated, mass-weighted sum of this term. The sign of $C_{K,1}$ varies with latitude: it is positive at the peaks of both prograde and retrograde jets but becomes weak or negative in the cores of belts and zones. For example, in run F2, $\hat{C}_{K,1}$ becomes negative where the zonal velocity approaches zero between two eastward jets. This behaviour indicates that eddies are transferring energy into the jet cores while extracting energy from their flanks, thus helping to maintain the sharpness and localisation of the jets. A further notable feature is that at the equator, $\hat{C}_{K,1}$ becomes negative at certain pressure levels, suggesting that the zonal jets are transferring energy to eddies. This may drive the formation of the double-cusp structure observed in some simulations. Both of these behaviours are consistent with patterns inferred from cloud feature tracking of Jupiter's winds (*Read et al.* 2025).

Overall, C_K decreases with increasing a_f, and becomes negative for $a_f > 5$ W m^{-2}, indicating a shift from an eddy-driven jet regime to one dominated by barotropic instability. While $C_{K,1}$ also declines with increasing a_f, it remains slightly positive at the highest a_f: for F1 with $a_f = 10.21$ W m^{-2}, a global mean value of 0.004 W m^{-2} is observed. The combined contribution from terms 2 to 5 in Eq. (3.23) is consistently negative. With increasing a_f, this contribution initially increases in magnitude from –0.069 W m^{-2} at $a_f = -2.55$ W m^{-2} to –0.086 W m^{-2} at $a_f = 0$ W m^{-2}, then decreases in magnitude to –0.025 W m^{-2} at $a_f = 10.21$ W m^{-2}.

Both loss terms, F_Z and F_E, decrease with increasing a_f, as illustrated in Fig. 3.23b. Their trends closely mirror those of C_Z and C_E, respectively. This correspondence arises because the kinetic energy conversion term, C_K, is relatively small compared to the other conversion terms and contributes minimally to the overall energy balance.

Fig. 3.22 summarises these results in a Lorenz energy cycle box diagram. Despite quantitative variations across the F-series, the overall structure of the energy cycle is robust: kinetic energy is dominated by the zonal component, and the primary energy pathway is the con-

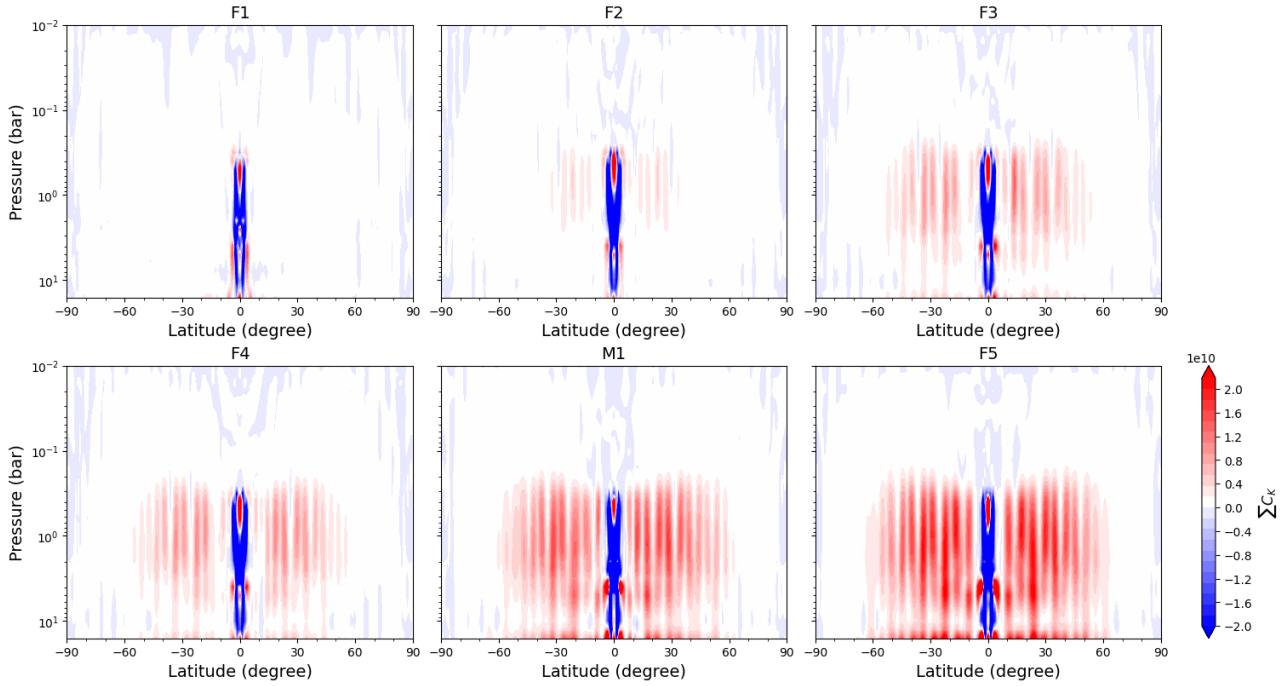


Figure 3.26: Latitude-Pressure profile of the full C_K term (Eq. (3.23)).

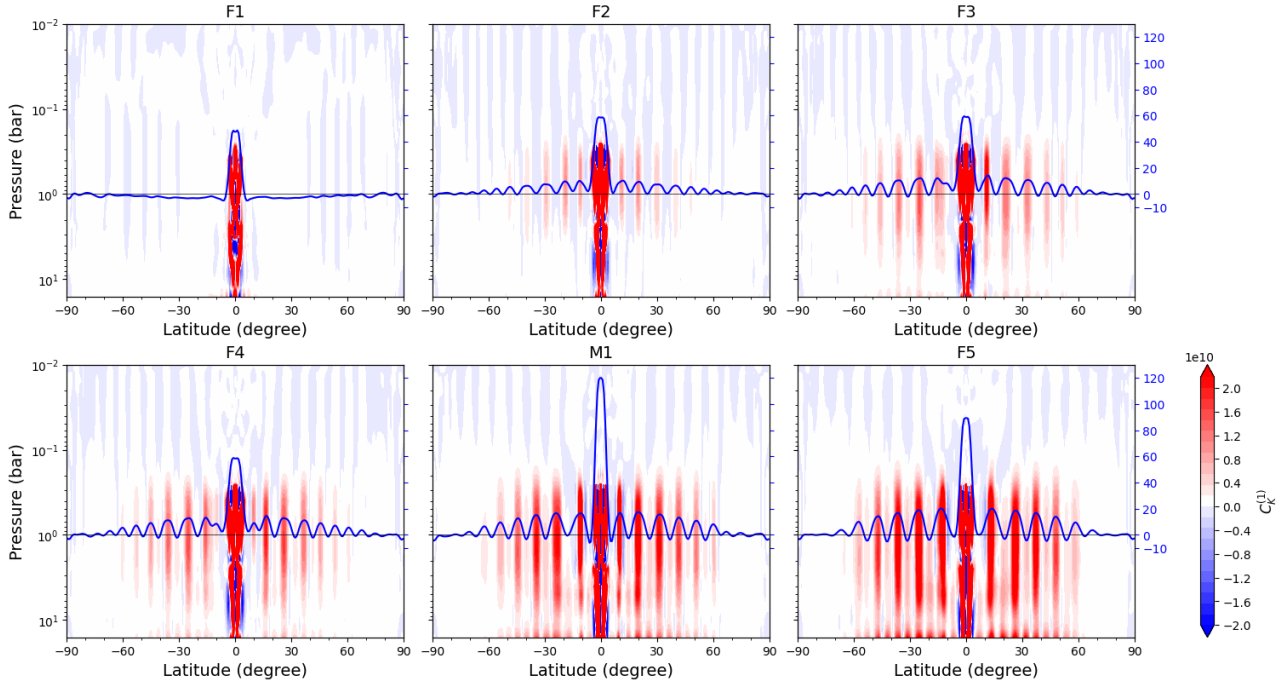


Figure 3.27: Latitude-Pressure profile of the locally meaningful version of the first part of the C_K term (Eq. (3.29)).

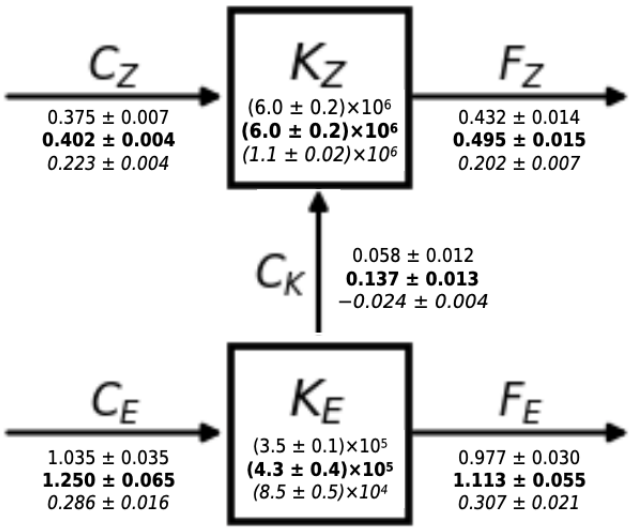


Figure 3.28: Lorenz energy cycle box diagram for the simulations with varying internal heat flux. Numbers in boxes represent the globally average energy (in J m^{-2}), Arrows represent the conversion rates (in W m^{-2}). The three rows are the value for the M1 run, maximum (bold) and minimum (italic) across all F-series runs, respectively.

version from eddy available potential energy to eddy kinetic energy, indicating that baroclinic instability is the dominant mechanism. The systematic decline of C_E with increasing a_f reflects a weakening of baroclinic instability as the meridional temperature gradient is reduced. This reduces eddy generation and leads to weaker eddy momentum flux convergence, as evidenced by the decrease in $C_{K,1}$ at jet centres, and ultimately results in the weakening of the mid-latitude jets. In this way, the Lorenz energy cycle provides a consistent energetic pathway linking changes in the internal heat flux profile to the changes in jet structure.

3.5 Comparison with a Deep Adiabat Run

The results discussed above highlight the differences in atmospheric behaviour as the deep-layer latitudinal temperature gradient transitions from positive to negative. A natural question arising from this is what the dynamical response is at the transition point, where the bottom boundary temperature is uniform in latitude.

Determining the exact interior heat flux profile that yields a perfectly uniform bottom temperature is non-trivial, requiring extensive trial and error. This is further complicated by the complexity of dynamical heat transport processes, which adjust the thermal structure in ways that are difficult to predict a priori. To circumvent this issue, we use the deep adiabat

configuration described in Section 2.3.3 as a proxy. This approach simplifies the lower boundary condition while still allowing exploration of how the absence of a latitudinal temperature gradient affects the atmospheric circulation and cloud structures.

In this section, we first describe the model setup used for this simulation in Section 3.5.1. We then examine the zonal jet structure and meridional circulation in Section 3.5.2, followed by an analysis of the temperature profile and static stability in Section 3.5.3. Section 3.5.4 then present the water cycle properties of this run. The Lorenz energy cycle is discussed in Section 3.5.5, and finally, in Section 3.5.6, we compute the equivalent interior heat flux to contextualise this configuration within the framework of the F-series simulations.

3.5.1 Run Setup

The deep adiabat simulation used here shares the same configuration as the F series run, with the key distinction being the imposition of a constant deep potential temperature in place of the latitudinally varying internal heat flux. The deep adiabat is set to a potential temperature of 182 K, which is slightly higher than the global mean value in the bottom layer at the end of the F series run. This value was selected to match the average potential temperature at the end of the resolution L in those simulations, as the resolution M simulations were still ongoing at the time of setup. Given that this difference is only about 1 K, it is not expected to introduce any qualitative changes to the dynamical properties.

To reduce the simulation time required, it was initialised using the state (velocity, temperature, and tracer fields) from the end of the M1 run. As a result, the simulation commenced directly at resolution M and was integrated forward for 20,000 days. This approach builds upon insights from previous test runs under similar configurations, which indicated that such a strategy could significantly reduce spin-up time while preserving dynamical consistency.

Evidence for the approach to equilibrium is shown in Fig. 3.29. After an initial phase of rapid adjustment, the kinetic energy density stabilises, suggesting that the system has reached a quasi-steady state. As in previous simulations, the net TOA flux exhibits slow temporal evolution. However, in contrast to the F-series runs where the net flux typically decays with time, the deep adiabat case shows a gradual increase toward the end of the integration period. We did not continue the simulation beyond this point for the same reason discussed in Section 3.2.2.

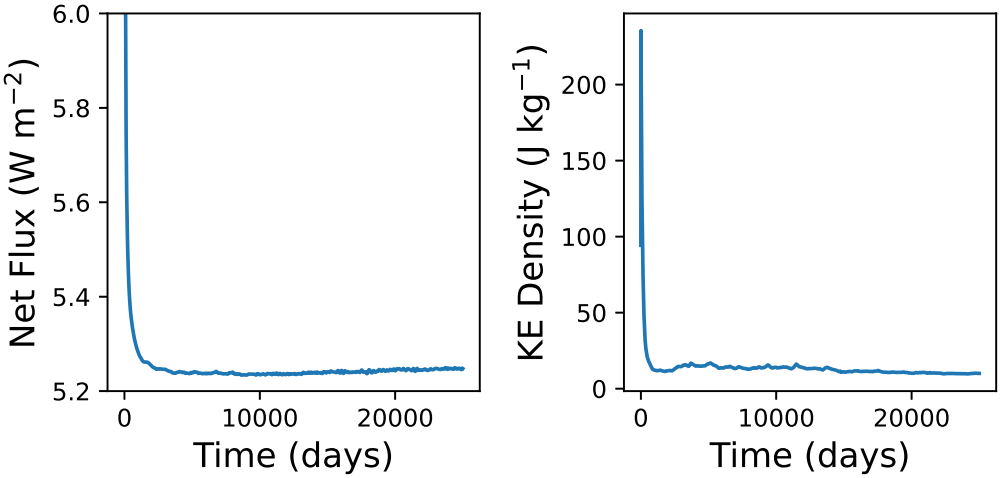


Figure 3.29: Net outgoing top-of-atmosphere fluxes (left) and kinetic energy densities (right) over time for the deep adiabat run.

3.5.2 Zonal and Meridional Flow

Fig. 3.30 shows the zonal-time mean of the zonal velocity in the deep adiabat simulation. The latitudinal–vertical structure features a pronounced prograde equatorial jet, with its peak velocity just off the equator. This jet closely resembles those in the F series, though it is weaker than those in the F series. The equatorial jet also splits into two jets at 0.3 bars and below 4 bars. In the polar region, the zonal wind remains relatively weak and dominated by retrograde jets. In the mid-latitudes, however, the zonal velocity approaches zero.

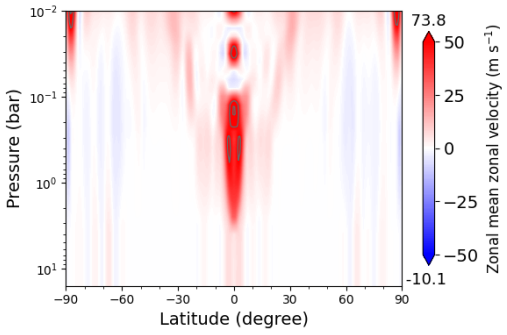


Figure 3.30: Zonal-time mean of the zonal velocity of the deep adiabat run, averaged over the last 100 d of the simulation.

The temporal evolution of the zonal winds at 1 bar is shown in the time–latitude diagram in Fig. 3.31. The off-equatorial jets are observed to gradually migrate toward the equator over time. In contrast, the jets in the polar region display less coherent migratory patterns. The difference in zonal jet profile and migration behaviour highlights the differing dynamical

regimes in the equatorial and polar regions.

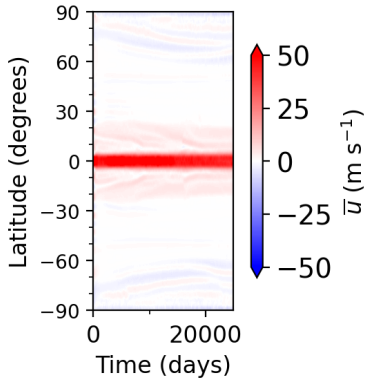


Figure 3.31: Time-latitude diagram of zonal mean zonal velocity at 1 bar of the deep adiabat run. The aspect ratio is the same as Fig. 3.2. Jets in the initial M1 state decay rapidly (within the first 100 days) and therefore do not persist on the timescales shown.

The Eulerian meridional streamfunction for the deep adiabat simulation, as shown in Fig. 3.32, reveals a circulation structure that differs significantly from that of the F-series runs. A clear vertical distinction exists in the circulation patterns above and below approximately 2–3 bars. Above this level, the northern hemisphere exhibits a clockwise overturning cell within about 20° of the equator, while a counter-clockwise cell emerges at latitudes poleward of 60°. The structure of the upper-level overturning is qualitatively consistent with the zonal-mean potential temperature distribution at comparable pressures (Fig. 3.34). However, as the potential temperature field reflects the combined effects of dynamical transport and thermal forcing, we do not interpret this as a purely thermally driven circulation. In contrast, the circulation below about 2–3 bar is more fragmented, consisting of multiple narrow cells in the form of thin strips. The overall circulation structure in this deeper region is more chaotic and lacks the large-scale coherence observed in the upper levels.

3.5.3 Temperature and Stability Structure

Fig. 3.33 shows the zonal-time mean temperature field for the deep adiabat simulation, averaged over the final 100 days. In the lower atmosphere, particularly at pressures greater than approximately 4 bar, the temperature distribution is remarkably uniform with latitude. To better illustrate the vertical and latitudinal variations in thermal structure, the zonal-mean potential temperature profiles at selected pressure levels are shown in Fig. 3.34.

From 4 to 16 bars, the potential temperature remains nearly invariant with both latitude

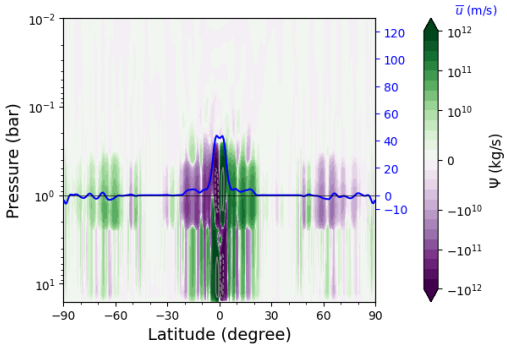


Figure 3.32: Eulerian meridional streamfunction at the end of the deep adiabat run. The plotting style follows that of Fig. 3.13.

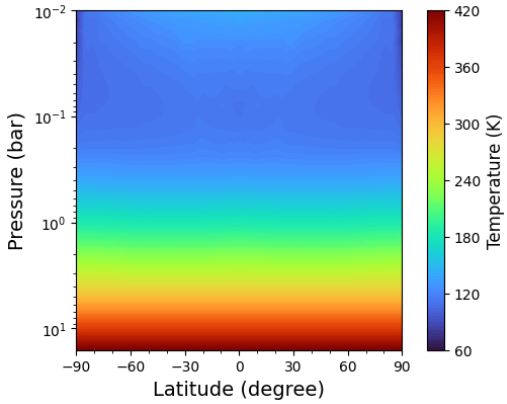


Figure 3.33: Zonal-time mean temperature at the end of the deep adiabat run.

and altitude, which is expected as the deep adiabat is constrained to a fixed temperature. In contrast, at lower pressure levels, the potential temperature varies significantly with latitude. It tends to be higher around the equator and near the poles, reaching a minimum near ±50° latitude. This latitudinal temperature gradient is consistent with the meridional circulation cell as discussed in Section 3.5.2. The rapid increase in potential temperature with decreasing pressure is most pronounced in the low- and mid-latitude regions. While for high latitude, a sharp increase in potential temperature is observed between 4 bar and 3.2 bar, corresponding to the cell centres of two adjacent pressure grid cells. The 3.2-bar level coincides with the water cloud deck, where condensation releases significant latent heat, driving this abrupt increase in potential temperature. This behaviour is also reflected in the dry buoyancy frequency shown in Fig. 3.35, where high positive values are observed in these regions. Above 3.2 bar, the increase in potential temperature at high latitudes becomes more gradual.

Fig. 3.35 shows the three zonal mean buoyancy frequencies discussed in Section 3.3.2 for the deep adiabat run. In the deep adiabat run, N^2 indicates a largely (dry) stable atmosphere

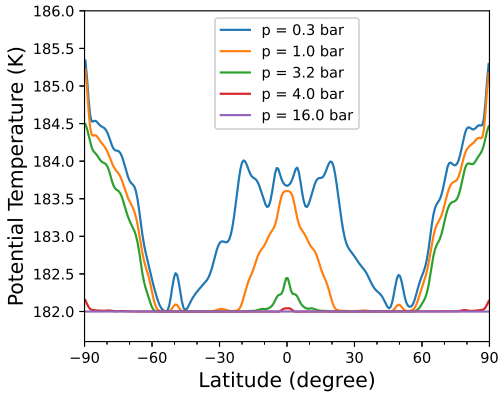


Figure 3.34: Zonal-time mean potential temperature of the deep adiabat run at different pressure levels at the end of the simulation.

between 1 to 3 bars. Compared to both F1 and F2 cases, the deep adiabat configuration exhibits greater overall stability, particularly in the polar regions, where it surpasses all runs of the F series in stability. The unstable region found below the water cloud base also appears more latitudinally uniform in this case.

N_L^2 in the deep adiabat run reveals a strong negative region spanning from 0° to 70° latitude at approximately 3 bar, peaking in magnitude near 50°. Compared to the broader and more diffuse patterns observed in F1 and F2, these strong negative values are more localised in latitude. Additionally, similar to the F1 simulation, a region of positive N_L^2 is seen near 4 bar around the pole, though in the deep adiabat run, this region is more intense and extends across a wider latitude range.

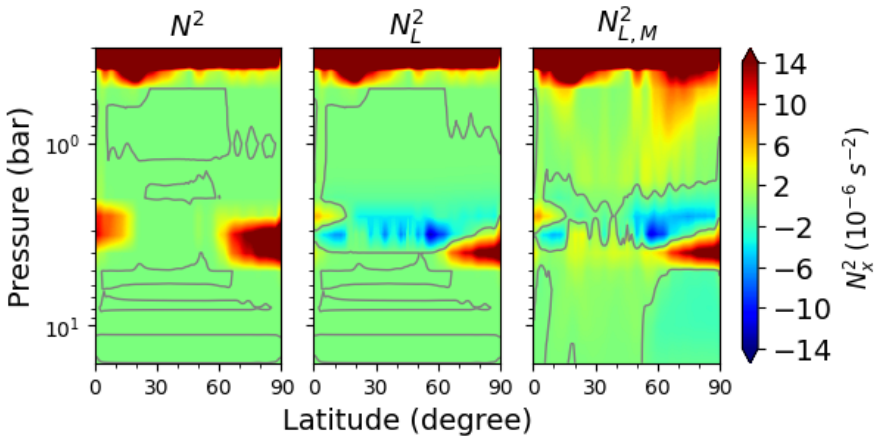


Figure 3.35: Static stability for the deep adiabat run. Left: dry case, middle: with latent heating, right: with latent heating and molecular weight.

As in the F series, the inclusion of molecular weight effects in $N_{L,M}^2$ enhances the atmospheric

stability above the cloud base. However, the stability below the cloud base exhibits a different pattern: it increases between 10° and 50° latitude while decreasing elsewhere. This diverges from the behaviour of run F2 to F5, in which $N^2_{L,M}$ remains negative almost uniformly below the water cloud. The contrasting behaviour can be attributed to differences in water cloud distribution (see Section 3.5.4). In particular, the deep adiabat simulation lacks water cloud in the mid-latitudes, which limits precipitation processes and consequently reduces water vapour enhancement below the cloud base, thereby suppressing the destabilising molecular weight gradient observed in the F series runs.

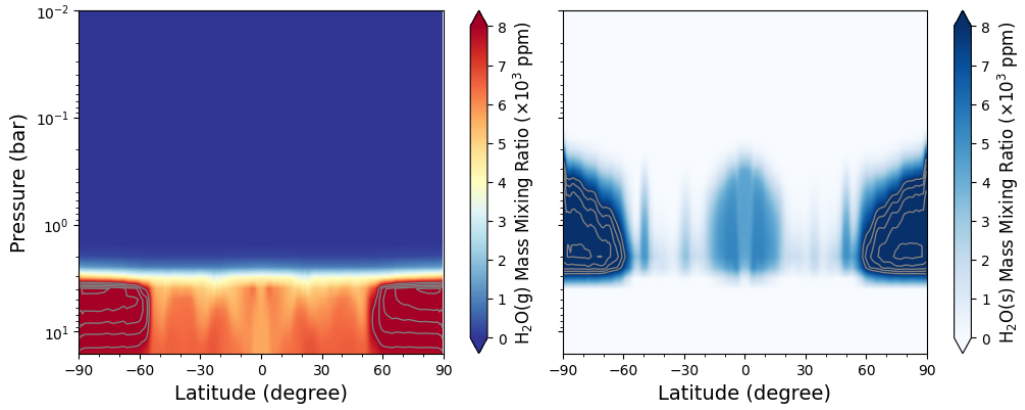


Figure 3.36: Time-zonal mean water vapour (left) and ice (right) mass mixing ratio at the end of the deep adiabat run. The grey contours are at 10^3 ppm increment for mass mixing ratio at and above the upper limit of the colour scale.

3.5.4 Water Distribution and Moist Convection

Water Distribution

Fig. 3.36 presents the 100-day averaged zonal-mean distribution of water vapour and ice mass mixing ratios for the deep adiabat simulation. Both vapour and solid phases of water are strongly concentrated in the polar regions, as highlighted by the grey contours. This behaviour is similar to the F1 case, although to a greater extent. The similarity between the deep-adiabat case and F1 suggests that the enhanced polar concentration of water cloud is unlikely to be controlled by temperature. Instead, it is more likely the result of the combined effects of large-scale transport and the cloud cycle, as discussed before. In this sense, the behaviour is qualitatively similar to tracer accumulation associated with Earth's Atlantic Meridional Overturning Circulation (AMOC), where large-scale overturning leads to nonlinear and regime-dependent tracer

storage rather than a simple thermodynamic response (e.g., *Buckley and Marshall* 2016; *Rahmstorf* 2002).

Elevated water cloud also appears in the equatorial region, albeit at a lower concentration. In this region, the enhancement in water vapour is confined to a few bars below the condensation level, consistent with the less concentrated water cloud. Aside from a few localised plumes, a pronounced depletion of water cloud is observed in the mid-latitudes, which aligns with the suppressed vertical motion in these regions, as shown in Fig. 3.32. The distribution of water vapour closely follows that of the condensed phase, with notably reduced vapour concentrations underlying depleted cloud regions. This depletion becomes narrower with increasing depth, indicative of mixing processes that gradually homogenise the vapour field.

TCAPE

Fig. 3.37 shows the zonal mean TCAPE as a function of latitude in the northern hemisphere. At Low Latitudes, TCAPE remains quite low, generally below 1 kJ kg^{-1}, and relatively flat with only small peaks around 18°. This suggests weak convective activities in the tropics. TCAPE dips at 30° - 40°, which is different from the plateau seen in the F series. TCAPE then increases with latitude and reaches a peak of approximately 3 kJ kg^{-1} at about 55°. At high latitudes, TCAPE increases sharply and non-linearly, exceeding 6 kJ kg^{-1} near the pole. This value is higher than the maximum TCAPE observed in the F series, i.e. 5 kJ kg^{-1} near the pole for run F1. These high values suggest very strong moist convection activity in the deep adiabat run. Overall, the region with high TCAPE coincides with the region of high water concentration as well as the region with low moist static stability (blue regions in the right panel of Fig. 3.35)

3.5.5 Lorenz Energy Cycle Analysis

Fig. 3.38 presents the latitude-pressure profiles of the contribution to the conversion terms in the Lorenz energy cycle for the deep adiabat simulation.

Like the F series run, $\hat{C}_Z$ (top right panel) exhibits a sequence of alternating positive and negative bands for the deep adiabat run. Similar to the F1 run, this pattern is tightly confined to the equatorial region. This suggests that the deep overturning circulation is also driving the equatorial jet under the deep adiabat setting.

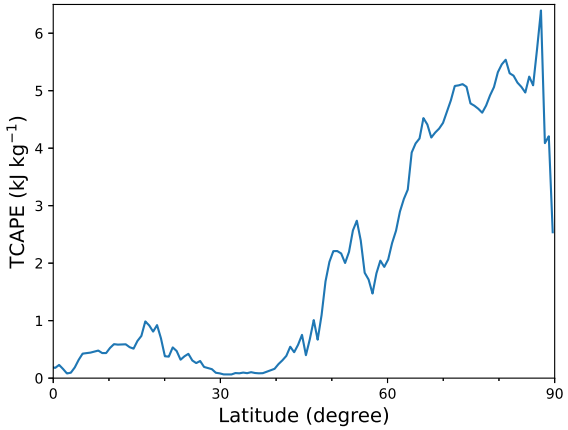


Figure 3.37: Time-zonal mean TCAPE as a function of latitude at the end of the deep adiabat run.

$\hat{C}_E$ (top left panel) is concentrated above the water cloud level and exhibits a strong positive signal in regions of the equatorial jet. Positive values are also observed at the low-latitude and high-latitude jets. This suggests that moist convection still plays a role in driving eddy activity locally, although its intensity is much diminished.

The $\hat{C}_K^{(1)}$ term (bottom left) shows small-scale alternating structures across the globe and is weak except near the equator, where it is positive on the flank of the equatorial jet and at the peak of the off-equatorial jets. The full $\hat{C}_K$ term (bottom right) is also strongest in the equatorial region, with mostly negative values. The global mean value of C_K is negative, indicating that the mean kinetic energy is converting to eddy component in this regime.

Overall, the magnitudes of all conversion terms are substantially lower compared to those in the F series simulations, both locally and for the global average as summarised by the box diagram in Fig. 3.39. This reduction is consistent with the observed weakening of the zonal jets and the disappearance of the mid-latitude jet, as previously discussed. The primary driver of this suppression appears to be the inhibition of baroclinic instability under the deep adiabat conditions. The equatorial jet is primarily maintained by the deep meridional overturning circulation and therefore persists in this setup.

3.5.6 Equivalent Heat Flux

To assess where the deep adiabat run fits within the a_f parameter spectrum, we compute the equivalent interior heat flux required to sustain the simulated thermal structure. This is separated into two components: a radiative component and a convective component.

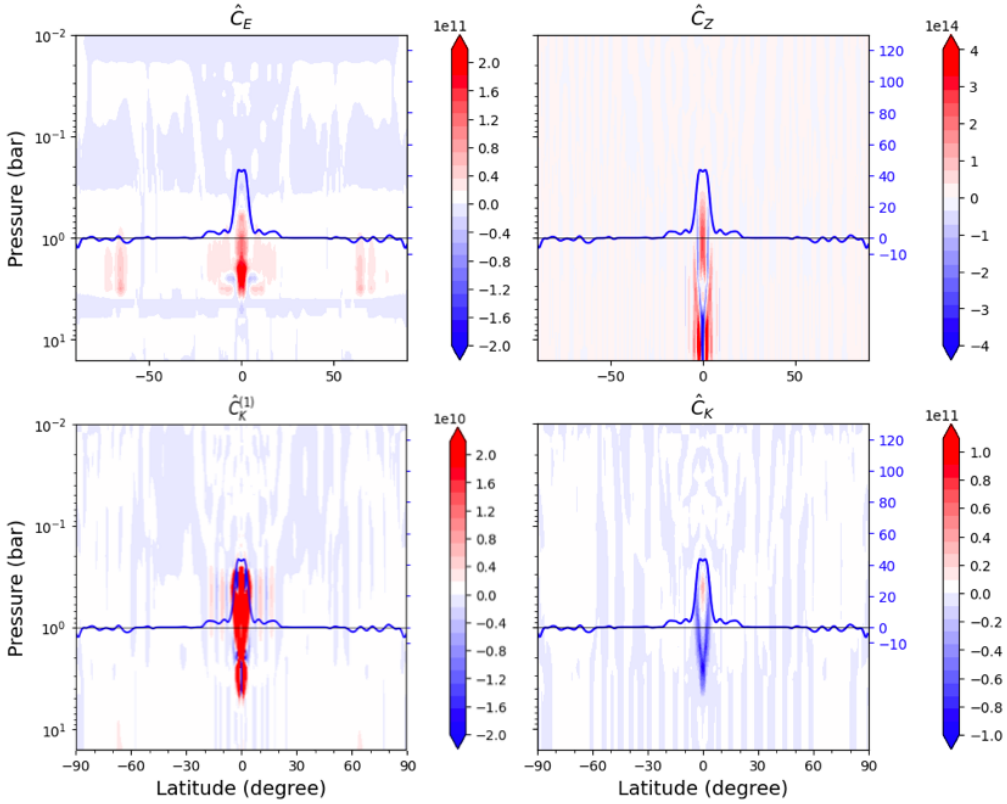


Figure 3.38: Latitude-Pressure profile of the conversion terms of the Lorenz energy cycle for the deep adiabat run: top left: C_E, top right: C_Z, bottom left: first term of C_K, bottom right: full C_K term.

The radiative component of the equivalent heat flux is obtained by examining the net upward longwave flux at the bottom boundary, as calculated by the radiative scheme. Equating Eq. (2.17) and Eq. (2.26) gives

$$F_{equiv,R} = \sigma T_1^4 - F^{\downarrow}_{\mathrm{S},\tilde{1}} - F^{\downarrow}_{\mathrm{L},\tilde{1}}, \tag{3.30}$$

where T_1 is the temperature of the bottom layer, $F^{\downarrow}_{\mathrm{S},\tilde{1}}$ and $F^{\downarrow}_{\mathrm{L},\tilde{1}}$ are the downward shortwave and longwave fluxes at the bottom surface, respectively. As shown in Fig. 3.42, $F_{equiv,R}$ peaks at the poles and the equator, with a relatively flat profile across the mid-latitudes. This behaviour is consistent with the temperature distribution illustrated in Fig. 3.34, where the few layers immediately above the bottom boundary exhibit slightly lower temperatures at the equator and polar regions. The reduced local temperature results in diminished downward longwave radiative fluxes, thereby requiring a larger interior flux to sustain the same net upward flux. The magnitude of $F_{\text{equiv, R}}$ is very small, with a global mean value of 0.33 W m^{-2}, implying that the interior heat flux is mainly in the form of convective heat flux. The peak-to-trough

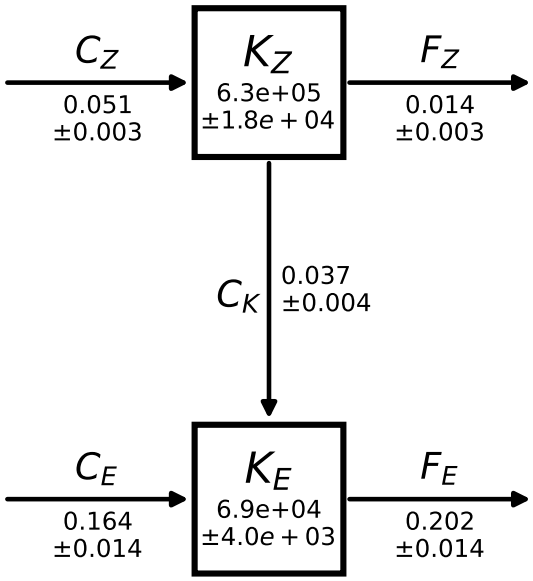


Figure 3.39: Lorenz energy cycle box diagram for the deep adiabat run. Numbers in boxes represent globally average energy (in J m^{-2}), Arrows represent globally averaged conversion rates (in W m^{-2}).

variation is about 0.05 W m^{-2}.

The convective component of the equivalent interior heat flux arises from the imposed relaxation of potential temperature toward a prescribed deep adiabat within convectively unstable columns. This process effectively adds (or removes) enthalpy from the column.[4] The convective contribution to the interior heat flux is computed as

$$F_{equiv,C} = \frac{c_p \delta\theta}{g \tau_{dryconv}} \sum_{i}^{conv} \Pi_i \Delta p_i, \tag{3.31}$$

where $\delta\theta = \theta_{1,\text{ stable}} - \theta_{\text{deep}}$ is the difference between the enthalpy-conserving neutrally stable potential temperature and the deep adiabat, and superscript *conv* indicates summation is taken over the vertical extent of convective columns.

Fig. 3.42 shows the time–zonal mean of $F_{\text{equiv,C}}$. The flux increases with latitude and exhibits significant local maxima at low and high latitudes. While these high-latitude spikes appear to align with zonal wind features, this region is subject to the influence of the polar filter

[4] In principle, the enthalpy change can be positive or negative under this setup. The imposed θ_{deep} is higher than the value expected under radiative-convective equilibrium in the absence of interior heating. As such, the convective relaxation predominantly increases the column's enthalpy. This is indeed the case for most of the latitude in the analysed time window, where the equivalent convective heat flux is consistently positive. Within a few degrees around the equator, however, the equivalent convective heat flux can become negative locally. The zonal mean value, however, is always positive for the analysed period.

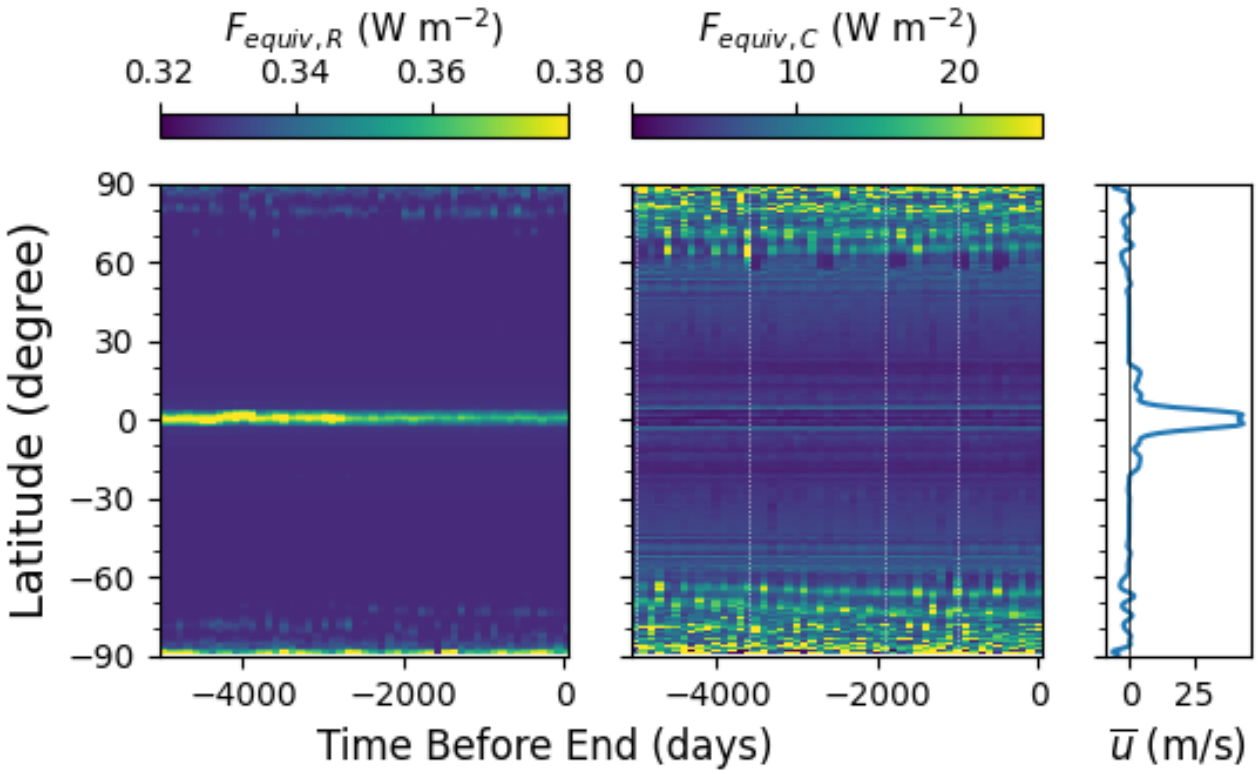


Figure 3.40: Time–latitude diagrams showing the zonal mean radiative component ($F_{\text{equiv},R}$, left) and convective component ($F_{\text{equiv},C}$, centre) of the equivalent heat flux, alongside the zonal mean zonal wind ($\overline{u}$, right) at the end of the simulation. The heat flux components are displayed using pixel shading to represent the value at each latitude and time step, rather than colour contours. White dotted vertical lines indicate time slices in Fig. 3.41.

and is thus excluded from detailed interpretation. At mid-latitude, $F_{\text{equiv, C}}$ increases smoothly with latitude. The global mean value of $F_{\text{equiv,C}}$ is 5.11 W m^{-2}, with a standard deviation of 0.17 W m^{-2} across multiple temporal snapshots. Notably, the convective heat flux shows substantial variability in both time and longitude, as demonstrated in Fig. 3.40 and Fig. 3.41, where transient hotspots can be more than ten times of the mean value. At high latitude, the heat flux anomaly has a wave-like structure, while at mid and low latitude, it is organised into patches.

The total equivalent interior heat flux, combining both radiative and convective contributions, is therefore $F_{\text{equiv,Tot}} = F_{\text{equiv,R}} + F_{\text{equiv,C}} = 5.44$ W m^{-2}, which is approximately two standard deviations lower than the globally averaged interior heat flux specified in Section 3.2.1. This discrepancy is justifiable, as the temperature of the deep adiabat chosen in this simulation is lower than the global average value in the RCM.

Fitting the calculated $F_{\text{equiv, Tot}}$ to Eq. (3.1) is challenging due to the presence of sharp

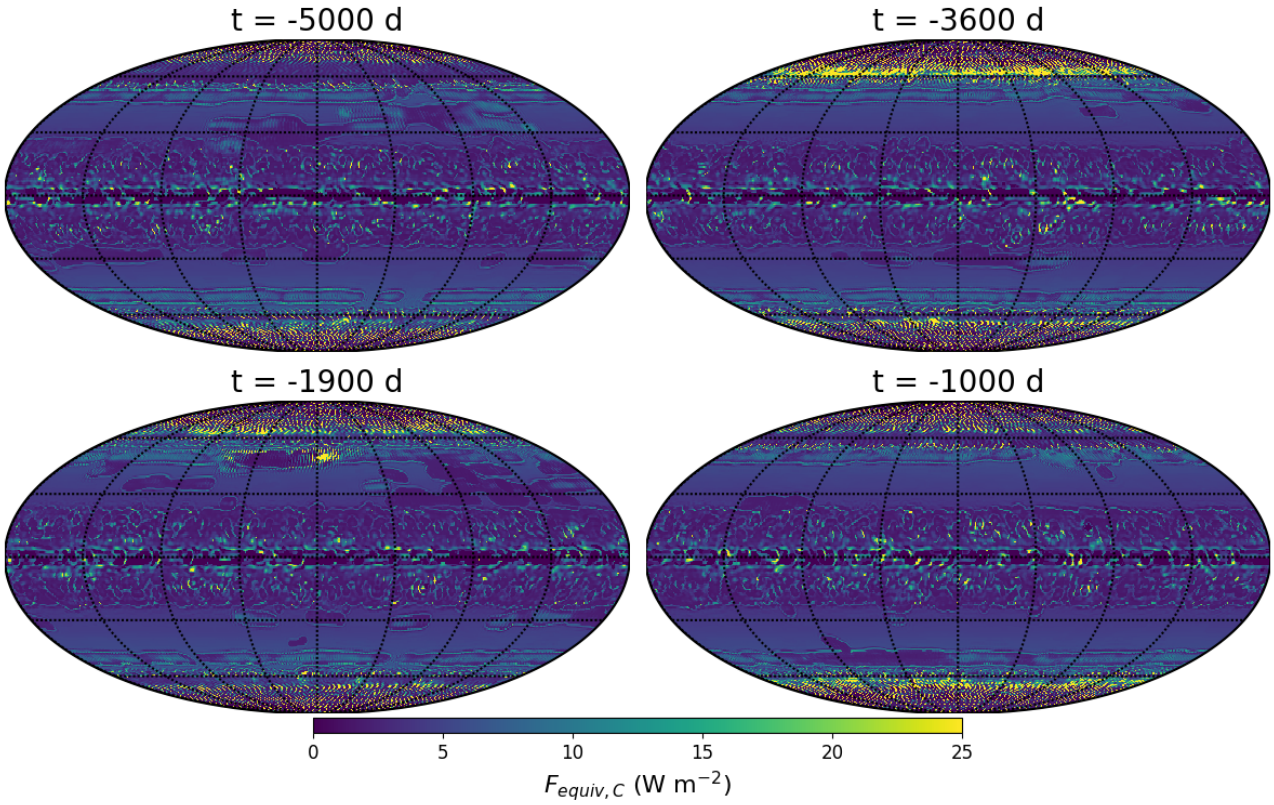


Figure 3.41: Mollweide projections of the equivalent convective heat flux, $F_{\text{equiv},C}$, at four different time slices during the deep adiabat simulation: $t = -5000$ d, $t = -3600$ d, $t = -1900$ d, and $t = -1000$ d. The time slices are also indicated as the white dotted line in Fig. 3.40.

flux spikes at high latitudes. The results from three different fitting ranges, along with their associated uncertainties, are summarised in Table 3.2, and the corresponding fitted flux profiles are shown in Fig. 3.42.

The fit over the full latitudinal domain captures all available data, but it is heavily influenced by anomalous behaviour in the polar and equatorial regions. The resulting value of a_f exceeds that used in run F1, indicating that such a profile would likely not yield a uniform bottom temperature. Restricting the fitting to $|\phi| < 60°$ mitigates these edge effects while still retaining a broad latitudinal range for analysis. The most robust result, however, is obtained when the fit is limited to the mid-latitudes ($25° < |\phi| < 45°$), as this region exhibits relatively smooth variations in $F_{\text{equiv, Tot}}$. This is further supported by lower RMS errors and smaller standard deviations in the fitted parameters.

Based on these considerations, the estimate of $a_f = 8.28$ W m^{-2} from the mid-latitudes fitting scenario is considered the most reliable. To ensure consistency with the global mean interior heat flux of 5.7 W m^{-2} used in the F-series simulations, the corresponding value of b_f

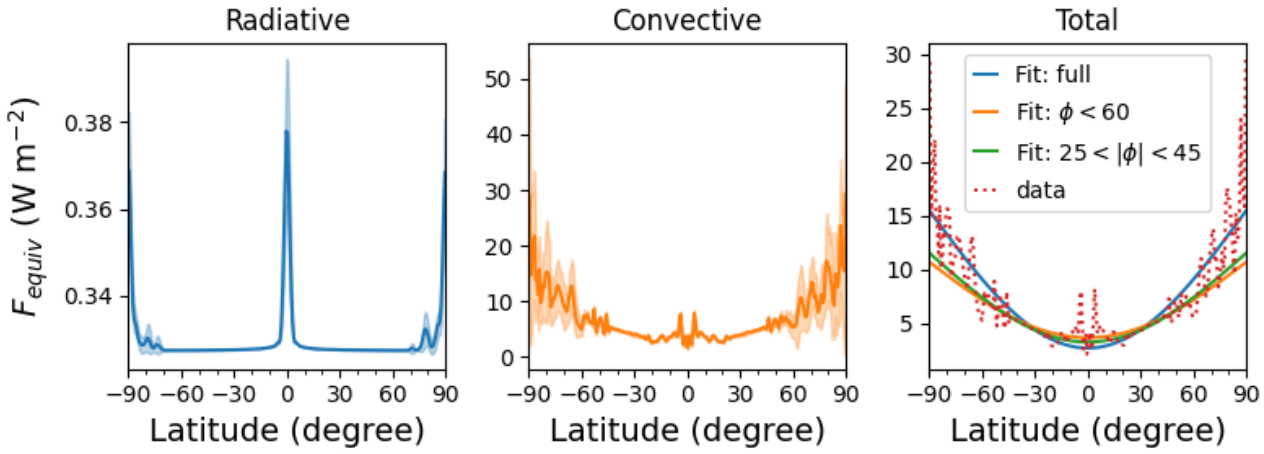


Figure 3.42: Time-zonal mean of the equivalent interior heat flux as a function of latitude. Left: radiative component (defined in Eq. (3.30)), middle: convective component (defined in Eq. (3.31)), right: total, where the dotted line is the calculated value and the solid lines are profiles obtained from fitting Eq. (3.1) to different latitude ranges. The shaded region in the left and middle panels represents the 1 standard deviation.

should be recalibrated to 11.22 W m^{-2}. We stress that these values are not intended to define a physically realistic deep interior heat-flux profile, but rather to facilitate comparison between the deep-adiabat simulation and the prescribed-flux experiments within a unified parameter framework.

More generally, this analysis highlights that even when the deep temperature is constrained to be horizontally uniform, the resulting equivalent interior heat flux exhibits substantial latitudinal structure. Achieving a strictly isothermal deep boundary is therefore not expected by a prescribed heat flux profile alone. While a simulation using the interior heat flux profile inferred from the equivalent flux would be an interesting numerical comparison with the deep-adiabat case, it would not reflect the observed thermal emission profile originating in the upper atmosphere and is therefore beyond the scope of this work.

Fit Scenario	a_f	σ_{a_f}	b_f	σ_{b_f}	RMS Error	Global Mean Flux
$\lvert\phi\rvert < 90$	12.79	0.45	15.49	0.32	2.19	5.44
$\lvert\phi\rvert < 60$	7.03	0.45	10.69	0.38	0.87	5.17
$25 < \lvert\phi\rvert < 45$	8.28	0.30	11.54	0.24	0.12	5.04

Table 3.2: a_f and b_f parameters and the error metrics obtained through fitting the calculated total equivalent interior heat flux, $F_{\text{equiv, Tot}}$, for various latitudinal ranges of the total equivalent flux. The parameters a_f and b_f are defined in Eq. (3.1). Their uncertainties, σ_{a_f} and σ_{b_f}, are obtained from the covariance matrix of the least-squares fit. The RMS error denotes the root mean square deviation between the fitted and calculated flux values over the corresponding latitudinal range, and the global mean flux is computed by integrating Eq. (3.1) using the corresponding a_f and b_f.

3.6 Discussion and Conclusion

This chapter has explored the sensitivity of Jovian-like atmospheric dynamics to the thermal boundary conditions at the bottom. Specifically, we imposed a latitudinally varying internal heat flux profile based on observational estimates by P84, and systematically varied the strength of the latitudinal gradient through the parameter a_f. The imposed flux gradient directly modifies the latitudinal temperature gradient, with larger values of a_f resulting in smaller equator-to-pole temperature contrasts. In particular, the case based on the original P84 profile (F1) produces a reversal of the usual gradient, resulting in a polar region warmer than the equator. A simulation using the deep adiabat setting is therefore performed to create a case where there is no temperature gradient from equator to pole. The equivalent interior heat flux profile of this simulation is also calculated to contextualise this simulation within the a_f spectrum.

The jet dynamics are strongly influenced by the imposed flux profile. As a_f increases, the mid-latitude jets become progressively weaker, and in the deep adiabat case, they disappear altogether. F1 shows markedly different behaviour from all other cases, including the development of retrograde mid-latitude jets and reversed meridional circulation. Meanwhile, the kinetic energy decreases with increasing a_f, with both the zonal and eddy components reaching their lowest values in the deep adiabat simulation. The equatorial jet persists in all cases, although its strength and vertical extent vary with the thermal boundary condition. The imposed heat flux also affects the temporal evolution of the jets. Higher a_f values reduce the equatorward migration rate of the jets, but are insufficient to stop this migration.

Analysis of the Lorenz energy cycle shows that the inhibition of baroclinic instability, associated with reduced meridional temperature gradients, is the main cause of reduced eddy activity and the eventual breakdown of mid-latitude jets. This is indicated by the reduced values of C_K in simulations with high a_f. In contrast, the equatorial jet is maintained across all configurations. The behaviour of the C_Z term suggests that it is likely to be driven by Hadley-like overturning circulation and eddy momentum convergence in the weather layer.

We did not perform a detailed assessment of dynamical stability using linear theory. Many classical criteria, such as the Charney-Stern condition, require positive static stability (i.e. $N^2 > 0$), which is not satisfied in any of our simulations. Furthermore, it should be stressed

that most linear stability criteria provide only necessary, not sufficient, conditions for instability. As such, their diagnostic utility is limited in moist, highly non-linear systems like those explored here.

The bottom thermal condition also affects water distribution. While the global mean vertical profiles of water vapour and ice remain relatively unchanged across simulations, the spatial distribution of water clouds is sensitive to a_f, with increased cloud concentrations observed at low and mid-latitudes as the flux gradient increases. This trend no longer holds when the latitudinal temperature gradient is reversed. Instead, for the deep adiabat run and F1, increased water vapour and cloud are observed in the polar region. The changes in cloud distribution are accompanied by a decrease in moist static stability with increasing a_f, However, the deep adiabat case does not follow this trend, possibly due to its slightly higher globally averaged temperature.

The equivalent interior heat flux diagnosed from the deep adiabat run exhibits a structure that closely mirrors the functional form prescribed in the F-series simulations. If sharp localised peaks at high latitudes are ignored, the overall time-zonal mean heat flux shows qualitative agreement with the latitudinal distribution imposed in the F-series. Fitting this profile to the same functional form and normalising to the global mean interior heat flux yields fitted parameters of $a_f = 8.28$ W m^{-2} and $b_f = 11.22$ W m^{-2}, placing it near the upper end of the F-series parameter range between F1 and F2. However, unlike the imposed radiative fluxes in the F-series, the diagnosed flux in the deep adiabat run is primarily due to convective adjustment.

Together, these results demonstrate that the specification of the internal heat flux plays a central role in shaping the thermodynamic structure and global circulation of a Jupiter-like atmosphere. Further work is needed to explore alternative formulations of the internal heat flux and the implications of deep adiabat configurations. While the functional form of the internal heat flux used in this study is motivated by observations from P84, it is extrapolated beyond 50° latitude. It is also by no means unique. For example, *Aurnou et al.* (2008) implemented a third-order polynomial fit to the heat flux resulting from their model. Such a profile can allow for hemispheric asymmetry in the internal heat flux. In addition, belt-zone scale variations in the heat flux have been proposed, possibly related to atmospheric oscillations (see e.g., *Hori et al.* 2023). The deep adiabat setup used in this chapter also has certain limitations. Given the vertical extent of the model, the imposed forcing may be unrealistically strong, potentially

exaggerating the dynamical response. In addition, observations have not yet confirmed the existence of a true 'deep thermostat' in Jupiter's atmosphere, and the applicability of this assumption remains uncertain. A fuller discussion of these issues, including their implications for observational interpretation and the overall realism of the JasonGCM, will be presented in Chapter 6.

Chapter 4

Mushball Parameterisation and Its Effect on Two-dimensional Simulations

4.1 Introduction

Guillot et al. (2020a, hereafter G20a) proposed a novel mechanism to explain the observed ammonia depletion in Juno and ground-based telescopes (see Section 1.3.3 for a detailed discussion). This is based on the hypothesis that relatively dense and massive hailstones, which consist of a water-ammonia mixture, tend to form preferentially inside intense moist convective clouds. They can form when moist convective storms lift a water ice particle to an altitude of about 1.5 bar. The initial water ice nucleus may melt due to the adsorption of ammonia, and then may start to accumulate ammonia solution and water ice particles. As it ascends further, it accretes H_2O-NH_3 solid and H_2O ice, forming an ice shell surrounding the liquid core. As it grows in size, it starts to fall, scavenging more water and ammonia on the way. When it crosses the water cloud, water ice accumulates on its surface, forming a shell of ice. This shell then melts and evaporates below the cloud, cooling the surrounding air. This forms an evaporative downdraft, allowing the H_2O-NH_3 core to sink to a greater depth. The requirement for water ice seeds from moist convection could potentially explain why belts, where lightning and hence moist convection storms are more prevalent, are slightly more depleted in ammonia than zones.

This hypothesis provides a plausible explanation for the observed depletion of ammonia in Jupiter's atmosphere, as demonstrated by the simplified model in *Guillot et al.* (2020b, hereafter G20b). However, this process does not act in isolation: the formation and downward transport of mushballs also transports water from the upper atmosphere, thereby altering the vertical distribution of condensible species. As water is a primary driver of moist convection, changes in its concentration directly impact moist convective activity. This, in turn, may affect the large-scale circulation. This introduces a non-trivial feedback loop, requiring a model that treats atmospheric dynamics, moist convection, and mushball formation within a self-consistent framework to test this hypothesis properly.

A GCM provides such capability by allowing the co-evolution of tracers, clouds, and circulation. Moreover, within a GCM, we can evaluate the contributions of different dynamical processes, such as moist convection, large-scale overturning circulation and eddy transport, to the distribution of tracers.

We developed a flux-based parameterisation scheme for the mushball based on G20b and G20a for the JasonGCM. In this approach, mushballs are not represented as explicit Eulerian tracers with prognostic advection and sedimentation. Instead, their effects are incorporated through diagnosed vertical mass flux and associated tendencies. Ideally, the mushball phase should be treated as a precipitate with a finite sedimentation velocity and allowed to evolve within the model. However, the fast-falling mushball would limit the timestep in the GCM. The required timestep for the model to resolve the falling of the mushball can be estimated using the mushball characteristics as shown in Fig. 3 of G20a. In the intermediate case with an upper atmosphere water ice abundance of 600 ppmv, a mushball can traverse approximately 0.004 of the pressure scale height per second. This implies that a mushball would fall through a typical Jason grid of 0.23 ln(bar) within 58 seconds, which is significantly shorter than the 300-second timestep for the middle resolution runs. Even in the case of 100 ppmv, where mushball falls slowest, it takes 77s for mushball to fall through one layer. As a result, representing mushballs as explicit Eulerian tracers would require substantial timestep reduction. Therefore, we refrain from adopting this approach at this stage.

As a first step, in this chapter, we present the parameterisation scheme developed to represent the effects of mushball formation and evolution on condensible distribution and apply it in a series of two-dimensional simulations. These simulations offer a computationally efficient way for exploring the impact and sensitivity of uncertain parameters on tracer transport and convective structure. The remainder of this chapter is organised as follows. In Section 4.2, we present the parameterisation scheme used. Section 4.3 describes the setup for the two-dimensional model and the simulation sets. In Section 4.4, we compare the results of the nominal mushball case and the case without the mushball. Section 4.5 explores the sensitivity to mushball parameters, while Section 4.6 shows the effect of changing the temperature profile. Finally, we summarise these results and their relevance to three-dimensional modelling in Section 4.7.

4.2 Mushball parameterisation scheme

The schematic model of G20b for mushball formation and evolution discusses the proposed mechanism in terms of five distinct layers of the atmosphere, in which different processes occur. Since these five layers may correspond to more than one grid layer of a GCM (with the exception that the deep layer corresponds to the lowest grid layer), it is evident that a change in terminology is needed to distinguish these two types of layers. From this point onwards, the layers in G20b will be designated as 'regions'.

We consider that mushball forms at an altitude that corresponds to the upper region and the mushball seed region of G20b. Once formed, the mushball descends through the water cloud region. Below the water cloud, the mushball starts to evaporate. Some of the water in the mushball phase may then be lost in the downdraft region, but most of the ammonia and water content would continue to sink in the form of an evaporative downdraft, within which drier environmental air may be entrained. After reaching the deep region, all water and ammonia would evaporate and mix with the environment. For convenience, we will use 'mushball-related mass flux' to describe the mass flux of mushball and the evaporative downdraft forms after it starts to evaporate. The major processes involved and their correspondence to layers of G20b are shown in Fig. 4.1. Symbols and parameters used in the derivation are summarised in Table 4.1.

4.2.1 The Source Term

Suppose that some mushballs originate from the kth vertical layer. This layer has a total mass, denoted by $\mathcal{M}^k$, a solid water mass mixing ratio w^k_{ice}, and an ammonia mass mixing ratio c^k. We assume that the mushball formation rate is proportional to the convective mass flux and limited by the availability of both ammonia and water. The rate at which ammonia is converted into mushballs, $\mathbb{s}_{c,k}$, is given by

$$\mathbb{s}_{c,k} = \varepsilon_{mush} \min\left\{ c^k - c_{crit},\, w^k_{avl} \frac{f_c}{f_w} \right\} \dot{M}^k_{conv}, \tag{4.1}$$

where f_c is the mass fraction of ammonia in the mushball, $f_w = 1 - f_c$ is the mass fraction of water, and ε_{mush} is a tunable parameter representing the mushball formation efficiency

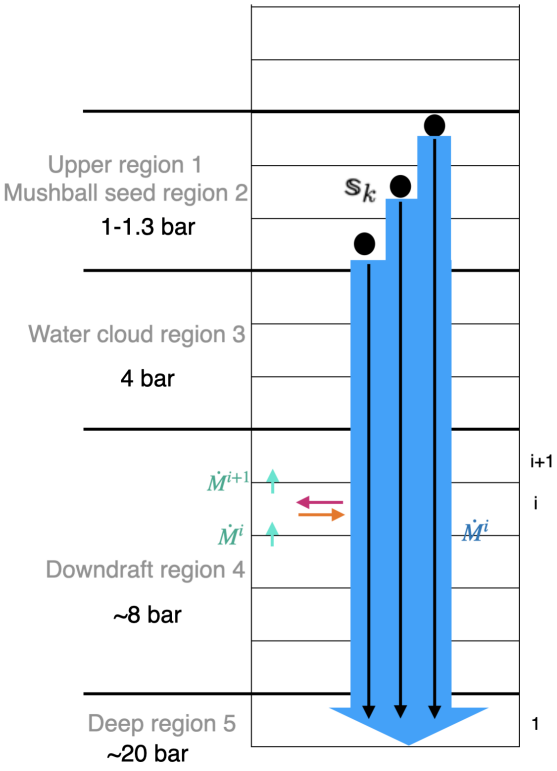


Figure 4.1: Schematic diagram of processes involved in mushball parametrisation. The label on the left corresponds to the region labels in G20b, and the pressure values indicate the approximate mean pressure of the region. The pressure levels associated with Regions 4 and 5 are largely unconstrained and should be regarded as indicative only. The labels on the right indicate the index of the vertical model layers.

$(0 < \varepsilon_{mush} < 1)$. The critical ammonia mass mixing ratio, c_{crit}, represents the threshold above which ammonia can participate in mushball formation. The term w^k_{avl} denotes the available water mass mixing ratio in layer k.

The value of c_{crit} is determined from thermodynamic equilibrium:

$$c_{crit} = \frac{p_{crit}}{k_b T} \frac{\mu_b}{\mu_c}, \tag{4.2}$$

where k_b is the Boltzmann constant, T is the temperature of the layer, μ_b and μ_c are the molar masses of the bulk atmosphere and ammonia, respectively. The term p_{crit} is the temperature-dependent equilibrium partial pressure of ammonia at the phase boundary between the NH_3-H_2O solution and the pure water ice.

We adopt a third-order polynomial fit for $\log_{10}(p_{crit})$, with coefficients derived from fitting the tabulated data in the International Critical Tables (*Council* 1930). A third-order polynomial was selected because increasing the order of the polynomial beyond three (up to fifth order) yields negligible improvement in accuracy. Given the larger uncertainties present in

Symbol	Meanings
x	Generic label for water (w) or ammonia (c); their mass mixing ratio
c_{crit}	Minimum ammonia mass mixing ratio required for mushball to form
f_x	Fraction of water ($x = w$) or ammonia ($x = c$) in mushballs
ε_{mush}	Efficiency of mushball formation
$\mathcal{M}^i$	Mass of layer i
$\mathbb{s}_k$	Rate of mushball formation in layer k
$\mathbb{s}_{x,k}$	Rate of water or ammonia being converted into mushball in layer k
$\dot{m}_k^i$	Mushball-related mass flux (mushball + downdraft) through face i for mushball formed in layer k
$\dot{m}_{x,k}^i$	Mushball-related mass flux of x through face i due to mushball formed in layer k
$\dot{M}^i$	Total mushball-related mass flux through face i
$\dot{M}_x^i$	Total mushball-related mass flux of water or ammonia through face i
a_x^i	Fraction of water or ammonia detrained to environment from downdraft in layer i ($a_c^i = 0$ for $i > 1$, $a_x^1 = 1$)
ϵ^i	Fraction of air entrained to mushball-induced downdraft in layer i
G_x^i	Mass mixing ratio tendency of x in layer i

Table 4.1: List of symbols used in the mushball scheme.

other parts of the scheme, the relative error in p_{crit} of less than 2% for the third-order fit is acceptable.

We also impose temperature bounds for mushball formation, requiring $-110°\text{C} \leq T \leq -20°\text{C}$. This reflects the physical range within which the NH_3-H_2O solution can coexist with pure water ice. In practice, however, mushball formation is more often constrained by the local concentrations of ammonia and water than by the upper temperature limit, since the equilibrium vapour pressure increases rapidly with temperature.

w_{avl}^k is computed by subtracting the part of the water mass that has already been consumed for mushball formation in the layers above from the total mass of water available for mushball formation, w_{avl}, i.e.,

$$w_{avl}^k = w_{avl} - \sum_{i=k+1}^{t} \mathbb{s}_{w,i} / \dot{M}_{conv}^i, \tag{4.3}$$

where

$$\mathbb{s}_{w,k} = \mathbb{s}_{c,k} \frac{f_w}{f_c}. \tag{4.4}$$

is the water source term associated with mushball formation, and

$$w_{avl} = \sum_{i=b}^{t-1} q_u^i - q_u^{i+1} = q_u^b - q_u^t \tag{4.5}$$

represents the total amount of water condensed throughout the updraft. Ideally, w_{avl} should reflect the water ice mixing ratio within the convective plume. However, our moist convection scheme does not explicitly track water ice within the plume. Instead, it assumes that any condensed water immediately falls to the base of the plume and re-evaporates. Consequently, the total water condensation within the updraft is used as a proxy here. This differs from the approach taken in G20b, in which the water mass mixing ratio within the cloud region is used directly.

The total mushball source term, representing the mass of mushballs formed per unit time, is given by

$$\mathbb{s}_k = \mathbb{s}_{c,k} + \mathbb{s}_{w,k}. \tag{4.6}$$

4.2.2 Mushball Related Mass Flux

In general, the mushball-related mass flux may evolve as it passes through grid level i: it can gain mass via local mushball formation, lose mass through detrainment, or be entrained by ambient air. The flux through the lower cell face $\tilde{i}$ is related to that through the upper face $\tilde{i}+1$ by

$$\dot{M}^i = (1+\epsilon^i)\dot{M}^{i+1} - a_w^i \dot{M}_w^{i+1} - a_c^i \dot{M}_c^{i+1} + \mathbb{s}_{c,i} + \mathbb{s}_{w,i}, \tag{4.7}$$

where ϵ^i is the entrainment coefficient, representing the fractional mass of ambient air entrained into the downdraft within layer i. The parameters a_w^i and a_c^i denote the fraction of water and ammonia mass, respectively, detrained into the environment at level i. These are tunable parameters of the scheme.

We define the mushball-related ammonia or water mass flux as

$$\dot{M}_x^i = (1-a_x^i)\dot{M}_x^{i+1} + x^i \epsilon^i \dot{M}^{i+1} + \mathbb{s}_{x,i}, \tag{4.8}$$

where the subscript x indicates either water ($x = w$) or ammonia ($x = c$), and x denotes the corresponding mass mixing ratio.

The downward transport of mass by the mushball-related flux induces a compensating updraft. Mass conservation within pressure coordinates requires that the total mass in each

layer remains constant. Thus, the compensating mass flux must satisfy

$$\dot{m}^{i\prime} \equiv \dot{m}^{i-1\to i} = \dot{m}^{i}. \tag{4.9}$$

4.2.3 Tendencies

To compute the ammonia and water mixing ratio tendencies due to mushball processes, we consider two contributions: the effect of mushball fluxes from layers above and the formation of mushballs within the current layer.

The tracer tendency due to the mushball flux from the layer above must account for the entrainment of ambient tracer into the downdraft, detrainment of tracer into the environment, and the effect of compensating mass fluxes entering from below and exiting from above. This yields

$$\mathcal{M}^i G_x^i\Big|_{above} = +a_x^i \dot{M}_x^{i+1} - x^i \epsilon^i \dot{M}^{i+1} + x^{i-1}\dot{M}^i - x^i \dot{M}^{i+1}. \tag{4.10}$$

In addition, the formation of mushballs within the layer contributes to the tracer tendency in two ways: by removing tracer species from the environment, and by inducing a compensating updraft. This contribution is provided by

$$\mathcal{M}^i G_x^i\Big|_i = x^{i-1}\dot{m}_i^i - \dot{m}_{x,i}^i = x^{i-1}\dot{m}_i^i - \mathbb{s}_{x,i}. \tag{4.11}$$

Summing both contributions, the net tracer tendency is

$$\mathcal{M}^i G_x^i = x^{i-1}\dot{M}^i - x^i \dot{M}_x^{i+1} - x^i \epsilon^i \dot{M}^{i+1} + a_x^i \dot{M}^{i+1} - \mathbb{s}_{x,i}. \tag{4.12}$$

This expression, in conjunction with Eqs. (4.1), (4.4) and (4.6) and the associated parameters, defines our mushball parameterisation scheme.

4.2.4 Choice of Default Parameters

Our scheme involves the following tunable parameters: ε_{mush}, f_x, a_x and ϵ. where a_x and ϵ may have different values in different vertical layers. This subsection explains the rationale for the default choices of these parameters and discusses their relationship to the values reported in G20b.

Based on the evolution model of G20a, G20b adopted a fiducial value of $\varepsilon_{mush} = 0.3$ in their model, which we also use as our default. However, we note that this value may overestimate the appropriate value for our context, since G20b considered thunderstorms, which are the most vigorous moist convective events and would occur less frequently than the more typical moist convection in our model. Nonetheless, in the absence of further observational or theoretical constraints, we adopt this value provisionally.

The fraction of ammonia in the mushball, determined by f_c, can be set based on the compositional evolution model of G20a. We adopt the default values $f_c = 0.1$ as used by G20b. This gives the water fraction $f_w = 0.9$. These values are more representative of the water-rich composition observed in the cloud region. Adopting a composition more similar to that found in the formation region would be justifiable if additional source terms in the water cloud were explicitly included. However, such a choice could lead to overdepleting ammonia and underrepresenting water transport in the formation region. Our selection can be interpreted as compensating for the lack of mushball growth in the water cloud, a process explicitly treated in the evolution model of G20a but omitted in our simplified scheme.

Determining the default vertical profiles for a_x and ϵ is more challenging, as these depend on the poorly constrained microphysical properties of melting mushballs and evaporative downdrafts. Nevertheless, the setup of this scheme imposes some constraints. We set $a_x^1 = 1$ and $\epsilon_1 = 0$, reflecting the full evaporation of mushballs and the absence of entrainment at the model bottom. In the mushball formation and water cloud regions, where no evaporation occurs, we set $a_x^i = 0$. Assuming no entrainment before evaporation begins, we also set $\epsilon^i = 0$ in these regions. G20b assumed no loss of ammonia in the downdraft region, corresponding to $a_c^i = 0$ for $i > 1$. Their treatment of water removal in the downdraft can be related to our a_w^i profile. In the limit of negligible entrainment, as assumed in their analytical solution, the total water flux due to mushball reaching the bottom layer is

$$\begin{aligned} \dot{M}_w^2 &= (1 - a_w^2)\dot{M}_w^3 \\ &= \Big(\prod_{i=2}^{l_0-1}(1 - a_w^i)\Big)\dot{M}_w^{l_0} \\ &= A_w \dot{M}_w^{l_0}. \end{aligned} \tag{4.13}$$

where l_0 is the topmost layer where mushball formation happens, $A_w = \prod_{i=2}^{l_0-1}(1 - a_w^i)$ is the

total fraction of water deposited in the downdraft region. This quantity is analogous to the parameter a_w in G20b. Given that our model domain only extends to 18 bar, which corresponds to approximately the midpoint of the downdraft layer in G20b, we assume that no entrainment or evaporation occurs except at the bottom layer of the model, where all mushballs are assumed to evaporate completely. This is justified in cases with a small ventilation factor, as discussed in G20a, where mushballs can penetrate deeply before evaporating. This assumption is further supported by the findings of *Markham et al.* (2023), who demonstrated that dense particles like the mushball can reach considerable depths before complete evaporation.

4.3 Model Setup

4.3.1 (Quasi) Two-Dimensional Model Configuration

Our test simulations use the JasonGCM at very low longitudinal resolution (8 grid cells), while retaining the same latitudinal (128 grid cells) and vertical (33 grid cells extending down to 18 bar) resolution as the low-resolution configuration of *Young et al.* (2019a). This setup produces a quasi-two-dimensional flow, in which variations in the longitudinal direction are negligible and the dynamics are effectively confined to the latitude–pressure plane.

Although the number of longitudinal grid cells could in principle be reduced further to the minimum periodic extent (e.g. two cells), we retain a small but finite longitudinal dimension to preserve numerical robustness and consistency with the full three-dimensional dynamical core. In our configuration, zonal variations in velocity and tracer fields are negligible, while the computational cost remains modest, with typical integrations completing within a few hours. We therefore do not pursue a further reduction in longitudinal resolution.

For each simulation, the zonally averaged temperature and velocity field from the three-dimensional simulation with the same parameters but no mushball parameterisation is used to initialise the model, so we do not need to run the model for a long time to reach thermal equilibrium in the deep layers. In reality, as long as the 3D simulation has the same reference optical depth as the 2D run, the exact choice of the run we pick as the starting point should not affect the results significantly, as the jet structure would quickly disappear due to the lack of eddy momentum forcing, as illustrated in Fig. 4.2. The simulation is first run for 1500 days to allow the velocity to reach an initial quasi-equilibrium. The water and ammonia is then

reinitiated with different mushball parameters. Each simulation is then continued for 8000 days to equilibrate.

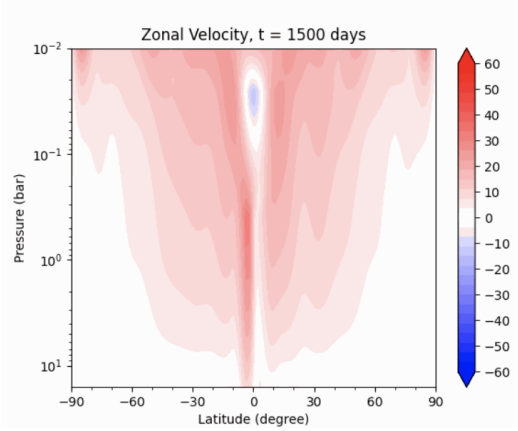


Figure 4.2: Zonal-mean jet profile at the end of the 2D simulation. Note that the alternative east and west jets have mostly disappeared.

4.3.2 Simulation Runs and Naming Convention

Two groups of simulations are conducted in the two-dimensional setup: a parameter sweep group and a group with a more Jupiter-like temperature profile.

The parameter sweep group contains 3 sets of runs, each varying one mushball parameter and a simulation with no mushball process. The simulation naming scheme employed here uses a four-character, positionally encoded code (`Sxyz`) to unambiguously specify three independent mushball parameters in a compact form. The leading "S" flag denotes that this run series is for the 2D model (slice), while each of the three subsequent digits occupies a fixed position and indexes one of the following model controls: the first digit indicates the ammonia mass fraction (f_c), the second the mushball formation efficiency (ε_{mush}), and the third is the water abundance. Each value of a specific digit encodes a unique value of the corresponding physical

Parameter	Digit	0	1	2	3	4
f_c	1st	no mushball	0.1	0.2	0.4	-
ε_{mush}	2nd	no mushball	0.3	0.03	0.003	-
H_2O solar abundance multiplier	3rd	-	-	2.0	3.0	4.0

Table 4.2: Mapping of run name digits to corresponding values of the physical parameter. The first column lists the physical parameters encoded in the run names, while the second column indicates the corresponding digit position within the identifier (formatted as `Sxyz`). The remaining columns show the values associated with each digit code.

parameter. For the first two digits, increasing code values correspond to progressively larger deviations from the nominal setting: an increase the first digit indicates increase in f_c, while an increase in the second digit indicate decrease in ε_{mush}. A code of '0' at either of these two digits indicates that the mushball process is disabled for that run. The third digit directly specifies the solar-abundance multiplier for water.

This naming scheme produces run identifiers that are both human-readable and trivially machine-parsable: because each identifier is exactly four characters long, extracting characters at fixed positions directly recovers the full parameter configuration without any external lookup. Table 4.2 summarises the mapping from each digit position to its corresponding parameter values. The run with nominal mushball parameters is S112, and the run with no mushball is S002. The set that varies f_c contains run S112, S212 and S312. The set that varies ε_{mush} contains S112, S122, S132 and S002. The set that varies the water abundance contains run S112, S113 and S114.

The temperature-profile group consists of two simulations: one with the nominal mushball parameters and one without the mushball parameterisation. Both simulations use the reference optical depth set B as defined in Table 2.2, and are initialised using the temperature–pressure profile obtained at the end of the three-dimensional simulation with this setup (i.e. the 'OB' case shown in Fig. 2.2). All other model parameters are identical to those in the preceding run group. Following the aforementioned naming scheme, we assign these runs the prefix flag `T`, which conveniently denotes 'temperature' while also being the alphabetical successor to `S`. The resulting run name is then T112 for the case with mushball and T002 for the case without mushball.

4.4 Results for the Nominal Case

4.4.1 General Features of Water and Ammonia Distribution

Fig. 4.3 shows the mass mixing ratios of ammonia and water for runs `S112` and `S002`. In `S112`, a pronounced depletion of ammonia is observed between latitudes of approximately 20° and 50° in both hemispheres. Poleward of this latitude, ammonia remains depleted compared to `S002`, particularly in regions with reduced cloud density, where an ammonia-poor layer develops between 3 and 7 bar. The limited depth of our model, which extends only to 18 bar,

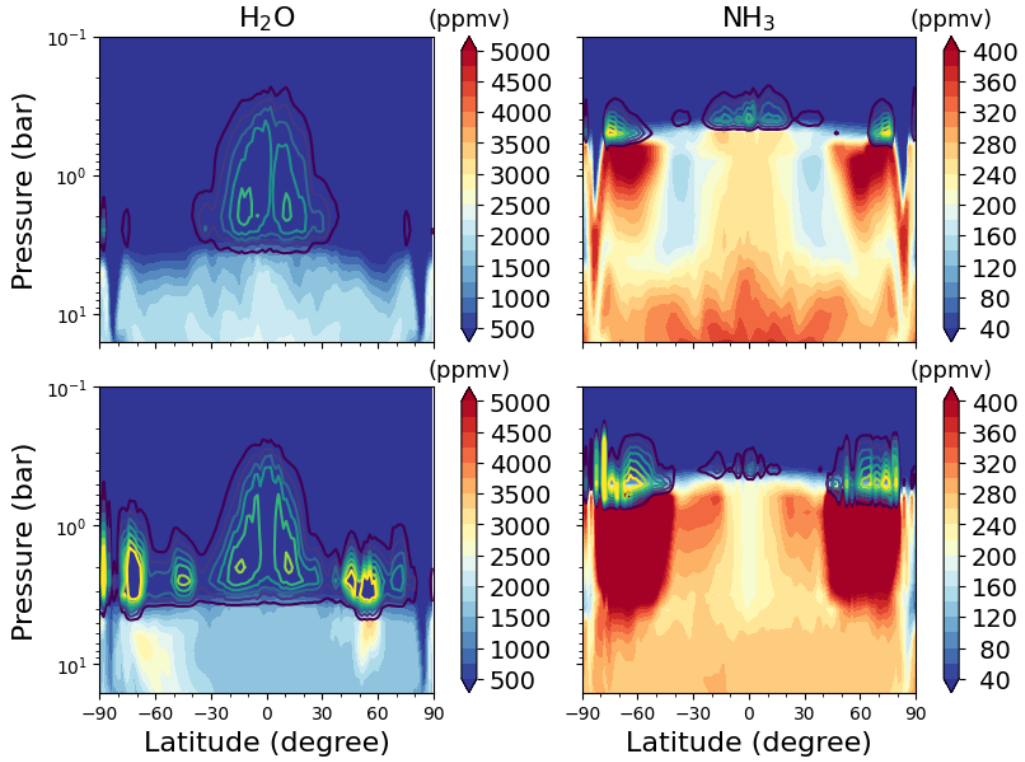


Figure 4.3: Water (left) and ammonia (right) volume mixing ratio for the simulation with nominal mushball parameter (S112, above) and the simulation without mushball (S002, below), averaged over the last 200 days of the simulation. The vapour volume mixing ratio for both species is shown in filled contours, and the solid (cloud) volume mixing ratio is represented as line contours. The contours for ammonia ice are spaced linearly from 40 ppmv to 200 ppmv, and the contours for water ice are spaced linearly from 200 ppmv to 1700 ppmv.

may restrict the time of ammonia and water deposited by mushballs, making upward advection by the circulation more efficient than would be expected for Jupiter's deeper atmosphere.

The water cloud density is also reduced in `S112`, with the cloud largely absent between 40° and 70° latitude. This is consistent with the role of mushball in transporting water to deeper layers. Notably, neither ammonia nor water exhibits a latitudinally banded structure in these simulations, as would be expected given the absence of eddy-driven zonal jets and cloud bands in the two-dimensional model.

An unexpected feature of `S002` is the relatively ammonia-depleted region near the equator, within roughly 10°. One possible explanation involves the interaction between the meridional circulation and condensation in the absence of mushball transport. Near the equator, strong upwelling lifts ammonia above its condensation level, allowing it to condense and be transported poleward. There, it gradually settles and re-evaporates. In `S112`, the deep transport of ammonia by mushball enables upwelling to replenish ammonia. In contrast, the absence of mushball in

S002 limits the amount of ammonia that can be transported upwards in the equatorial region, which could potentially account for the observed depletion.

The location of the descending branch of this meridional circulation is less clear. The ammonia- and water-rich regions between 40° and 80° suggest the possibility of hemispheric-scale cells, but the streamfunction shown in Fig. 4.4 indicates a more segmented circulation pattern. This discrepancy may be due to the short 200-day averaging window used in the calculation: the timescale for meridional transport is likely much longer; over such a timescale, smaller, transient structures in the stream function may average out. Given that the two-dimensional model cannot realistically capture Jupiter-like meridional circulations with jet-scale Ferrel-like cells, we refrain from analysing it in detail here. A more detailed analysis of vertical tracer transport, including advection and mixing timescales and correlations between tracer abundance and vertical velocity, would be valuable for further understanding the tracer distribution.

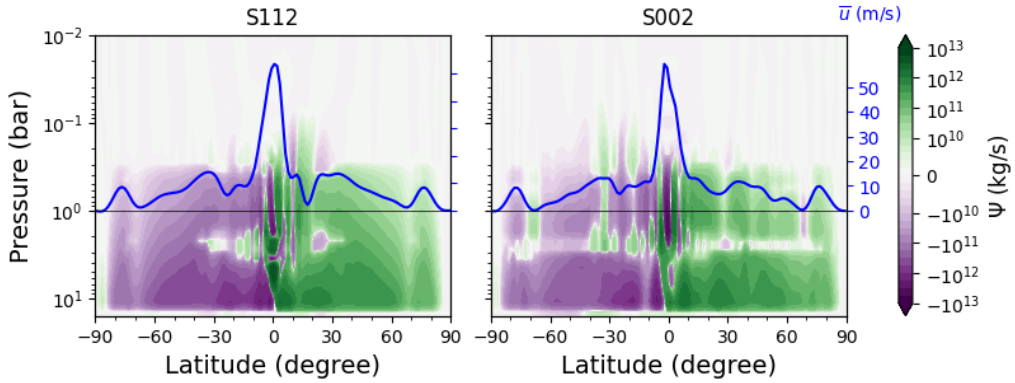


Figure 4.4: Meridional mass stream function (colour map) and zonal jet profile at 1 bar (blue line) for the simulation with nominal mushball parameter (left) and the one without mushball (right).

4.4.2 Mushball Diagnostics

As shown in Fig. 4.5, the mushball flux is strongly correlated with moist convective activity, for which TCAPE is used as a proxy. Since the mushball flux becomes vertically uniform below its formation region, its value at 14 bar (the top face of the model's bottom layer) is used as a representative measure. This correlation is expected, since the mushball source term is proportional to both the moist convective flux and the availability of water ice produced by moist convection. The correlation is not perfect, however, as the local ammonia mixing ratio also constrains the source term.

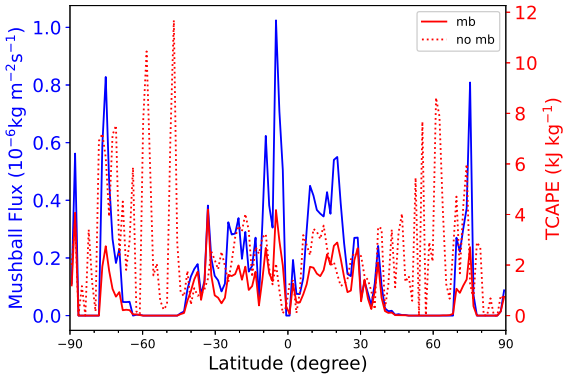


Figure 4.5: Mushball associated flux (blue) and TCAPE (red) for the 2D simulation with normal mushball parameter. The TCAPE for the simulation with no mushball is plotted in dashed red lines. The mushball-associated flux is the downward flux evaluated at 14 bar (i.e the top face of the bottom cell). In the current setup, it is constant below the formation region for a given latitude.

Fig. 4.6 presents the amount of ammonia available for mushball formation ($c - c_{\text{crit}}$, as defined in Eq. (4.2)) along with the resulting mushball source term. Due to the strong dependence of the critical ammonia threshold on temperature, mushball formation typically occurs in just one or two model layers. Although more ammonia is available for condensation at latitudes poleward of 40°, the source term remains concentrated within ±40°, as mushball formation at higher latitudes is limited by the reduced availability of water ice. There are two ways to assess

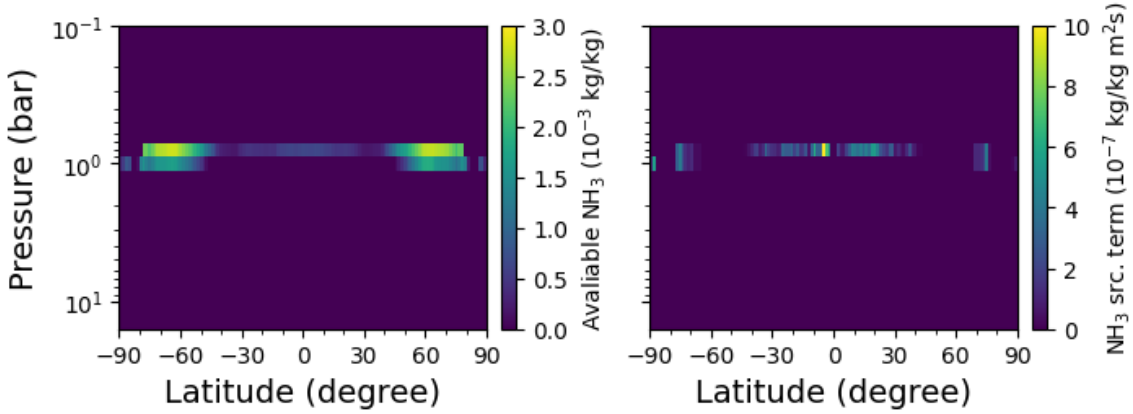


Figure 4.6: Ammonia available for mushball formation (left) and ammonia source term (right) for the two-dimensional simulation with nominal mushball parameter.

whether mushball formation is ammonia-limited. The first is the ammonia saturation ratio, defined as the ratio of the actual source term to the maximum amount of ammonia that could, in principle, be converted into mushball. This maximum is given by $\varepsilon_{mush}(c^k - c_{crit})\dot{M}^k_{conv}$. The second is the ammonia-limited fraction, which is the proportion of time steps in which the actual source term equals the maximum possible value. As illustrated in Fig. 4.7, both metrics

yield very similar patterns, differing only in a few grid cells. We therefore focus our discussion on the ammonia-limited fraction.

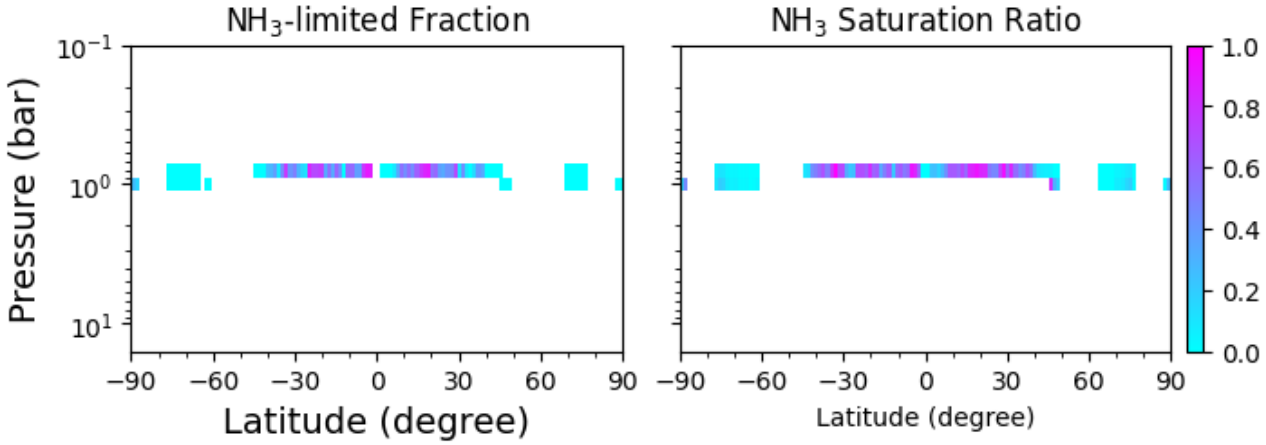


Figure 4.7: Ammonia-limited fraction (left) and ammonia saturation ratio (right) for mushball formation for the two-dimensional simulation with default mushball parameter.

Within the latitude band of ±40°, this fraction approaches unity in many locations, indicating that mushball formation is frequently limited by ammonia availability. In contrast, outside this latitude band, the ammonia-limited fraction drops to nearly zero, implying that mushball formation is almost always limited by water ice in higher latitudes. This interpretation is supported by Fig. 4.3, which shows depleted water clouds and reduced water vapour mass mixing ratios within the same latitude range.

4.5 Effect of Varying Mushball Parameters

4.5.1 Varying Water Abundance

Increasing the abundance of water leads to several non-linear changes in the simulation outcomes. While the equatorial 'plume' feature of ammonia persists across all water abundances, the enhancement of ammonia below the high-latitude cloud becomes less prominent as water abundance increases, suggesting that the mushball process becomes more efficient in depleting ammonia at higher latitudes. The spatial distribution of water also evolves in a complex manner. When water abundance increases from 2× to 3× solar, both the vapour and cloud components of water show enhanced mass mixing ratios, although their overall spatial distribution remains qualitatively similar. However, the transition from 3× to 4× solar reveals a

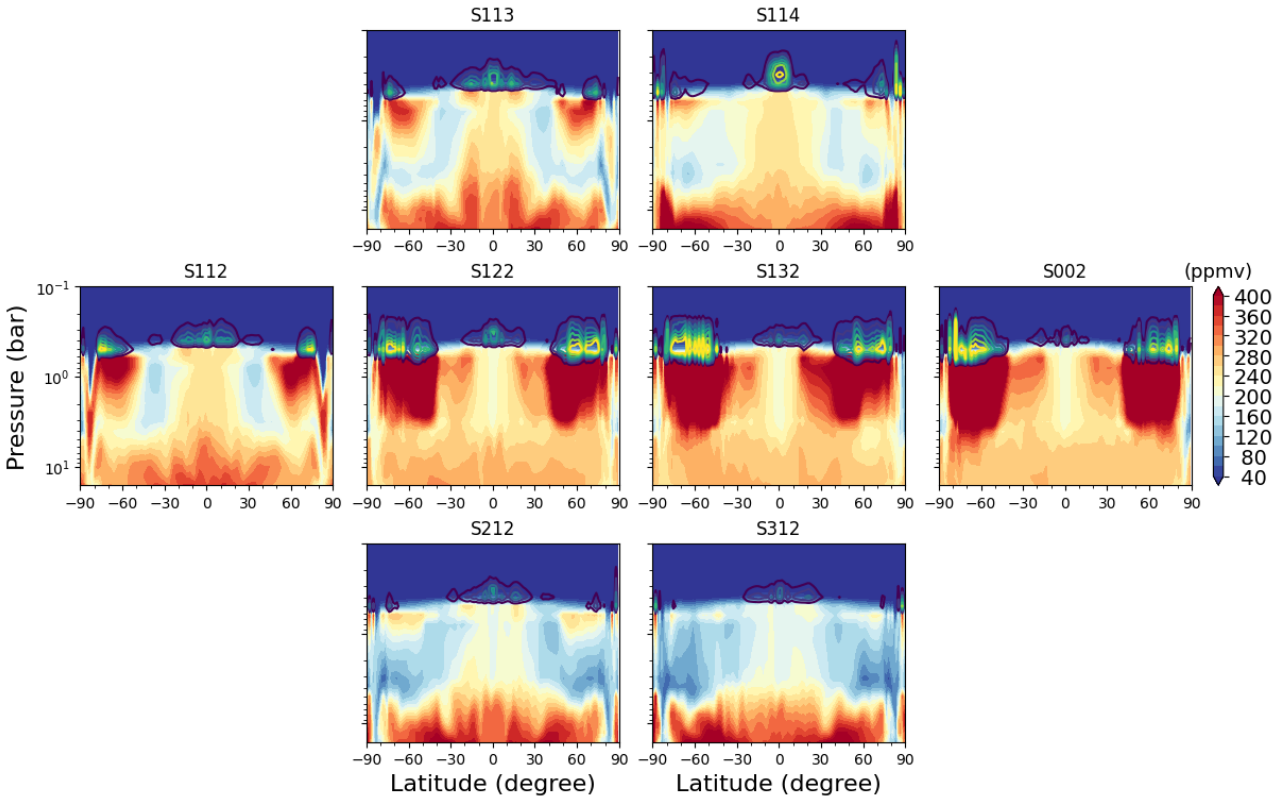


Figure 4.8: Ammonia volume mixing ratio for 2D simulations with different water abundance (top row), mushball efficiency (middle), ammonia fraction (bottom). For comparison, the leftmost figure of the middle row is the simulation with nominal mushball parameters, and the rightmost figure is the simulation with no mushball. Spacing for filled and line contour is the same as Fig. 4.3.

notable difference: water concentration decreases near the equator and increases at higher latitudes in both phases. The equatorial water content is even lower in the 4× case than in the 3× case, indicating that increasing water abundance does not simply scale the entire profile, but redistributes it latitudinally instead. This effect is likely driven by enhanced meridional transport toward the poles. Similar behaviour is observed in the corresponding three-dimensional simulations without mushballs (*Young and Read* 2019), in which increasing the water abundance to 4× solar leads to preferential enhancement of water in the polar regions, albeit without reducing the equatorial water content below that of the lower-abundance case. This similarity suggests that the redistribution is influenced by the dynamics, with mushball processes acting to further amplify the depletion at low latitudes. A more detailed understanding of tracer transport by the large-scale circulation is therefore important for interpreting these responses.

Fig. 4.10 shows various diagnostics for this series of simulations. Latitudinal trends in TCAPE are also affected by water abundance. In S113, TCAPE increases near the equator,

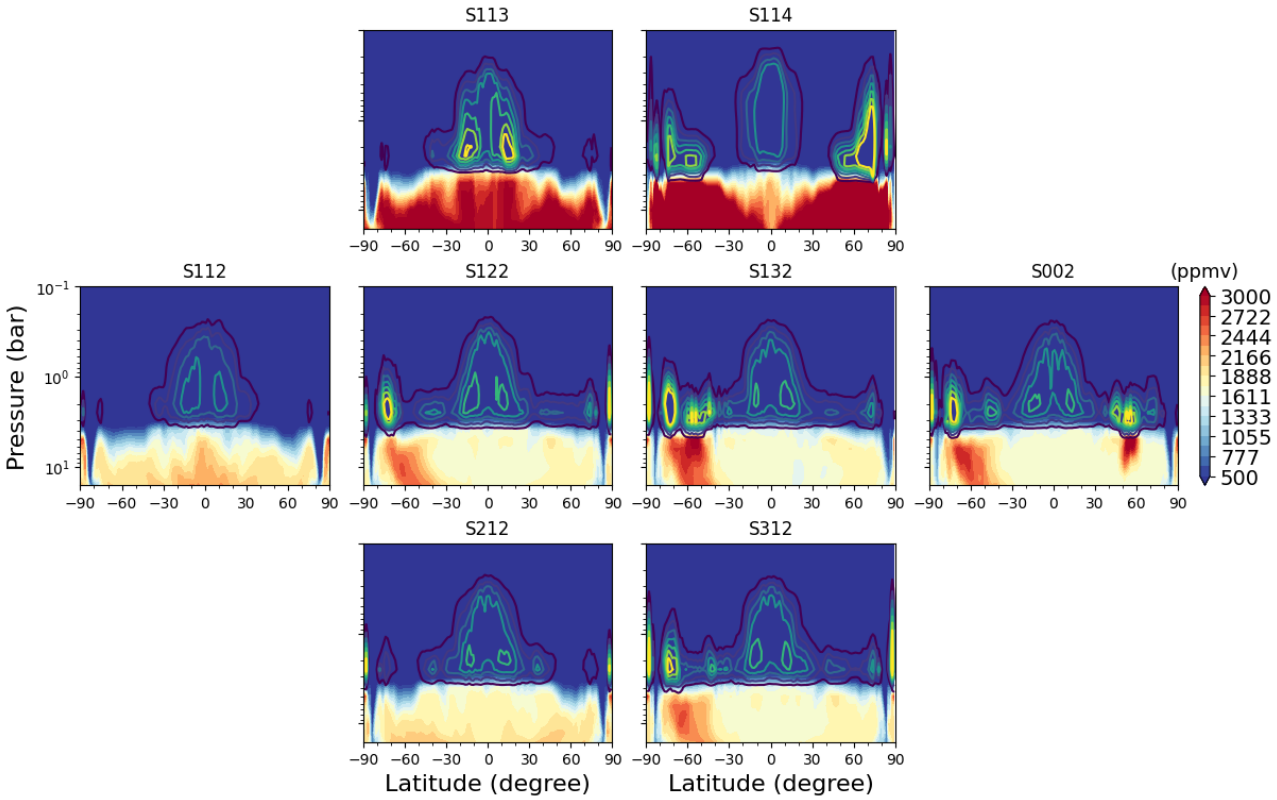


Figure 4.9: Same as Fig. 4.8 but for water vapour.

particularly between 0 and 20°, and also in the high-latitude regions where moist convection is already active. In S114, the increase is more pronounced, with significantly higher TCAPE appearing above 40° latitude. This is consistent with the increase in water mass mixing ratio. The increase in TCAPE with water abundance aligns with theoretical expectations: a greater water abundance increases its concentration within convecting parcels, amplifying latent heat release during condensation. This mechanism, also documented by *Young and Read* (2019), leads to an increase in both the latent heating component and the total TCAPE. However, we caution that we only tested a small range of water abundance, and this trend may not apply to simulations with higher water abundance, where the molecular weight of water can inhibit moist convection (*Leconte et al.* 2017).

Mushball fluxes exhibit similar trends to TCAPE. In S113, the mushball flux is notably higher at low latitudes, which is consistent with the observed increase in convective energy. S114 also exhibits non-zero mushball flux in high-latitude regions, which is consistent with the enhanced TCAPE profiles described above.

However, the frequency of mushball events displays more complex behaviour. When water

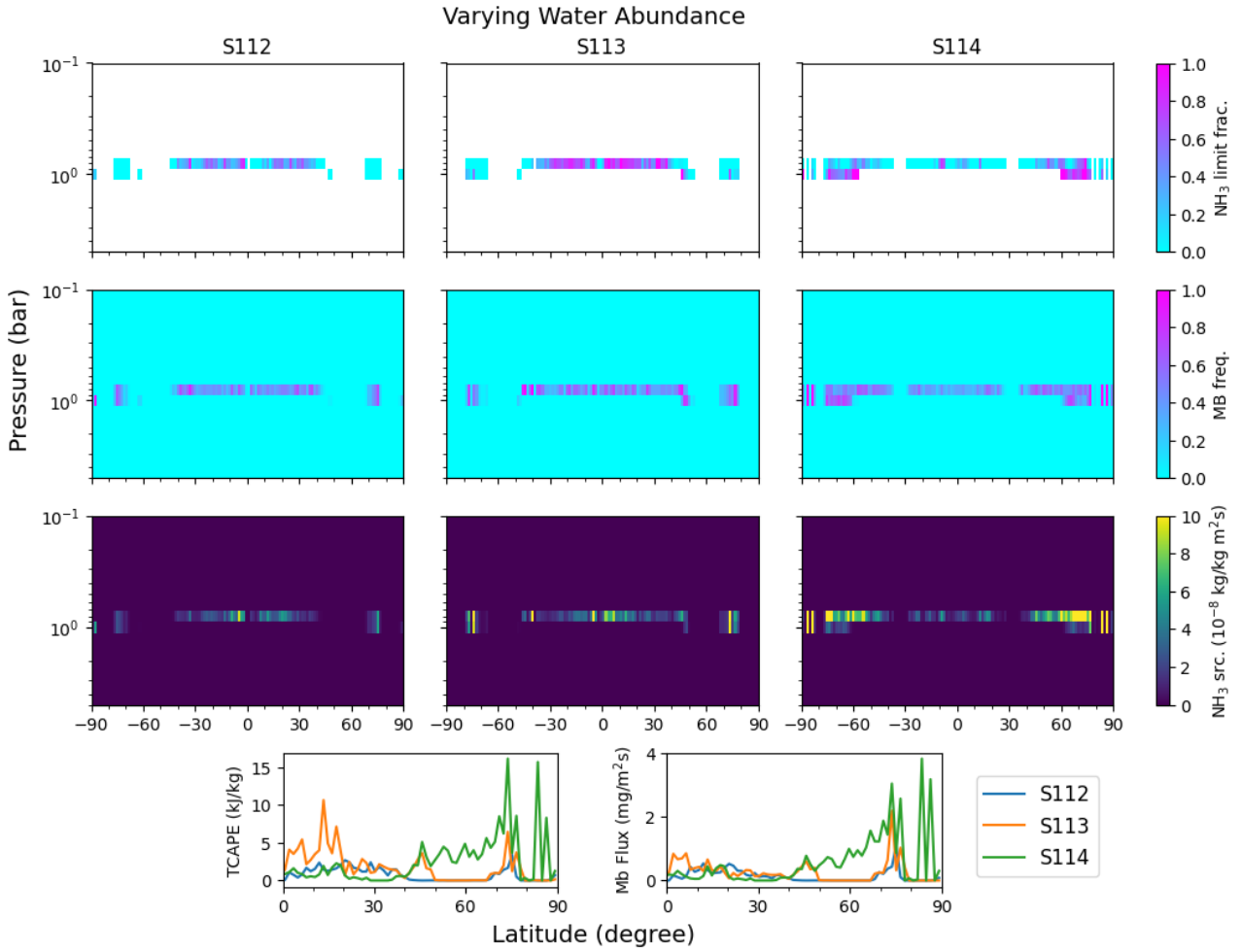


Figure 4.10: Mushball parameterisation scheme diagnostics for the simulations with different water abundance, the top three rows, from top to bottom, are the ammonia limiting fraction, mushball frequency, and the mean ammonia source term (in 10^{-8} kg/kg m^{-2} s^{-1}). The water abundance used in the simulation is increasing from left to right. The two panels at the bottom show the total convective available potential energy (left) and mean MB flux (right) as a function of latitude for these simulations.

abundance increases from 2× to 3× solar, the mushball frequency, defined as the ratio of the number of instances in which mushball formation is triggered to the total number of diagnostic evaluations, remains relatively unchanged. In contrast, increasing from 3× to 4× solar results in a decrease in mushball frequency at low latitudes and an expansion of the latitude band experiencing mushball formation.

The ammonia source term shows a slight increase at high latitudes between the 2× and 3× solar cases. Beyond this, its trend follows that of the mushball frequency: it decreases at low latitudes while increasing at high latitudes in the 4× solar case.

Changes in the limiting fraction for mushball formation provide further insight into these trends. In S113, the low- to mid-latitude regions exhibit an increased fraction of grid cells that are ammonia-limited. This explains why an increase in water abundance does not lead to a proportional rise in mushball formation in these regions: ammonia becomes the bottleneck. In contrast, the high-latitude regions in S113 remain water-limited; therefore, increasing water directly enhances mushball formation and convective fluxes. This transition in the limiting factor helps to explain the greater mushball flux enhancement in S113, despite the mushball frequency remaining similar.

In S114, this pattern reverses. The number of ammonia-limited cells decreases in the low latitudes, while the high-latitude regions experience an increase in the ammonia-limited fraction. This shift in behaviour reflects the changed water distribution in the 4× solar case, leading to reduced mushball formation and diminished mushball flux in the polar regions despite the higher water abundance.

Together, these results emphasise the model's complex response to increased water abundance. Latitudinally varying limitations in tracer abundance, coupled with changes in moist convective activity, create differences in mushball flux and tracer distribution across space.

4.5.2 Varying Mushball Efficiency

Reducing the efficiency of the mushball formation results in ammonia and water distributions that increasingly resemble those of the no-mushball case. This transition is most evident in the transition from S112 to S122, where the efficiency is reduced by a factor of ten. Only a small difference is seen between simulations S122 and S132, in which the efficiency of mushball formation decreased by a further tenfold. This behaviour is expected, as lower efficiency corresponds

to a slower mushball formation process, which effectively weakens the influence of mushball-related transport and hence reduces depletion of tracer distributions. A notable feature of the diagnostics plots is that the vertical extent of the mushball formation region increases as the efficiency decreases. This increase is particularly prominent in the high-latitude bands, with the formation region expanding to encompass three model layers. The reduction in efficiency from S122 to S132 also coincides with the emergence of a hemispheric asymmetry, with mushball frequency increasing in the southern hemisphere and decreasing in the northern hemisphere. Such an asymmetry is also reflected in the water and ammonia profile. This asymmetry does not arise from the model configuration, which is symmetric across two hemispheres. Instead, it likely reflects the amplification of small stochastic differences introduced by the initial random perturbations by the nonlinear cloud processes. Similar hemispheric asymmetries have been reported previously in the JasonGCM (*Young et al.* 2019b).

Overall, the ammonia source term decreases significantly as efficiency decreases. This is consistent with expectations, as lower mushball efficiency means that less ammonia is converted into mushball. The same trend is also evident in the decrease in total mushball flux with decreasing efficiency. However, in the mid-latitude region, a small ammonia source term (and therefore mushball flux) emerges in S112, in contrast to the nominal case, where the flux is almost zero. While this may seem counterintuitive at first, it can be explained by the changes in tracer limitation: lower mushball efficiency means that ammonia is less depleted, so its abundance remains relatively high. Grid cells that had no mushball formation in the default case now have a sufficient amount of ammonia for mushball formation, allowing a low but persistent flux to be maintained.

Furthermore, in the low efficiency case, ammonia is so abundant that water, which is transported by moist convective activity, becomes the limiting factor, as shown in Fig. 4.11 When the efficiency is reduced, the fraction of grid cells in which ammonia acts as the limiting factor for mushball formation is nearly zero, except along the edges of the formation region in simulations S122 and S132. Even in these regions, the extent of ammonia limitation is smaller in S132 than in S122.

In terms of moist convective activity, TCAPE increases systematically as mushball efficiency decreases, particularly at high latitudes. This is consistent with the role of mushball in the vertical redistribution of water. Efficient mushball formation transports water to deeper layers,

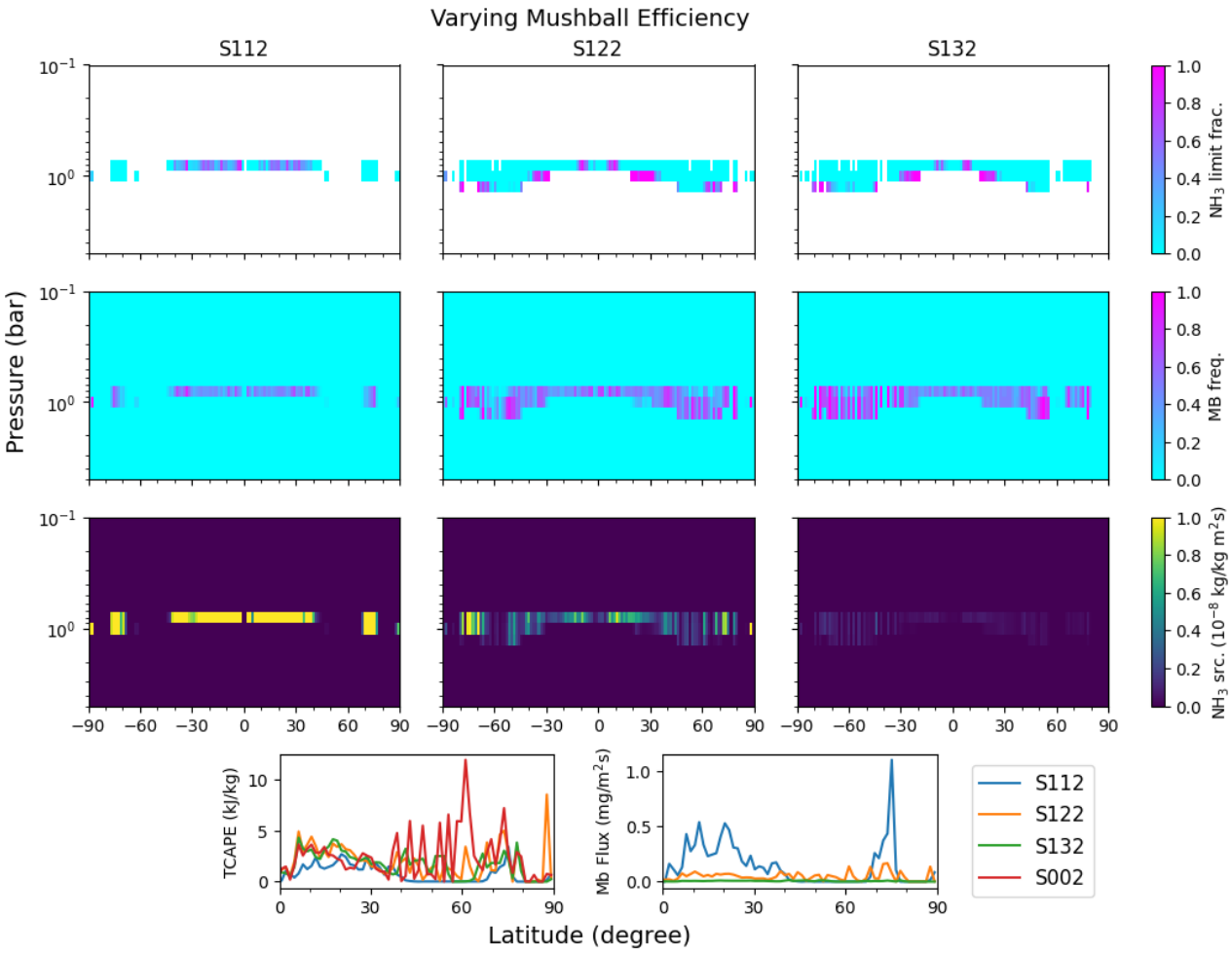


Figure 4.11: Same as Fig. 4.10 but for simulations with different mushball formation efficiencies, decreasing from left to right.

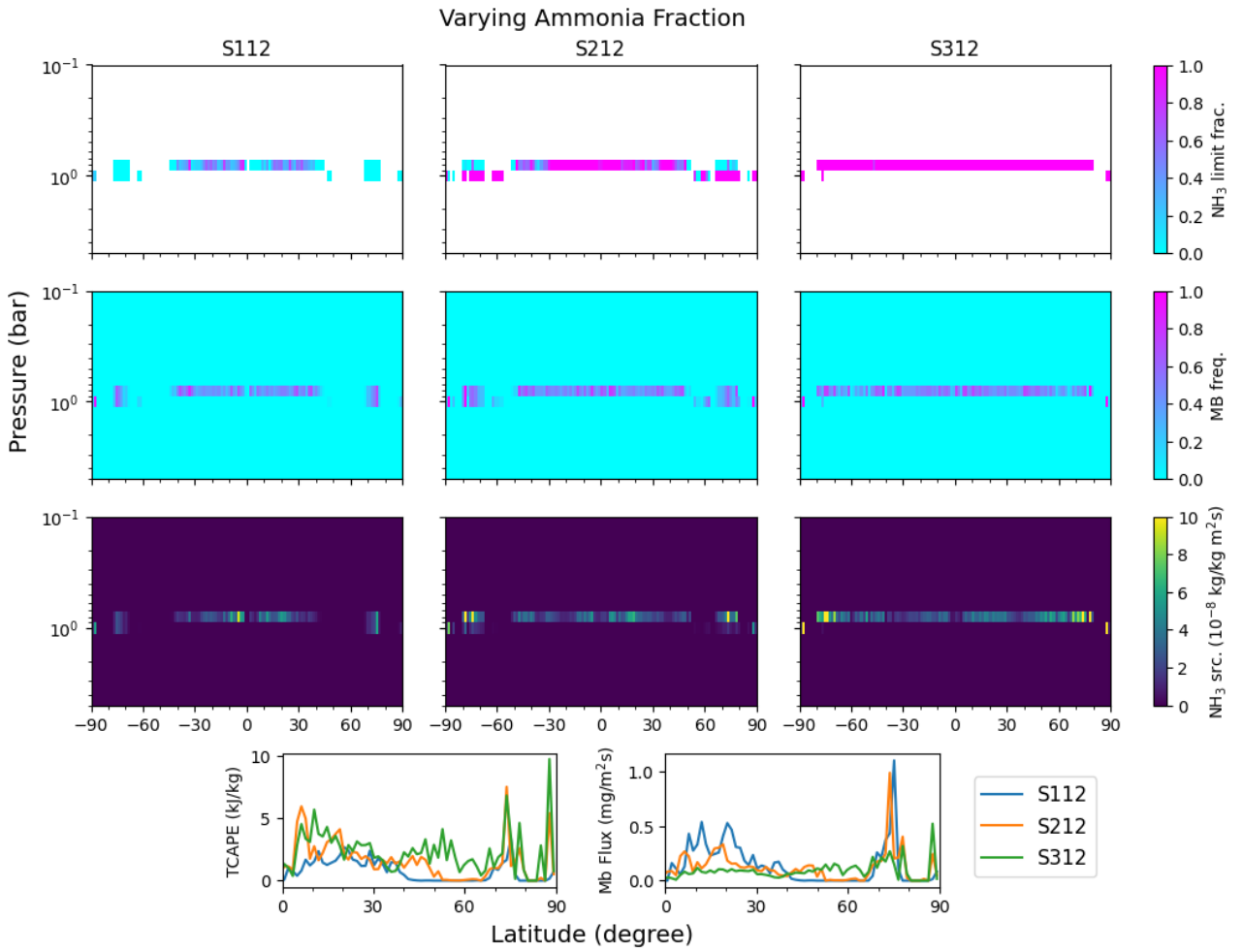


Figure 4.12: Same as Fig. 4.10 but for simulations with different ammonia fraction, increasing from left to right.

where its contribution to moist convection in the upper troposphere is reduced. When this transport is suppressed due to lower efficiency, more water remains in the convecting layers, thereby enhancing latent heat release and increasing TCAPE.

In summary, varying the efficiency of mushball formation affects tracer distributions and induces complex changes in mushball activity and moist convection. Reduced ammonia and water transport increases their local availability, thereby sustaining mushball formation and enhancing convective potential. This interplay highlights the complex feedback mechanism in the GCM.

4.5.3 Varying Ammonia Fraction

Increasing f_c leads to more efficient ammonia depletion. Unlike the strongly latitude-dependent patterns observed when increasing water abundance, ammonia depletion is more uniform across latitudes in this case, as illustrated in Fig. 4.12. Conversely, the water distribution progressively resembles that of the no-mushball case. Notably, the water pattern in run S312 closely resembles that in S122. This is consistent with the expectation that a higher f_c results in more ammonia transport than water, thereby reducing the net removal of water by mushball fluxes.

The spatial extent of mushball formation increases with f_c. However, in run S312, mushball formation remains confined to a single layer vertically, except near the poles. This indicates that, unlike when reducing ε, increasing ammonia content in mushballs does not broaden the vertical extent of mushball formation.

The ammonia source term remains comparable across f_c values in the low latitudes and increases only slightly in the high-latitude regions. This can be explained by the relatively high ammonia-limiting fraction at low latitudes. In these regions, further increase in the ammonia fraction in mushballs does not enhance the source term; rather, it reduces the overall mushball flux due to decreased water content in the mushballs.

At high latitudes, the proportion of ammonia-limited cells increases with f_c. In S212, only a small portion of the first formation layer is water-limited. In contrast, all latitudes are ammonia-limited, and mushball formation is restricted to a single layer in S312. This reflects a key transition: when f_c is large, more ammonia is depleted in the lower mushball formation layer to the extent that insufficient ammonia remains to sustain mushball formation in the upper layers. This depletion structure is also evident in the ammonia distributions.

TCAPE increases with f_c, particularly above 50° latitude. At lower latitudes, the increase from $f_c = 0.2$ to $f_c = 0.4$ is smaller than in previous parameter variations. This moderate increase aligns with a higher water concentration at these latitudes, reflecting that more ammonia-rich mushballs reduce water transport and thus allow TCAPE to accumulate.

Overall, the total mushball flux decreases with increasing f_c. This is because mushball formation becomes increasingly ammonia-limited: as more ammonia is incorporated into mushballs, less water is incorporated, resulting in a drop in the total mass flux. This trend is partially reversed in the 50–60° region when going from $f_c = 0.2$ to $f_c = 0.4$, where the increase in TCAPE leads to more frequent moist convection and thus more mushball formation.

4.6 Effect of Changing Temperature Profile

Fig. 4.13 compares the water and ammonia mass mixing ratios at the end of the simulations with the new reference optical depth. Several features are consistent with earlier findings for run S112, discussed in Section 4.4. These include the enhancement of water vapour in low latitudes and the increased ammonia mixing ratio in the deep layers in the simulation, including mushball.

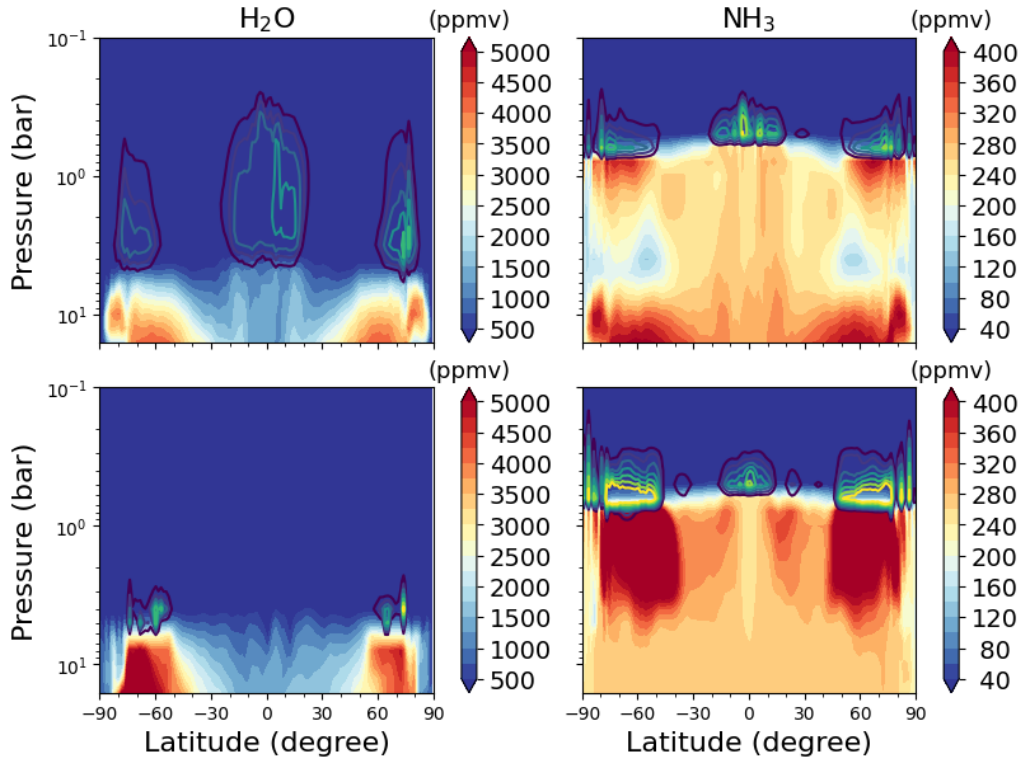


Figure 4.13: Water (left) and ammonia (right) volume mixing ratio for the two-dimensional simulation with updated reference optical depth (and therefore a temperature profile that is more similar to Jupiter), averaged over the last 200 days of the simulation. The figures on the top row are from the simulation with nominal mushball parameters (T112), and the figures on the bottom are from the simulation without mushball (T002). Filled contours represent the vapour mixing ratio, and line contours represent the solid (cloud) mass mixing ratio. The contour levels for the solid phase are the same as in Fig. 4.3, but the colour scale for water vapour is adjusted to account for its higher mixing ratio in these simulations.

However, the mid-latitude depletion of ammonia appears less pronounced. A similar level of ammonia depletion to that in S112 only occurs within a triangular region centred on 4 bar and located near 60° latitude. Compared to T002, run T112 exhibits an elevated water cloud around the equator. This contrasts with Section 4.4.1, where the equatorial water cloud in S112 has a similar density to that in S002. In addition, the water cloud between 50° and

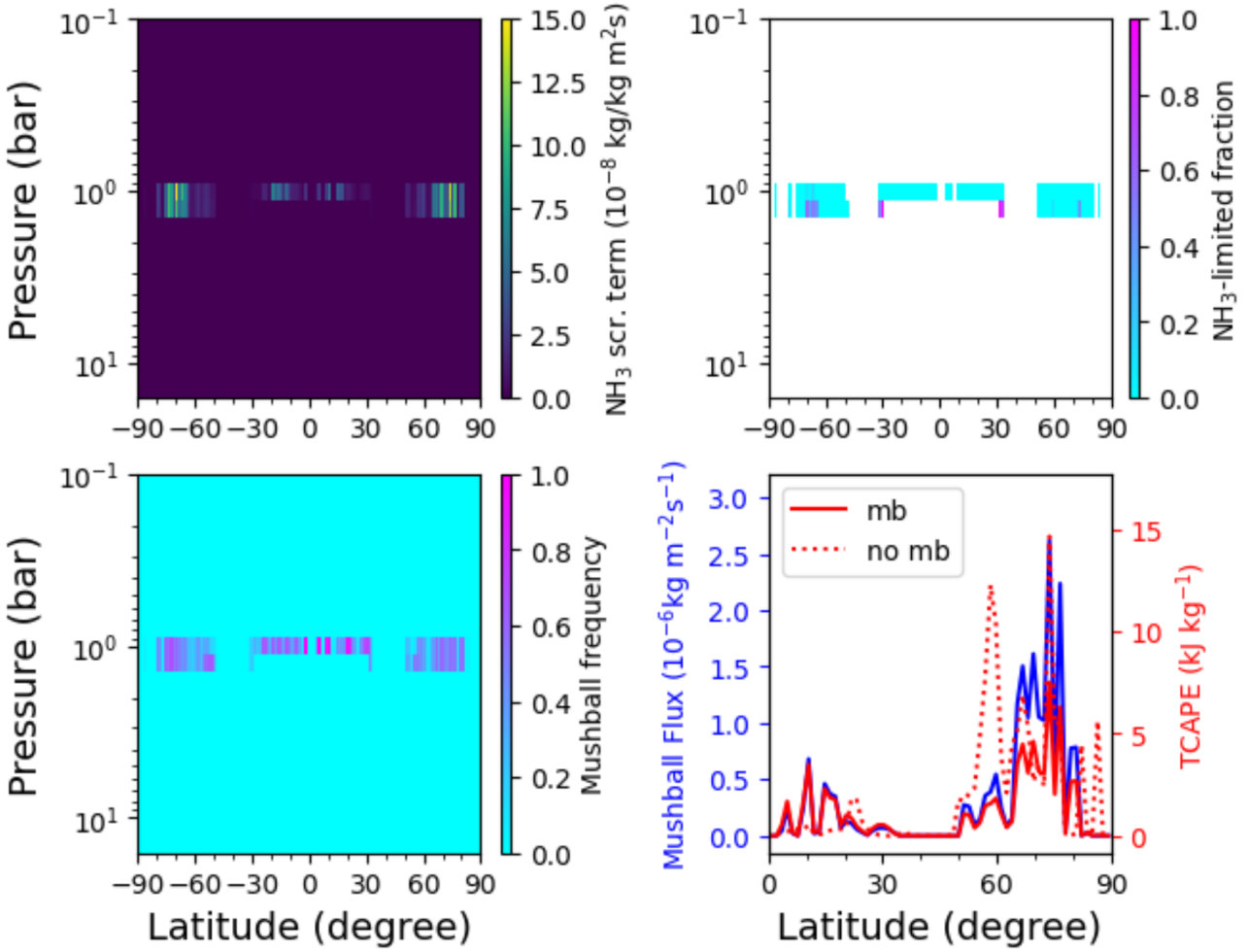


Figure 4.14: Mushball ammonia source term (top left), ammonia-limited fraction (top right), frequency of mushball formation (bottom left), mushball flux (blue line, bottom right) and TCAPE (red line, bottom right) for the simulation with updated reference optical depth, all averaged over the last 200 days of the simulation. The bottom-right panel shows only the value for the Northern Hemisphere for clarity. The solid line represents the value for the simulation with mushball, and the dotted line represents the value for the simulation without mushball.

80° latitude appears more elevated and less concentrated in T112 than in T002. The strongly concentrated water vapour and cloud in T002 in the polar regions is a more extreme case of the polar accumulation discussed previously in Section 3.5.4. In addition, because this setup is zonally symmetric, cloud structure can be particularly sensitive to the meridional circulation, and should therefore be interpreted with caution.

As shown in Fig. 4.14, the mushball source term is restricted to two model layers near the 1 bar level. The frequency of mushball formation increases in T112, and the latitude band in which it forms expands relative to S112. The source term and the flux of mushball are both higher in T112 than in S112 at high latitudes, while remaining comparable at low latitudes. This

suggests that the formation of mushball is favoured in colder environments. This is consistent with our scheme's setup, in which the critical mass mixing ratio for ammonia increases with temperature. This means that more ammonia is available for mushball formation in cooler environments. In contrast to S112, mushball formation in T112 is primarily constrained by water ice availability. Only in a few isolated grid cells in the lower mushball formation layer, near the 30° latitudes and above the 50° latitudes, was ammonia the limiting factor.

The mushball flux in T112 is, as in S112, correlated with TCAPE. However, the nature of this correlation differs between latitudinal regimes. At low latitudes, the TCAPE and mushball flux curves overlap almost perfectly after appropriate rescaling. At high latitudes, however, the mushball flux curve sits above the TCAPE curve. This discrepancy arises because the mushball formation region spans two vertical layers at high latitudes compared to one at low latitudes, resulting in higher fluxes.

As with S112, T112 exhibits lower TCAPE at high latitudes than T002. However, unlike the nominal mushball case, T112 shows higher TCAPE at low latitudes. This may be due to the increased water vapour in T112, which enhances the potential for moist convection and allows more convective energy to accumulate.

4.7 Conclusion

Our circulation model, coupled with a self-consistent moist convection scheme and a simplified parameterisation of mushball formation and transport, can produce ammonia depletion that is qualitatively consistent with Juno observations under the nominal mushball scenario. The spatial distributions of ammonia and water result from the complex interaction between mushball-driven transport, moist convection and the mean overturning circulation. As mushball preferentially transports water to deeper layers, the availability of condensable material in the upper troposphere is reduced, which suppresses moist convection and influences the large-scale dynamical structure.

As the detailed microphysics of mushballs are uncertain and poorly understood, we have implemented a flexible yet simplified scheme governed by a small set of tunable parameters. This enables us to investigate the impact of variations in the ammonia fraction and formation efficiency on the tracer distributions and convective behaviour. Increasing the ammonia

fraction in mushballs results in more uniform ammonia depletion but reduced water transport. Conversely, decreasing the formation efficiency yields a tracer structure that increasingly resembles the no-mushball scenario. We also varied the water abundance, which is uncertain due to degeneracy in the observational data, and found that an increase in water abundance leads to greater ammonia depletion at high latitudes. It can sometimes be difficult to determine the causal relationship between mushball properties and tracer distribution, as mushball properties depend on the availability of tracers, which in turn affects the distribution of tracers.

Our sensitivity experiments further reveal that the tracer response depends heavily on the underlying thermal structure. A cooler temperature simulation observes less pronounced mid-latitude ammonia depletion and different mushball properties.

In order to investigate how mushball processes interact with large-scale atmospheric circulation, particularly concerning zonal jets and eddy-driven tracer transport, we must extend our framework into three dimensions. These effects cannot be captured in a two-dimensional setup, as this lacks zonal dynamics and eddy mixing and transport which significantly impacts material transport and atmospheric structure. Nevertheless, the two-dimensional simulations presented here are essential for building a foundation. By eliminating zonal variability, they facilitate a clearer understanding of the interactions between mushball microphysics, tracer depletion and convective strength. The 2D framework's simplicity makes it computationally efficient, allowing broad parameter sweeps to inform the choice of plausible parameter regimes for 3D simulations. For instance, our findings indicate that a mushball formation efficiency of 0.003 produces tracer distributions that are almost indistinguishable from those in the absence of mushballs, suggesting that future 3D exploration should concentrate on the efficiency range between 0.03 and 0.3.

In the following chapter, we build on this foundation by applying the mushball parameterisation in a 3D GCM. This will enable us to examine the atmosphere's full dynamical response to mushball-induced tracer transport and assess whether the observed belt–zone contrasts in ammonia can be reproduced under more Jupiter-like conditions.

Chapter 5

Three-dimensional Simulations with Mushball Parameterisation

Building on the results of the two-dimensional simulations, we now extend the simulation to the three-dimensional setup. This allows for a more realistic representation of planetary dynamics and material transport, including the development of zonal jets, eddy transport and belt–zone circulation, all of which are absent in the 2D framework. The main objective of this chapter is to examine whether, when embedded in a fully dynamical atmosphere, the mushball-driven tracer transport can account for the observed ammonia depletion patterns on Jupiter. Additionally, we explore how the interaction between moist convection, large-scale overturning and zonal asymmetries influences the vertical and latitudinal distribution of ammonia and water vapour.

The rest of this chapter is organised as follows: Section 5.1 describes the configuration of the three-dimensional GCM simulations. Section 5.2 presents the impact of mushball processes on the zonal mean flow, tracer distributions, and the properties of the mushball scheme. In Section 5.3, we examine the contributions of different processes in shaping the water and ammonia distributions. Section 5.4 discusses the results of a simulation under more Jupiter–like conditions. Finally, Section 5.5 summarises the main findings of the three-dimensional simulations and outlines directions for future work.

5.1 Simulation Runs

We ran several simulations with different model configurations and mushball parameters. Here, we present the three most informative simulations. Table 5.1 summarises the main differences between these runs. All of these runs were initialised from a state of rest with no clouds and a uniform vapour profile, as well as a temperature distribution produced by a radiative-convective model (RCM). The RCM uses the same radiation and dry convection parameters as the corresponding simulation, as well as the same latitudinal and vertical grids as the low-resolution part of the simulation. The simulations are first run at low resolution. Once the total kinetic energy and the net radiative flux at the top of the atmosphere have equilibrated, the

horizontal resolution is doubled. In both resolutions, the states are saved at 100-day intervals to save storage space. After equilibrium is reached at mid-resolution, the simulations run for an additional 200-day diagnostic period. During this period, the state and tracer mixing ratios are saved at 10-day intervals, and additional diagnostics are generated directly from the GCM. The detailed configuration of the low and mid resolutions is documented in Section 2.2.1.

Run	p_b (bar)	Nz	τ_{ref} set	Time in Res L (d)	Time in Res M (d)	Mushball scheme
N0	18	33	OA	20,000	10,000	No
N1	18	33	OA	20,000	20,000	Yes
W1	56	38	OB	40,000	20,000	Yes

Table 5.1: Summary of the key differences between the 3D simulations analysed in this chapter. All the simulations use a 3× solar abundance for water and a 2.7× solar abundance for ammonia. The other parameters, and the corresponding values of reference optical depth sets, can be found in Table 2.2.

Runs N1 and N0[1] mostly follow the same setup as M1 in Chapter 3. The main difference is the abundance of cloud-forming species used: 3× solar abundance for water and 2.7× solar abundance for ammonia. The rationale behind choosing a 3 times solar abundance for water, rather than the 2 times used in the 2D default simulation, was to avoid the localised sink of water condensates at high latitude described in *Young et al.* (2019b). The N1 run uses the default mushball parameters, which correspond to parameter code S113 in the 2D simulation. The N0 run has the mushball scheme turned off for comparison. Both simulations are run at low resolution for 20,000 days, after which they are increased to mid resolution for a further 10,000 days. This time is sufficient for both the flow and the tracers to reach equilibrium, as demonstrated in *Young et al.* (2019b). As the mushball scheme enables tracer transport to greater depths, the N1 run was extended by an additional 10,000 days to allow the tracer distributions to adjust under the influence of the large-scale circulation.

With a depth of 56 bars, Run W1 allows the mushball precipitate to fall to a greater depth. Furthermore, it uses the calibrated reference optical depths for the radiative transfer scheme that gives a temperature profile more similar to Jupiter, as discussed in Section 2.3.1. This set of optical depths is also listed in Table 2.2 as OB. This simulation employs the same tracer abundances and mushball parameters as the N1 run. It was initially run for 40,000 days at low resolution, followed by an additional 20,000 days at high resolution. The extended integration time was chosen to account for the longer radiative timescale at higher pressures, as well as

[1]N denotes nominal reference optical depth.

the longer overturning timescale associated with the greater domain depth. Like the N1 run, mushballs are assumed to fully evaporate within the bottom grid cell. For a 56-bar domain, this is not a realistic evaporation profile. However, it is adopted here as a simplified reference configuration, which will be compared with an evaporation profile distributed over several layers in future work.

For this deeper configuration, we only present simulations that include the mushball parameterization. The corresponding no-mushball case exhibited unphysical tracer distributions, with ammonia depleted in most of the Southern Hemisphere. This behaviour is not believed to arise from any physical process, but is instead attributed to numerical issues associated with the restart procedure. Resolving this issue requires additional simulations with long integration times, making such an investigation impractical within the scope of the present study. We therefore do not present the no-mushball simulation here.

5.2 N0 and N1: Nominal-depth Simulations

5.2.1 Zonal Mean Flow

Figure 5.1 shows the equilibrated zonal mean zonal velocity, $\overline{u}$, for the two simulations at nominal model depth. Both simulations exhibit broadly similar jet structures, featuring strong equatorial superrotation extending into the deep atmosphere and flanked by alternating prograde and retrograde extra-tropical jets. The overall jet profiles are very similar in these two cases, indicating that the inclusion of mushball microphysics does not substantially alter the

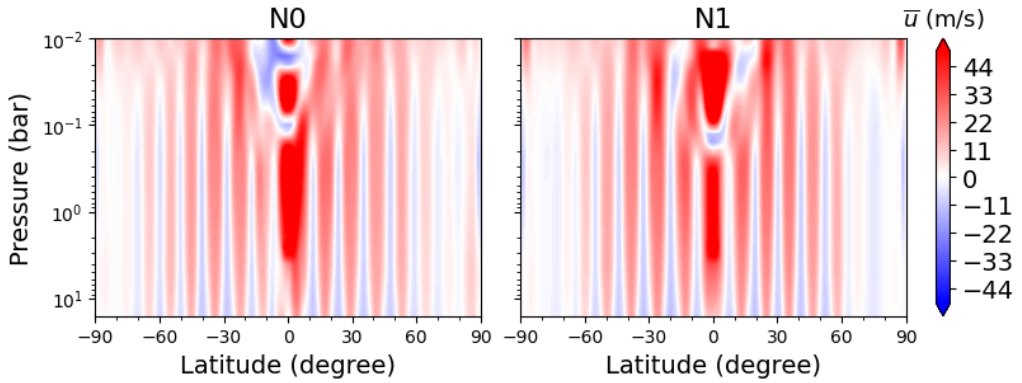


Figure 5.1: Zonal-time mean zonal velocity profiles at the end of the simulation with (right) and without (left) mushball.

large-scale dynamics. A noticeable difference appears near the equator at above 0.1 bar, where the N1 simulation exhibits a stronger and more vertically coherent equatorial jet; however, this region lies in the stratosphere, which is not the primary focus of the present study and is subject to strong temperature variability.

Fig. 5.2 provides a more direct comparison of the zonal jet profile. At 1 bar, the jets in the two simulations are closely aligned in both amplitude and distribution. The equatorial superrotating jet reaches comparable peak velocities in both cases, while the alternating jets at higher latitudes retain similar spacing and magnitude. A slight dip in equatorial velocity is visible in the no-mushball simulation, but is absent in the mushball case. In addition, there are small latitudinal shifts in some jets. However, given that the jets in these simulations undergo gradual migration, these offsets are not interpreted as systematic differences. Overall, the large-scale zonal wind structure remains robust across the two simulations.

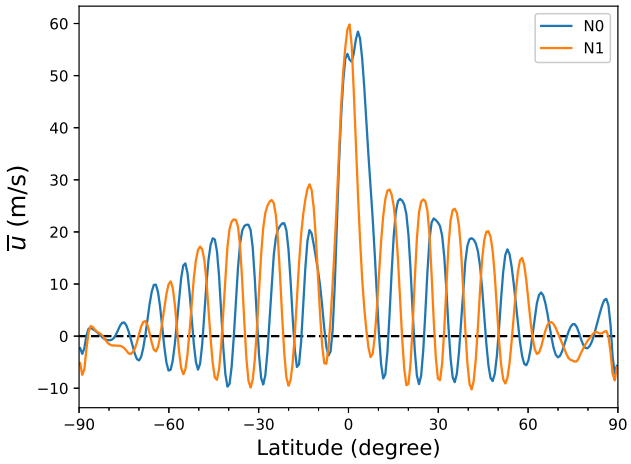


Figure 5.2: Zonal-time mean zonal velocity at 1 bar at the end of the simulation with (N1) and without (N0) mushball.

Similarly, the large-scale structure of the meridional overturning circulation is not significantly affected by the mushball process, as illustrated in Fig. 5.3. Both simulations exhibit comparable overturning cells across most latitudes and pressure levels. The only significant difference occurs in the polar region of the northern hemisphere, where the circulation cell reverses direction.

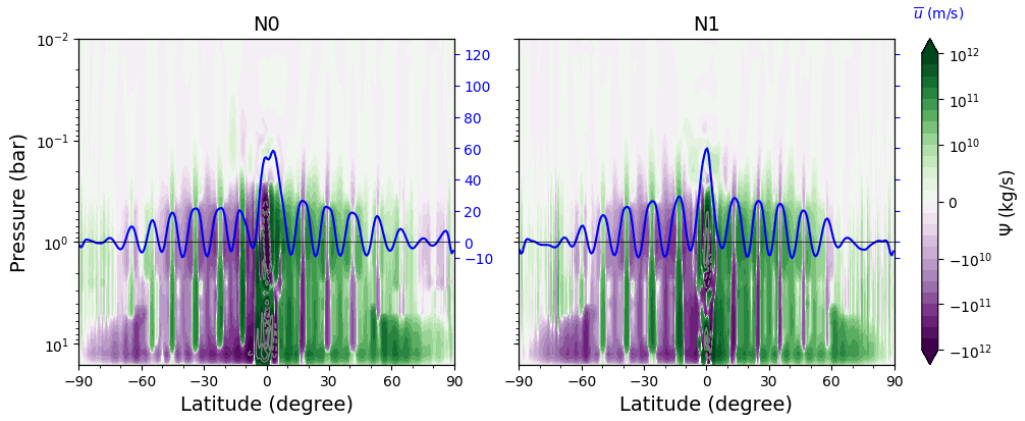


Figure 5.3: Meridional mass streamfunction for the 3D case with and without mushball.

5.2.2 Water and Ammonia Distribution

Fig. 5.4 shows the zonally averaged distribution of vapour and cloud condensates for simulations with and without the mushball parameterisation. Including mushball parameterisation results in significant differences in the vertical and latitudinal structures of these condensibles.

For water vapour, both simulations exhibit significant equatorial depletion, which coincides with reduced cloud density in this region. However, the extent of this depletion is smaller in N0, which produces denser water clouds at the equator. In contrast, N1 produces more localised equatorial clouds. At high latitudes, cloud density is greater in the no-mushball case, while the mushball case exhibits a deeper reservoir of water vapour. These differences are consistent with the mushball mechanism, where water ice formed during moist convection melts with NH_3, combining into larger particles and is transported into deeper layers, reducing the availability of vapour aloft.

The response of ammonia is qualitatively similar, but more complex. In N0, vapour density is enhanced beneath the ammonia cloud layer at latitudes above 60°, and the clouds appear denser than in N1. While both simulations demonstrate significant equatorial depletion of ammonia, the mushball simulation exhibits depletion across a broader latitude range, extending below the water cloud deck. At high latitudes, the mushball case also exhibits a reversal in the vertical ammonia gradient, with volume mixing ratios increasing with depth, a feature reminiscent of Juno MWR retrievals (e.g. *Li et al.* 2020b). However, we must caution that in the published Juno so far, the ammonia volume mixing ratio at high latitudes is not available, and that ammonia is not depleted at the equator.

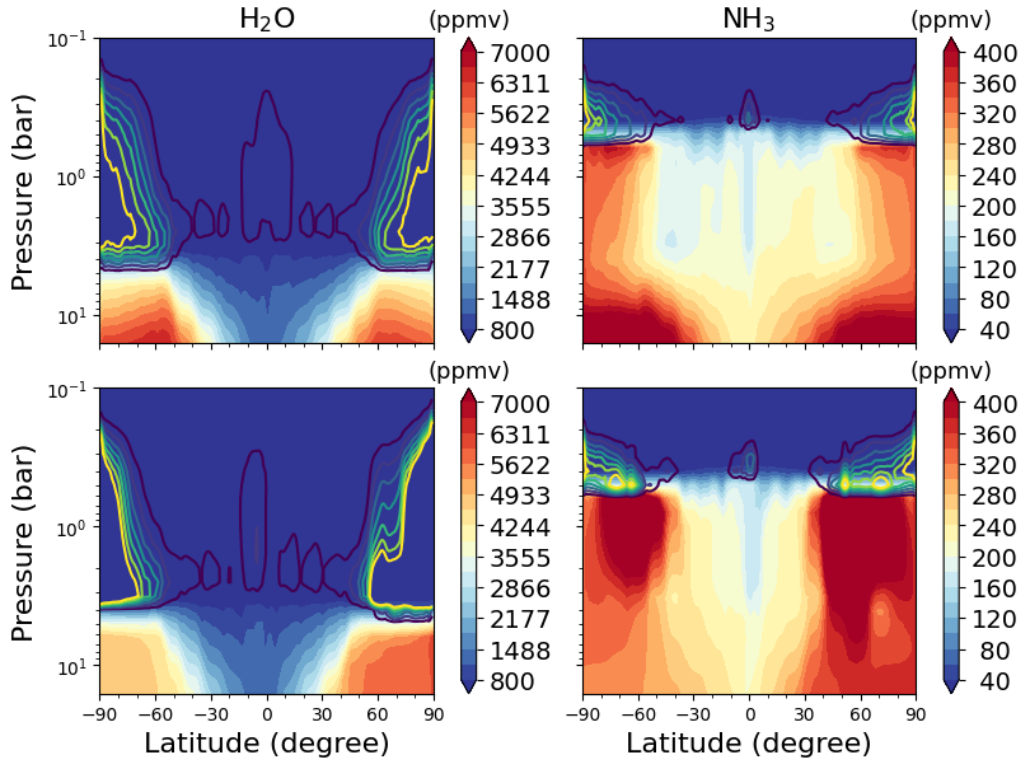
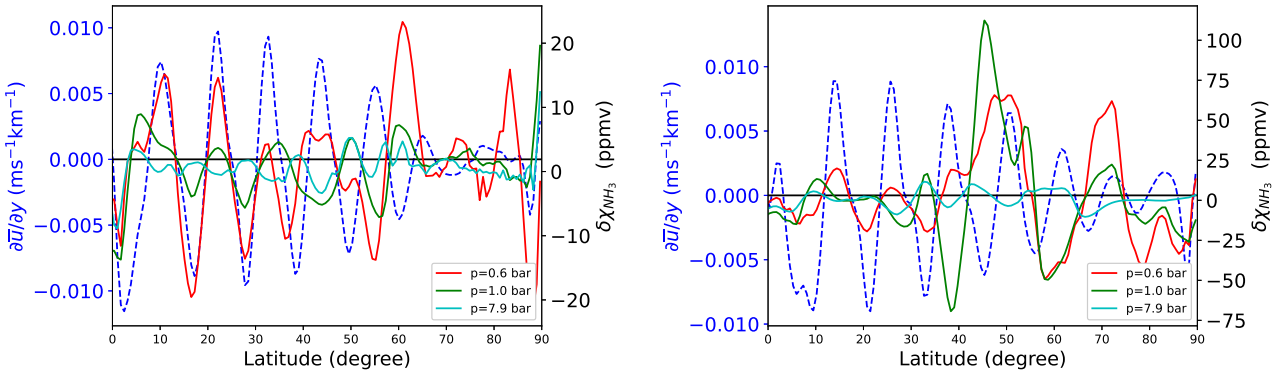


Figure 5.4: Water (left) and ammonia (right) volume mixing ratio for the nominal 3D simulation with (top) and without (bottom) mushball parameterization. The vapour volume mixing ratio for both species is shown in filled contours, and the solid (cloud) volume is represented as line contours. The contours for ammonia ice are spaced linearly from 40 ppmv to 200 ppmv, and the contours for water ice are spaced linearly from 200 ppmv to 1700 ppmv.



(a) With mushball **(b)** Without mushball

Figure 5.5: Zonal mean velocity gradient at 1 bar (blue dashed), $\partial\overline{u}/\partial y$, and the deviation of ammonia vapour volume mixing ratio from a rolling mean at 0.6 bar (red), 1 bar (green) and 7.9 bars (cyan) for the simulation with (left) and without mushball (right). The rolling mean is computed using a 15° latitudinal window to remove the large-scale belt–zone contrast. The deviation highlights correlations with the belt–zone structure, which reverses sign with increasing pressure below 40°, though the pressure level at which this reversal occurs differs between these two simulations.

In addition to these large-scale features, both species exhibit a modest hemispheric asymmetry, particularly in the no mushball case. This case shows increased vapour and cloud density in the northern hemisphere. Since the external forcing and boundary conditions in our setup are hemispherically symmetric, there is no intrinsic reason for such an asymmetry to occur. One possible explanation is that the initial temperature variation, determined by the random seed, is amplified by non-linear feedback in moist convection and tracer transport. However, the precise cause of the asymmetry remains uncertain. We do not perform any further analysis here, since this asymmetry does not affect the qualitative contrast between the mushball and no-mushball simulations. Both simulations also display latitudinal fluctuations in ammonia abundance that suggest belt–zone contrasts. To investigate this further, Fig. 5.5 compares the zonal mean velocity gradient at 1 bar, $\partial\overline{u}/\partial y$, with the deviation of ammonia vapour volume mixing ratio from the moving average over a 15°, $\delta\chi_{\mathrm{NH_3}}$, at three different pressure levels. In the mushball simulation, zones ($\partial\overline{u}/\partial y > 0$) are associated with increased ammonia concentrations at 0.6 and 1 bar, at least within 40° of the equator. At 7.9 bar, increased ammonia concentration is associated with belts. Without mushballs, such a reversal occurs between 0.6 and 1 bar, and the belt–zone contrast weakens substantially.

Overall, the mushball mechanism substantially alters both the vapour and cloud distributions of H_2O and NH_3, enhancing the condensible concentration at deep levels. It also results in a belt–zone contrast that more closely resembles Jupiter's observed structure than the no-

mushball case.

5.2.3 Mushball Properties

Figure 5.6 shows the zonally averaged properties of the mushball scheme for the nominal 3D simulation. Below 50° latitude, mushball formation is confined to a single layer centred near 0.8 bar. Poleward of this latitude, an additional formation layer appears immediately below the main level, albeit with smaller production rates, as indicated by the ammonia source term. The mushball frequency is broadly similar in these two layers. In the upper layer, mushball formation is primarily limited by water availability, whereas in the lower layer, it is controlled by local ammonia concentration. This behaviour contrasts with that observed in the two-dimensional simulations, where, for the same mushball parameters and water abundance, low-latitude production is limited by ammonia and high-latitude production by water (see Fig. 4.10). This difference in behaviour is most likely due to the difference in water distribution in these two cases. In the 3D simulation, water is more abundant at high latitudes, whereas in the 2D simulation, it is more abundant near the equator.

The zonal mean profiles of TCAPE for both simulations, together with the mushball flux for the mushball run, are also shown in Fig. 5.6. Both cases exhibit a similar overall latitudinal distribution: TCAPE reaches its minimum at the equator, remains relatively flat across the tropics, and then rises sharply in the mid- and high-latitude regions. In the southern polar region, TCAPE shows more localised peaks, whereas in the northern polar region, it exhibits a flatter structure. This hemispheric asymmetry mirrors the corresponding asymmetry in the water distribution. There is no systematic difference in the overall amplitude of TCAPE between the two cases. Although values are somewhat higher in the mid to high latitude northern hemisphere in the no-mushball run, they are lower at high southern latitudes. This is in sharp contrast to the 2D simulations, in which TCAPE decreased significantly when mushball processes were included.

As in the two-dimensional case, mushball flux in the three-dimensional simulation remains closely correlated with TCAPE; this reflects the intrinsic coupling between moist convection and mushball production.

Although the ammonia distributions exhibit clear belt-zone contrasts, none of the mushball properties show visible differences between belts and zones. This is probably because the

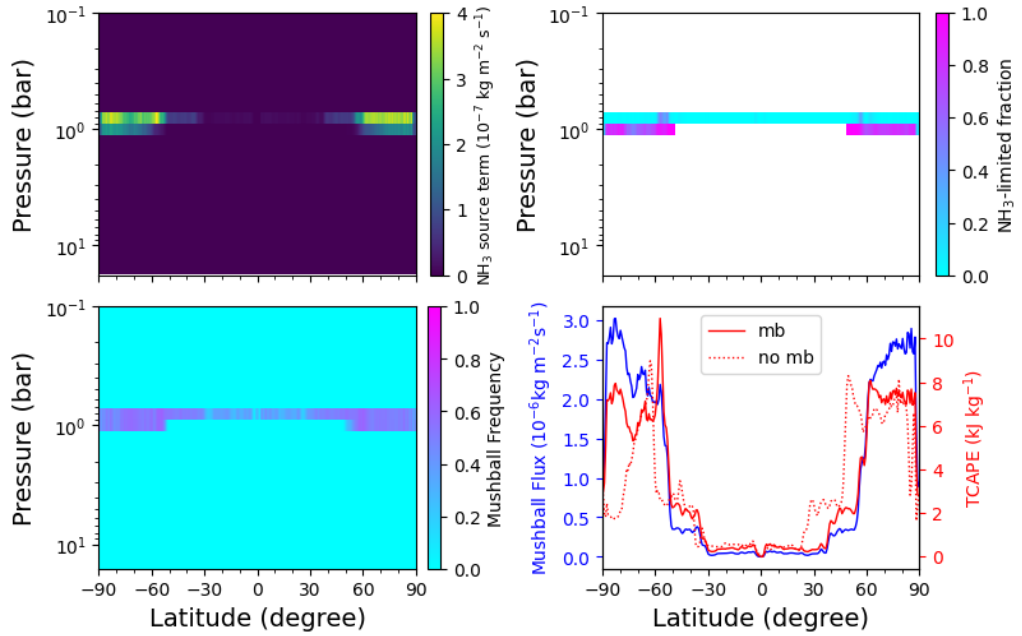


Figure 5.6: Mushball ammonia source term (top left), ammonia-limited fraction (top right), mushball formation frequency (bottom left), mushball flux (blue line, bottom right) and TCAPE (red line, bottom right) for the nominal three-dimensional simulation. In the bottom right panel, the solid line represents the value for the simulation with mushball, and the dotted line represents the value for the simulation without mushball.

diagnostic period used here was relatively short and may not have been long enough to capture the variability associated with the jets.

5.3 Zonal Mean Tracer Balance

In order to assess the role of different processes in shaping the tracer distribution, we examine the Eulerian mean equation for the mass mixing ratio of the tracers. Following *Young and Read* (2019), this can be written as

$$\frac{\partial \overline{q}}{\partial t} = -\frac{\partial(\bar{q}\bar{v})}{\partial y} - \frac{\partial \overline{q'v'}}{\partial y} - \frac{\partial(\bar{q}\bar{\omega})}{\partial p} - \frac{\partial \overline{q'\omega'}}{\partial p} + \overline{G_q} + \frac{\overline{\Delta q_{\mathrm{adj}}}}{\Delta t}, \tag{5.1}$$

where $G_q = G_{\mathrm{q,phase}} + G_{\mathrm{q,sed}} + G_{\mathrm{q,mc}} + G_{\mathrm{q,mb}}$ is the sum of all forcing to the tracer. $G_{\mathrm{q,phase}}$ and $G_{\mathrm{q,sed}}$ is documented in Section 2.4, while $G_{\mathrm{q,mc}}$ and $G_{\mathrm{q,mb}}$ are described in Section 2.5 and Section 4.2.3 respectively. All the terms due to advection are written in Cartesian coordinates for simplicity, as they are evaluated using the discretisation consistent with the GCM's tracer advection scheme, detailed in Appendix A. We omitted $G_{\mathrm{q,reac}}$ as the chemical reaction,

occurring between NH_3 and H_2S, is absent in this setup. The last term, $\overline{\Delta q_{\mathrm{adj}}}/\Delta t$, represents the effect of the three adjustments applied to the tracer field as described in Section 2.4.3. These adjustments cannot be computed directly due to the current model setup, and we ignored these terms when collecting the diagnostics, as they are assumed to be small.

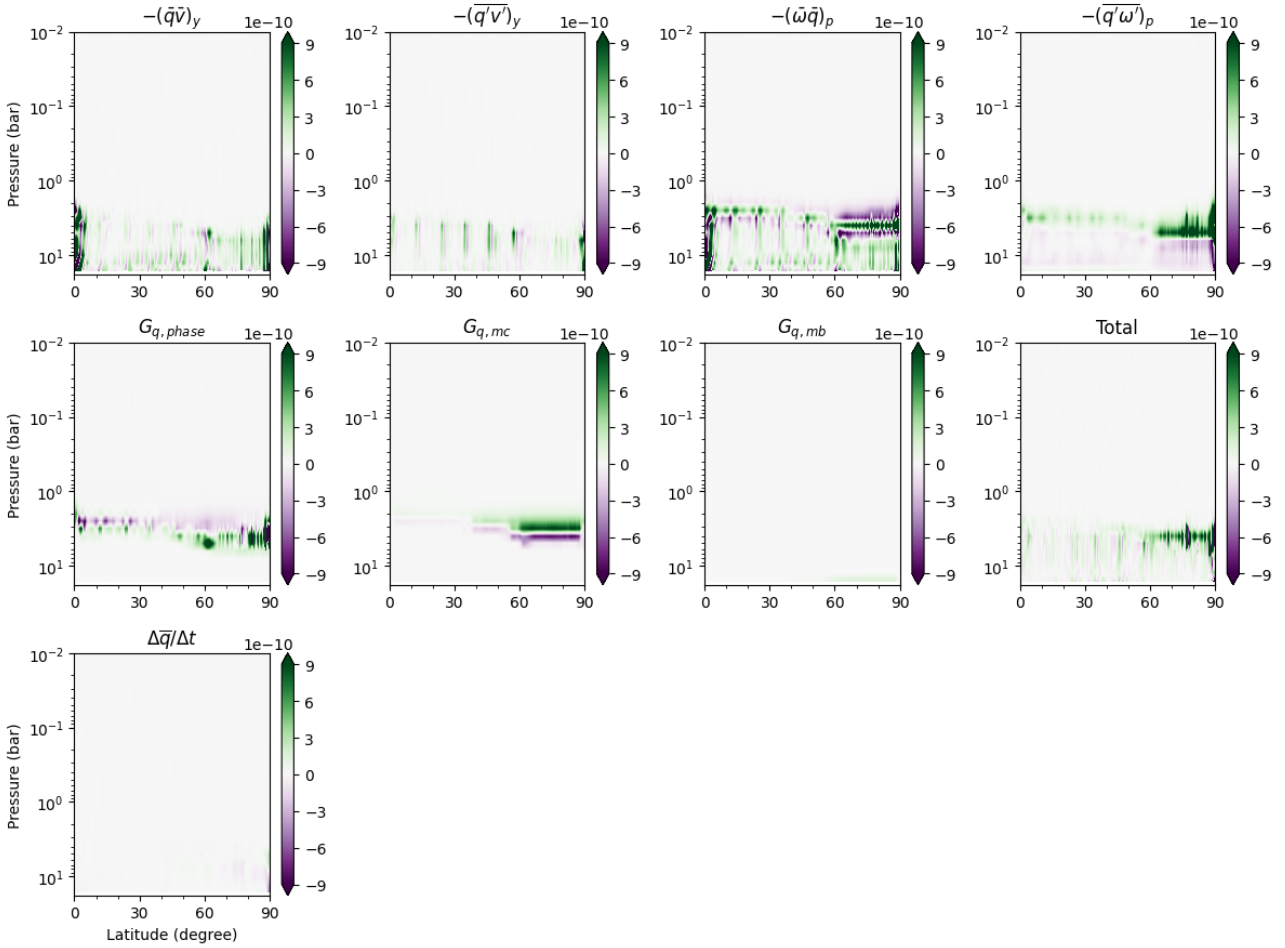


Figure 5.7: Terms in the zonal mean tracer transport equation for water vapour. Panels on the top row are the advection terms. The first three panels on the second row are the tendency due to phase change, moist convection, and mushball transport, respectively. The final panel on the second row is the sum of all seven terms, and the bottom row shows the finite-difference tendency between the start and end of the diagnostic period. The unit of every term in this figure is kg/kg s^{-1}.

For example, Fig. 5.7 and Fig. 5.8 show the terms in the zonal mean tracer equation for water vapour and water ice, respectively, over the diagnostic period. The dynamical terms are computed using snapshots of velocity and tracer mixing ratio. The components of G_q use the time mean saved directly from the GCM.

For water vapour, both the mean and eddy meridional advection are generally weak and noisy. While the mean meridional advection forcing is strong near the equator, this is largely

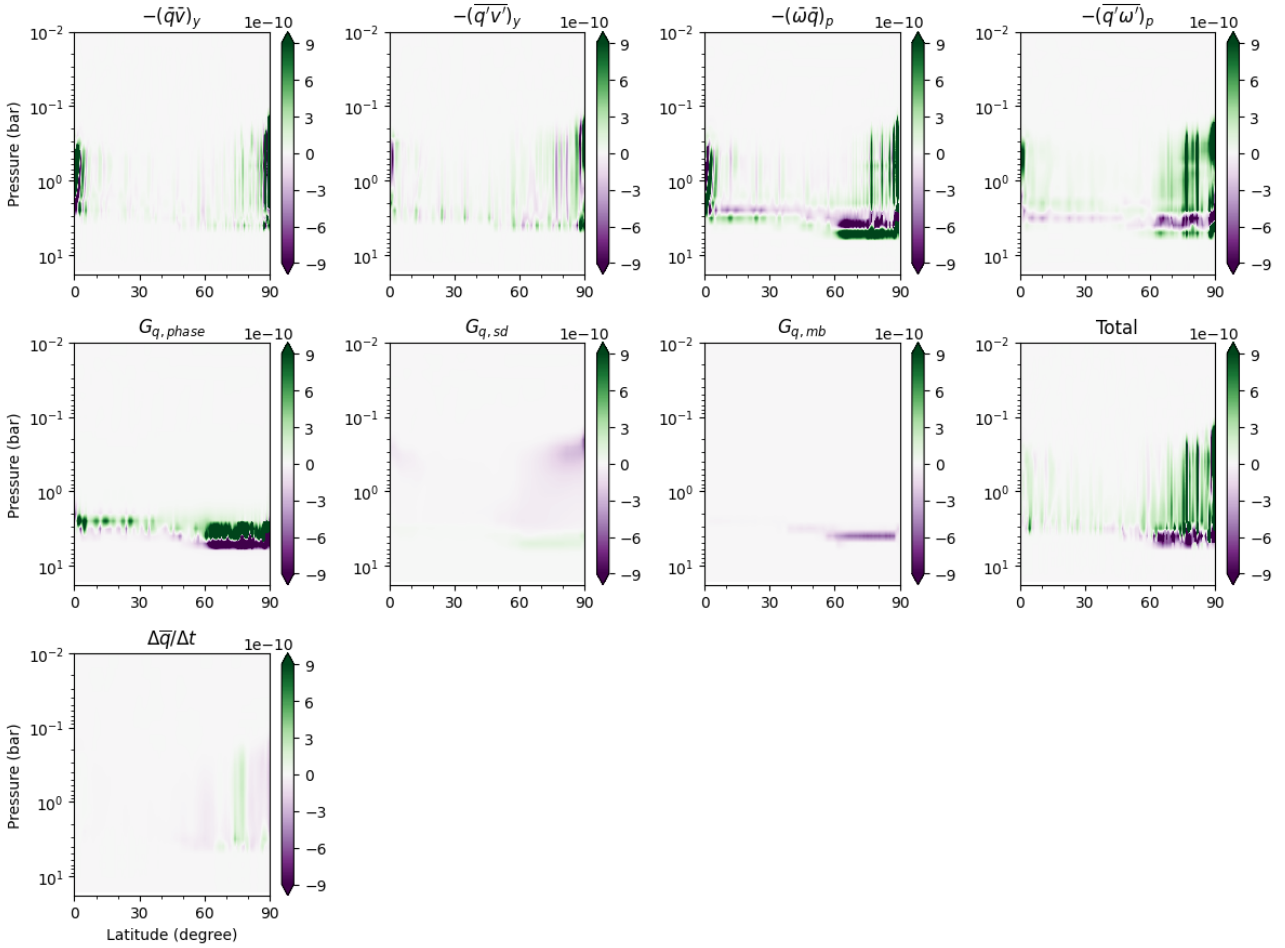


Figure 5.8: Same as Fig. 5.7 but for water ice. The three tendency terms in the second row are phase change, sedimentation and mushball process, respectively.

offset by the mean vertical convergence. Of the transport processes, mean vertical advection is the strongest contributor, exhibiting coherent, vertically banded structures at high latitudes. Eddy vertical transport is weaker than the mean vertical term but shows noticeable signals near the condensation level: positive values are found above the level and negative values below. The net effect is therefore to advect water vapour upwards.

The zonal mean G_q terms show more coherent structures. The phase change tendency is centred near the condensation level, with negative values above and positive values below. This reflects the removal of water vapour through condensation and its reintroduction through evaporation. The moist convection tendency is also centred near the condensation level, with positive values above and negative values below. It is also more uniform across latitudes than the phase change tendency. The net effect of moist convection is to lift water from the condensation level to higher altitudes, consistent with the mechanism described in *Young and*

Read (2019). The mushball-related transport is concentrated in the bottom layer and is much smaller in magnitude than the corresponding water ice tendency, as the water vapour is spread out over a layer with a greater total mass at depth.

The water ice tendency shows a similar overall behaviour in the dynamic terms, although the vertical advection terms are more variable. The phase change term acts in the opposite direction to that of the vapour term and is stronger at high latitudes. These excess tendencies are balanced by phase change to liquid water instead (shown in Appendix A). As with the mushball properties, the tendency terms do not show significant belt-zone contrast, possibly due to the short diagnostic period used.

For both water vapour and condensate, the total forcing obtained by summing all diagnosed terms is considerably larger than the finite-difference tendency, $\Delta q/\Delta t$, between the start and end of the diagnostic period. Due to this lack of closure, it is not possible to establish a quantitative balance between the individual processes. Consequently, we restrict our discussion to qualitative aspects of the tracer evolution. One possible contributing factor is that the advection terms were derived from the relatively sparse sampling of the velocity and tracer fields, which may not capture high-frequency variability adequately. It is also possible that, although the corrective terms were assumed to be small, they have a non-negligible contribution. A more rigorous budget closure would require targeted diagnostics saved at a higher temporal resolution, together with the explicit inclusion of the correction terms.

5.4 W1: Simulation with Greater Domain Depth and Different Temperature Profile

5.4.1 Zonal Wind

Fig. 5.9 presents the zonal-mean zonal velocity and the meridional mass stream function for simulation W1. While the overall morphology of these fields remains similar to that of the nominal depth simulations, several notable differences emerge. Firstly, the amplitudes of the off-equatorial jets are decreased, with retrograde jets being suppressed more than prograde jets (as shown in Fig. 5.10). By contrast, the equatorial jet intensifies markedly. Secondly, the number of prograde jets increases from 15 in the previous runs to 21. This increase is

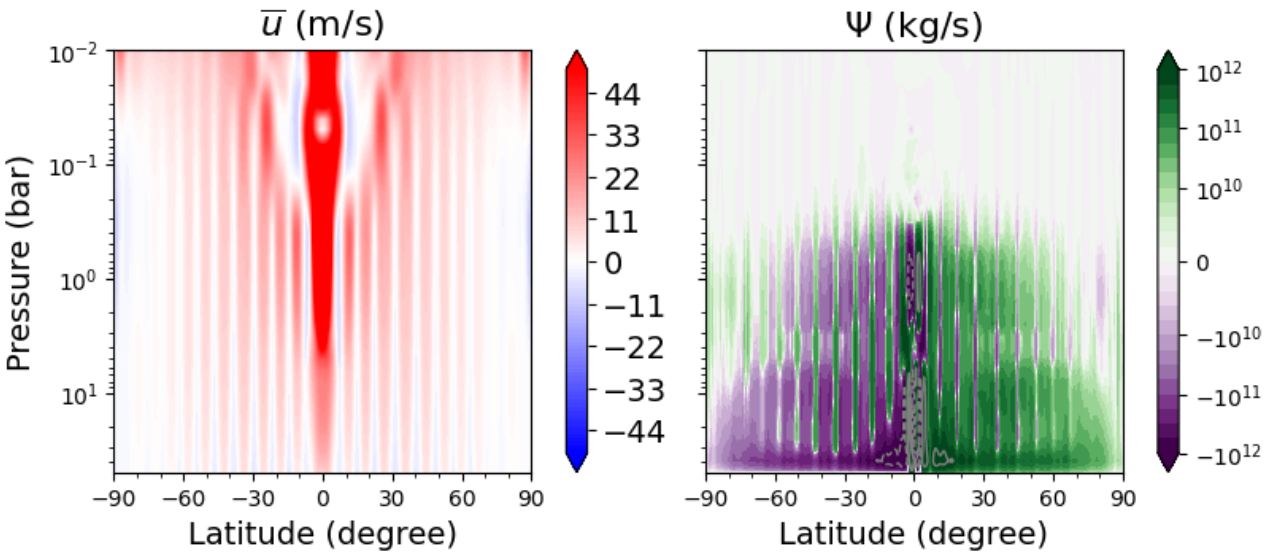


Figure 5.9: Zonal mean zonal velocity profile and the meridional mass stream function for the simulation with deeper domain depth and warmer temperature profile (W1). The height of these figures is slightly increased to reflect the increased domain depth.

accompanied by a corresponding rise in the number of meridional circulation cells, reflecting their link with the jets. The off-equatorial jet also develops a double-peaked structure, a feature that resembles the N0 run. This structure also appears in some of the off-equatorial jets.

The weakened off-equatorial jets in the W1 simulation may be due to both the altered reference optical depth and the increased model depth. The change in reference optical depth results in a colder global mean temperature and may also alter the latitudinal temperature gradient. A reduced lateral temperature gradient weakens the off-equatorial jets, as demonstrated in Chapter 3. Increasing the model depth distributes the eddy momentum fluxes over a thicker column, thereby weakening the vertically averaged shear and reducing the jet amplitude. The

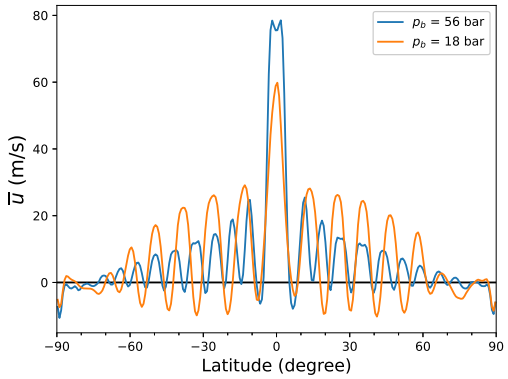


Figure 5.10: Zonal jet profile at one bar for the three-dimensional simulation that extends to 56 bars (blue line) and to 18 bars (orange line).

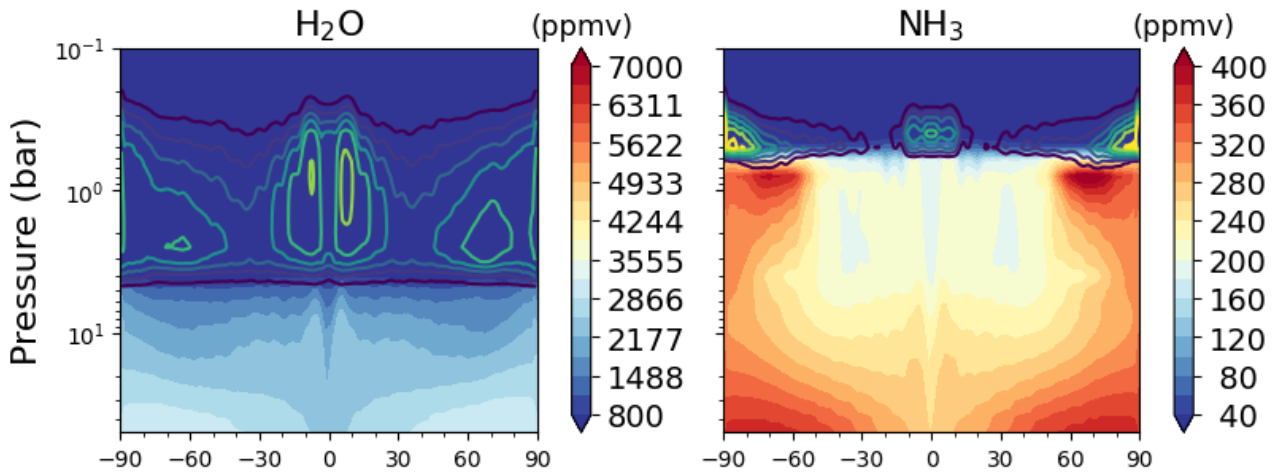


Figure 5.11: Pressure-latitude profile of zonal mean water and ammonia volume mixing ratio for the deeper and warmer three-dimensional simulation. The colour scale and contour spacing are the same as in Fig. 5.4.

narrowing of the jets is consistent with their reduced strength since the meridional jet scale, determined by the Rhines length, depends on the characteristic flow speed. The reader is referred to Section 3.3.1 for a more detailed discussion of this relationship.

5.4.2 Tracer Distribution

Fig. 5.11 shows the zonally averaged volume mixing ratio of water and ammonia in this simulation. The ammonia cloud is spread more uniformly across latitudes than in the previous case. The ammonia vapour distribution has the same overall structure as in the nominal depth simulations: depletion at the equator and mid-latitudes, and enhanced vapour abundance beneath the cloud at high latitudes. As expected, the depletion now extends to greater depths due to the mushball transporting ammonia to the model bottom, now at a higher pressure. The reversal in the belt–zone contrast within 40∘ persists, although the transition now occurs at a greater depth in the atmosphere and is only apparent down to approximately 32 bar, as shown in Fig. 5.12. Above 40∘, the reversal is not observed, where an increased ammonia mixing ratio is always associated with belts.

The distribution of water has changed significantly compared to the previous case. While the vapour remains relatively depleted near the equator, the enhancement at high latitudes becomes less pronounced, and the cloud deck does not accumulate as strongly. By contrast, the cloud density at the equator is higher than at high latitudes.

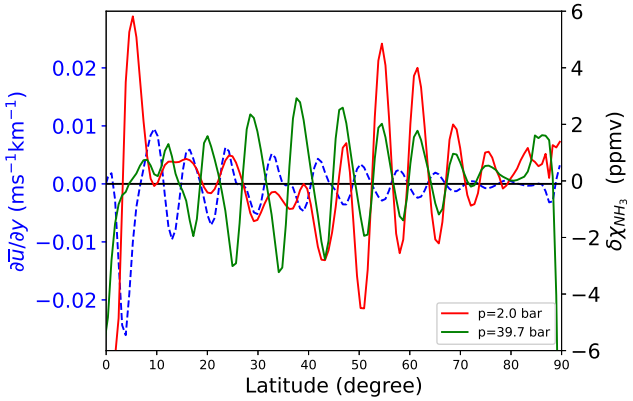


Figure 5.12: Zonal mean velocity gradient (blue dashed), $\partial\overline{u}/\partial y$, and deviations of the ammonia vapour volume mixing ratio from a rolling mean at 2.0 bar (red) 6.3 (green) and 31.5 bar (cyan) for the deeper and warmer three-dimensional simulation. The rolling mean window is reduced to 10° to reflect the reduction in jet width.

5.5 Summary and Discussion

The three-dimensional simulations presented in this chapter build upon the two-dimensional experiments described in Chapter 4. The main conclusions are as follows.

First, the large-scale dynamics are largely unaffected by the inclusion of mushballs. The zonal wind and the meridional overturning circulation retain the same overall structure in both the mushball (N1) and no mushball (N0) simulations, with only minor differences, such as the shallow equatorial velocity dip and the reversal of a polar overturning cell. Therefore, mushball processes primarily affect tracer distributions directly by transporting them vertically, rather than indirectly by altering the mean flow. This is expected in the present setup, since water affects the circulation through latent heating and moist convection, while cloud radiative feedbacks are not represented.

Second, the simulation with mushballs results in an ammonia distribution more similar to the Juno MWR observations, with strongly depleted ammonia vapour in the mid-latitudes. The simulations also produce equatorial depletion, whereas Juno indicates a high concentration at the equator. This discrepancy may reflect limitations in the current representation of mushball parameterisation or the model's tendency to overestimate the strength of the circulation in the region near the equator (see *Young et al.* (2019b) for a more detailed discussion). Including mushballs enhances the deep vapour reservoir for water and reduces high-latitude cloud accumulation, in line with the expected downward transport.

The effect of mushballs on tracers and the properties of the mushball scheme in three-dimensional simulations are broadly consistent with those in two dimensions. However, there are also some important differences. Firstly, in three dimensions, TCAPE is not systematically reduced by mushballs. Additionally, the limiting factor for mushball formation is different.These contrasts indicate that, while two-dimensional models are useful for testing parameter sensitivities, three-dimensional simulations are necessary to allow the belt-zone structure to emerge and fully evaluate the impact of mushball on tracer distribution under realistic dynamical conditions.

The deeper, warmer run (W1) produces broadly similar results to the N1 run, though the jet structure exhibits narrower, weaker off-equatorial jets. The origin of this difference is unclear, as both the reference optical depth and the domain depth were modified in this configuration. Therefore, it is difficult to determine whether the change reflects an altered temperature gradient, an increased column mass, or the combined influence of both. To allow a more direct comparison with the N1 run, adjustments to other model parameters may be necessary to maintain dynamical consistency.

One particularly interesting aspect of the results is the reversal of the ammonia belt–zone contrast at depth. To our knowledge, this is the first time that such behaviour has been reproduced in a GCM. Both the mushball and no-mushball runs exhibit this reversal, but it occurs at a pressure close to the water condensation level in the former, which is more consistent with what *Fletcher et al.* (2020) suggested based on observations. In the deep simulation, however, the reversal occurs at greater depths. This indicates the reversal is likely due to a combination of the mushball process and large-scale circulation. Attempts to understand the tracer distribution using the zonal mean tracer equation were inconclusive due to the short diagnostic period and the budget not closing. Addressing these issues will require more frequent sampling, the explicit computation of correction terms and a longer diagnostic period. A more complete zonal-mean budget, or alternative diagnostics of tracer transport by the large-scale dynamics, would be valuable, given that mushball formation and evolution depend on the availability of both ammonia and water. More generally, these diagnostics are also required to fully interpret the resulting tracer structures.

Chapter 6

Summary and Outlook

6.1 Thesis Summary

6.1.1 Latitudinally-varying Internal Heat Flux

We demonstrated that latitudinal variation in internal heat flux plays a significant role in determining the dynamics of a weather-layer model of Jupiter's atmosphere. Increasing the latitudinal internal heat flux gradient by raising the parameter a_f reduces the equator-to-pole temperature contrast. In the observationally inferred case with the highest a_f, this temperature contrast is eventually reversed. To study the dynamics in a case with no equator-to-pole temperature contrast, a simulation is run under a deep adiabat setup with a temperature similar to that in the varying heat flux run. The overall latitudinal profile of the equivalent heat flux from this simulation closely resembles that of the prescribed case, but arises primarily from convective flux.

The change in thermal conditions leads to the weakening of the mid-latitude jets and their eventual disappearance when the latitudinal temperature contrast disappears, as seen in the deep adiabat case. For the highest a_f case, retrograde off-equator jets are observed. In contrast, the equatorial jet persists across all configurations. Both zonal and eddy kinetic energy decrease with increasing a_f. The Lorenz energy cycle analysis shows that the breakdown of mid-latitude jets is linked to reduced baroclinic instability, as indicated by declining C_K values.

Water vapour and ice profiles remain qualitatively similar across runs, but their latitudinal distribution varies with a_f. Cases with the highest a_f exhibit enhanced polar concentrations, whereas those with low a_f have a higher concentration of water just off the equator.

These experiments are not intended to reproduce Jupiter's present state directly, but instead to explore how non-uniform interior heat flux can regulate baroclinicity, eddy activity, and jet profile in the weather layer. This perspective becomes increasingly relevant as Juno extends observational constraints to greater depths, highlighting the need to understand how deep thermal forcing couples to the observable circulation.

6.1.2 Mushball

We have developed a simple parameterisation scheme for water-ammonia hailstones. When coupled with a self-consistent moist convection scheme, the mushball scheme can produce a depletion of a similar magnitude to that observed in the Juno observations in the two-dimensional simulation. In contrast, the no-mushball case sees an enhancement of ammonia concentration in the polar region. The mushball mechanism suppresses moist convection activity by reducing the availability of water near the water condensation level.

Experimenting with different mushball parameters shows their importance on tracer distribution. Reducing the efficiency of the mushball formation results in a water and ammonia distribution that progressively resembles that of the no mushball case, while increasing the ammonia fraction in the mushball leads to more uniform ammonia depletion and reduced water transport. Increasing water abundance enhances moist convection and shifts the mushball formation to a more ammonia-limited regime. The two-dimensional simulation is a computationally efficient way of exploring parameter sensitivity and helps to identify ranges for use in three-dimensional simulations. However, the setup prohibits the spontaneous formation of alternating zonal jets and therefore the emergence of belt-zone contrast in the tracer distribution.

The behaviour of the mushball scheme differs slightly in the three-dimensional simulation: zonal jets and meridional circulation remain largely unaltered by the inclusion of the mushball parameterisation. Conversely, the distribution of water and ammonia changed significantly when the mushball parameterisation was included. While mid-latitude ammonia depletion similar to Juno observations is seen in the mushball case, our model shows equatorial depletion, which contrasts with both the two-dimensional simulation and the Juno MWR result.

In contrast to the two-dimensional case, convective activities are not significantly altered by the inclusion of the mushball. This highlights that, while two-dimensional simulations are important for parameter exploration, the results need to be confirmed in 3D to capture the full dynamic feedback. The simulation in a warmer and deeper configuration produced weaker, narrower off-equatorial jets, reflecting changes in latitudinal temperature contrasts and greater column masses. Taking this into account, the tracer response remains broadly similar to that in the nominal case.

A particularly notable result is the reversal of the belt–zone contrast in ammonia mass mixing ratio with depth within 40° of the equator. This feature is exhibited by both the

mushball and no-mushball runs, though in the nominal case, it occurs at shallower levels when mushballs are included, which is more consistent with the inference drawn from observations. In the deep run, this reversal occurs at a much deeper level. Although the precise mechanism resulting in this could not be confirmed due to the unclosed tracer budget, it most likely reflects a complex interaction between the mushball process and large-scale circulation.

Overall, our simulations show that the mushball mechanism provides a physically plausible explanation for the mid-latitude ammonia depletion observed by Juno. However, the persistence of equatorial ammonia depletion in the model, in contrast to the equatorial enhancement inferred from Juno observations, highlights a key discrepancy that need addressing within the present framework.

6.2 Limitations and Future Work

Our work uses a general circulation model to explore the effect of latitudinally varying deep thermal forcing and mushball transport on Jupiter's dynamics and tracer distributions. While GCMs are essential for capturing the coupled, three-dimensional nature of these processes, their intrinsic complexity can make it difficult to isolate the underlying physical mechanisms. This motivates the complementary use of simplified analytic and idealised models to further elucidate the fundamental processes driving the behaviour observed in the GCM and to understand their relevance to observations.

Within the GCM framework presented in this thesis, several aspects could also be improved, some of which have already been discussed in the individual chapters. Here, we summarise the key limitations of our work and outline directions for future work.

6.2.1 Internal Heat Flux

The internal heat flux profiles tested in Chapter 3 were based on the observationally inferred profile of *Pirraglia* (1984), which is available only within ±50° of the equator. It would be valuable to explore an alternative profile at high latitude. Further work should also include belt–zone scale variations in flux, which may be related to oscillatory processes as suggested by *Hori et al.* (2023).

Our work also motivates coupling deep convection models with a weather layer model. In

our framework, further improvements to the treatment of the lower boundary conditions are required. This is important because the vertical domain of the simulation used in this chapter extends only to 18 bar, which may be insufficient to capture interactions with Jupiter's deep convective interior. This has a more significant impact for the 'deep adiabat' configuration, where the assumption of the 'deep thermostat' used for this configuration is not directly supported by observations at present, at least not at the 18 bar level. Consequently, the forcing towards the fixed potential temperature at the lower boundary may be unrealistically strong. Future work should therefore explore extending the vertical domain and testing alternative thermal boundary conditions. Additionally, velocity forcing at the bottom of the domain can also be explored to study the impact of the deep jets on weather layer dynamics (*Thomson* 2020).

6.2.2 Mushball Parameterisation

The mushball scheme employed here is highly simplified and can be improved in several different areas. First of all, the potential temperature forcing associated with mushball–related fluxes has not been included. This prevents assessment of its impacts on the atmospheric energetics. The current scheme also neglects the gradual accumulation of water ice through water ice clouds. The mushball parameters are fixed rather than dependent on the local environment. Further work can incorporate the one-dimensional evolution models, such as the one in G20a. Our parametrisation also needs to be calibrated against convection–resolving simulations on the downdraft properties and laboratory measurements on the microphysical properties of water-ammonia hailstone.

For the simulations, extending the lower boundary to ∼100 bar would allow better comparison with Juno MWR retrievals. In addition, the vertical resolution, at least around the cloud levels, should be increased to resolve the mushball formation layers, which are currently confined to 1 or 2 layers in the nominal simulations. Increasing the vertical resolution will also help to resolve the cloud scale height, as noted by *Young et al.* (2019b).

6.2.3 JasonGCM Formulation

The JasonGCM used in this thesis also requires some improvement. First, the mass of water and ammonia is not included in the equation of state. While the moist convection scheme

accounts for the molecular weight effect of water, this treatment remains incomplete. This has significant implications for static stability, as demonstrated in Section 3.5.3. A more consistent approach would require incorporating the weight of condensible species directly into Eq. (2.5). This may require redesigning the tracer implementation, although ad-hoc corrections are also possible. Second, moist convection and cloud microphysics are represented using idealised schemes with fixed parameters. While some observational inferences constrain the effective radius of cloud particles, its connection to the effective size for sedimentation remains uncertain. Some further limitations and possible improvements on these two schemes can be found in *Young and Read* (2019). Third, the radiative transfer scheme employed here is simplified and not fully calibrated. Future studies should compare the thermal forcing with results of more sophisticated radiative transfer schemes (e.g., *Guerlet et al.* 2020; *Li et al.* 2018a) to design a more accurate representation of the radiative process. In addition, radiative effect of clouds should be included, as recent exoplanet GCM studies showed that radiatively active cloud can alter cloud distribution and thermal structure (e.g., *Malsky et al.* 2024; *Roman et al.* 2021).

As discussed before, both the simulations on interior heat flux and mushball will benefit from extending the model to a greater pressure level. The challenge on this is twofold. First, the deep three-dimensional simulation (W1) suggested that the jet weakens with increasing model depth, implying that additional adjustments, such as reducing the bottom drag, are required. However, modifying the bottom drag can significantly alter jet morphology, as demonstrated in *Liu and Schneider* (2015). Second, the integration time required to reach equilibrium will increase substantially due to the increasing radiative timescale with depth. Overcoming these challenges requires experiments with model configurations and techniques to accelerate the equilibration.

6.2.4 Extension to Other Planets

Both the work on latitudinally varying internal heat flux and the mushball parameterisation scheme can be extended to other giant planets. Recent work by *Wang et al.* (2024) indicated that Saturn also exhibits significant latitudinal variation in internal heat flux, with a strong seasonal dependence. Running similar simulations for a Saturn-like condition would therefore provide a valuable comparative test.

The mushball mechanism may be relevant for ice giants and for exoplanets with ammonia-

rich atmospheres. It has been suggested that the mushball process could operate more efficiently on Neptune and Uranus, and could therefore be responsible for the ammonia depletion in their atmospheres (*Guillot* 2021). With an improved mushball scheme, future work could extend the current model to these ice giants. The current estimation suggests that the water cloud could extend down to thousands of bars (*Hueso et al.* 2020), which can be a challenge to the JasonGCM. Application to exoplanets requires running the GCM in a broader range of planetary conditions. Such experiments would help to identify the atmospheric regimes under which ammonia is observable and to assess how the measured ammonia abundance reflects the nitrogen abundance in the planetary interior. More generally, the mushball parameterization scheme developed here, can be applicable to a wider range of planetary atmospheres with other mixed phase clouds. While the mushball mechanism relies on the specific phase properties of the water–ammonia mixture that allow large, dense droplets to form, analogous mixed-phase processes involving other condensate pairs may operate on hotter worlds.

Appendix A

The Eulerian Mean Tracer Equation

A.1 Advection terms in the Eulerian mean tracer equation

The advection operator is discretised as

$$\mathcal{A}_c \Delta r_f h_c G^{\tau}_{\text{adv}} = \delta_i F_x + \delta_j F_y + \delta_k F_r, \tag{A.1}$$

where $\mathcal{A}_c$ denotes the area of the grid cell surrounding θ points, Δr_f is the pressure thickness between adjacent θ-cell faces, h_c is the fraction of the cell depth available for flow, which is unity throughout our simulations. The operator δ represents the discrete difference, and F denotes the area-integrated flux, whose form depends on the choice of the advection scheme.

For tracer transport, we employ the second-order flux-limiter scheme. Following Eq. 2.151 of the MITgcm manual, the limited flux in any coordinate direction can be expressed as

$$F = U\overline{\tau}^{i} - \frac{1}{2}(1 - \psi + c\psi)|U|\delta_i \tau, \tag{A.2}$$

where U is the volume flux[1], τ is the tracer mass mixing ratio, $c = |u|\Delta t/\Delta x$ is the Courant number, and the function ψ is the flux limiter. In the MITgcm, the superbee limiter, $\psi(r) = \max[0, \min[1, 2r], \min[2, r]]$, is applied. The slope ratio

$$\begin{aligned} r &= \frac{\tau_{i-1} - \tau_{i-2}}{\tau_i - \tau_{i-1}} \quad \forall u > 0, \\ &= \frac{\tau_{i+1} - \tau_i}{\tau_i - \tau_{i-1}} \quad \forall u < 0, \end{aligned} \tag{A.3}$$

measures how smooth or sharp the local tracer profile is. The first term on the right-hand side of Eq. (A.2) is identical to the discretisation used in the centred second-order advection–diffusion

[1]The MITgcm manual denotes this quantity by u, but the implementation uses U. We adopt the latter, which is also consistent with the remainder of the manual.

scheme, which is also the default advection scheme for potential temperature. Following *Young and Read* (2019), the contribution of this centred second-order advection–diffusion term to the first four terms of Eq. (5.1) can be written as

$$\left[\frac{\partial(\overline{q}\cos\phi)}{a\cos\phi\partial\phi}\overline{v}\right]_{\mathrm{c2},j} = \frac{\Delta x_{g,j+1}\,\overline{v}_{j+1}\,\left(\overline{\tau}_{j+1}+\overline{\tau}_j\right) - \Delta x_{g,j}\,\overline{v}_j\,\left(\overline{\tau}_j+\overline{\tau}_{j-1}\right)}{2\,\mathcal{A}_{c,j}}, \tag{A.4}$$

$$\left[\frac{\partial\left(\overline{q'v'}\cos^2\phi\right)}{a\cos^2\phi\partial\phi}\right]_{\mathrm{c2},j} = \frac{\Delta x_{g,j+1}\,\overline{v'_{j+1}\,\left(\tau'_{j+1}+\tau'_j\right)} - \Delta x_{g,j}\,\overline{v'_j\,\left(\tau'_j+\tau'_{j-1}\right)}}{2\,\mathcal{A}_{c,j}}, \tag{A.5}$$

$$\left[\frac{\partial\overline{q}}{\partial p}\overline{\omega}\right]_{\mathrm{c2},k} = \frac{w_{b,k+1}\,\left(\overline{\tau}_{k+1}+\overline{\tau}_k\right) - w_{b,k}\,\left(\overline{\tau}_k+\overline{\tau}_{k-1}\right)}{2\,\Delta r_{f,k}}, \tag{A.6}$$

$$\left[\frac{\partial\overline{q'\omega'}}{\partial p}\right]_{\mathrm{c2},k} = \frac{\overline{w'_{b,k+1}\,\left(\tau'_{k+1}+\tau'_k\right)} - \overline{w'_{b,k}\,\left(\tau'_k+\tau'_{k-1}\right)}}{2\,\Delta r_{f,k}}. \tag{A.7}$$

We refer to the second term on the right-hand side of Eq. (A.2) as the additional flux-limiter term. and we simplifying it by defining $B = -\frac{1}{2}(1-\psi+c\psi)$, then discretizing gives, in the meridional direction,

$$G^{\tau}_{\mathrm{adv},j} = \left(\Delta x_{\tilde{j}+1}|v_{\tilde{j}+1}|B_{\tilde{j}+1}(\tau_{j+1}-\tau_j) - \Delta x_{\tilde{j}}|v_{\tilde{j}}|B_{\tilde{j}}(\tau_j-\tau_{j-1})\right)/\mathcal{A}_{c,j}. \tag{A.8}$$

Decomposing this into zonal mean and eddy component is non-trivial with the B term, as it introduces additional cross terms that do not vanish when performing zonal averaging. The more sensible way is to group B and v when doing the decomposition. in this way $|v|B$ acts as a modified velocity. The decomposition, therefore, gives:

$$\left[\frac{\partial(\overline{q}\cos\phi)}{a\cos\phi\partial\phi}\overline{v}\right]_{\mathrm{lim},j} = \frac{\Delta x_{g,j+1}\,\overline{|v|_{j+1}B_{\tilde{j}+1}}\,\left(\overline{\tau}_{j+1}-\overline{\tau}_j\right) - \Delta x_{g,j}\,\overline{|v|_j B_{\tilde{j}}}\,\left(\overline{\tau}_j-\overline{\tau}_{j-1}\right)}{\mathcal{A}_{c,j}}, \tag{A.9}$$

$$\left[\frac{\partial\left(\overline{q'v'}\cos^2\phi\right)}{a\cos^2\phi\partial\phi}\right]_{\mathrm{lim},j} = \frac{\Delta x_{g,j+1}\,\overline{(|v|_{j+1}B_{\tilde{j}+1})'\,\left(\tau'_{j+1}-\tau'_j\right)} - \Delta x_{g,j}\,\overline{(|v|_j B_{\tilde{j}})'\,\left(\tau'_j-\tau'_{j-1}\right)}}{\mathcal{A}_{c,j}}, \tag{A.10}$$

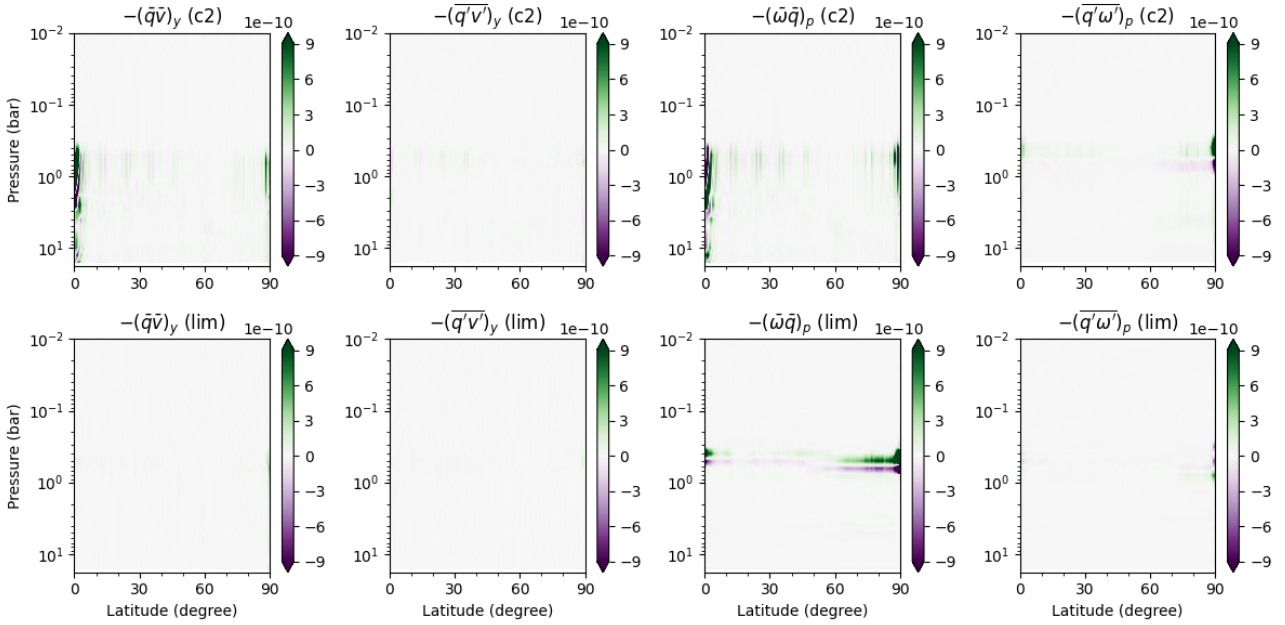


Figure A.1: Components of the advection terms for ammonia vapour. The term equivalent to the centred second-order advective diffusion scheme is on the top row, and the additional term is on the second row.

Similarly, decomposing the vertical advection terms gives:

$$\left[\frac{\partial \overline{q}}{\partial p}\,\overline{\omega}\right]_{\mathrm{lim},k} = \frac{\overline{|\omega|_{k+1}B_{k+1}}\;\left(\overline{\tau}_{k+1}-\overline{\tau}_k\right) - \overline{|\omega|_k B_k}\;\left(\overline{\tau}_k-\overline{\tau}_{k-1}\right)}{\Delta r_{f,k}}, \tag{A.11}$$

$$\left[\frac{\partial \overline{q'\omega'}}{\partial p}\right]_{\mathrm{lim},k} = \frac{\overline{\left(|\omega|_{k+1}B_{k+1}\right)'\left(\tau'_{k+1}-\tau'_k\right)} - \overline{\left(|\omega|_k B_k\right)'\left(\tau'_k-\tau'_{k-1}\right)}}{\Delta r_{f,k}}. \tag{A.12}$$

Fig. A.1 compares the contributions of the centred second-order terms and the additional flux-limiter terms to the zonal-mean tracer equation of ammonia vapour. In most cases, the additional term is an order of magnitude smaller than the centred second-order contribution. An exception occurs in the case of the convergence of zonal mean vertical advection, where the additional term becomes comparable to, or even exceeds, the centred second-order term near the cloud base. This enhanced contribution reflects the sharp vertical gradient in the ammonia mass mixing ratio near the cloud base, and highlights the importance of using the complete flux-limiter discretisation when evaluating advection terms.

A.2 Additional Zonal Mean Tracer Equation Plots

Fig. A.2 and Fig. A.3 show the terms in the zonal mean tracer equations for ammonia vapour and ice, respectively. An important point to note is that the phase change term largely balances the moist convection term. This is because the moist convection scheme does not handle the phase change of ammonia transported by the scheme directly; therefore, the ammonia vapour transported above the condensation level, and the ice transported below, will contribute to the phase change tendency.

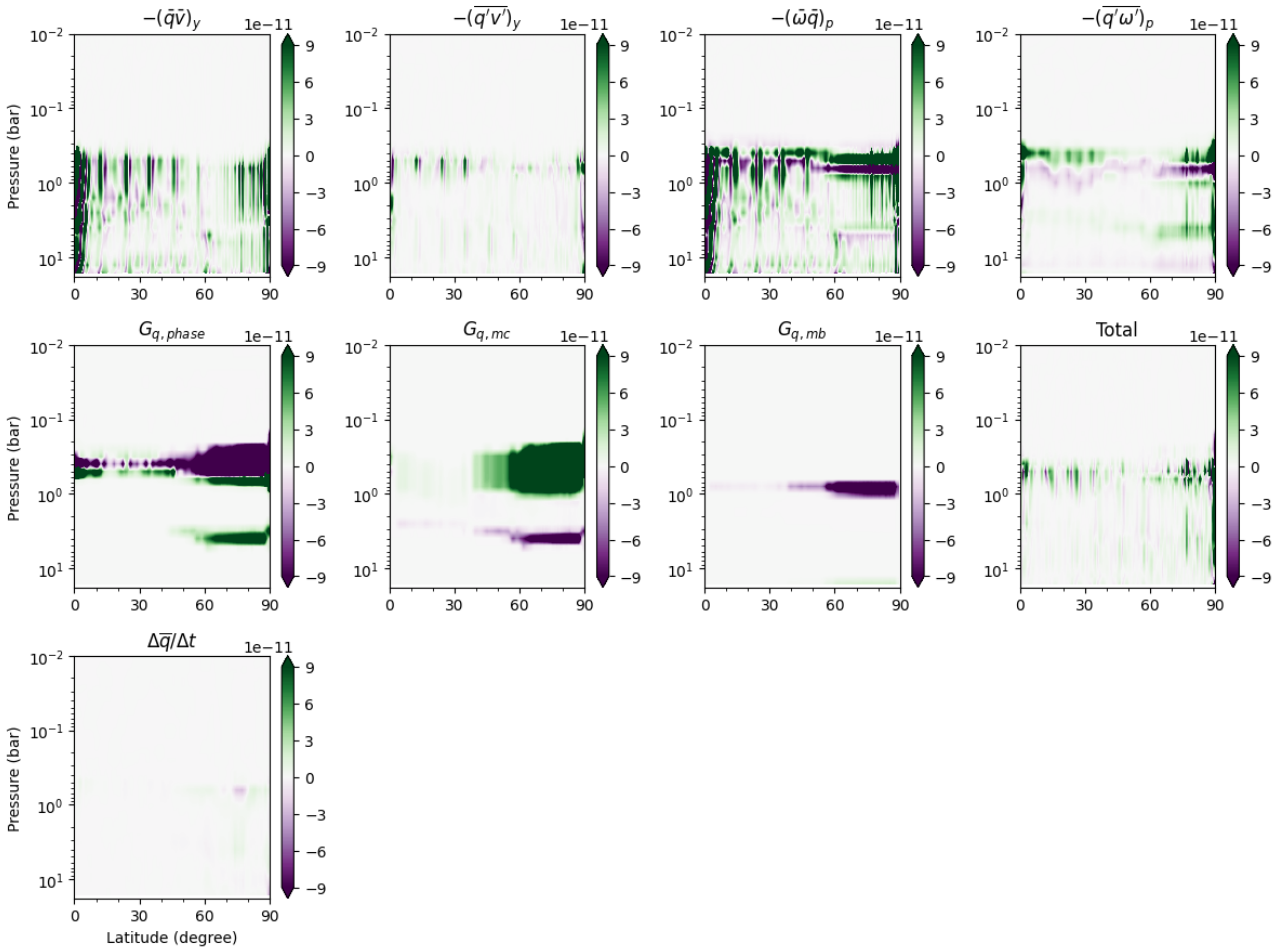


Figure A.2: Terms in the zonal mean tracer transport equation for ammonia vapour. Panels on the top row are the advection terms. The first three panels on the second row are the tendency due to phase change, moist convection, and mushball transport, respectively. The final panel on the second row is the sum of all seven terms, and the bottom row shows the finite-difference tendency between the start and end of the diagnostic period. The unit of every term in this figure is kg/kg $s^{-}1$.

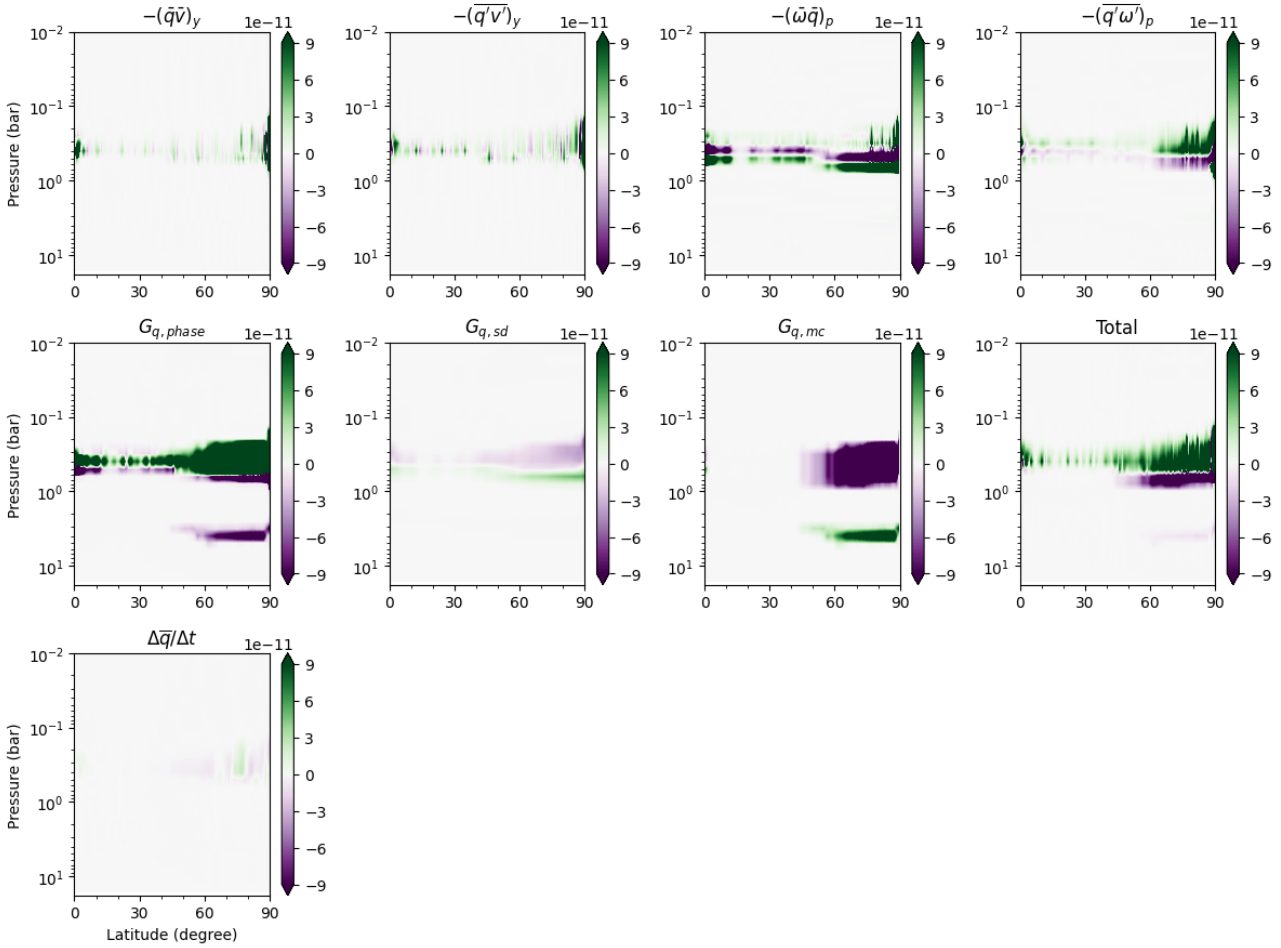


Figure A.3: Same as Fig. A.2 but for ammonia ice. The three tendency terms in the second row are phase change, sedimentation and moist convection, respectively.

Fig. A.4 shows the terms in the zonal mean tracer equation for water liquid. This term is concentrated in the polar region, as this is the only region where there is significant liquid water.

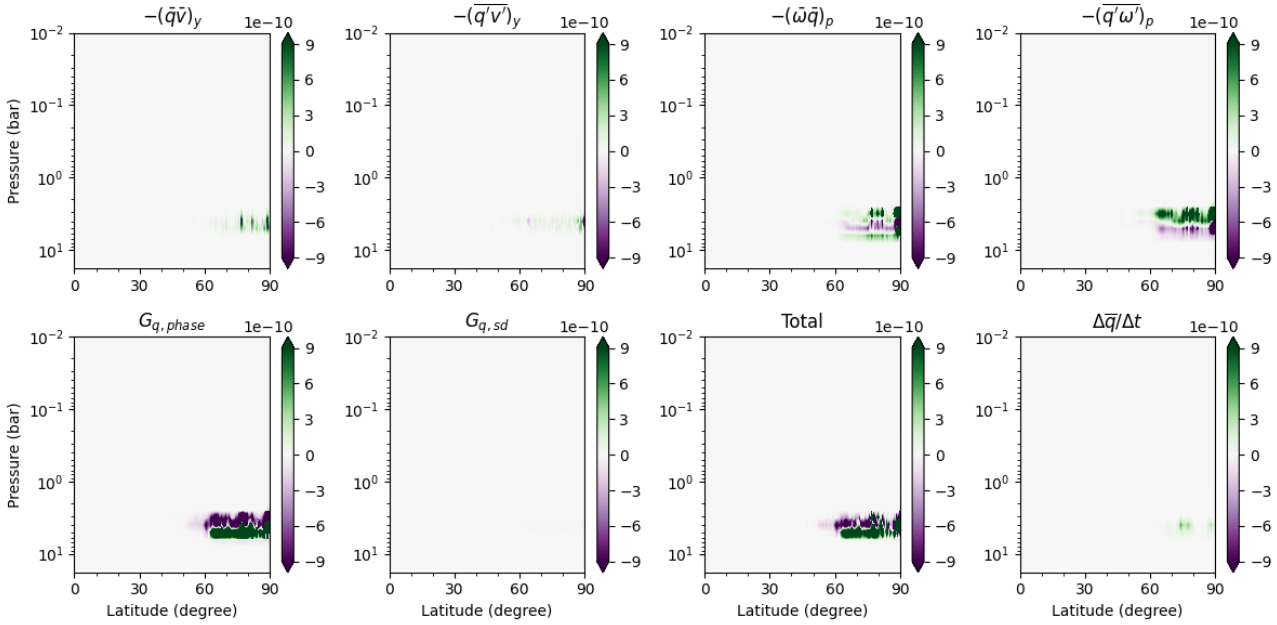


Figure A.4: Same as Fig. A.2 but for water liquid cloud. The two tendency terms in the second row are phase change and sedimentation.

Bibliography

Abalos, M., W. J. Randel, D. E. Kinnison, and R. R. Garcia, Using the artificial tracer e90 to examine present and future UTLS tracer transport in WACCM, *Journal of the Atmospheric Sciences*, *74*(10), 3383–3403, doi:10.1175/JAS-D-17-0135.1, 2017.

Ackerman, A. S., and M. S. Marley, Precipitating Condensation Clouds in Substellar Atmospheres, *The Astrophysical Journal*, *556*(2), 872–884, doi:10.1086/321540, 2001.

Adcroft, A., et al., *MITgcm Documentation, Release checkpoint69g-4-g0fa8d50*, accessed: 5 October 2025.

Adriani, A., et al., Clusters of cyclones encircling Jupiter's poles, *Nature*, *555*(7695), 216–219, doi:10.1038/nature25491, 2018.

Aglyamov, Y. S., et al., Lightning Generation in Moist Convective Clouds and Constraints on the Water Abundance in Jupiter, *Journal of Geophysical Research: Planets*, *126*(2), doi:10.1029/2020JE006504, 2021.

Andrews, D. G., *An introduction to atmospheric physics*, Cambridge University Press, 2010.

Anguiano-Arteaga, A., S. Pérez-Hoyos, A. Sánchez-Lavega, J. F. Sanz-Requena, and P. G. Irwin, Temporal Variations in Vertical Cloud Structure of Jupiter's Great Red Spot, Its Surroundings and Oval BA From HST/WFC3 Imaging, *Journal of Geophysical Research: Planets*, *128*(9), 1–27, doi:10.1029/2022JE007427, 2023.

Atkinson, D. H., J. B. Pollack, and A. Seiff, The Galileo Probe Doppler Wind Experiment: Measurement of the deep zonal winds on Jupiter, *Journal of Geophysical Research: Planets*, *103*(E10), 22,911–22,928, doi:10.1029/98JE00060, 1998.

Atreya, S. K., M. H. Wong, T. C. Owen, P. R. Mahaffy, H. B. Niemann, I. De Pater, P. Drossart, and T. Encrenaz, A comparison of the atmospheres of Jupiter and Saturn: Deep atmospheric composition, cloud structure, vertical mixing, and origin, *Planetary and Space Science*, *47*(10-11), 1243–1262, doi:10.1016/s0032-0633(99)00047-1, 1999.

Atreya, S. K., A. Wong, K. H. Baines, M. H. Wong, and T. Owen, Jupiter's ammonia clouds—localized or ubiquitous?, *Planetary and Space Science*, *53*(5), 498–507, doi:10.1016/j.pss.2004.04.002, 2005.

Aurnou, J., M. Heimpel, L. Allen, E. King, and J. Wicht, Convective heat transfer and the pattern of thermal emission on the gas giants, *Geophysical Journal International*, *173*(3), 793–801, doi:10.1111/j.1365-246X.2008.03764.x, 2008.

Baines, K. H., R. W. Carlson, and L. W. Kamp, Fresh ammonia ice clouds in Jupiter. I. Spectroscopic identification, spatial distribution, and dynamical implications, *Icarus*, *159*(1), 74–94, doi:10.1006/icar.2002.6901, 2002.

Banfield, D., P. J. Gierasch, M. Bell, E. Ustinov, A. P. Ingersoll, A. R. Vasavada, R. A. West, and M. J. Belton, Jupiter's Cloud Structure from Galileo Imaging Data, *Icarus*, *135*(1), 230–250, doi:10.1006/icar.1998.5985, 1998.

Becker, H. N., et al., Small lightning flashes from shallow electrical storms on Jupiter, *Nature*, *584*(7819), 55–58, doi:10.1038/s41586-020-2532-1, 2020.

Biagiotti, F., et al., Evidence of pure ammonia clouds in Jupiter's Northern Temperate domain from

Juno/JIRAM infrared spectral data, *Monthly Notices of the Royal Astronomical Society*, *538*(3), 1535–1564, doi:10.1093/mnras/staf381, 2025.

Bjoraker, G. L., M. H. Wong, I. de Pater, and M. Ádámkovics, Jupiter's Deep Cloud Structure Revealed Using Keck Observations of Spectrally Resolved Line Shapes, *Astrophysical Journal*, *810*(2), 122, doi:10.1088/0004-637X/810/2/122, 2015.

Boer, G. J., On exact and approximate energy equations in pressure coordinates, *Tellus, Series A*, *41 A*(2), 97–108, doi:10.3402/tellusa.v41i2.11823, 1989.

Boer, G. J., and S. Lambert, The energy cycle in atmospheric models, *Climate Dynamics*, *30*(4), 371–390, doi:10.1007/s00382-007-0303-4, 2008.

Boissinot, A., A. Spiga, S. Guerlet, S. Cabanes, and D. Bardet, Global climate modeling of the Jupiter troposphere and effect of dry and moist convection on jets, *Astronomy and Astrophysics*, *687*(45220), A274, doi:10.1051/0004-6361/202245220, 2024.

Bolton, S. J., et al., The Juno Mission, *Space Science Reviews*, *213*(1-4), 5–37, doi:10.1007/s11214-017-0429-6, 2017.

Böttger, H. M., Modelling the water cycle on Mars, Dphil. thesis, University of Oxford, 2003.

Braude, A. S., P. G. Irwin, G. S. Orton, and L. N. Fletcher, Colour and tropospheric cloud structure of Jupiter from MUSE/VLT: Retrieving a universal chromophore, *Icarus*, *338*(November 2019), 113,589, doi:10.1016/j.icarus.2019.113589, 2020.

Briggs, F. H., and P. D. Sackett, Radio observations of Saturn as a probe of its atmosphere and cloud structure, *Icarus*, *80*(1), 77–103, doi:10.1016/0019-1035(89)90162-0, 1989.

Brokaw, R. S., *Viscosity of gas mixtures*, vol. 4496, National Aeronautics and Space Administration, 1968.

Brooke, T. Y., R. F. Knacke, T. Encrenaz, P. Drossart, D. Crisp, and H. Feuchtgruber, Models of the ISO 3-μm Reflection Spectrum of Jupiter, *Icarus*, *136*(1), 1–13, doi:10.1006/icar.1998.6013, 1998.

Brown, S., et al., Prevalent lightning sferics at 600 megahertz near Jupiter's poles, *Nature*, *558*(7708), 87–90, doi:10.1038/s41586-018-0156-5, 2018.

Brueshaber, S. R., et al., Multi-instrument sounding of a Jovian thunderstorm from Juno, *Icarus*, *432*(December 2024), 116,465, doi:10.1016/j.icarus.2025.116465, 2025.

Buckley, M. W., and J. Marshall, Observations, inferences, and mechanisms of the atlantic meridional overturning circulation: A review, *Reviews of Geophysics*, *54*(1), 5–63, doi:https://doi.org/10.1002/2015RG000493, 2016.

Carlson, B. E., W. B. Rossow, and G. S. Orton, Cloud Microphysics of the Giant Planets, *Journal of the Atmospheric Sciences*, *45*(14), 2066–2081, doi:10.1175/1520-0469(1988)045<2066:CMOTGP>2.0.CO;2, 1988.

Carlson, R. W., K. H. Baines, M. S. Anderson, G. Filacchione, and A. A. Simon, Chromophores from photolyzed ammonia reacting with acetylene: Application to Jupiter's Great Red Spot, *Icarus*, *274*, 106–115, doi:10.1016/j.icarus.2016.03.008, 2016.

Chan, C. J., R. A. Plumb, and I. Cerovecki, Annular modes in a multiple migrating zonal jet regime, *Journal of the Atmospheric Sciences*, *64*(11), 4053 – 4068, doi:10.1175/2007JAS2156.1, 2007.

Chemke, R., and Y. Kaspi, Poleward migration of eddy-driven jets, *Journal of Advances in Modeling Earth*

Systems, *7*(3), 1457–1471, doi:10.1002/2015MS000481, 2015.

Cheng, A. F., et al., Changing characteristics of jupiter's little red spot, *Astronomical Journal*, *135*(6), 2446–2452, doi:10.1088/0004-6256/135/6/2446, 2008.

Clark, T. L., A small-scale dynamic model using a terrain-following coordinate transformation, *Journal of Computational Physics*, *24*(2), 186–215, 1977.

Conrath, B. J., P. J. Gierasch, and S. S. Leroy, Temperature and circulation in the stratosphere of the outer planets, *Icarus*, *83*(2), 255–281, doi:https://doi.org/10.1016/0019-1035(90)90068-K, 1990.

Council, N. R., *International Critical Tables of Numerical Data, Physics, Chemistry and Technology*, The National Academies Press, Washington, DC, doi:10.17226/20230, 1930.

Dahl, E. K., N. J. Chanover, G. S. Orton, K. H. Baines, J. A. Sinclair, D. G. Voelz, E. A. Wijerathna, P. D. Strycker, and P. G. J. Irwin, Vertical Structure and Color of Jovian Latitudinal Cloud Bands during the Juno Era, *The Planetary Science Journal*, *2*(1), 16, doi:10.3847/psj/abd400, 2021.

De Pater, I., D. Dunn, P. Romani, and K. Zahnle, Reconciling Galileo Probe Data and Ground-Based Radio Observations of Ammonia on Jupiter, *Icarus*, *149*(1), 66–78, doi:10.1006/icar.2000.6527, 2001.

de Pater, I., R. J. Sault, B. Butler, D. DeBoer, and M. H. Wong, Peering through Jupiter's clouds with radio spectral imaging, *Science*, *352*(6290), 1198–1201, doi:10.1126/science.aaf2210, 2016.

de Pater, I., R. J. Sault, M. H. Wong, L. N. Fletcher, D. DeBoer, and B. Butler, Jupiter's ammonia distribution derived from VLA maps at 3–37 GHz, *Icarus*, *322*(November 2018), 168–191, doi:10.1016/j.icarus.2018.11.024, 2019.

Del Genio, A. D., and K. B. McGrattan, Moist convection and the vertical structure and water abundance of Jupiter's atmosphere, *Icarus*, *84*(1), 29–53, doi:10.1016/0019-1035(90)90156-4, 1990.

Del Genio, A. D., W. Zhou, and T. P. Eichler, Equatorial Superrotation in a Slowly Rotating GCM: Implications for Titan and Venus, doi:10.1006/icar.1993.1001, 1993.

Dias Pinto, J. R., and R. P. da Rocha, The energy cycle and structural evolution of cyclones over south-eastern South America in three case studies, *Journal of Geophysical Research: Atmospheres*, *116*(D14), doi:https://doi.org/10.1029/2011JD016217, 2011.

Dowling, T. E., and P. Gierasch, Cyclones and Moist Convection on Jovian Planets, in *Bulletin of the American Astronomical Society*, p. 946, 1989.

Dowling, T. E., et al., The EPIC atmospheric model with an isentropic/terrain-following hybrid vertical coordinate, *Icarus*, *182*(1), 259–273, doi:10.1016/j.icarus.2006.01.003, 2006.

Duer, K., E. Galanti, and Y. Kaspi, Gas Giant Simulations of Eddy-Driven Jets Accompanied by Deep Meridional Circulation, *AGU Advances*, *4*(6), 1–14, doi:10.1029/2023AV000908, 2023.

Durran, D. R., and J. B. Klemp, On the Effects of Moisture on the Brunt-Väisälä Frequency, *Journal of the Atmospheric Sciences*, *39*(10), 2152–2158, doi:10.1175/1520-0469(1982)039<2152:OTEOMO>2.0.CO;2, 1982.

Fletcher, L. N., G. S. Orton, N. A. Teanby, and P. G. Irwin, Phosphine on Jupiter and Saturn from Cassini/CIRS, *Icarus*, *202*(2), 543–564, doi:10.1016/j.icarus.2009.03.023, 2009.

Fletcher, L. N., T. K. Greathouse, G. S. Orton, J. A. Sinclair, R. S. Giles, P. G. Irwin, and T. Encrenaz, Mid-infrared mapping of Jupiter's temperatures, aerosol opacity and chemical distributions with IRTF/TEXES,

Icarus, *278*, 128–161, doi:10.1016/j.icarus.2016.06.008, 2016.

Fletcher, L. N., G. S. Orton, J. H. Rogers, R. S. Giles, A. V. Payne, P. G. J. Irwin, and M. Vedovato, Moist convection and the 2010–2011 revival of Jupiter's South Equatorial Belt, *Icarus*, *286*, 94–117, doi:10.1016/j.icarus.2017.01.001, 2017.

Fletcher, L. N., Y. Kaspi, T. Guillot, and A. P. Showman, How Well Do We Understand the Belt/Zone Circulation of Giant Planet Atmospheres?, *Space Science Reviews*, *216*(2), 1–33, doi:10.1007/s11214-019-0631-9, 2020.

Fletcher, L. N., F. A. Oyafuso, M. Allison, A. P. Ingersoll, L. Li, and Y. Kaspi, Jupiter 's Temperate Belt / Zone Contrasts Revealed at Depth by Juno Microwave Observations, *JGR: Planets*, (May), 1–35, doi:10.1002/essoar.10506297.2, 2021.

Galanti, E., and Y. Kaspi, Combined magnetic and gravity measurements probe the deep zonal flows of the gas giants, *Monthly Notices of the Royal Astronomical Society*, *501*(2), 2352–2362, doi:10.1093/mnras/staa3722, 2021.

Galanti, E., et al., Constraints on the Latitudinal Profile of Jupiter's Deep Jets, *Geophysical Research Letters*, *48*(9), 1–10, doi:10.1029/2021GL092912, 2021.

García-Melendo, E., A. Sánchez-Lavega, J. M. Gómez, J. Lecacheux, F. Colas, I. Miyazaki, and D. Parker, Long-Lived Vortices and Profile Changes in the 23.7°N High-Speed Jovian Jet, *Icarus*, *146*(2), 514–524, doi:10.1006/icar.2000.6411, 2000.

Gierasch, P., A. P. Ingersoll, D. Banfield, S. P. Ewald, P. Helfenstein, A. Simon-Miller, A. R. Vasavada, H. H. Breneman, and D. A. Sensko, Observation of moist convection in Jupiter's atmosphere, *Nature*, *403*(6770), 628–630, doi:10.1038/35001017, 2000.

Gierasch, P. J., and R. M. Goody, Radiative time constants in the atmosphere of jupiter, *Journal of Atmospheric Sciences*, *26*(5), 979–980, 1969.

Giles, R. S., L. N. Fletcher, and P. G. J. Irwin, Cloud structure and composition of Jupiter's troposphere from 5-$$m Cassini VIMS spectroscopy, *Icarus*, *257*, 457–470, doi:10.1016/j.icarus.2015.05.030, 2015.

Gonçalves, I., et al., First measurements of Jupiter's zonal winds with visible imaging spectroscopy, *Icarus*, *319*(February 2018), 795–811, doi:10.1016/j.icarus.2018.10.019, 2019.

Grasset, O., et al., JUpiter ICy moons Explorer (JUICE): An ESA mission to orbit Ganymede and to characterise the Jupiter system, *Planetary and Space Science*, *78*, 1–21, doi:10.1016/j.pss.2012.12.002, 2013.

Grassi, D., et al., On the clouds and ammonia in Jupiter's upper troposphere from Juno JIRAM reflectivity observations, *Monthly Notices of the Royal Astronomical Society*, *503*(4), 4892–4907, doi:10.1093/mnras/stab740, 2021.

Guerlet, S., A. Spiga, H. Delattre, and T. Fouchet, Radiative-equilibrium model of Jupiter's atmosphere and application to estimating stratospheric circulations, *Icarus*, *351*(June), 113,935, doi:10.1016/j.icarus.2020.113935, 2020.

Guillot, T., Mushballs and the lack of ammonia in uranus and neptune, in *European Planetary Science Congress*, pp. EPSC2021–422, 2021.

Guillot, T., D. J. Stevenson, S. K. Atreya, S. J. Bolton, and H. N. Becker, Storms and the Depletion of

Ammonia in Jupiter: I. Microphysics of "Mushballs", *Journal of Geophysical Research: Planets*, *125*(8), 1–20, doi:10.1029/2020JE006403, 2020a.

Guillot, T., et al., Storms and the Depletion of Ammonia in Jupiter: II. Explaining the Juno Observations, *Journal of Geophysical Research: Planets*, *125*(8), 1–23, doi:10.1029/2020JE006404, 2020b.

Gupta, P., et al., Jupiter's Temperature Structure: A Reassessment of the Voyager Radio Occultation Measurements, *The Planetary Science Journal*, *3*(7), 159, doi:10.3847/PSJ/ac6956, 2022.

Hall, C. F., Pioneer 10 and Pioneer 11, *Science*, *188*(4187), 445–446, doi:10.1126/science.188.4187.445, 1975.

Hanel, R., B. Conrath, L. Herath, V. Kunde, and J. Pirraglia, Albedo, internal heat, and energy balance of jupiter: Preliminary results of the voyager infrared investigation, *Journal of Geophysical Research: Space Physics*, *86*(A10), 8705–8712, 1981.

Hansen, C. J., S. J. Bolton, D. L. Matson, L. J. Spilker, and J. P. Lebreton, The Cassini-Huygens flyby of Jupiter, *Icarus*, *172*(1 SPEC.ISS.), 1–8, doi:10.1016/j.icarus.2004.06.018, 2004.

Harkett, J., et al., The Thermal Structure and Composition of Jupiter's Great Red Spot From JWST/MIRI, *Journal of Geophysical Research: Planets*, *129*(10), 1–39, doi:10.1029/2024JE008415, 2024.

Haynes, P. H., M. E. McIntyre, T. G. Shepherd, C. J. Marks, and K. P. Shine, On the "downward control" of extratropical diabatic circulations by eddy-induced mean zonal forces, *Journal of Atmospheric Sciences*, *48*(4), 651 – 678, doi:10.1175/1520-0469(1991)048<0651:OTCOED>2.0.CO;2, 1991.

Heimpel, M., T. Gastine, and J. Wicht, Simulation of deep-seated zonal jets and shallow vortices in gas giant atmospheres, *Nature Geoscience*, *9*(1), 19–23, doi:10.1038/ngeo2601, 2016.

Hill, S. M., P. G. Irwin, C. Alexander, and J. H. Rogers, Spatial Variations of Jovian Tropospheric Ammonia via Ground-Based Imaging, *Earth and Space Science*, *11*(8), doi:10.1029/2024EA003562, 2024.

Hori, K., C. A. Jones, A. Antuñano, L. N. Fletcher, and S. M. Tobias, Jupiter's cloud-level variability triggered by torsional oscillations in the interior, *Nature Astronomy*, *7*(7), 825–835, doi:10.1038/s41550-023-01967-1, 2023.

Hourdin, F., and A. Armengaud, The Use of Finite-Volume Methods for Atmospheric Advection of Trace Species. Part I: Test of Various Formulations in a General Circulation Model, *Monthly Weather Review*, *127*(5), 822–837, doi:10.1175/1520-0493(1999)127<0822:TUOFVM>2.0.CO;2, 1999.

Hubbard, W. B., Thermal structure of Jupiter, *Astrophysical Journal*, *152*, 745–754, doi:10.1086/149591, 1968.

Hueso, R., and A. Sánchez-Lavega, A Three-Dimensional Model of Moist Convection for the Giant Planets: The Jupiter Case, *Icarus*, *151*(2), 257–274, doi:10.1006/icar.2000.6606, 2001.

Hueso, R., T. Guillot, and A. Sánchez-Lavega, Convective storms and atmospheric vertical structure in Uranus and Neptune: Moist convection in Ice Giants, *Philosophical Transactions of the Royal Society A: Mathematical, Physical and Engineering Sciences*, *378*(2187), 1–24, doi:10.1098/rsta.2019.0476, 2020.

Hueso, R., et al., An intense narrow equatorial jet in Jupiter's lower stratosphere observed by JWST, *Nature Astronomy*, *7*(12), 1454–1462, doi:10.1038/s41550-023-02099-2, 2023.

Ingersoll, A. P., et al., Implications of the ammonia distribution on Jupiter from 1 to 100 bars as measured by the Juno microwave radiometer, *Geophysical Research Letters*, *44*(15), 7676–7685, doi:10.1002/2017GL074277, 2017.

Iribarne, J., and W. Godson, Atmospheric thermodynamics, 1973.

Irwin, P. G., S. M. Hill, L. N. Fletcher, C. Alexander, and J. H. Rogers, Clouds and Ammonia in the Atmospheres of Jupiter and Saturn Determined From a Band-Depth Analysis of VLT/MUSE Observations, *Journal of Geophysical Research: Planets*, *130*(1), doi:10.1029/2024JE008622, 2025.

Irwin, P. G., et al., Cloud structure and atmospheric composition of Jupiter retrieved from Galileo near-infrared mapping spectrometer real-time spectra, *Journal of Geophysical Research E: Planets*, *103*(E10), 23,001–23,021, doi:10.1029/98JE00948, 1998.

Irwin, P. G. J., A. L. Weir, F. W. Taylor, and S. B. Calcutt, The Origin of Belt / Zone Contrasts in the Atmosphere of Jupiter and Their Correlation with 5- μ m Opacity, *Icarus*, *149*(2), 397–415, doi:10.1006/icar.2000.6542, 2001.

James, I. N., *Transient disturbances in the midlatitudes*, pp. 112–163, Cambridge Atmospheric and Space Science Series, Cambridge University Press, 1994.

Jiang, T., Y. Deng, and W. Li, Local kinetic energy budget of high-frequency and intermediate-frequency eddies: Winter climatology and interannual variability, *Climate dynamics*, *41*, 961–976, 2013.

Kaspi, Y., et al., Jupiter's atmospheric jet streams extend thousands of kilometres deep, *Nature*, *555*(7695), 223–226, doi:10.1038/nature25793, 2018.

Kaspi, Y., et al., Observational evidence for cylindrically oriented zonal flows on Jupiter, *Nature Astronomy*, *7*(12), 1463–1472, doi:10.1038/s41550-023-02077-8, 2023.

Kennedy, D. T., R. M. B. Young, and P. L. Read, Investigating Jupiter's complex energy cycle using a general circulation model, *Tech. rep.*, 2016.

Kessler, E., *On the Distribution and Continuity of Water Substance in Atmospheric Circulations*, pp. 1–84, American Meteorological Society, Boston, MA, doi:10.1007/978-1-935704-36-2_1, 1969.

Kliore, A., G. Fjeldbo, B. L. Seidel, T. T. Sesplaukis, D. W. Sweetnam, and P. M. Woiceshyn, Atmosphere of Jupiter from the Pioneer 11 s-band occultation experiment: Preliminary results, *Science*, *188*(4187), 474–476, doi:10.1126/science.188.4187.474, 1975.

Kohlhase, C. E., and P. A. Penzo, Voyager mission description, *Space Science Reviews*, *21*(2), 77–101, doi:10.1007/BF00200846, 1977.

Kuroda, T., A. S. Medvedev, and P. Hartogh, Parameterization of radiative heating and cooling rates in the stratosphere of jupiter, *Icarus*, *242*, 149–157, 2014.

Leconte, J., F. Selsis, F. Hersant, and T. Guillot, Condensation-inhibited convection in hydrogen-rich atmospheres, *Astronomy & Astrophysics*, *598*, A98, doi:10.1051/0004-6361/201629140, 2017.

Lee, C., and M. I. Richardson, A general circulation model ensemble study of the atmospheric circulation of Venus, *Journal of Geophysical Research: Planets*, *115*(4), 1–11, doi:10.1029/2009JE003490, 2010.

Lee, C., S. R. Lewis, and P. L. Read, A bulk cloud parameterization in a Venus General Circulation Model, *Icarus*, *206*(2), 662–668, doi:10.1016/j.icarus.2009.09.017, 2010.

Lewis, J. S., The clouds of Jupiter and the NH3—H2O and NH3—H2S systems, *Icarus*, *10*(3), 365–378, doi:10.1016/0019-1035(69)90091-8, 1969.

Li, C., and X. Chen, Simulating Nonhydrostatic Atmospheres on Planets (SNAP): Formulation, Validation, and Application to the Jovian Atmosphere, *The Astrophysical Journal Supplement Series*, *240*(2), 37,

doi:10.3847/1538-4365/aafdaa, 2019.

Li, C., T. Le, X. Zhang, and Y. L. Yung, A high-performance atmospheric radiation package: With applications to the radiative energy budgets of giant planets, *Journal of Quantitative Spectroscopy and Radiative Transfer*, *217*, 353–362, doi:10.1016/j.jqsrt.2018.06.002, 2018a.

Li, C., et al., The distribution of ammonia on Jupiter from a preliminary inversion of Juno microwave radiometer data, *Geophysical Research Letters*, *44*(11), 5317–5325, doi:10.1002/2017GL073159, 2017.

Li, C., et al., The water abundance in Jupiter's equatorial zone, *Nature Astronomy*, *4*(6), 609–616, doi:10.1038/s41550-020-1009-3, 2020a.

Li, C., et al., Super-adiabatic temperature gradient at Jupiter's equatorial zone and implications for the water abundance, *Icarus*, *414*(September 2023), 116,028, doi:10.1016/j.icarus.2024.116028, 2024.

Li, L., A. P. Ingersoll, X. Jiang, D. Feldman, and Y. L. Yung, Lorenz energy cycle of the global atmosphere based on reanalysis datasets, *Geophysical Research Letters*, *34*(16), doi:https://doi.org/10.1029/2007GL029985, 2007.

Li, L., et al., Less absorbed solar energy and more internal heat for Jupiter, *Nature Communications*, *9*(1), 1–10, doi:10.1038/s41467-018-06107-2, 2018b.

Li, W., D. Kong, K. Zhang, and Y. Pan, Depth of Jupiter's Zonal Flow under the "Shallow-wind" Assumption, *The Astrophysical Journal*, *897*(1), 85, doi:10.3847/1538-4357/ab959d, 2020b.

Lian, Y., and A. P. Showman, Deep jets on gas-giant planets, *Icarus*, *194*(2), 597–615, doi:10.1016/j.icarus.2007.10.014, 2008.

Lian, Y., and A. P. Showman, Generation of equatorial jets by large-scale latent heating on the giant planets, *Icarus*, *207*(1), 373–393, doi:10.1016/j.icarus.2009.10.006, 2010.

Lide, D. R., Handbook of chemistry and physics, 1995.

Little, B., C. D. Anger, A. P. Ingersoll, A. R. Vasavada, D. A. Senske, H. H. Breneman, and W. J. Borucki, Galileo Images of Lightning on Jupiter, *Icarus*, *142*(2), 306–323, doi:10.1006/icar.1999.6195, 1999.

Liu, J., and T. Schneider, Mechanisms of jet formation on the giant planets, *Journal of the Atmospheric Sciences*, *67*(11), 3652–3672, doi:10.1175/2010JAS3492.1, 2010.

Liu, J., and T. Schneider, Convective Generation of Equatorial Superrotation in Planetary Atmospheres, *Journal of the Atmospheric Sciences*, *68*(11), 2742–2756, doi:10.1175/JAS-D-10-05013.1, 2011.

Liu, J., and T. Schneider, Scaling of Off-Equatorial Jets in Giant Planet Atmospheres, *Journal of the Atmospheric Sciences*, *72*(1), 389–408, doi:10.1175/JAS-D-13-0391.1, 2015.

Lorenz, E. N., Available Potential Energy and the Maintenance of the General Circulation, *Tellus A: Dynamic Meteorology and Oceanography*, *7*(2), 157–167, doi:10.3402/tellusa.v7i2.8796, 1955.

Machado, P., J. E. Silva, F. Brasil, J. Ribeiro, R. Gonçalves, and M. Silva, Jupiter's Atmosphere Dynamics Based on High-Resolution Spectroscopy with VLT/ESPRESSO, *Universe*, *9*(12), doi:10.3390/universe9120491, 2023.

Malsky, I., E. Rauscher, M. T. Roman, E. K. Lee, H. Beltz, A. Savel, E. M.-R. Kempton, and L. Cinque, A direct comparison between the use of double gray and multiwavelength radiative transfer in a general circulation model with and without radiatively active clouds, *The Astrophysical Journal*, *961*(1), 66, 2024.

Manabe, S., J. Smagorinsky, and R. F. Strickler, Simulated climatology of a general circulation model with a hydrologic cycle., *Monthly Weather Review*, *93*(12), 769 – 798, doi:10.1175/1520-0493(1965)093<0769:SCOAGC>2.3.CO;2, 1965.

Markham, S., T. Guillot, and C. Li, Rainy downdrafts in abyssal atmospheres, *Astronomy Astrophysics*, *674*, A177, doi:10.1051/0004-6361/202245609, 2023.

Marques, C. A., A. Rocha, and J. Corte-Real, Global diagnostic energetics of five state-of-the-art climate models, *Climate Dynamics*, *36*(9-10), 1767–1794, doi:10.1007/s00382-010-0828-9, 2011.

Matcheva, K. I., B. J. Conrath, P. J. Gierasch, and F. M. Flasar, The cloud structure of the jovian atmosphere as seen by the Cassini/CIRS experiment, *Icarus*, *179*(2), 432–448, doi:10.1016/j.icarus.2005.06.020, 2005.

Michaelides, S., Lorenz atmospheric energy cycle in climatic projections, *Climate*, *9*(12), doi:10.3390/cli9120180, 2021.

Moeckel, C., I. de Pater, and D. DeBoer, Ammonia Abundance Derived from Juno MWR and VLA Observations of Jupiter, *Planetary Science Journal*, *4*(2), 25, doi:10.3847/PSJ/acaf6b, 2023.

Mura, A., et al., Five Years of Observations of the Circumpolar Cyclones of Jupiter, *Journal of Geophysical Research: Planets*, *127*(9), 1–10, doi:10.1029/2022JE007241, 2022.

Niemann, H. B., et al., The composition of the Jovian atmosphere as determined by the Galileo probe mass spectrometer, *Journal of Geophysical Research: Planets*, *103*(E10), 22,831–22,845, doi:10.1029/98JE01050, 1998.

Norwood, J., et al., Giant planet observations with the james webb space telescope, *Publications of the Astronomical Society of the Pacific*, *128*(959), 1–8, doi:10.1088/1538-3873/128/959/018005, 2016.

Palotai, C., and T. E. Dowling, Addition of water and ammonia cloud microphysics to the EPIC model, *Icarus*, *194*(1), 303–326, doi:10.1016/j.icarus.2007.10.025, 2008.

Palotai, C., T. E. Dowling, and L. N. Fletcher, 3D Modeling of interactions between Jupiter's ammonia clouds and large anticyclones, *Icarus*, *232*, 141–156, doi:10.1016/j.icarus.2014.01.005, 2014.

Palotai, C., S. Brueshaber, R. Sankar, and K. Sayanagi, Moist Convection in the Giant Planet Atmospheres, *Remote Sensing*, *15*(1), 1–41, doi:10.3390/rs15010219, 2023.

Pan, Y., L. Li, X. Jiang, G. Li, W. Zhang, X. Wang, and A. P. Ingersoll, Earth's changing global atmospheric energy cycle in response to climate change, *Nature Communications*, *8*, 1–8, doi:10.1038/ncomms14367, 2017.

Pappalardo, R. T., et al., Science Overview of the Europa Clipper Mission, *Space Science Reviews*, *220*(4), doi:10.1007/s11214-024-01070-5, 2024.

Peixoto, J. P., and A. H. Oort, *Physics of climate*, New York, NY (United States); American Institute of Physics, 1992.

Pérez-Hoyos, S., A. Sánchez-Lavega, J. F. Sanz-Requena, N. Barrado-Izagirre, O. Carrión-González, A. Anguiano-Arteaga, P. G. Irwin, and A. S. Braude, Color and aerosol changes in Jupiter after a North Temperate Belt disturbance, *Icarus*, *352*(July), 114,031, doi:10.1016/j.icarus.2020.114031, 2020.

Pirraglia, J., Meridional energy balance of Jupiter, *Icarus*, *59*(2), 169–176, doi:10.1016/0019-1035(84)90020-4, 1984.

Porco, C. C., et al., Cassini imaging of Jupiter's atmosphere, satellites, and rings, *Science*, *299*(5612), 1541–1547, doi:10.1126/science.1079462, 2003.

Ragent, B., D. S. Colburn, K. A. Rages, T. C. Knight, P. Avrin, G. S. Orton, P. A. Yanamandra-Fisher, and G. W. Grams, The clouds of Jupiter: Results of the Galileo Jupiter mission probe nephelometer experiment, *Journal of Geophysical Research E: Planets*, *103*(E10), 22,891–22,909, doi:10.1029/98JE00353, 1998.

Rahmstorf, S., Ocean circulation and climate during the past 120,000 years, *Nature*, *419*(6903), 207–214, 2002.

Read, P. L., Super-rotation and diffusion of axial angular momentum: I. 'Speed limits' for axisymmetric flow in a rotating cylindrical fluid annulus, *Quarterly Journal of the Royal Meteorological Society*, *112*(471), 231–251, doi:10.1002/qj.49711247113, 1986.

Read, P. L., The Dynamics of Jupiter's and Saturn's Weather Layers: A Synthesis After Cassini and Juno, *Annual Review of Fluid Mechanics*, *56*(1), 271–293, doi:10.1146/annurev-fluid-121021-040058, 2024.

Read, P. L., and S. Lebonnois, Superrotation on Venus, on Titan, and Elsewhere, *Annual Review of Earth and Planetary Sciences*, *46*, 175–202, doi:10.1146/annurev-earth-082517-010137, 2018.

Read, P. L., P. J. Gierasch, B. J. Conrath, A. Simon-Miller, T. Fouchet, and Y. H. Yamazaki, Mapping potential-vorticity dynamics on Jupiter. I: Zonal-mean circulation from Cassini and Voyager 1 data, *Quarterly Journal of the Royal Meteorological Society*, *132*(618 A), 1577–1603, doi:10.1256/qj.05.34, 2006.

Read, P. L., F. Tabataba-Vakili, Y. Wang, P. Augier, E. Lindborg, A. Valeanu, and R. M. B. Young, Comparative terrestrial atmospheric circulation regimes in simplified global circulation models. Part II: Energy budgets and spectral transfers, *Quarterly Journal of the Royal Meteorological Society*, *144*(717), 2558–2576, doi:10.1002/qj.3351, 2018.

Read, P. L., D. Kennedy, N. T. Lewis, H. Scolan, F. Tabataba-Vakili, Y. Wang, S. Wright, and R. M. Young, Baroclinic and barotropic instabilities in planetary atmospheres: Energetics, equilibration and adjustment, *Nonlinear Processes in Geophysics*, *27*(2), 147–173, doi:10.5194/npg-27-147-2020, 2020a.

Read, P. L., R. M. Young, and D. Kennedy, The turbulent dynamics of Jupiter's and Saturn's weather layers: order out of chaos?, *Geoscience Letters*, *7*(1), 10, doi:10.1186/s40562-020-00159-3, 2020b.

Read, P. L., A. Antunano, H. Bobas, G. Colyer, S. Ding, T. del Río Gaztelurrutia, A. Sanchez-Lavega, and R. Young, Characterising turbulent cascades and zonal jet formation processes from observations of cloud level winds on jupiter and saturn, doi:10.5194/epsc-dps2025-1019, 2025.

Rennó, N. O., and A. P. Ingersoll, Natural Convection as a Heat Engine: A Theory for CAPE, *Journal of the Atmospheric Sciences*, *53*(4), 572–585, doi:10.1175/1520-0469(1996)053<0572:NCAAHE>2.0.CO;2, 1996.

Robinson, T. D., and D. C. Catling, AN ANALYTIC RADIATIVE-CONVECTIVE MODEL FOR PLANETARY ATMOSPHERES, *The Astrophysical Journal*, *757*(1), 104, doi:10.1088/0004-637X/757/1/104, 2012.

Roman, M. T., E. M.-R. Kempton, E. Rauscher, C. K. Harada, J. L. Bean, and K. B. Stevenson, Clouds in three-dimensional models of hot jupiters over a wide range of temperatures. i. thermal structures and broadband phase-curve predictions, *The Astrophysical Journal*, *908*(1), 101, 2021.

Roos-Serote, M., S. K. Atreya, M. Wong, and P. Drossart, On the water abundance in the atmosphere of Jupiter, *Planetary and Space Science*, *52*(5-6), 397–414, doi:10.1016/j.pss.2003.06.007, 2004.

Rossow, W. B., Cloud microphysics: Analysis of the clouds of Earth, Venus, Mars and Jupiter, *Icarus*, *36*(1), 1–50, doi:10.1016/0019-1035(78)90072-6, 1978.

Sánchez-Lavega, A., E. García-Melendo, J. Legarreta, A. Miró, M. Soria, and K. Ahrens-Velásquez, The Origin

of Jupiter's Great Red Spot, *Geophysical Research Letters*, *51*(12), 1–10, doi:10.1029/2024GL108993, 2024.

Sánchez-Lavega, A., et al., Depth of a strong jovian jet from a planetary-scale disturbance driven by storms, *Nature*, *451*(7177), 437–440, doi:10.1038/nature06533, 2008.

Sankar, R., and C. Palotai, A new convective parameterization applied to Jupiter: implications for water abundance near the $24^$ N region, *Icarus*, 2022.

Sankar, R., C. Klare, and C. Palotai, The aftermath of convective events near Jupiter's fastest prograde jet: Implications for clouds, dynamics and vertical wind shear, *Icarus*, *368*, 114,589, doi:10.1016/j.icarus.2021.114589, 2021.

Schmider, F. X., et al., Three-dimensional Atmospheric Dynamics of Jupiter from Ground-based Doppler Imaging Spectroscopy in the Visible, *Planetary Science Journal*, *5*(4), doi:10.3847/PSJ/ad3066, 2024.

Schneider, T., and J. Liu, Formation of jets and equatorial superrotation on Jupiter, *Journal of the Atmospheric Sciences*, *66*(3), 579–601, doi:10.1175/2008JAS2798.1, 2009.

Schubert, G., and J. L. Mitchell, Planetary Atmospheres as Heat Engines, in *Comparative Climatology of Terrestrial Planets*, edited by S. J. Mackwell, A. A. Simon-Miller, J. W. Harder, and M. A. Bullock, pp. 181–192, doi:10.2458/azu_uapress_9780816530595-ch008, 2013.

Seiff, A., et al., Thermal structure of Jupiter's atmosphere near the edge of a 5-μm hot spot in the north equatorial belt, *Journal of Geophysical Research: Planets*, *103*(E10), 22,857–22,889, doi:10.1029/98JE01766, 1998.

Shaw, C. L., D. J. Gulledge, R. Swindle, S. M. Jefferies, and N. Murphy, PMODE I: Design and Development of an Observatory for Characterizing Giant Planet Atmospheres and Interiors, *Frontiers in Astronomy and Space Sciences*, *9*(March), doi:10.3389/fspas.2022.768452, 2022.

Showman, A. P., Numerical simulations of forced shallow-water turbulence: Effects of moist convection on the large-scale circulation of Jupiter and Saturn, *Journal of the Atmospheric Sciences*, *64*(9), 3132–3157, doi:10.1175/JAS4007.1, 2007.

Showman, A. P., and I. de Pater, Dynamical implications of Jupiter's tropospheric ammonia abundance, *Icarus*, *174*(1), 192–204, doi:10.1016/j.icarus.2004.10.004, 2005.

Showman, A. P., and T. E. Dowling, Nonlinear simulations of Jupiter's 5-micron hot spots, *Science*, *289*(5485), 1737–1740, doi:10.1126/science.289.5485.1737, 2000.

Showman, A. P., and Y. Kaspi, Atmospheric dynamics of brown dwarfs and directly imaged giant planets, *The Astrophysical Journal*, *776*(2), 85, 2013.

Showman, A. P., P. J. Gierasch, and Y. Lian, Deep zonal winds can result from shallow driving in a giant-planet atmosphere, *Icarus*, *182*(2), 513–526, doi:10.1016/j.icarus.2006.01.019, 2006.

Showman, A. P., J. Y. Cho, and K. Menou, Atmospheric circulation of exoplanets, *Exoplanets*, *526*, 471–516, 2010.

Simon, A. A., M. H. Wong, and G. S. Orton, FIRST RESULTS from the HUBBLE OPAL PROGRAM: JUPITER in 2015, *Astrophysical Journal*, *812*(1), 55, doi:10.1088/0004-637X/812/1/55, 2015.

Simon-Miller, A. A., B. Conrath, P. J. Gierasch, and R. F. Beebe, A Detection of Water Ice on Jupiter with Voyager IRIS, *Icarus*, *145*(2), 454–461, doi:10.1006/icar.2000.6359, 2000.

Simon-Miller, A. A., D. Banfield, and P. J. Gierasch, Color and the vertical structure in Jupiter's belts, zones, and weather systems, *Icarus*, *154*(2), 459–474, doi:10.1006/icar.2001.6742, 2001.

Simon-Miller, A. A., B. J. Conrath, P. J. Gierasch, G. S. Orton, R. K. Achterberg, F. M. Flasar, and B. M. Fisher, Jupiter's atmospheric temperatures: From Voyager IRIS to Cassini CIRS, *Icarus*, *180*(1), 98–112, doi:10.1016/j.icarus.2005.07.019, 2006.

Smith, B. A., et al., The Jupiter system through the eyes of Voyager 1, *Science*, *204*(4396), 951–972, doi:10.1126/science.204.4396.951, 1979.

Smith, E. J., K. P. Wenzel, and D. E. Page, Ulysses at Jupiter: An Overview of the Encounter, *Science*, *257*(5076), 1503–1507, doi:10.1126/science.257.5076.1503, 1992.

Sromovsky, L. A., A. D. Collard, P. M. Fry, G. S. Orton, M. T. Lemmon, M. G. Tomasko, and R. S. Freedman, Galileo probe measurements of thermal and solar radiation fluxes in the Jovian atmosphere, *Journal of Geophysical Research: Planets*, *103*(E10), 22,929–22,977, doi:10.1029/98JE01048, 1998.

Sromovsky, L. A., K. H. Baines, P. M. Fry, and R. W. Carlson, A possibly universal red chromophore for modeling color variations on Jupiter, *Icarus*, *291*, 232–244, doi:10.1016/j.icarus.2016.12.014, 2017.

Sugiyama, K. I., K. Nakajima, M. Odaka, K. Kuramoto, and Y.-Y. Hayashi, Numerical simulations of Jupiter's moist convection layer: Structure and dynamics in statistically steady states, *Icarus*, *229*, 71–91, doi:10.1016/J.ICARUS.2013.10.016, 2014.

Sánchez-Lavega, A., et al., *Gas Giants*, p. 72–103, Cambridge University Press, 2019.

Tabataba-Vakili, F., Dynamical circulation regimes in planetary (and exo-planetary) atmospheres, Ph.D. thesis, University of Oxford, 2017.

Tabataba-Vakili, F., P. L. Read, S. R. Lewis, L. Montabone, T. Ruan, Y. Wang, A. Valeanu, and R. M. Young, A Lorenz/Boer energy budget for the atmosphere of Mars from a "reanalysis" of spacecraft observations, *Geophysical Research Letters*, *42*(20), 8320–8327, doi:10.1002/2015GL065659, 2015.

Tabataba-Vakili, F., et al., Long-term tracking of circumpolar cyclones on Jupiter from polar observations with JunoCam, *Icarus*, *335*(April 2019), 113,405, doi:10.1016/j.icarus.2019.113405, 2020.

Thomson, S. I., The influence of deep jets on Jupiter's weather layer in a 1.5-layer shallow-water model, *Quarterly Journal of the Royal Meteorological Society*, *146*(729), 1608–1625, doi:10.1002/qj.3755, 2020.

Thomson, S. I., and M. E. McIntyre, Jupiter's unearthly jets: A new turbulent model exhibiting statistical steadiness without large-scale dissipation, *Journal of the Atmospheric Sciences*, *73*(3), 1119–1141, doi:10.1175/JAS-D-14-0370.1, 2016.

Tollefson, J. W., et al., Changes in Jupiter's Zonal Wind Profile preceding and during the Juno mission, *Icarus*, *296*, 163–178, doi:10.1016/j.icarus.2017.06.007, 2017.

Vallis, G. K., *Atmospheric and oceanic fluid dynamics*, Cambridge University Press, 2017.

Vardavas, I. M., and F. W. Taylor, *Radiation and climate*, vol. 18, Oxford University Press, USA, 2007.

Vasavada, A. R., and A. P. Showman, Jovian atmospheric dynamics: An update after Galileo and Cassini, *Reports on Progress in Physics*, *68*(8), 1935–1996, doi:10.1088/0034-4885/68/8/R06, 2005.

Wang, S., and J. Yang, Lorenz Energy Cycle: Another Way to Understand the Atmospheric Circulation on Tidally Locked Terrestrial Planets, *The Planetary Science Journal*, *4*(5), 84, doi:10.3847/psj/accf11, 2023.

Wang, X., et al., Cassini spacecraft reveals global energy imbalance of Saturn, *Nature Communications*, *15*(1), 5045, doi:10.1038/s41467-024-48969-9, 2024.

Weidenschilling, S. J., and J. S. Lewis, Atmospheric and cloud structures of the Jovian planets, *Icarus*, *20*(4), 465–476, doi:10.1016/0019-1035(73)90019-5, 1973.

West, R. A., D. F. Strobel, and M. G. Tomasko, Clouds, aerosols, and photochemistry in the Jovian atmosphere, *Icarus*, *65*(2-3), 161–217, doi:10.1016/0019-1035(86)90135-1, 1986.

West, R. A., K. H. Baines, A. J. Friedson, D. Banfield, B. Ragent, and F. W. Taylor, Jovian Clouds and Haze, in *Jupiter: The Planet, Satellites and Magnetosphere*, edited by F. Bagenal, T. E. Dowling, and W. B. McKinnon, chap. 5, pp. 79–104, Cambridge University Press, Cambridge, 2004.

Williams, G. P., Jovian dynamics. Part III: Multiple, migrating, and equatorial jets, *Journal of the Atmospheric Sciences*, *60*(10), 1270–1296, doi:10.1175/1520-0469(2003)60<1270:JDPIMM>2.0.CO;2, 2003.

Wong, M. H., G. L. Bjoraker, M. D. Smith, F. M. Flasar, and C. A. Nixon, Identification of the 10-μm ammonia ice feature on Jupiter, *Planetary and Space Science*, *52*(5-6), 385–395, doi:10.1016/j.pss.2003.06.005, 2004.

Wong, M. H., S. K. Atreya, W. R. Kuhn, P. N. Romani, and K. M. Mihalka, Fresh clouds: A parameterized updraft method for calculating cloud densities in one-dimensional models, *Icarus*, *245*, 273–281, doi:10.1016/j.icarus.2014.09.042, 2015.

Wulff, P. N., W. Dietrich, U. R. Christensen, and J. Wicht, Zonal winds in the gas planets driven by convection above a stably stratified layer, *Monthly Notices of the Royal Astronomical Society*, *517*(4), 5584–5593, doi:10.1093/mnras/stac3045, 2022.

Yadav, R. K., H. Cao, and J. Bloxham, A Dynamo Simulation Generating Saturn-Like Small Magnetic Dipole Tilts, *Geophysical Research Letters*, *49*(5), doi:10.1029/2021GL097280, 2022.

Yair, Y., Z. Levin, and S. Tzivion, Microphysical Processes and Dynamics of a Jovian Thundercloud, *Icarus*, *114*(2), 278–299, doi:10.1006/icar.1995.1062, 1995.

Yamazaki, Y. H., D. R. Skeet, and P. L. Read, A new general circulation model of Jupiter's atmosphere based on the UKMO Unified Model: Three-dimensional evolution of isolated vortices and zonal jets in mid-latitudes, *Planetary and Space Science*, *52*(5-6), 423–445, doi:10.1016/j.pss.2003.06.006, 2004.

Yamazaki, Y. H., P. L. Read, and D. R. Skeet, Hadley circulations and Kelvin wave-driven equatorial jets in the atmospheres of Jupiter and Saturn, *Planetary and Space Science*, *53*(5), 508–525, doi:10.1016/j.pss.2004.03.009, 2005.

Young, R. E., The Galileo probe: How it has changed our understanding of Jupiter, *New Astronomy Reviews*, *47*(1), 1–51, doi:10.1016/S1387-6473(02)00272-5, 2003.

Young, R. M., and P. L. Read, Forward and inverse kinetic energy cascades in Jupiter's turbulent weather layer, *Nature Physics*, *13*(11), 1135–1140, doi:10.1038/nphys4227, 2017.

Young, R. M., P. L. Read, and Y. Wang, Simulating Jupiter's weather layer. Part I: Jet spin-up in a dry atmosphere, *Icarus*, *326*, 225–252, doi:10.1016/j.icarus.2018.12.005, 2019a.

Young, R. M., P. L. Read, and Y. Wang, Simulating Jupiter's weather layer. Part II: Passive ammonia and water cycles, *Icarus*, *326*, 253–268, doi:10.1016/j.icarus.2018.12.002, 2019b.

Young, R. M. B., and P. L. Read, Simulating Jupiter's weather layer. Part III: Latent heating and moist

convection on a global scale, *Submitted*, 2019.

Zhang, X., Atmospheric regimes and trends on exoplanets and brown dwarfs, *Research in Astronomy and Astrophysics*, *20*(7), 099, doi:10.1088/1674-4527/20/7/99, 2020.

Zuchowski, L. C., P. L. Read, Y. H. Yamazaki, and N. O. Rennó, A heat engine based moist convection parametrization for Jupiter, *Planetary and Space Science*, *57*(13), 1525–1537, doi:10.1016/j.pss.2009.05.008, 2009a.

Zuchowski, L. C., Y. H. Yamazaki, and P. L. Read, Modeling Jupiter's cloud bands and decks. 2. Distribution and motion of condensates, *Icarus*, *200*(2), 563–573, doi:10.1016/j.icarus.2008.11.015, 2009b.